POLITECNICO DI TORINO

Master’s Degree
in Automotive Engineering

Master’s Degree Thesis

Process Development and Characterization of Novel VARTM Fiber-reinforced Thermoplastic Composites

Supervisor
Prof. Giovanni Belingardi
Co-supervisor
Prof. John Montesano

Candidate
Matteo Rosso

Academic Year 2019/2020

Abstract

Fiber-reinforced plastic (FRP) composite materials offer numerous advantages compared to traditional materials, such as very low density, very high strength-to-weight ratio, higher fatigue resistance and better corrosion resistance. For these reasons, FRPs have found large employment in applications where high performance and low components weight are required, as in the aeronautics and wind energy sectors. In the automotive sector, their utilization has been limited mainly in the design of race, high performance or luxury cars. In fact, despite their great advantages, employing FRP materials in vehicles components is more expensive than utilizing common materials like steel and plastics and it is not economically feasible for mass productions. Therefore, a fundamental aspect for increasing the utilization of FRP in the automotive sector is the need to reduce the cost of raw materials and manufacturing processes. Another important aspect in the modern engineering is the possibility of recycling materials and structures. Currently, most FRP composite structures make use of thermosetting resins matrices, which cannot be easily recycled.

The objective of this Thesis was to investigate the use of an innovative acrylic thermoplastic resin for manufacturing glass fiber-reinforced plastic (GFRP) panels using a vacuum assisted resin transfer molding (VARTM) process. The novel thermoplastic resin has a low viscosity and can be processed at room temperature with the same processes typically used for thermosetting-based FRP materials. The thermoplastic resin is also recyclable, and it has higher toughness and fatigue resistance compared to more commonly employed thermosetting resins. The VARTM process enables the production of composite materials at low cost, exploiting the vacuum inside the mold for infusing the resin and consolidating the fiber preform. The acrylic resin, which initially is in its monomeric form, must be mixed with the catalyst prior to infusion. The polymerization can be carried out inside the mold at room temperature, allowing to decrease further the production costs.

The initial part of the work was dedicated to developing the set up for the VARTM process. During the production of flat panels, the main difficulties encountered were analyzed and possible improvements were applied to the process. The infusion system was optimized in order to allow for improved control, avoiding the introduction of air inside the mold and minimizing the waste of resin. The influence on the resin flow given by the position of the inlet and outlet hoses and the direction of the fibers of the preform was studied experimentally.

The second phase consisted in testing the quality of the panels produced in order to validate the manufacturing process. The testing phase was divided in three operations. The acid digestion of the matrix was employed for discovering the fiber volume fraction of the specimens, the microstructure of the material was investigated using optical microscopy and, finally, the material glass transition temperature was found with the dynamic mechanical analysis (DMA). The results showed that the overall quality of the panels was good. The thermoplastic resin was able to impregnate completely the preform, obtaining full fiber wetting and low void content. The polymerization of the resin was carried out correctly.

The thesis includes also a computational work involving the characterization of the growth of microscopic cracks in GFRP tubular test specimen subjected to combined compressive and shear loads using a computational model. The objectives of this work were to model the fracture behavior observed during the experimental tests performed on the tubular specimens in a previous study, and computing the strain energy release rate (SERR) related to the crack initiation and propagation using fracture mechanics-based theory.

To Claudia, Claudio, Giovanni, Michele and Maria

Acknowledgments

I would like to thank Politecnico di Torino and Fiat Chrysler Automobiles Group for having funded the scholarship for the project, and the University of Waterloo for the hospitality.

Many thanks to Prof. Giovanni Belingardi for the support during the mobility period and his mentorship through the years I have spent at Politecnico di Torino.

I would like to express my gratitude to Prof. John Montesano for the opportunity of joining the CRG group, for his guidance and his fundamental suggestions for the development of this project. I have really appreciated the help given me during my visiting period, which allowed me to carry out the research and the experimental work despite of the limitations imposed by the pandemic crisis.

I also want to thank the members of the CRG group and, in particular, Mehdi, Khizar, Farzad and Yu for the availability, suggestions and the time dedicated for helping me with the project.

Thanks to Enrico, Reza and Fares for all the nice moments spent at Waterloo. I am happy to have shared my visiting period with you. Reza, thanks for the help and the suggestions that you gave me for learning how to use Abaqus, which were fundamental for my project.

Many thanks to all the good friends that I had the fortune of meeting at Politecnico di Torino and with whom I shared the path during the years of studies.

Thanks to all my dearest friends for the support and the patience. Now that I have concluded my studies, I will definitely spend more time with you.

I want to thank my parents Claudia and Claudio, and my brothers Michele and Giovanni. You encouraged me to follow my dreams, supporting me during the years of study and giving me the strength to overcome the difficulties. This work, which represents the achievement of one important objective and the beginning of a new chapter of my life, is dedicated to you.

Special thanks to Maria, who encouraged me to take part to the mobility project, despite it meant being distant for seven months. Thank you for your love and support throughout these years. Thanks for having shared with me joys, difficulties, fears and for having been my study partner. This work is dedicated to you, since I could have not reached this objective without you.

Index of Contents

Abstract i

Acknowledgments iv

List of Figures ix

List of Tables xvii

1. Introduction 1

1.1. General Overview 1

1.2. Research Objectives 5

1.3. Project Outline 6

2. Composite Materials 7

2.1 Matrix 7

2.1.1. Polymeric materials 9

2.1.1.1. Thermoplastic polymers 11

2.1.1.2. Thermosetting polymers 15

2.2. Reinforcement 19

2.2.1. Reinforcement materials 23

2.2.1.1. Glass Fibers 24

2.2.1.2. Carbon Fibers 27

2.3. Thermosetting Composites Manufacturing Processes 30

2.3.1. Open Molding of Engineering Composites 31

2.3.1.1. Hand Lay-Up 31

2.3.1.2. Spray-Up 32

2.3.2. Open Molding for Continuous Fiber Composites 33

2.3.3. Filament Winding 34

2.3.4. Pultrusion 35

2.3.5. Compression Molding 36

2.3.6. Resin Infusion Technologies 38
    2.3.6.1. Theoretical considerations of LCM processes 39
        Requirements for high quality LCM components 40
        In-Mold Curing 43
    2.3.6.2. Resin Transfer Molding 44
    2.3.6.3. Vacuum Assisted Resin Transfer Molding 45
        SCRIMP method 46
2.4. Thermoplastic Composites Manufacturing Processes 48
2.5. Mechanics of Continuous Fiber-Reinforced Composites 51
    2.5.1. Unidirectional Composites Properties 51
    2.5.2. Lamina Properties 54
    2.5.3. Laminates Properties 57
        2.5.3.1. Interlaminar Stresses 64
    2.5.4. Damage of Composite Materials 67
        2.5.4.1. Interfacial Debonding 67
        2.5.4.2. Matrix Intralaminar Cracking 68
        2.5.4.3. Interlaminar Cracking (Delamination) 69
        2.5.4.4. Fiber Breakage 69
        2.5.4.5. Void Growth 70
    2.5.5. Fatigue in Composites 71
        2.5.5.1. Unidirectional Composites Longitudinally Loaded 71
        2.5.5.2. Unidirectional Composites Loaded Inclined to the Fibers 73
        2.5.5.3. Fatigue in Laminates 74
3. Literature Review 76
3.1. Thermoplastic GFRP Panels Manufacturing 76
        VARTM Process 76
        Thermoplastic Composites Infusion Processes 77

3.2. Multiaxial Fatigue Characterization of Laminates 79
Characterization of Damage in Composite Laminates during Fatigue 82
4. Thermoplastic GFRP Panel Manufacturing.. 84
4.1. Materials 85
4.1.1. Elium® 188 XO acrylic resin 85
4.1.2. Glass Fiber Reinforcement 87
4.1.3. VARTM Process Equipment 88
4.2. VARTM Setup.. 91
4.3. Results and Process Improvements 100
4.4. Process Validation 113
4.4.1. Acid Digestion Test 114
4.4.1.1. Results 117
4.4.1.2. Discussion 118
4.4.2. Optical Microscopy Analysis... 119
4.4.2.1. 54 g of resin Panel... 119
4.4.2.2. 50 g of resin Panel... 123
4.4.2.3. 46 g of resin Panel... 127
4.4.3. DMA Test 132
4.4.3.1. Results 132
4.4.3.2. Discussion 133
4.5. Discussion.. 134
4.5.1. Manufacturing Process Setting Up 134
4.5.2. Process Validation Tests... 136
5. Ply Crack Growth in GFRP Composites 139
5.1. Energy Release Rate... 141
5.1.1. Manual VCCT Method 144
5.2. FE Model 146

5.2.1. Parts Definition 146
5.2.2. Mesh 150
5.2.3. Parts Merging 152
5.2.4. Material Properties Definition 155
5.2.5. Boundary Conditions 157
5.2.6. Modelling Contact 160
5.3. Post-Processing 162
5.3.1. Uncracked Specimen Stress 162
5.3.2. Crack Surface Displacements 167
5.3.3. Strain Energy Release Rate Calculation 170
5.4. Results 171
5.4.1. Fatigue Tests 173
5.4.2. Friction Effect on SERR 178
5.5. Discussion 182
6. Conclusions 186
6.1. Thermoplastic GFRP Panels Manufacturing 186
6.1.1. Recommendations and Areas of Future Investigation 187
6.2. Ply Crack Growth in GFRP Composites 189
6.1.2. Recommendations and Areas of Future Investigation 190
References 191

List of Figures

Figure 1. Monomers liked together by covalent bonds to form a polymer molecule [10]......... 9
Figure 2. Addition polymerization process [10]. 10
Figure 3. Example of linear and branched chains of a thermoplastic polymer. 11
Figure 4. Comparison between amorphous (a) and semi-crystalline (b) structures of thermoplastic polymers [6]... 12
Figure 5. Elastic modulus versus temperature behavior for a generic amorphous thermoplastic polymer [6]. 14
Figure 6. Schematic representation of the structure of a thermosetting polymer. 16
Figure 7. Comparison between the typical behavior of the viscosity of generic thermosetting and thermoplastic polymers as the temperature changes [10].. 18
Figure 8. Schematic representation of the different types of fabrics obtainable with continuous fibers [10]. Different weaving patterns can be adopted for woven fabric plies. The one represented is a plain weave pattern... 20
Figure 9. Schematic representation of dry fibers bundle (a) and wet fibers bundle (b) [11]... 22
Figure 10 – Average specific strength of various materials [10]. 23
Figure 11 – Average specific elastic modulus of various materials [10]. 24
Figure 12. Glass amorphous 2D structure [6]. 25
Figure 13. Scheme of the marble process for the fabrication of glass fibers [10]. 26
Figure 14. Graphite layer structure (a) and graphite lattice (b) [6]. 27
Figure 15. Scheme of the production process of carbon fibers for PAN or pitch precursor fibers [10]. 28
Figure 16. Manufacturing processes for producing thermosetting composites. 30
Figure 17. Hand lay-up process scheme [10]. 31
Figure 18. Spray-up process scheme [10]. 32
Figure 19. Scheme of an autoclave [20].. 33
Figure 20. Scheme of a filament winding machine [10]. 34
Figure 21. Pultrusion machine scheme [10]. 35
Figure 22. Scheme of a press for compression molding [10]... 36
Figure 23. Different flows inside reinforcement channels [11]. 42
Figure 24. Scheme of Resin Transfer Molding operations [20]... 44
Figure 25. Scheme of VARTM operations [20]... 45
Figure 26. Difference between a VARTM process (a) and a SCRIMP process (b) [20]......... 47

Figure 27. Manufacturing processes for producing thermoplastic composites. 48
Figure 28. Generic unidirectional composite material with randomly dispersed fibers and the principal coordinate system [26]. Material with this configuration are transversely isotropic. 52
Figure 29. Orthotropic lamina with principal (123) and non-principal (xyz) coordinate systems [26]. 54
Figure 30. Sign convention for the orientation of the lamina [26]. 56
Figure 31. Coordinate system and stress resultants for the laminated plate [26]. 57
Figure 32. Scheme of a laminate cross section with the relative numbering system [26]. 59
Figure 33. Coupling phenomena of a composite laminate [10]. 62
Figure 34. Example of special stacking sequences for laminates design [6]. 63
Figure 35. Model utilized by Pipes and Pagano for the analysis of interlaminar stresses in a laminate under uniaxial extension [26]. 64
Figure 36. Distribution of all the stresses from the Pipes and Pagano analysis [26]. The interlaminar stresses are present only in the boundary layer region near the free edge of the laminate. 66
Figure 37. Schematic of fiber matrix debonding in a transversely loaded ply (left image) and coalescence of fiber-matrix debonding in a ply-crack (right image) [28]. 67
Figure 38. Mechanics of interfacial debonding in a continuous fiber composite: (a) perfect laminate; (b) differential deformation of fiber and matrix crack causes high stress at the fiber/matrix interface; (c) when the shear stress exceeds the interfacial shear strength debonding is nucleated [27]. 68
Figure 39. Fatigue behavior of a unidirectional composite subjected to longitudinal tension [27]. 72
Figure 40. Schematic fracture in a unidirectional composite under inclined cyclic load. Fracture happens when one of the cracks present in the matrix grows unstably propagating in the entire cross-section [27]. 73
Figure 41. Schematic of multiple ply cracks inside a laminate [29]. The ply cracks grow through the entire cross-section of the ply propagating along the fibers direction. 75
Figure 42. Development of damage in a composite laminate subjected to tension [27]. 75
Figure 43. Addition polymerization of poly methyl methacrylate from methyl methacrylate monomer [54]. 86
Figure 44. Images of the E-glass non-crimp fabric utilized for the panels: top surface or veil side (left) and bottom surface or stitching side (right) 87

Figure 45. Magnified image of the E-glass fiber rovings and stitching on the bottom surface of the fabric. 87
Figure 46. Airtech Econostich® peel ply. 88
Figure 47. Airtech Greenflow 75 resin distribution mesh. 89
Figure 48. Vacuum bag. 89
Figure 49. Disposition of the four fiber reinforcement plies on the mold. The two bottom layers (left image) had the veil facing the mold while the two upper layers (right image), stacked on the two bottom layers, had the veil facing upward. 91
Figure 50. Peel ply covering the reinforcement layers. 92
Figure 51. Infusion mesh applied on the top of the peel ply. Note the uncovered portion of reinforcement near the outlet side (on the right) to interrupt the quick spreading of the resin toward the suction hose. 93
Figure 52. In the picture is shown how the sealant tape and the inlet and outlet hoses were positioned. 94
Figure 53. The vacuum bag is laid on the sealant tape to close the mold. 94
Figure 54. Series of hoses connecting the mold, the catch pot and the vacuum pump. 95
Figure 55. When vacuum is applied inside the mold, the vacuum bag is pressed on the layer below by the atmospheric pressure. 96
Figure 56. Luperox® AFR40 peroxide is added to the Elium® resin and mixed in order to obtain a uniform mixture. 96
Figure 57. Funnel used as resin reservoir during the infusions. 97
Figure 58. Diffusion of the resin inside the infusion mesh. The seconds passed since the start of the infusion process are reported in each frame. The yellow arrows indicate the position of the flow front in the infusion mesh. 98
Figure 59. Diffusion of the resin through the thickness of the plies and in the last portion of preform, left uncovered from the infusion mesh. The seconds passed since the start of the infusion process are reported in each frame. The yellow arrows indicate the flow front of the resin inside the preform. 99
Figure 60. In the first panel produced the resin was not able to wet completely the plies. In the picture, the position and direction of the inlet and outlet hoses are indicated with blue arrows on the top and on the bottom surfaces. 101
Figure 61. The top and bottom surfaces of the second panel. On the bottom surface it is possible to observe many white horizontal lines, that are the grooves running between the fiber rovings. 102

Figure 62. Inclined non-wetted regions on the upper surface of the third panel produced.... 103
Figure 63. Excessive waste of resin inside the mixing container, inlet and outlet hoses was obtained. 104
Figure 64. New inlet configuration, with the utilization of a funnel as resin reservoir and two clamps in series for controlling the flow of resin. 105
Figure 65. Initial hoses configuration. The inlet was placed at the top left corner of the plies, while the outlet was at the bottom right corner of them. The yellow arrows indicate the direction of the resin flow front inside the infusion mesh, while the orange arrows indicate the direction of the resin flow inside the channels between the fiber rovings. 106
Figure 66. Alternative configuration of the inlet and outlet hoses position. The yellow arrows indicate the direction of the resin flow front inside the infusion mesh, while the orange arrows indicate the direction of the resin flow inside the channels between the fiber rovings. This setup allowed to obtain a symmetric flow front but caused some difficulties in the application of the vacuum bag, therefore it was abandoned. 107
Figure 67. Final configuration adopted for the hoses position. The hoses were placed near the horizontal middle line but they were parallel to the vertical symmetry line. The yellow arrows indicate the direction of the resin flow front inside the infusion mesh, while the orange arrows indicate the direction of the resin flow inside the channels between the fiber rovings.......... 108
Figure 68. Panel produced with 54 g of resin. 109
Figure 69. Panel produced with 50 g of resin. 110
Figure 70. Panel produced with 46 g of resin. 110
Figure 71. Grooves near the inlet side on the bottom surface of the panels. The problem was caused by some resin that was remaining attached to the mold during the part release, causing a damage on the component. 111
Figure 72. Example of samples of different dimensions cut from the panel produced using 46 g of resin. 113
Figure 73. The left image shows the operation of dissolution of the matrix inside the nitric acid solution heated by the hot plate. The right image shows the filtering system utilized for separating the fibers from the solution. 115
Figure 74. Initial specimen (left image) and glass fibers obtained from the matrix digestion (right image). 115
Figure 75. Position of the samples cut from the 54 g panel. The panels A, B and C were utilized for the acid digestion test while M_1 and M_2 were analyzed with the optical microscope...... 119
Figure 76. Microscope images of sample M1 cross-section. 120

Figure 77. 25X image of the sample M2 cross-section. 121
Figure 78. 100X images of region A (left image) and region B (right image). The red circles highlights the presence of a void on the vacuum bag side surface. 122
Figure 79. 100X (right) and 200X (left) images of region C. 122
Figure 80. 500X images of two tow of fibers of sample M2. 122
Figure 81. Position of the samples cut from the 50 g panel. The panels A and B were utilized for the acid digestion test while M_{IN} and M_{OUT} were analyzed with the optical microscope. A yellow line highlights the cross sections of the samples that were analyzed with the microscope. 123
Figure 82. 25X image of the sample M_{IN} cross-section. 124
Figure 83. 100X images of regions A (top left image), B (bottom image) and C (top right image). The red circles highlight the voids. The bottom image shows a deep valley caused by a void on the surface that was in contact with the vacuum bag. 124
Figure 84. 100X image of the region D of the cross-section. The dimension of a void have been measured. 125
Figure 85. 50X image of the regions D and E of the cross-section. The red line placed on the higher crest highlights the variation in the thickness of the sample. Voids are highlighted by the red circles. 125
Figure 86. Sample M_{OUT} cross-section images with different levels of magnification (25X, 100X and 200X). 126
Figure 87. Position of the samples cut from the 46 g panel. The panels A, B, C and D were utilized for the acid digestion test while M_{IN}, M_1 and M_2 were analyzed with the optical microscope. A yellow line highlights the cross section of the samples that was analyzed with the microscope. 127
Figure 88. Sample M_{IN} cross-section images with different levels of magnification (25X, 100X and 200X). Defects are highlighted by red circles. 128
Figure 89. Sample M_1 cross-section images with different levels of magnification (25X, 100X and 200X). 129
Figure 90. Images of fiber rovings (500X and 1000X) 130
Figure 91. Sample M_2 cross-section images with different levels of magnification (25X, 100X and 200X). 131
Figure 92. DMA test results of the samples cut from the panel produced using 48 g of resin. 132

Figure 93. DMA test results of the samples cut from the panel produced using 50 g of resin. 133
Figure 94. Schematic representation of the circumferential propagation of transverse compressive cracks in the tubes [19]........ 140
Figure 95. Schematic of a 3D crack in a solid material with the local reference system defined along the crack line [60]........ 141
Figure 96. The three modes of crack surface displacement [61]. 142
Figure 97.Schematic of VCCT procedure for computing the SERR [60]. 144
Figure 98. Upper (left image) and lower (right image) halves of the unidirectional layers. It is possible to notice the inclined surfaces defined for modelling the crack surface........ 147
Figure 99. Example of cylinder used for modelling the internal and external woven plies... 148
Figure 100. Upper (left image) and lower (right image) halves of the tubular specimen...... 149
Figure 101. Tubular specimen obtained from the assembly of the various parts........ 149
Figure 102. Seed applied on the upper unidirectional layer........ 150
Figure 103. Upper unidirectional layer meshed........ 151
Figure 104. External upper woven layer meshed........ 151
Figure 105. New meshed parts obtained from merging the nodes of the unidirectional and woven fabric layers. 152
Figure 106. Set of nodes utilized for applying the tie constraints of the woven fabric layers (left image) and unidirectional layers (right image). 154
Figure 107. The crack surfaces were simulated by unconstrained regions (regions of nodes excluded from the tie constraint). The crack was expanded by removing radial row of nodes from the set. In the example, it is possible to observe the set of nodes for the uncracked specimen and for increasing crack opening angles (COA). 154
Figure 108. Orientation of the material properties in the unidirectional plies. 155
Figure 109. Orientation of the material properties in the woven fabric plies. 156
Figure 110. Displacement constraints on the lower surface of the tubular specimen model. 157
Figure 111. Compressive stress applied on the upper surface of the unidirectional layer..... 158
Figure 112. Shell element used for simulating the aligning fixtures on the upper side of the tubular specimen. 158
Figure 113. Boundary conditions applied on the tubular specimen model........ 159
Figure 114. Mises stress and total displacement on the upper crack surface for 11° COA. Contact Pairs algorithm stress and displacement (images 1 and 3 respectively) are compared with those obtained with General Contact algorithm (images 2 and 4 respectively)............ 161

Figure 115. Mises stress and total displacement on the upper crack surface for 50° COA. Contact Pairs algorithm stress and displacement (images 1 and 3 respectively) are compared with those obtained with General Contact algorithm (images 2 and 4 respectively)............ 161
Figure 116. Shear stress S23 induced by the torsion load represented in the cylindrical reference frame.. 162
Figure 117. Example of circular path of nodes utilized for extracting the values of the stress on the inclined surface of the tubular specimen model.. 163
Figure 118. The stress values extracted were referring to the cylindrical reference frame (yellow) and subsequently transformed in the reference frame laying on the crack surface (red). 163
Figure 119. Values of the compression stress S33 along one circular path of nodes on the inclined surface for the uncracked specimen (top image) and for a specimen with 120° COA (bottom image). The stress values of the uncracked specimen and of the uncracked region of the specimen with the crack are the same. 166
Figure 120. Compression stress S33 (cylindrical reference frame) for a specimen with 120° COA. The color pattern shows how the stress remains constant until one row of elements before the crack surface.. 166
Figure 121. Magnitude of the displacements on the upper (top image) and lower (bottom image) inclined surfaces for 50° COA. The crack surfaces can be recognized by the different color distributions.. 167
Figure 122. Path of nodes utilized for extracting the nodal displacements on the crack surfaces. 168
Figure 123. Mode II SERR for frictionless compression-torsion crack propagation. Results obtained with effective stress on the crack surface equal to 1 MPa..................................... 171
Figure 124. Mode III SERR for frictionless compression-torsion crack propagation. Results obtained with effective stress on the crack surface equal to 1 MPa..................................... 171
Figure 125. Mode II SERR comparison between the results obtained from the simulation procedure and those calculated starting from the results of 1 MPa stress case..................... 175
Figure 126. Mode III SERR comparison between the results obtained from the simulation procedure and those calculated starting from the results of 1 MPa stress case..................... 176
Figure 127. Mode II SERR results for the different load cases. 176
Figure 128. Mode III SERR results for the different load cases. 177
Figure 129. Total SERR results for the different load cases... 177

Figure 130. Comparison of the Mode II SERR between the frictionless case and the friction f = 0.3 case for 1 MPa of effective tangential shear stress. 178

Figure 131. Comparison of the Mode III SERR between the frictionless case and the friction f = 0.3 case for 1 MPa of effective tearing shear stress. 179

Figure 132. Comparison of the Mode II SERR between different friction coefficients for 1 MPa of effective tangential shear stress. 179

Figure 133. Comparison of the Mode III SERR between different friction coefficients for 1 MPa of effective tearing shear stress. 180

Figure 134. Comparison of the Mode II SERR between different friction coefficients for the load case $0.8\ F2C - \lambda 12 = 0.4$. 181

Figure 135. Comparison of the Mode III SERR between different friction coefficients for the load case $0.8\ F2C - \lambda 12 = 0.4$. 181

Figure 136. Mode I and Mode II SERR related to the crack propagation of a GFRP tubular specimen subjected to combined tensile and torsion loads [44]. The trend is similar to those of the Mode II and Mode III SERR in this thesis. 182

Figure 137. S-N data for $\lambda 12 = 0.21$. Diamond markers represent data points obtained at 10 Hz, while circle markers represent data points obtained at 5 Hz [19]. 184

Figure 138. S-N data for $\lambda 12 = 0.4$. Diamond markers represent data points obtained at 10 Hz, while circle markers represent data points obtained at 5 Hz [19]. 184

List of Tables

Table 1. Average chemical composition, in percentage on the total weight, of the most common glass fibers [6]. 25

Table 2. Average mechanical properties for different carbon fiber types (data taken from [10]) 29

Table 3. Mechanical properties of non-reinforced cured Elium 188 XO resin [36]. 85

Table 4. The table contains the measurements and the results of the acid digestion test. 117

Table 5. Elastic properties of the unidirectional GFRP plies [19]. 155

Table 6. Elastic properties of the woven fabric GFRP plies [19]. 156

Table 7. Loading conditions of the tubular specimen during the simulations for finding the uncracked specimen stress state. 174

Table 8. Effective Mode II tangential shear stress and Mode III tearing shear stress on the inclined surface of the model. 174

1. Introduction

1.1. General Overview

During the last forty years, the automotive field has faced a continuous increase in the average vehicle weight due to the improvements in the safety, comfort and technological levels of the cars. The need for increased passenger comfort while also respecting more severe safety standards in order to homologate the cars on the markets, have led to an overall increase of the dimensions and of the weight of modern vehicles. Since a higher vehicle weight negatively affects the performance and causes higher fuel consumption and vehicle polluting emissions, this has become a problem for the car manufacturers. In fact, in the last few years the environmental regulations related to vehicles have been continuously updated and have become increasingly strict in most countries around the world. For example, the *Regulation (EU) 2019/631* [1] limits the CO_2 fleet average emissions on new passenger cars to 95 gCO_2/km starting from January 2020, with further reductions of 15% and 37.5% with respect to the 2021 target starting from 2025 and 2030 respectively. When failing to comply with this regulation, a fee equal to 95 € per each exceeding gCO_2/km is imposed on each newly registered vehicle [1]. For this reason, car manufacturers are motivated to respect this regulation in order to avoid highly penalizing fines.

In this current scenario, lightweighting assumes a crucial role for the future of the automotive industry. Reducing the vehicle weight can directly lead to a decrease in the fuel consumption and the related polluting emissions, and an increase of the vehicle performance. Several studies have highlighted that a 10% reduction in the weight of a car can lead to a reduction in the fuel consumption by about 6-8 % while maintaining constant the vehicle performance through the resizing of the engine [2]. Lightweighting is also important for electric cars even if the vehicle emissions are almost null. In fact, by reducing the weight of the car, it is possible to obtain higher range from the batteries or utilizing smaller batteries and motors while maintaining performance and range constants [3].

Initially, lightweighting was achieved by using plastic materials in non-structural components of the vehicle. However, since plastics are now widely employed in cars, the next approach for obtaining further weight reductions is to redesign structural components by utilizing innovative materials [4]. In the last years, many innovative materials have been used for designing components of the vehicles, such as light aluminum alloys, magnesium alloys or ultra-high strength steels, which can reach the same performance of the conventional steels requiring less material and so allowing to reduce the overall mass of the components. Among these novel materials, the most outstanding weight savings can be obtained adopting fiber-reinforced plastic (FRP) composite materials, such as glass or carbon fiber-reinforced plastics. Owing to their high strength-to-weight and stiffness-to-weight ratios, FRP composites enable the production of components with the same or improved performance of conventional structural materials while reducing weight. FRPs have several other advantages compared to the traditional materials employed in the automotive industry, such as higher fatigue resistance, good corrosion resistance and improved crashworthiness, which is fundamental for designing body elements [5, 6]. Moreover, the anisotropy of the mechanical properties can be exploited in order to obtain tailor-made materials, which allows to optimize the components design in order to obtain the maximum performance during service [6].

Despite all the great advantages, there are some difficulties that must be faced when FRP are employed for producing vehicles components. The main problem is the higher cost of these composites with respect to the traditional materials used for vehicle structural components, such as ultra-high strength steel and high-strength aluminum. This is due to the high cost of the raw material, especially in the case of carbon fiber composites, and the manufacturing processes needed for obtaining high quality parts. The other important issue is the complexity and the high economic effort required to adopt the manufacturing processes of composites on large-scale productions [5]. For these reasons, the utilization of FRPs in passenger vehicles have been mostly limited to high performance and luxury cars, targeting a niche market, while their employment in mass produced vehicles has been limited to date. Therefore, the current challenge for researchers and car manufacturers is to reduce the raw material and manufacturing costs of FRP vehicle structures, while also maintaining the high performance requirements such as fatigue performance. This will allow for a more widespread utilization of FRP composites in the automotive sector.

Another field in which the utilization of composite materials is fundamental is the wind energy sector, which is always more adopted as sustainable source for producing energy. Since the length of the blades in wind turbines with power generation capacity in the order of MW is usually >25 m, FRP composites are the only materials that enable structures to retain high performance in strength and stiffness while maintaining low mass. Moreover, the need to increase power generation capacity and efficiency is leading to an increase of the wind turbines dimensions, with relative increase in weight [7]. Therefore, the principal objective of the wind turbine manufacturers is to reduce the weight of the blades and the gravitational loading on the blade structure. Wind turbine blades are typically produced using glass fiber reinforcements and epoxy resin through resin infusion processes, but recently also carbon fibers composites have been used for certain structural areas of the blades in order to decrease their weight [8, 9]. The main advantage of having lighter blades structures is a reduced gravitational loading, which improves the blades lifetime. Moreover, also the inertia of the system is reduced, allowing the use of less robust turbine and tower components since the solicitation on them are reduced. In conjunction with the research of lighter materials, also reducing the cost of raw materials and manufacturing processes is an objective of primary importance that will allow a further increase in the utilization of this renewable energy source for decreasing the environmental pollution.

For the production of FRP composites, two different classes of plastics are used as the matrix material, namely thermosetting and thermoplastic polymers. At present, most FRP composites adopt thermosetting materials as the matrix, such as epoxy and polyester resins. The choice is due to the low viscosity that characterizes the liquid thermosetting resins before they undergo the process of curing, which facilitate the manufacturing processes allowing easy fiber wetting [10, 11]. The utilization of thermoplastic polymers in FRP composites has been limited because of their high viscosity when they are in liquid state. Manufacturing fiber composites with thermoplastics also requires very high temperatures in order to melt and decrease the viscosity of the resin, which however remains higher than that of thermosetting, and this causes considerably higher production costs. Nevertheless, in recent years, studies have been conducted with the purpose of overcoming this limitation in order to increase the utilization of fiber-reinforced thermoplastic composites and take advantage of their benefits. Thermoplastic materials have higher ductility and toughness than thermosetting polymers, which can have beneficial effects on the fatigue behavior of FRP composites. Studies have demonstrated how thermoplastic resins have higher fatigue resistance with respect to thermosetting ones [12, 13]. In addition, the stiffness degradation under fatigue loadings, which is a typical behavior of composites structures, has found to be lower in thermoplastics [12, 14]. The higher fracture toughness of thermoplastics compared to thermosetting allows increased specific energy absorption capabilities, which improve the crashworthiness that is a fundamental property for the utilization of FRP composites in vehicle body structures [5, 15]. Finally, since thermoplastic polymers can be melted for a repeated number of times, thermoplastic composites can be thermoformed, welded and recycled. Recyclability is one of the main advantages of thermoplastic composites over thermosetting ones, since it allows to design components that will not be completely wasted at the end of life, reducing the environmental impact. Moreover, in some engineering sectors, as the automotive, there are some regulations that set minimum targets of recyclability that must be respected in order to sell the products on the markets [16]. Therefore, the advantage of recyclability can favor an increase of the utilization of composite materials.

Another important aspect of composite materials is their long-term durability characteristics when subjected to cyclic loading, since fatigue is cause of most of the failures in dynamic applications. As it was reported above, composite components can undergo stiffness degradation during cyclic loading caused by microscopic damage evolution. This particular behavior is important for applications where maintaining a high stiffness is fundamental for efficient operation, such as wind turbine blades or automotive applications like driveshafts, leaf springs and body components. For this reason, there is the need to improve our understanding of the fatigue performance of composite structures in order to exploit the maximum performance from them.

1.2. Research Objectives

The scope of this thesis was developed through a collaboration between the Composites Research Group (CRG) at the University of Waterloo and Borrum Energy Solutions (BES), which is a manufacturer of domestic microgeneration wind turbine blades in Southwestern Ontario [17]. The overall goal of the thesis was to support the design and fabrication of the blades for a new microgeneration of wind turbine product.

The first objective of the project was the development and optimization of the setup for a Vacuum Assisted Resin Transfer Molding (VARTM) manufacturing process in order to produce unidirectional (UD) non-crimp fabric (NCF) glass fiber-reinforced plastic (GFRP) panels using an innovative thermoplastic resin for the matrix material. The novel resin developed by Arkema [18] allows to produce thermoplastic composites using the same manufacturing methods commonly employed for thermosetting materials.

The second objective was the validation of the process through quality testing on the panels produced, investigating the microstructure of the material with optical microscopy, finding the material glass transition temperature using dynamic mechanical analysis (DMA) and performing acid digestion of the matrix in order to find the fiber volume fraction of the specimens.

The third objective of the thesis was to characterize the growth of microscopic cracks in GFRP tubular specimens subjected to combined compressive and shear loads. The fracture behavior observed during experimental tests, which were performed in a previous study [19], was modelled using the commercial finite element software Abaqus CAE. The strain energy release rate (SERR) corresponding to the initiation and propagation of ply cracks was computed using fracture mechanics-based theory.

1.3. Project Outline

The experimental work was divided in two main phases, which were the setting up of the VARTM process and the quality testing of the specimens. Initially, a research on the equipment needed for preparing the VARTM setup was developed performing a literature survey of similar works (Chapter 3). When all the supplies were delivered, it was possible to start the preparation of the process and manufacturing of flat panels (Chapter 4). The first panels were realized with a trial glass fabric reinforcement, since at the beginning it was important to gain confidence with the operations and therefore was preferable to not waste the UD-NCF material of interest. During this phase, different problems were encountered and possible solutions were implemented in order to solve them and optimize the process. When enough experience was obtained, the production of panels with the correct reinforcement started. The second phase consisted in characterizing samples obtained from some of the panels produced, with the purpose of verifying the quality of the components and validating the process (Chapter 4). The testing phase was divided in three operations. The acid digestion test was employed for discovering the fiber volume fraction of the specimens, the microstructure of the material was investigated using optical microscopy and finally the material glass transition temperature was found with the dynamic mechanical analysis (DMA).

The numerical work of the thesis started with a literature survey aimed in gaining knowledge in the fracture mechanics field and selecting the most suitable method for the computation of the strain energy release rate (SERR) for ply crack initiation and propagation (Chapter 3). After that the method was chosen, some preliminary simulations were performed in Abaqus CAE in order to learn the application of it on the models. When this preliminary operation was concluded, the final model was built and the simulations of crack propagation on the tubular specimens were performed (Chapter 5).

2. Composite Materials

A composite material can be defined as a manufactured material consisting in two or more chemically distinct constituents, properly arranged together but separated by an interface, of which properties are considerably different from those of the original phases taken alone [6]. The continuous constituent is called *matrix*. The objective of adding another material is improving the properties of the matrix one, so the other constituent is known as *reinforcement*.

In the following chapters, the fundamental theory of composite materials is presented. Initially the matrix and reinforcement materials are analyzed, and then the main production processes for realizing FRP composites are described. Finally, the mechanical properties, damage mechanisms and fatigue behavior of composite materials are discussed from a theoretical point of view.

2.1 Matrix

The matrix has the function of giving shape to the component, keeping the fibers in position, transferring the load to the fibers and protecting them from the external environment [10]. Moreover, the matrix properties have a dominant influence on the shear strength of the composites. The load applied on the component is taken by the matrix and transferred to the fibers through shear at the fiber/matrix interface, causing axial stresses on the fibers [11]. In order to achieve an effective load transfer from the matrix to the fibers and obtain the maximum performance from a composite material, there are two important requirements. First, the fibers must be completely surrounded by the matrix phase. This is possible if the matrix completely consolidates or wets the fibers during processing. This condition is influenced by the surface roughness of the fibers, the viscosity of the resin (affected by temperature), the processing pressure and the surface energy of the two phases. Second, the bond between the fibers and matrix must be sufficient to allow for adequate load transfer. There are two types of bonds that can form, namely mechanical and chemical bonds. Mechanical bonds are influenced by the surface roughness of the fibers, while the sizing coated on the fibers promotes an indirect chemical bond between the fibers and matrix [6].

Complying with these two requirements is fundamental for obtaining a good fiber/matrix interface and it influences the choice of the matrix material. The materials that can be utilized for the matrix of a composite component can be polymeric, metallic or ceramic. The most common types of composite materials, particularly for structural applications, use polymeric matrix materials. The density of polymers is much lower than that of metals and ceramics, thus higher specific properties for the composites can be obtained. Moreover, processing polymeric composites is easier than manufacturing those with metallic and ceramic matrices. In order to obtain good fiber wetting, there is the need of having thermodynamic compatibility between fibers and matrix, which is a condition that verifies when the surface energy of the liquid matrix is lower than that of the solid fibers [11]. Polymers in liquid state usually have the surface energy lower than that of the fiber reinforcements commonly used (e.g. glass, carbon and aramid fibers), therefore they have high thermodynamic compatibility. Metals and ceramics, instead, have very high surface energy in liquid state that causes low thermodynamic compatibility with many reinforcement systems. The lower is the compatibility, the more difficult is the wetting process between the matrix and the fibers and, consequently, the production process [11]. The processing temperatures for producing metal and ceramic matrix composites are usually very high, thus implying high manufacturing costs with respect to polymers composites. Metallic and ceramic matrices therefore are used only when particular performance is required at high temperatures, since polymers have lower melting and degradation temperatures with respect to them.

2.1.1. Polymeric materials

Polymers are formed by many molecular units, called *monomers*, linked together by strong covalent bonds to form long chains through a process called *polymerization*. The unitary long chain, shown in Figure 1, is called *polymer molecule*. When the polymer is in its liquid form it can be called a *resin*, and when it is cast into a solid it can be called a *plastic* [10].

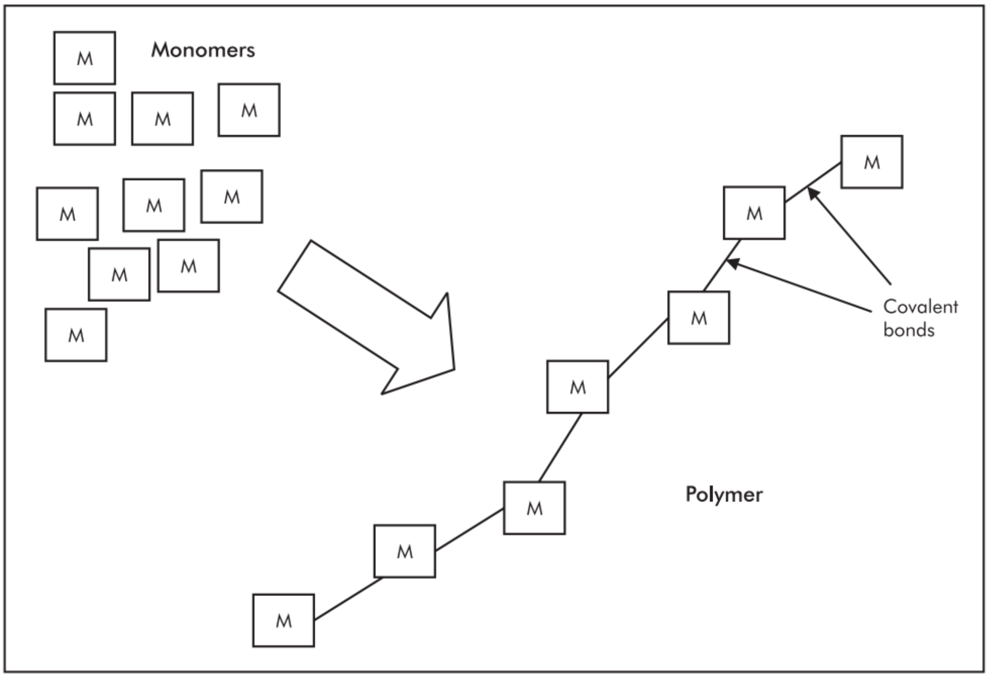

Figure 1. Monomers liked together by covalent bonds to form a polymer molecule [10].

The polymerization process can occur through several processes, but the two most common are the *addition polymerization* and the *condensation polymerization*. The matrix material utilized in this work undergoes an addition polymerization, thus the following discussion will be focused on this process. In the addition polymerization, the resin monomer is combined with a catalyst, such as peroxide, to initiate the chemical reaction [10]. The catalyst molecules are activated once mixed with a high concentration of the resin monomers. The activated catalyst molecules, called *free-radicals*, become highly reactive since they have an unpaired electron. The free-radical tends to take an electron from a near molecule with a weak bond, in order to pair it with its unpaired electron. The easiest molecule with which react is a monomer, since there is a high concentration of them inside the resin, that gives an electron to the free-radical and becomes bonded with it. After this reaction, also the monomer becomes activated, since it presents an unpaired electron. At this point, the activated monomer reacts with another monomer in the same way described before, and the new monomer is added to the chain and becomes active. The reaction can continue many times and the polymer molecule can become very long. The addition polymerization reaction can end by means of a terminating agent, added to the resin, or through contamination or reaction of the chain with second constituents of the mixture [10]. One powerful terminating agent are the unreacted molecules of peroxide, that is the same catalyst added for starting the reaction. For this reason, the quantity of peroxide added to the monomeric resin must be chosen carefully. The amount of it must be high enough in order to start the reaction with several monomers, but not excessive in order to avoid its interference with the chain growth. A scheme of the addition polymerization process can be observed in Figure 2.

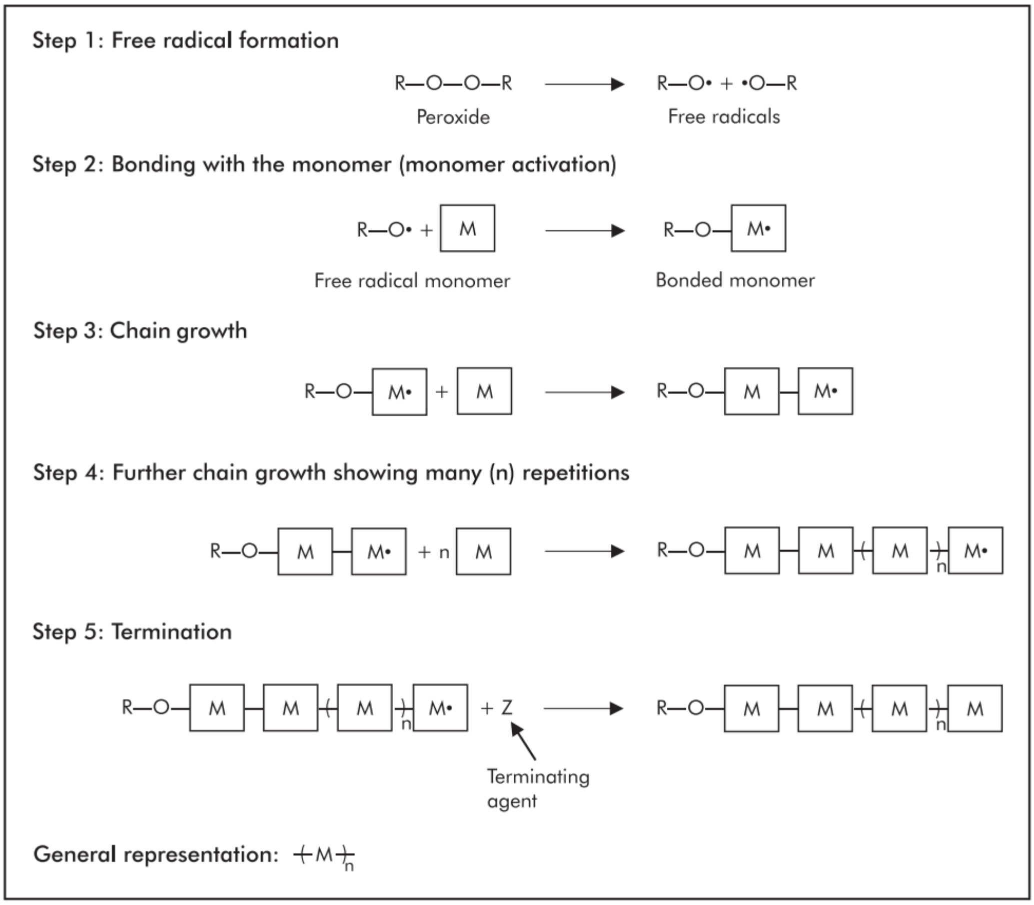

Figure 2. Addition polymerization process [10].

The length of the polymer molecules, which is proportional to the number of monomers in the chain or the degree of polymerization, can be characterized by the molecular weight. Polymers with longer molecular chains have higher molecular weight; however, since the length of the chains within a polymer can vary an average value of molecular weight is assigned.

Some important properties of polymers depend on the length of the molecules. Polymers with high molecular weights usually have high mechanical properties as strength, stiffness and toughness, but also high melting temperature and high viscosity in liquid form, that make their processing more difficult [10].

The polymers can be distinguished in two families, called thermoplastics and thermosetting, characterized by their molecular structure.

2.1.1.1. Thermoplastic polymers

Thermoplastic materials are characterized by long chains of repeating units, which can be linear or branched, as shown in Figure 3. When the material is in its solid state, other secondary interactions can be created between molecules. These weaker bonds are due to van der Waals' forces and are generally one order of magnitude lower than the primary covalent bonds. Nevertheless, their action on the material is evident, since they keep the atoms in position limiting their movements and giving stiffness to the solid polymer. Polymerized thermoplastic materials are solid at room temperature [10].

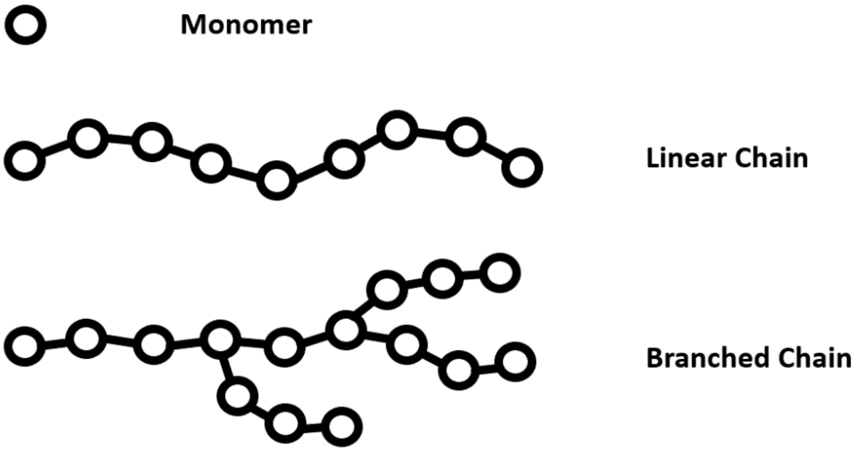

Figure 3. Example of linear and branched chains of a thermoplastic polymer.

The long chains are entangled together to form the microstructure of the thermoplastic polymer, which can have two main forms. When the structure has chains organized randomly, the material is called *amorphous*. When instead inside an amorphous structure are present some regions in which the chains are organized and parallel, forming crystals, the material is called *semi-crystalline*. The difference between an amorphous structure and a semi-crystalline one can be observed in Figure 4. Starting from the thermoplastic polymer in its liquid form it is possible to obtain a microstructure either amorphous or with different levels of crystallinity, depending on the cooling rate [20]. In fact, when the polymer is liquid, the molecules can move freely inside the melt. If the cooling rate is high, the van der Waals' forces that are generated between molecules form quickly limiting the creation of crystalline regions and resulting in an amorphous molecular structure. Instead, if the resin is cooled slowly, the molecules have the time for organizing in regular crystals, that is the configuration with the lowest energy state, and a semi-crystalline microstructure can be obtained. Other parameters influencing the degree of crystallinity are temperature, pressure and molecular weight, but the most effective is the cooling rate. The molecular structure of a polymer cannot be completely crystalline, so the material will always have some amorphous regions and for this reason will be semi-crystalline. Therefore, starting from the same material in liquid form, two different microstructures that have different properties can be obtained. Amorphous materials have lower shrinkage, a wide melting temperature range and lower resistance to chemical agents with respect to semi-crystalline, which instead show a higher shrinkage because the crystals occupy less volume than a random entanglement.

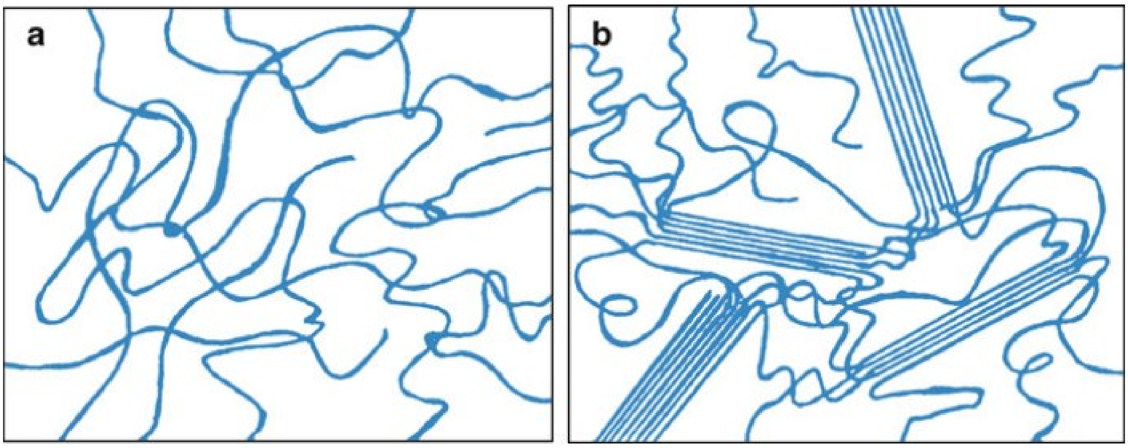

Figure 4. Comparison between amorphous (a) and semi-crystalline (b) structures of thermoplastic polymers [6].

The understanding of the thermal behavior of polymers is of extreme importance, since a large difference in the properties can be obtained at different temperatures. As described previously, in the solid state the thermoplastic polymers have a microstructure with the chains entangled together and with weak secondary bonds between molecules that limit their mobility. This configuration gives stiffness and hardness to the material. As the temperature increases, the mobility of the molecules, under the form of vibrations and rotations around the fixed position, increases too. At a certain point, they become high enough to break the secondary order attractions between the molecules, which allows the molecules to move more freely in the lateral direction. However, the entanglements of the chain are still acting as a constraint. In this situation, the material becomes soft but still solid, assuming a behavior similar to that of rubbers. The range of temperature at which this change of stiffness happens is called *glass transition temperature* (T_g). The change in elastic modulus is more evident in amorphous thermoplastics, since the crystalline structure in semi-crystalline thermoplastics keeps the molecules in position [20]. With a further increment of the temperature, the movements of the atoms composing the molecules become so high that they start to disentangle. When the molecules are disentangled, they can move freely inside the material structure and, when a complete disentanglement is reached, the material is in its liquid state. The temperature at which the material becomes liquid is called *melting temperature* (T_m). It is important to understand that T_m for the thermoplastic polymers is not a precise temperature but the change of state occurs in a range of temperatures, since the disentanglement of the chains is not immediate. The melting temperature range can be very wide (30-40 °C) in the case of amorphous thermoplastics, since the chains are highly entangled and organized randomly, while it is narrow (2-3 °C) in the semi-crystalline thermoplastics, because the crystalline regions have a precise melting point. The higher is the average molecular weight of the material, the higher will be its melting temperature range, since the chains will be longer and so more entangled. The general trend of the elastic modulus variation with respect to the temperature for amorphous materials can be observed in Figure 5.

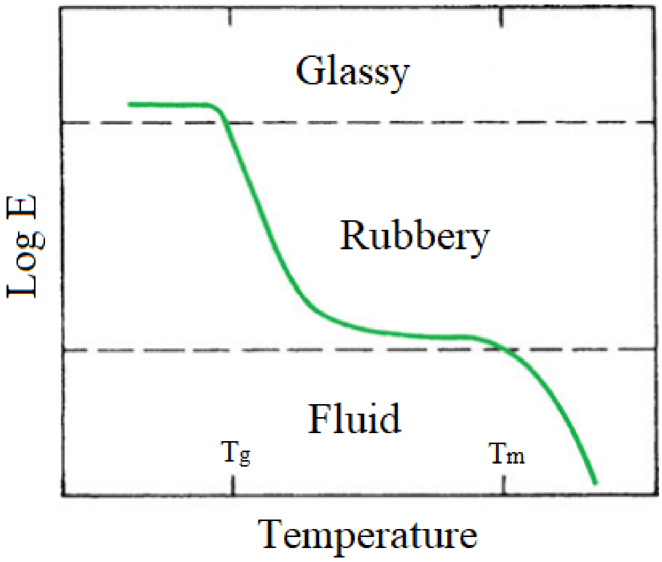

Figure 5. Elastic modulus versus temperature behavior for a generic amorphous thermoplastic polymer [6].

If the rise of temperature continues even after the material is melt, the vibrations and translations of the atoms inside the molecules become so high that can break the primary bonds inside the chains, destroying them. This temperature is called *degradation temperature*, since after that this phenomenon happens the polymer cannot be utilized anymore. The degradation temperature is generally very high and the polymer can oxidize, becoming similar to charcoal [10].

The most important aspect of thermoplastic polymers, that is also the greatest difference between them and the thermosetting, is that they can be melted and then reshaped in solid form numerous times [11]. This is an important advantage for the manufacturing aspect, since they can be worked in liquid form, thermoformed and welded. Moreover, they can be recycled at the end of their life cycle, and this is a fundamental aspect for obtaining an environmentally sustainable production and respecting recycling regulations present in some sectors as the automotive industry. Other advantages of the thermoplastic materials are the absence of shelf life and the short cycle time in processing, since when they are cooled down from the liquid state they become quickly solids. The most appreciated mechanical characteristics are their higher ductility and higher fracture toughness compared to the thermosetting polymers. The former can be explained by the presence of the secondary bonds between molecules and molecular entanglement, that are going to disappear with rising temperature, while the latter is due to the large free volumes present in the amorphous structure, that can absorb the crack propagation energy [6, 11].

Nevertheless, thermoplastic materials have a disadvantage that have limited their utilization in the composite materials applications. In fact, the viscosity of a thermoplastic material in its liquid state is much higher than that of an uncured thermosetting resin. This is because the polymer molecules of thermoplastics are very long and entangled, so more effort is required to promote flowing. The higher the viscosity, the more difficult is the flow of the resin through the fibers and the capacity of wetting them completely. This can cause a higher occurrence of voids in the final component [11]. The viscosity can be decreased using high processing temperature and applying high pressures if the material has to be injected, but this requires more energy and more expensive tooling that increase the manufacturing costs. However, even applying these parameters, the viscosity remains higher than the thermosetting one. For this reason, although thermoplastics are the most utilized polymers in the global plastic market, considering the FRPs market only 20% of the components are realized with these materials [10].

2.1.1.2. Thermosetting polymers

Polymerized thermosetting resins typically have notably shorter molecular chains when compared with thermoplastic resins, with no interactions between the molecules. Thus, they are generally liquid at room temperature and not useful as structural materials. A second chemical reaction denoted as *curing* is required to solidify thermosetting resins [10]. Once cured, strong covalent bonds called *cross-links* form between the atoms of different molecules as can be seen in the schematic of Figure 6, which depicts a typical amorphous molecular structure. The curing process begins by adding linking molecules called curing agents to the resin. The curing agents react with the polymer molecules creating cross-links between them. Typically, the reaction needs an initiator, which is a chemical agent added to the liquid resin for starting the cross-linking process. The curing process for conventional thermosetting resins is usually long and can require hours if not days to be completed. This is a disadvantage of thermosetting resins, since the processing time is higher than that of thermoplastics. Nevertheless, it is possible to take advantage from this factor because the process can be interrupted by lowering the temperature or adding inhibitors in order to obtain a partially cured resin. This principle is exploited for obtaining preimpregnated layers, called *prepregs*, which are layers of fibers already impregnated with the matrix material and stored at low temperature. In this way, they can be manufactured by specialized companies, stored at low temperatures and transported to the final user, which will work them in the final shape and will complete the curing process [11]. The most utilized thermosetting resins for the production of composites are epoxies and polyesters.

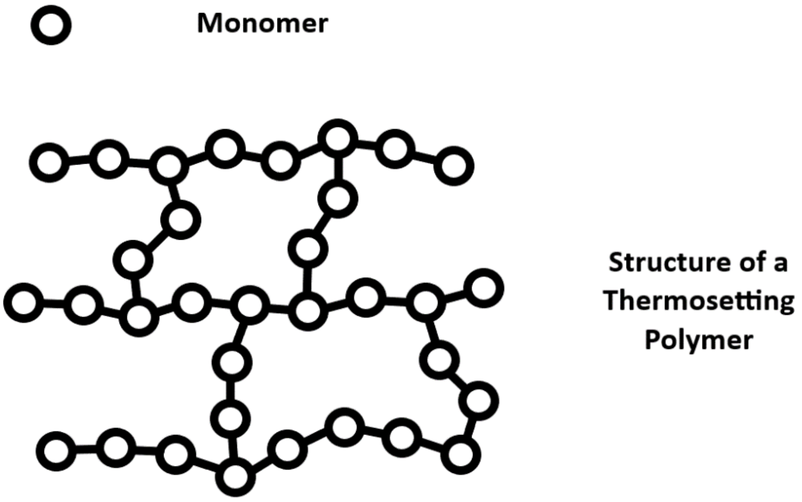

Figure 6. Schematic representation of the structure of a thermosetting polymer.

The strong interactions between different polymer molecules that are created during curing keep the atoms firmly in their position, limiting their movement to a greater extent than what is done by secondary order interactions and entanglements in thermoplastic materials. For this reason, thermosetting polymers are stiffer and harder than thermoplastic materials. However, this brings also disadvantages, because thermosetting polymers have lower fracture toughness and so show higher brittleness.

From the point of view of thermal behavior, the presence of cross-links limits the movement of the atoms even at high temperatures and, since the intra-molecular bonds are very strong, they cannot be broken rising the temperature like it happens with the secondary order bonds of thermoplastic materials. The glass transition temperature becomes very high in a cross-linked thermosetting and, therefore, these materials have a higher thermal stability. The most particular aspect of thermosetting polymers is that they cannot be melted after that they are cured. If they are subjected to very high temperatures they reach decomposition without becoming liquid, so they are not recyclable [10, 20].

The main advantage of thermosetting polymers for the manufacturing of composite materials is the very low viscosity of the resin before of the curing process. This property is due to the length of the molecules chains, which are shorter than that of thermoplastic materials. The low viscosity allows the resin to penetrate easily inside the reinforcement, ensuring a complete wetting of the fibers. The curing is obtained after that the fibers are completely impregnated, allowing the material to solidify in the required shape. This advantage in the manufacturing process has made thermosetting the most utilized materials for the matrix of composites. A comparison between the viscosities of thermosetting and thermoplastics as the temperature changes is shown in the graph of Figure 7. The viscosity of the thermosetting polymers has a particular behavior, since it depends on two different phenomena that take place simultaneously. These are the viscosity decrement due to the rise of temperature and the cross-linking process, which instead increases the viscosity and occurs more rapidly at high temperatures. The resulting viscosity trend, represented with the continuous red line in Figure 7, can be divided in two regions. In the first region, the effect of the reduction of resin viscosity due to the temperature increment is predominant and viscosity is reduced. As temperature increases, the cross-linking process increases and always more molecules begin to crosslink. This has an opposite effect on the viscosity that tends to grow. Overall, the viscosity reaches a minimum, then starts increasing faster until the gelation point is reached and the resin becomes solid [10]. The process is not reversible and, obviously, the fibers impregnation must happen in the first region of the curve in order to exploit the advantage of the lower viscosity of the material. A typical viscosity range for thermosetting resins is between 0.05 and 0.5 Pa·s, while for thermoplastic polymers in liquid state can be between 10^2 and 10^6 Pa·s [20].

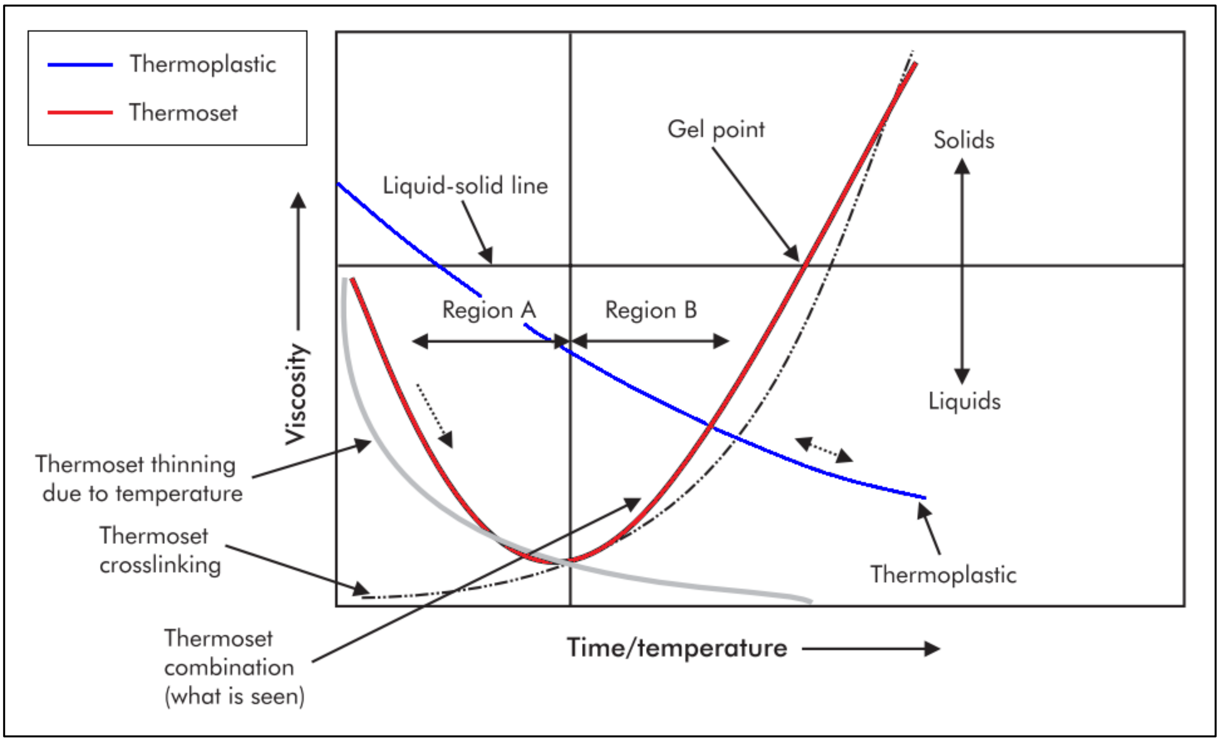

Figure 7. Comparison between the typical behavior of the viscosity of generic thermosetting and thermoplastic polymers as the temperature changes [10].

2.2. Reinforcement

The reinforcing fiber phase is added to the matrix in order to enhance its properties, providing strength and stiffness to the composite, and its contribution depends on the type, the direction and the volume fraction of the reinforcement used. Materials in fiber are characterized by a high aspect ratio, which is defined as the ration between the length and the diameter of the fiber. A high aspect ratio allows to a large fraction of the load to be transferred from the matrix to the fibers and be sustained along the longer axis [10]. Depending on the length of the fibers employed, two different classes of fiber-reinforced composite materials can be distinguished [21].

Discontinuous fiber composites have fibers shorter than the dimension of the part, which are dispersed inside the matrix phase. Depending on the length of the reinforcement, it is possible to distinguish between whiskers (length < 0.5 cm), short-fibers (length 0.5-1.5 cm) and long fibers (length > 1.5 cm) [10]. The orientation of the fibers in the matrix can be along a preferred direction, giving anisotropic properties to the material, or random, giving quasi-isotropic properties.

Continuous-fiber composites are obtained using long continuous fibers that span the dimension of the part. Long fibers are characterized by a very high aspect ratio and, since the reinforcement effect depends on the aspect ratio value, long continuous fibers are the form of reinforcement that has the greatest influence on the mechanical properties of the finished material. For this reason, continuous fibers composites are also called *high performance composites* [20].

The main advantages of the material in fibrous form are the high flexibility and the high strength with respect to the same material in the bulk form and, for these reasons, continuous fiber reinforcements are the most used for the production of composite materials. It can be demonstrated that the flexibility is a sensitive inverse function of the diameter so, since the diameter of a fiber is very small, it is possible to obtain high values of flexibility also from brittle materials as glass [6]. A high flexibility allows to produce components of composite materials with almost no limitation in the shape. The small diameter of the fibers, usually in the range of 10 μm, allows to achieve higher strength values compared with the material in bulk form. In fact, according to the size effect, the smaller is the volume of a certain piece of material, the lower is the probability of having defects in it [6, 11]. The fabrication process utilized for shaping the materials in fiber form, called drawing, usually orients the molecular structure along the fiber longer axis. This results in very high strength and stiffness values in the principal axis direction, giving anisotropic properties to the fibers bundle [10]. Several continuous fiber bundles (called rovings in case of glass fiber and tows in case of carbon fiber) are grouped together in order to control their orientation, composing fabric materials. Different orientations of fibers can be obtained in fabrics. Unidirectional non-crimp fabrics (UD-NCF) are composed by parallel fibers bundles stitched together, while bidirectional (or multidirectional) non-crimp fabrics are composed by multiple unidirectional layers of fibers placed perpendicularly (or at different angles) on top of each other and fixed by stitching. Woven fabrics instead are obtained by weaving the fiber bundles perpendicularly or in multiple directions and, since the fibers are crimp, they have lower mechanical properties than NCF [22]. An example of NCF and woven fabric is schematically represented in Figure 8. The mechanical properties of the final component will depend on the orientation of the fibers inside the plies with respect to the loading directions and on the disposition of the different plies composing it. In fact, different plies are usually stacked together with specific orientations and sequence in order to form multilayered composites called *laminates*.

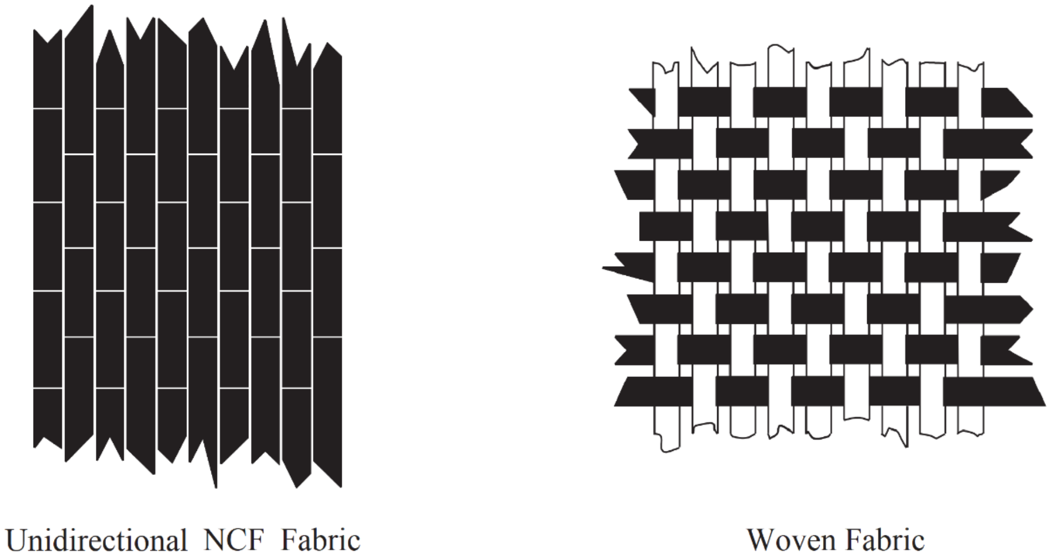

Figure 8. Schematic representation of the different types of fabrics obtainable with continuous fibers [10]. Different weaving patterns can be adopted for woven fabric plies. The one represented is a plain weave pattern.

The parameters that affect mostly the contribution of the reinforcement on the composite properties are the length of the fibers and the concentration of them [10]. The longer are the fibers, the higher are the tensile strength, the elastic modulus, the flexural strength and the elongation of the composite. For this reason, continuous fiber-reinforced composites, also called high performance composites, are the most utilized because of their higher mechanical characteristics. Similar effects are obtained increasing the concentration of fibers inside the matrix, with tensile strength, elastic modulus and flexural strength that increase. The only difference is that the elongation decreases with the increase of the quantity of fibers inside the material.

It is possible to define the *fiber volume fraction* as:

$$V_f = \frac{Volume\ of\ fibers}{Total\ Volume}$$

It is desirable to have a high value of V_f inside a composite. However, there is a limitation in the maximum fiber volume fraction achievable, which is around 60-70%, because above this value there is the risk of not obtaining complete wetting of the fibers and having contact between them.

As it was reported in Section 2.1, in order to achieve an effective load transfer from the matrix to the fibers, each single fiber must be surrounded by the matrix material that acts as a bond. Since the strength of the fibers depend on their microstructure, there is a high variability in the strength values between the fibers of a bundle. If they were not bonded together by the matrix, the total strength of the bundle would depend on the strength of the weakest fiber. This is called *domino effect* [11], and can be explained thinking at the fiber bundle as a series of rods sustaining a load, as it is shown in Figure 9.

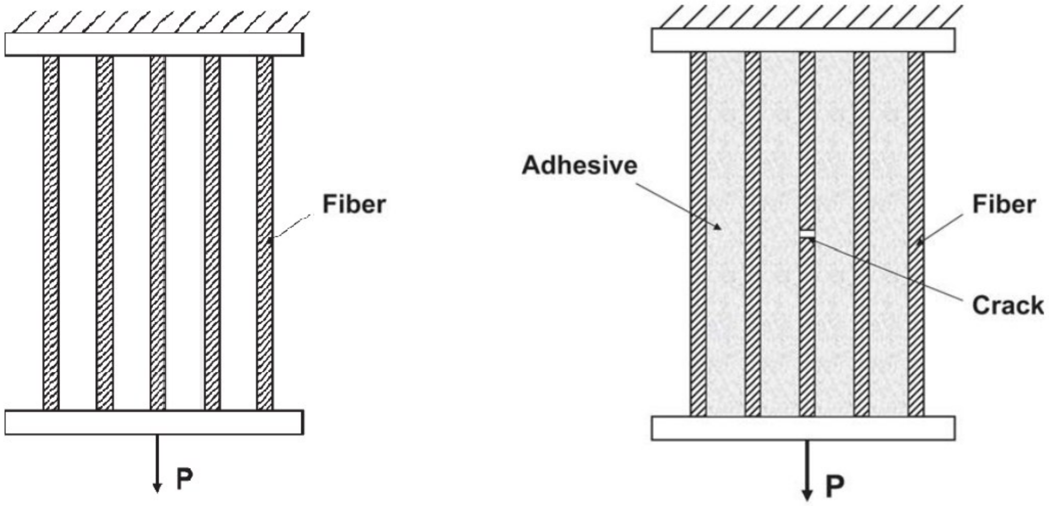

Figure 9. Schematic representation of dry fibers bundle (a) and wet fibers bundle (b) [11].

The load is shared equally between the various fibers but, when the stress on the weakest one reaches its failure strength, the fiber will break. At this point, the load is shared between the remaining fibers, causing an increment in the stress. It is likely that another fiber reaches the ultimate tensile strength and fails. The failure of the weakest fiber begins a cascade process that leads to the complete failure of the bundle. If the fibers are bonded together by the matrix instead, when one of the fiber fails, it can continue to support part of the load, since the load is transferred from the matrix to the fibers through shear. This explains why the presence of dry spots, which are region where the fibers have not been completely wetted, limits the mechanical properties and compromises the quality of the final component.

2.2.1. Reinforcement materials

The fibers most commonly utilized for producing composite materials with polymeric matrices are glass, carbon and aramid, which present a very high specific strength with respect to the metals alloys commonly used in structural applications, as it can be observed in Figure 10. Moreover, carbon and aramid fibers have also a specific modulus about one order of magnitude higher than common metals alloys, as shown in Figure 11, and for this reason they are called advanced fibers.

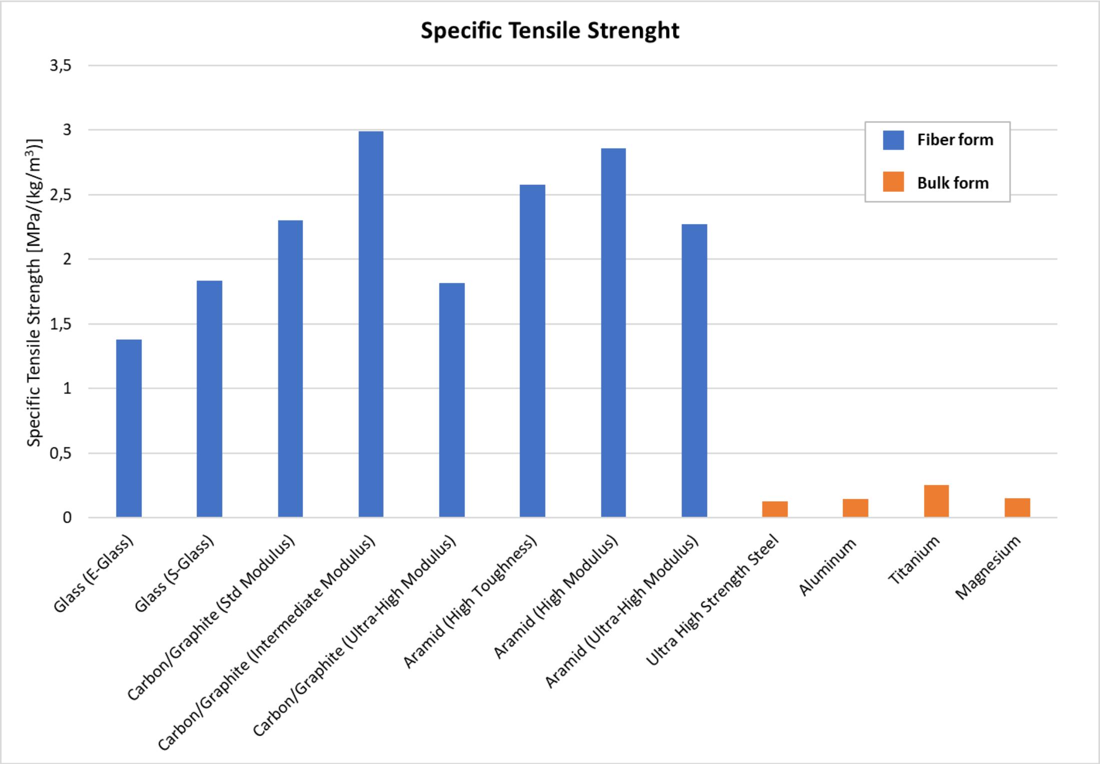

Figure 10 – Average specific strength of various materials [10].

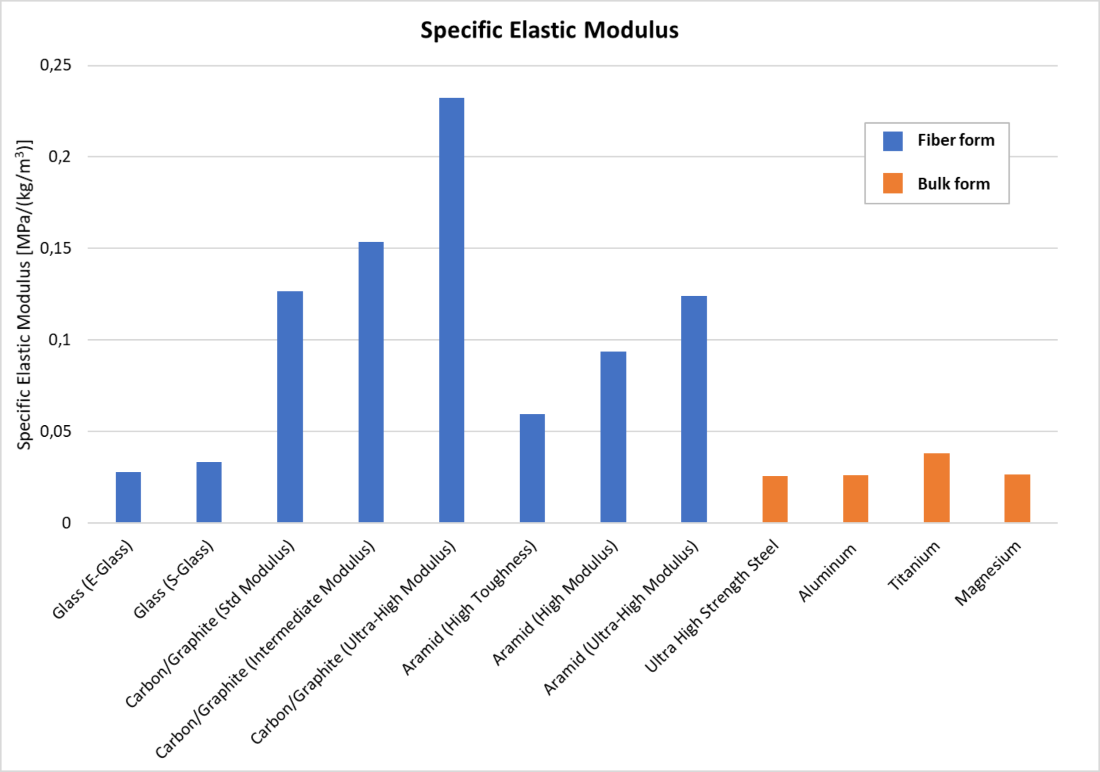

Figure 11 – Average specific elastic modulus of various materials [10].

2.2.1.1. Glass Fibers

Glass fibers-reinforced plastics (GFRP) are the most utilized type of composites in the market. The reason behind such wide utilization is found in their low price compared to the other advanced composites like those utilizing aramid and carbon fibers, and their very good mechanical properties. In fact, as it is shown in Figure 10, glass fibers have much higher specific strength compared to metals. Their specific elastic modulus instead is lower than that of advanced fibers like carbon and aramid, but is comparable to that of metals. The major constituent of glass fibers is silica (SiO_2), usually present in a percentage between 50 and 60%. Other oxides are added in order to obtain specific composition and properties. Different types of glass fibers are available on the market, but the most common are E-glass, S-glass and C-glass. The composition of these three different types of glass is given in Table 1.

Composition	E glass	C glass	S glass
SiO_2	55.2	65.0	65.0
Al_2O_3	8.0	4.0	25.0
CaO	18.7	14.0	–
MgO	4.6	3.0	10.0
Na_2O	0.3	8.5	0.3
K_2O	0.2	–	–
B_2O_3	7.3	5.0	–

Table 1. Average chemical composition, in percentage on the total weight, of the most common glass fibers [6].

E-glass, where the "E" stands for "electrical" because it has good electrical isolation properties, is the most utilized since it is the most cost effective [6, 10]. It has good mechanical properties, given by low density (2.55 g/cm^3) and high tensile strength (3445 MPa). The elastic modulus is comparable to that of the Aluminum alloys (about 70 GPa). S-glass has a high content of silica and presents tensile strength about 35% higher than E-glass with a similar density. It shows also better resistance to high temperatures, but it is more expensive. Finally, C-glass is used when higher chemical corrosion resistance is needed.

The structure of glass fiber is amorphous, with oxygen atoms connected to silicon ones through covalent bonds. Since the isotropy of the tridimensional structure, the glass fibers show almost isotropic properties, with the tensile modulus and the coefficient of thermal expansion almost equal along the principal and radial fiber axes [6]. The two-dimensional amorphous structure of glass is shown in Figure 12.

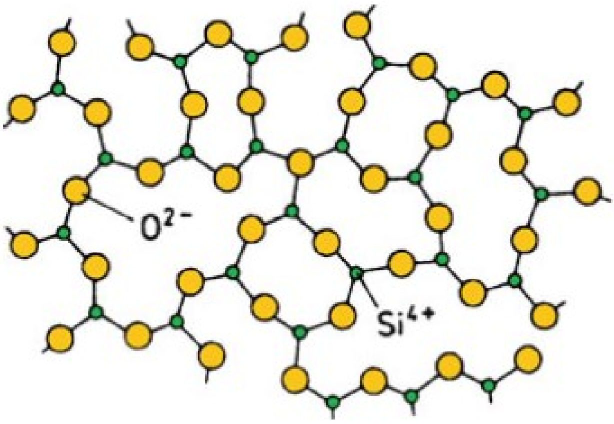

Figure 12. Glass amorphous 2D structure [6].

The production process of glass fibers, called *marble process*, is schematically represented in Figure 13. Initially, the raw materials are mixed inside a blender and, when the mixture is completed, it is transported in a furnace that thanks to the high temperature melts the material. The temperature of the molten material is about 1260°C. When it exits from the furnace, the material is cooled and shaped into marbles, which are easily transported. Then, the marbles are melted again in a second furnace and the melted glass is poured inside bushing plates. The bushings are metal plates with numerous tiny holes. The molten glass passes through these holes, exiting exits in the shape of filaments, and it is cooled. At this point, the filaments surface is usually treated with the application of *sizing*, which is a chemical coating that has the function of protecting the fibers from surface defects caused by the mechanical equipment and transport. Sizing usually has also some coupling agents that enhance the bonding between the fibers and the matrix. After the sizing application, the filaments are grouped together into bundles called rovings. The fibers obtained are mechanically elongated (drawn) and finally wounded on rolls.

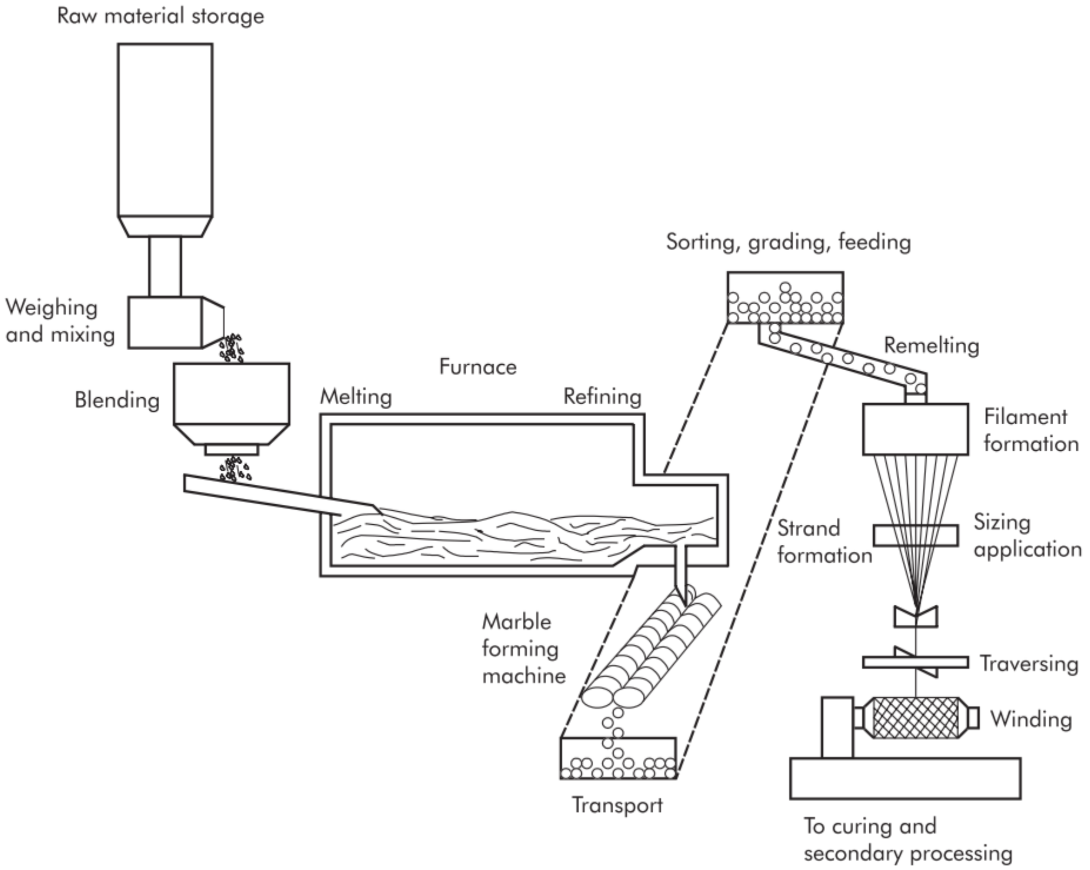

Figure 13. Scheme of the marble process for the fabrication of glass fibers [10].

Thanks to the technological improvements, modern plants are able to use the *direct-melt process*. In this process, after that the raw material is mixed and melted inside the furnace, it goes directly inside the bushing from which the filaments are extracted. In this way, the fabrication of marbles is avoided and the cycle time is lower. In the past, the production of marbles was needed because it allowed an improved control over the quality of the fibers, but nowadays the same quality can be obtained with the direct method. The diameter of the glass fibers can be controlled through the bushing holes diameter, the temperature of the process, the viscosity of the melt, the method adopted for cooling and the cooling rate of the filaments [6, 11, 10].

2.2.1.2. Carbon Fibers

Carbon is a light element that can exist in three different crystalline forms, which are graphite, diamond and fullerene. The one that is of interest for the production of fibers is the graphitic form, in which carbon is arranged in hexagons forming layers, as it is represented in Figure 14. The structure of graphite presents strong covalent bonds between the carbon atoms of a layer, and weaker Van der Waal's interactions between the layers. This makes graphite highly anisotropic, with a theoretical tensile modulus of about 1000 GPa in the layer plane and only 35 GPa perpendicular to it. For this reason, the objective of the carbon fiber manufacturing processes is to orient the hexagonal layers along the main fiber axis, in order to exploit the maximum possible characteristics of the material [6].

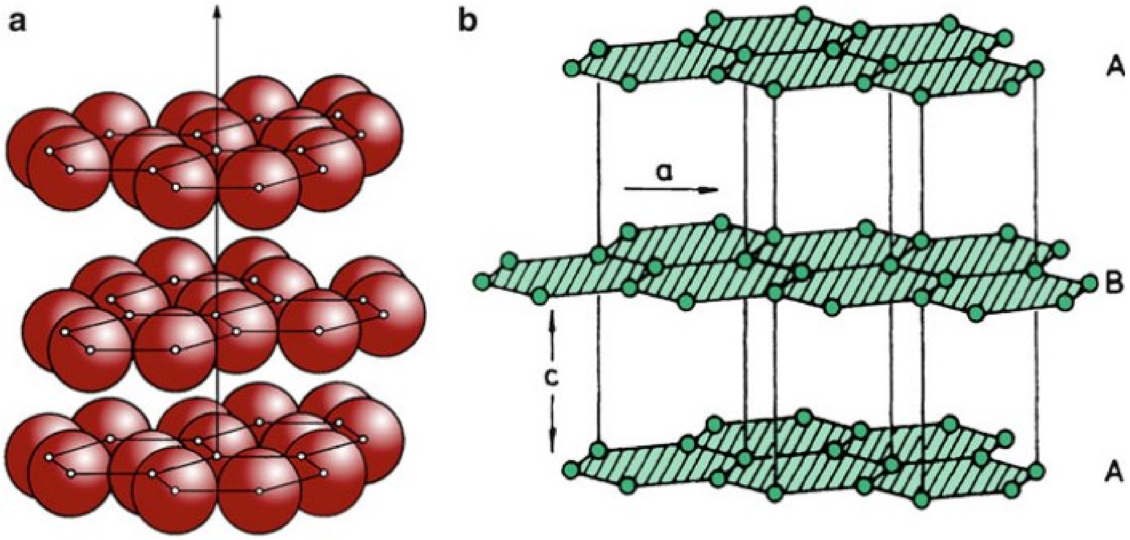

Figure 14. Graphite layer structure (a) and graphite lattice (b) [6].

All the production processes of carbon fibers start from the precursor fibers, which are textile polymeric fibers with high amount of carbon, that are converted into graphite [6, 10]. The most utilized are polyacrylonitrile (PAN) and pitch, while rayon, that historically was the first material utilized, is now less used. Despite the initial difference between PAN fibers, which are textile fibers, and pitch, that is a product of the distillation of petroleum and appears as an amorphous mass, the production process is very similar. In fact, after that the pitch is transformed into fibers, it can undergo the same steps of the PAN. The steps of the production process of carbon fibers are summarized in the scheme of Figure 15

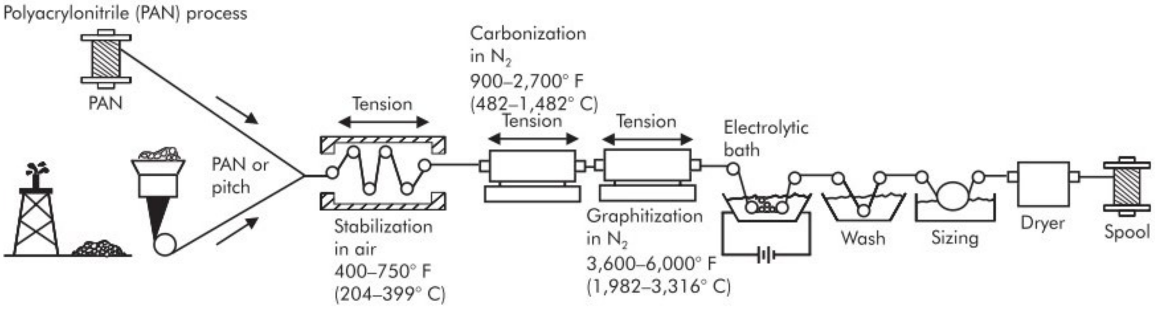

Figure 15. Scheme of the production process of carbon fibers for PAN or pitch precursor fibers [10].

The first step of the process is the *stabilization*, during which polymer cross-links are formed in the precursor fibers. This thermosetting transformation avoids that the fiber melt during the following high temperature steps. During stabilization the fibers are also put under tension, since they are held at constant length to counteract the shrinkage that they have when stabilize. The following step is the *carbonization*, in which the fibers are placed in a nitrogen atmosphere at high temperature meanwhile the tension is maintained. This cause the hydrogen molecules to disappear and the carbon molecules merge together forming hexagonal plates. The carbon content at the end of this step is around 80-95%. The third step is the so called *graphitization*, that is needed in order to increase further the strength and the stiffness of the fibers. Always inside a nitrogen atmosphere, the fibers are still stretched and the temperature is increased up to 2000-3300 °C depending on the desired properties that must be achieved. The nitrogen atoms present in the structure are eliminated and new hexagonal rings of carbon are formed, which merge the smaller plates in a single larger plate with few nitrogen atoms at the extremities. The fibers, now transformed in graphite, has a carbon content around 99%. The high temperature and the tension applied on the fibers orient the graphite plates along the fiber long axis.

The higher is the temperature and the time of the process, the higher will be the tensile modulus of the carbon fibers [10]. After graphitization, the fibers pass in an electrolytic bath, that has the function of cleaning them from the debris formed during the previous steps and oxidize their surface. The oxidation can enhance successive bonding. Subsequently, the fibers are washed and then *sizing* is applied on them, so that it helps the formation of a good bonding with the matrix. Finally, the fibers are dried and bundles of fibers called tows are wrapped on spools.

The properties of the carbon fibers vary depending on the precursor fiber employed and the parameters of the manufacturing process [6, 10]. The average values of tensile strength and elastic modulus for different types of carbon fibers are reported in Table 2.

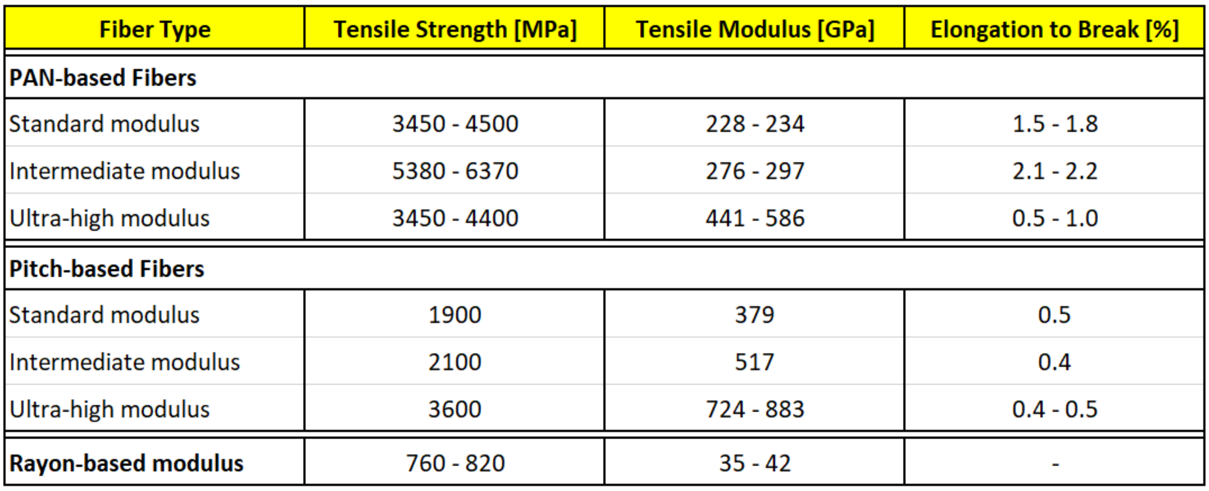

Fiber Type	Tensile Strength [MPa]	Tensile Modulus [GPa]	Elongation to Break [%]
PAN-based Fibers			
Standard modulus	3450 - 4500	228 - 234	1.5 - 1.8
Intermediate modulus	5380 - 6370	276 - 297	2.1 - 2.2
Ultra-high modulus	3450 - 4400	441 - 586	0.5 - 1.0
Pitch-based Fibers			
Standard modulus	1900	379	0.5
Intermediate modulus	2100	517	0.4
Ultra-high modulus	3600	724 - 883	0.4 - 0.5
Rayon-based modulus	760 - 820	35 - 42	-

Table 2. Average mechanical properties for different carbon fiber types (data taken from [10])

The performance of carbon fibers is better than that of glass fibers thanks to the lower density (1.6 - 2.0 g/cm^3) and the very high tensile strength and elastic modulus. Carbon fibers have a negative thermal expansion coefficient along their axis. This means that, differently from most of the other materials, the dimensions of the fibers decrease when the temperature increases. The coefficient of thermal expansion is measured along the fiber major axis. Carbon fibers then have very high thermal conductivity, generally higher than that of metals, they are good electrical conductors and they are chemically inert.

Nevertheless, carbon fibers have also disadvantages, as their high brittleness, low toughness and high cost. In fact, carbon fiber-reinforced plastics (CFRPs) are more expensive than metals and GFRPs and this aspect has partially limited their employment, especially in mass production applications.

2.3. Thermosetting Composites Manufacturing Processes

The processes for manufacturing fiber-reinforced composite materials components can be distinguished in two main categories, which are *Open Mold Processes* and *Closed Mold Processes* [20]. A further distinction can be made between the processes for manufacturing *engineering composites* and those for producing *high performance composites*. The engineering composites are those that present a reinforcement in short fibers form and make use of low-cost resins for the matrix [10]. They are usually distinguished from the composites made with long continuous fibers, called high performance composites, since they have lower mechanical properties. Therefore, engineering composites are less expensive than high performance composites. The different categories of manufacturing processes for thermosetting composites are reported in the diagram of Figure 16.

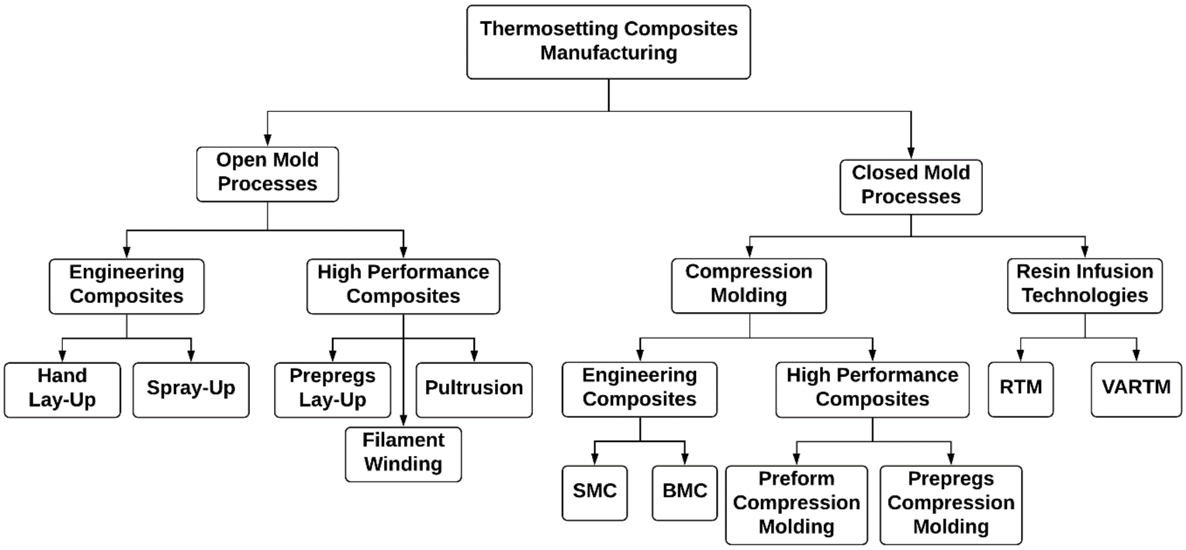

Figure 16. Manufacturing processes for producing thermosetting composites.

2.3.1. Open Molding of Engineering Composites

The open mold techniques for the production of engineering composites are the simplest processes for manufacturing composites and are mainly manual. Usually the steps consist in the initial application of the reinforcement on the mold surface, followed by pouring of the resin on it. After the resin is evenly spread in order to ensure wetting, curing can occur. There are two main processes for the production of engineering composites, which are *hand lay-up* and *spray-up*.

2.3.1.1. Hand Lay-Up

It is a simple manual process for producing thermosetting composite material parts [10]. The process starts applying the gel-coat on the mold, which is a first layer of special resin that allows a better final surface quality. Then, the reinforcement, usually in the form discontinuous fibers, is laid on the coated mold. The thermosetting resin is mixed with the curing agent and is poured on the mold in order to cover completely the reinforcement. The most utilized resin for this process is polyester. The resin is spread evenly on the surface of the mold using a consolidation roller. This operation, called rolling, ensures the full wetting of the reinforcement. At this point, the curing process can occur. Curing can take place at room temperature or inside an oven depending on the type of resin. The curing is an exothermic reaction and care must be taken if the thickness of the component is too high, since it can cause problems in the final quality of the part. Usually, in order to obtain thick parts, the *secondary bonding technique* is utilized, in which a layer of reinforcement and resin is added on the mold before that the previous layer has cured completely. Finally, The part is extracted from the mold at the end of curing.

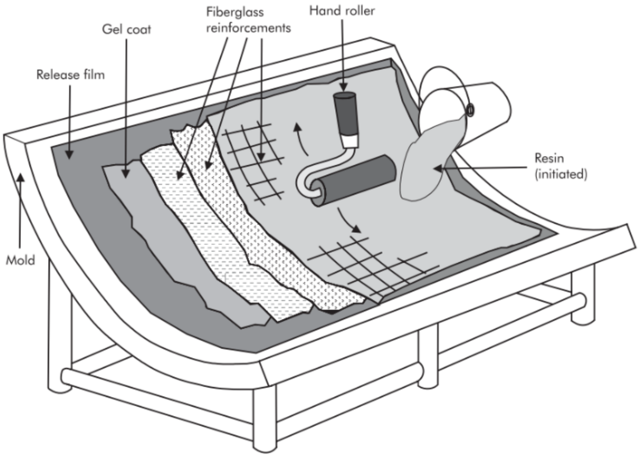

Figure 17. Hand lay-up process scheme [10].

Since the operations are completely manual, the hand lay-up method allows to manufacture components of any dimension and shape. This process is widely employed for the production of boat hulls. The labor cost is obviously high and this make this process economically advantageous for small-scale productions only [10, 20].

2.3.1.2. Spray-Up

This method is used for the production of simple and sufficiently large parts [10]. The main difference from the hand lay-up is that the fibers are not laid on the mold but they are chopped upstream from the nozzle that sprays the resin. The chopped fibers fall into the stream of resin and are sprayed with it on the mold surface. After the spraying operation, the process is very similar to the hand lay-up one, with the rolling operation performed for uniformly spreading the resin and ensuring wetting of the fibers and the final curing.

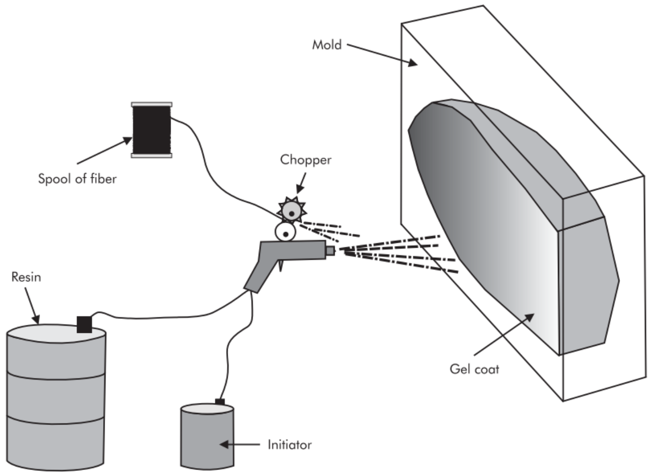

Figure 18. Spray-up process scheme [10].

Despite of its simplicity, the spray-up method presents many disadvantages. A special spraying equipment is needed and the operator must be highly skilled. The spraying of the resin is a problem from the environmental point of view, since harmful substances are released together with the resin. Finally, it is not possible to control the direction of the fibers.

2.3.2. Open Molding for Continuous Fiber Composites

The two processes described previously have many limitations if high performance composites components must be realized. It is very difficult to control the direction of the fiber reinforcement, as well as controlling the fiber amount and its ratio with respect to the resin quantity. Moreover, the final components quality is usually affected by the presence of voids and the processes release toxic substances in the environment.

For all these reasons, a different process is employed for the production of high performance composites [10]. Open molding of advanced composites make use of *prepregs*, which are plies of reinforcement pre-impregnated by resin. The resin is already initiated so, in order to not make it cure before fabrication of the FRP, the prepregs are stored at low temperatures. The most utilized thermosetting resin is the epoxy. Prepregs are cut and laid on the mold surface in the desired position and direction. The operation can be manual or automated. After it, the curing of the resin can be restarted and concluded. The curing reaction can be carried out under vacuum or with the application of pressure. Usually, in order to obtain high performance parts, curing takes place inside the *autoclave*. The autoclave, schematically represented in Figure 19, is a pressure vessel inside which is possible to apply simultaneously vacuum, pressure and heat [20]. Typical values of temperature and pressure applied for the curing of an epoxy resin are between 200-300 °C and 500-600 kPa.

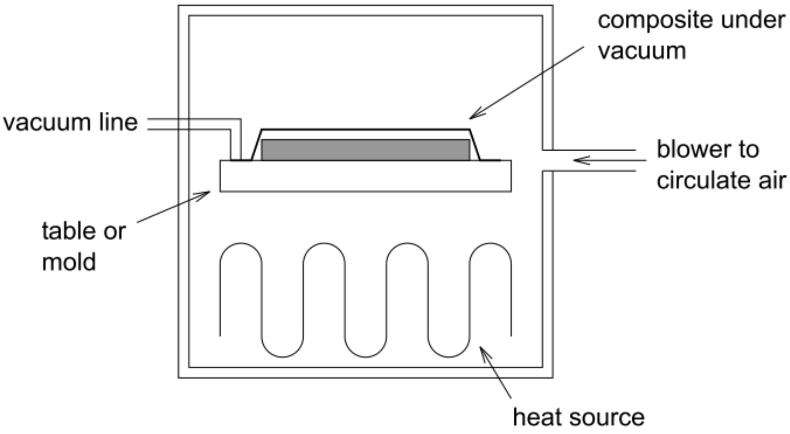

Figure 19. Scheme of an autoclave [20].

The quality of the components obtained is very high, since the simultaneous application of vacuum and high pressure on the part ensures low void content and the possibility of reaching high fiber volume fractions. However, the process is very expensive, since an autoclave has a high capitalization cost and the need of applying heat for a long time requires a lot of energy. The slow curing cycles, which can last also several hours, make it unsuitable for high volume productions. As a result, this method is the most widely utilized in the aeronautic sector, where the production volumes are not that high and the quality of the final component is the most important aspect. For the same reasons, it is also widely employed in the production of composite components for high performance cars.

2.3.3. Filament Winding

Filament winding is one of the most utilized composites manufacturing methods in the market [10]. It can be considered an open molding process, in which continuous fibers are wrapped on a rotating mandrel that acts as mold. The process is reported schematically in Figure 20.

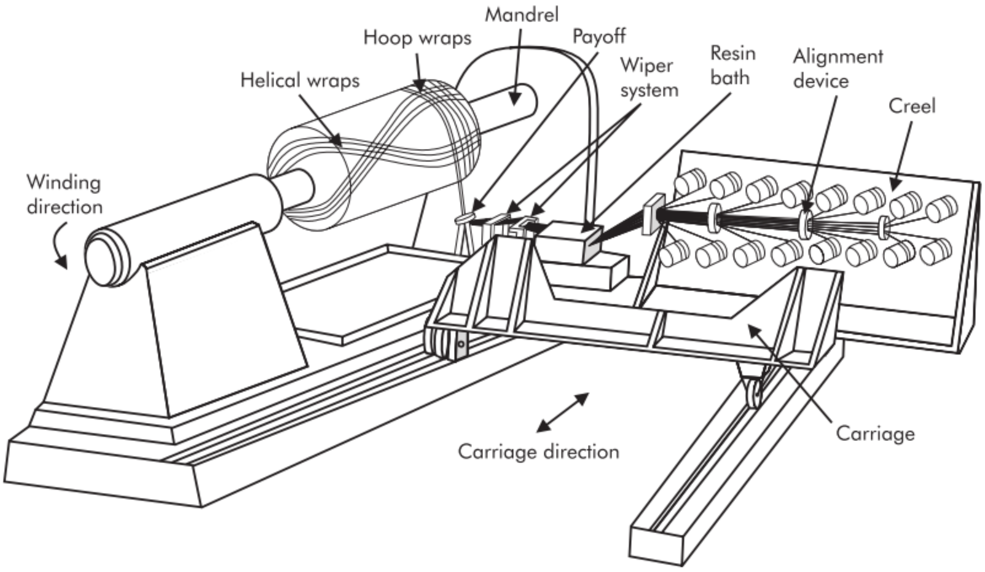

Figure 20. Scheme of a filament winding machine [10].

The fibers spools are mounted on the creel, which is a rack with alignment devices. After that the fibers are aligned, they are impregnated inside a thermosetting resin bath and finally are directed on the mandrel by the payoff. The entire system is mounted on a sliding carriage. The mandrel rotation pulls the fibers from the spool, so the process can proceed automatically. The fibers direction depends on the transversal movements of the sliding carriage and on the rotational speed of the mandrel. When the mandrel has been completely covered by the impregnated fibers with the desired direction and number of layers, it is removed from the machine for concluding the curing operation, which can take place at room temperature or inside an oven or an autoclave. When curing is finished, usually the mandrel is removed from the composite shell.

This process has many advantages, such as very high productivity and low labor required, since it is highly automated. The cost is much lower compared to other composite manufacturing methods. Moreover, since it makes use of continuous fibers, it is possible to obtain high performance components, with high values of stiffness and strength.

However, as it is easily understandable, the components that can be produced by filament winding must be cylindrical or having a rotational axis with simple design. The process therefore is widely employed for producing pressure vessels, tanks and in the automotive sector can be applied for the realization of driveshafts [11].

2.3.4. Pultrusion

Pultrusion is an open molding continuous process that allows to produce parts with constant cross section at a high volume rate. The manufacturing method is similar to the extrusion process for plastic and metals, with the material that is forced to pass through a die that gives shape to it, but with the difference that here the material is pulled instead of being pushed. This is possible thanks to the continuous fibers of the reinforcement, which are pulled by the machine. A scheme of the process is shown in Figure 21.

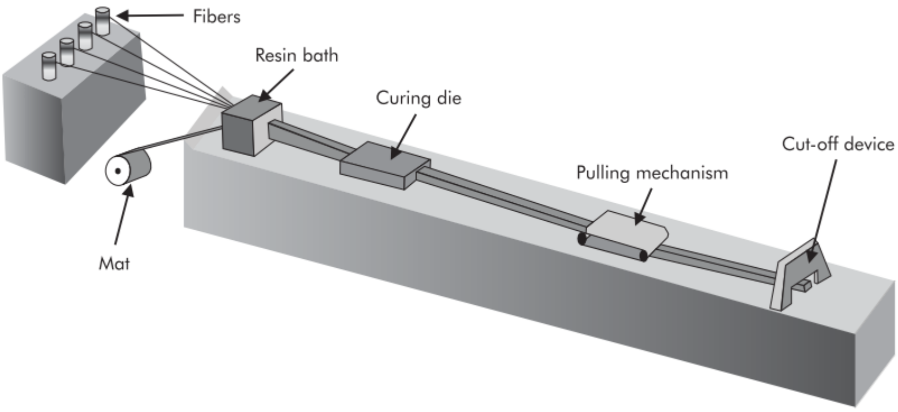

Figure 21. Pultrusion machine scheme [10].

The fibers are pulled from the spools and grouped together to be impregnated in the resin bath, where a die placed at the exit gives an initial shape to them. After it, the impregnated fibers are forced through the curing die, which imparts the final cross section to the composite and applies heat in order to cure the resin. The cured fibers are collected by the pulling mechanism, which applies the motion force that make work the entire upstream system automatically. Finally, the material arrives at the cut-off device, where it is cut and trimmed to obtain the final components.

Since the process is continuous, it has the highest productivity among all the composite manufacturing methods [10]. Then, thanks to the high automation, it has low labor requirement. Other advantages are the high material utilization and the low cost per part produced. Nevertheless, since the initial investment for the machine is quite high and there is a strong limitation in the obtainable components shapes, this process is not widely employed.

2.3.5. Compression Molding

Compression molding is a closed molding process in which the component is shaped inside a two-side mold closed by a press, similarly to what happens in sheet metal forming. In the bulk molding compound (BMC), chopped fibers are mixed with the resin to form the charge and placed inside the mold. Then the press closes the two halves of the mold, causing a squeezing of the charge that fills the entire mold cavity. At this point, the mold is heated while the pressure is maintained and the material cures inside the closed mold. At the end of the process, the mold is open and the component removed.

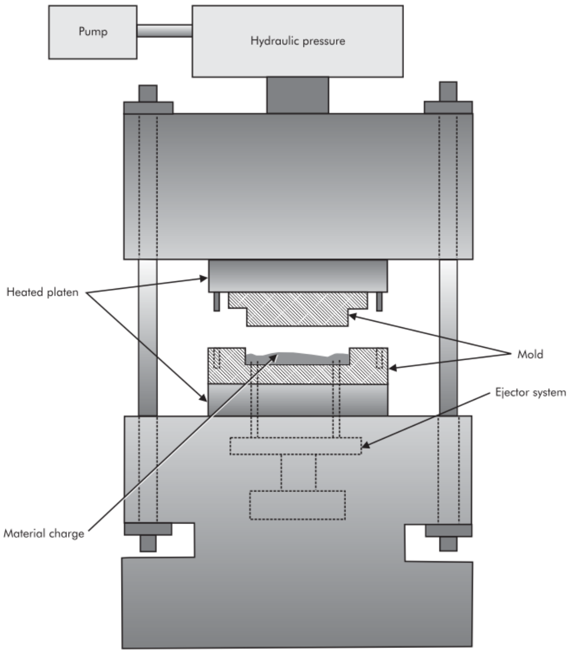

Figure 22. Scheme of a press for compression molding [10].

Similar to BMC, the sheet molding compound (SMC) differs in the way the reinforcement is added to the resin. In fact, the initiated thermosetting resin is spread on a carrier film covering a wider area of the mold compared to the bulk. Then, the fibers are chopped and sprinkled on the resin surface. After that, another carrier film is laid on top of it and the sheet is pressed and shaped.

However, using BMC and SMC it is not possible to have high fiber content and short fiber-reinforced composites have lower properties than long continuous fiber ones. In order to overcome this limitation, *preform compression molding* can be employed [10]. In this process, a dry reinforcement preform formed by long continuous fibers is placed inside the mold and the thermosetting resin is poured on it after being initiated. The resin must be spread evenly on the preform. At this point, the mold is closed and the compression action makes the resin flow through the preform wetting the fibers. The mold is then heated so that the curing process can conclude inside it. A similar method makes use of prepregs, which are laid on the mold and then they are compressed and cured. In this case, the process is called *prepreg compression molding*.

The advantages of these processes are low labor requirement, good part reproducibility, low amount of scrap, low void content and the rapid mold cycles, which can ensure high production volumes and make this method suitable for the automotive industry [10].

Nevertheless, the parts design complexity that can be obtained is lower than other open molding processes. Since high pressures are needed, large press must be employed, requiring quite high initial investments.

2.3.6. Resin Infusion Technologies

Resin infusion technologies, also called liquid composite molding (LCM) processes, include different production methods in which dry fibers are placed inside a closed mold and are subsequently wet by the infusion of resin inside the mold cavity [10]. The resin can be infused inside the mold under pressure, as it happens in the RTM process, or thanks to the vacuum obtained inside the mold, as in the VARTM process. A common aspect of all the processes is that curing of the resin is performed inside the closed mold after the infusion.

The use of dry fibers instead of prepregs has an economical advantage, since they are cheaper and do not have a shelf life. The tooling cost is lower than that of other processes like compression molding or metal forming. Usually LCM methods are cost effective for middle range production volumes (20-60000 units per year) and the cycle time is usually lower than that of open molding processes that make use of autoclave for curing [11, 20]. Finally, since they are closed mold operations, they are good from the environmental point of view because the evaporation and release of harmful substances during the curing of the resin is avoided.

2.3.6.1. Theoretical considerations of LCM processes

The main objective of the LCM processes is to fill completely the mold, reaching a complete fiber wetting and limiting voids, dry spots and rich resin areas [11]. The flow of the resin through the reinforcement can be considered equivalent to the flow of an incompressible fluid through a porous medium, so its physics is based on the mass conservation principle and makes use of the Darcy's law as momentum balance [11, 20]. The equation of conservation of mass for the fluid phase is equal to:

$$\nabla . \bar{\boldsymbol{u}} = 0 \tag{2.1}$$

Where $\bar{\boldsymbol{u}}$ is the superficial fluid velocity vector, which corresponds to the components in the three orthogonal directions of the velocity at which the fluid is actually travelling inside the reinforcement.

Applying Darcy's law, the superficial fluid velocity vector can be defined as:

$$\bar{\boldsymbol{u}} = -\frac{1}{\mu}[\boldsymbol{K}]\nabla P \tag{2.2}$$

Here, μ is the viscosity of the fluid, $[\boldsymbol{K}]$ is the permeability tensor, which collects the values of permeability of the reinforcement in all the directions, and ∇P is the pressure gradient. In the extended form, the formula can be written as:

$$\begin{pmatrix} \overline{u_x} \\ \overline{u_y} \\ \overline{u_z} \end{pmatrix} = -\frac{1}{\mu} \begin{bmatrix} K_{xx} & K_{xy} & K_{xz} \\ K_{yx} & K_{yy} & K_{yz} \\ K_{zx} & K_{zy} & K_{zz} \end{bmatrix} \begin{pmatrix} \partial P/\partial x \\ \partial P/\partial y \\ \partial P/\partial z \end{pmatrix} \tag{2.3}$$

It is important to notice that in the permeability tensor, when the coordinate axes coincide with the material principal directions, only the diagonal coefficients K_{xx}, K_{yy} and K_{zz} are non-zero [11]. For unidirectional plies, that are transversely isotropic, the principal directions correspond to the fiber axis and the two perpendicular transverse axes. The previous tridimensional formula can be simplified for many LCM processes and only a mono- or two-dimensional equation can be considered when the values of in-plane permeability of the stacked layers are of the same order of magnitude [20].

Requirements for high quality LCM components

In order to obtain high quality components from resin infusion methods, some requirements must be fulfilled. These are:

- High reinforcement permeability;
- High reinforcement wettability;
- Low viscosity resin;
- Balanced resin flow speed;
- Resin with balanced gel time.

The reinforcement must have high *permeability*. The permeability can be defined as the inverse of the resistance that the reinforcement applies on the resin flow and it is an indication of the easiness with which the resin can flow through the fibers [20]. If the permeability values of the reinforcement are high, the resin will encounter low resistance in penetrating through it and, looking at the Darcy's law equation, the fluid velocity will be higher. If instead the permeability is low, the resin will struggle in penetrating the reinforcement and the speed of the flow will be lower, with consequent higher filling time or the need of higher infusion pressure for maintaining it at acceptable values. Moreover, with a low permeability there is also a higher risk of failing in filling the mold and obtaining short shots. The permeability depends on the type of reinforcement employed and on its physical characteristic, like porosity, roughness, tortuosity and length of the channels and preform thickness [11, 23]. In addition, the orientation of the fibers with respect to the flow affects the final permeability of the reinforcement, since the permeability is usually higher in the direction along the fibers and lower perpendicular to them and through the thickness. The reinforcement permeability shows a quadratic decrement with the increase of the fiber volume fraction [11, 24]. Studies have demonstrated how the permeability depends on the porosity of the preform [23]. The porosity is defined as the ratio in percentage between the total non-solid volume and the total volume of the preform, and the higher it is, the higher will be the permeability. The phenomenon is easily explainable because having high porosity means having many void spaces in the preform, inside which the resin can easily penetrate. Increasing the fiber volume fraction of the preform reduces the spaces between the fibers and, therefore, reduces the porosity and leads to a decrease in the permeability. Finally, also the compaction pressure affects the final reinforcement permeability [24]. An empirical relation links the compaction pressure with the fiber volume fraction. The higher will be the compaction pressure, the higher will be the fiber volume fraction and so the permeability will decrease with a quadratic trend. This behavior is related to the fact that, increasing the compaction pressure, the space between fibers is reduced, causing a constriction of the flow channels.

The fibers of the reinforcement must have high *wettability* [20]. The wettability is a measure of how easy the fibers inside a bundle can be reached by the resin flow. If the wettability is low, the resin risks to wet only the external surface of the fiber bundles, without penetrating inside it. The wettability of the reinforcement can be enhanced by the application of sizing on the fibers, which can also increase bonding between fiber and matrix.

The resin must have low viscosity in order to ease infusion, flow through the reinforcement and fibers wetting. As it can be observed in the Darcy's low (Eq. 2.2), a low viscosity has the same effect of a high permeability of the reinforcement, since it ensures high fluid velocity. In order to be suitable for resin infusion processes, a resin should have a viscosity lower than 1 Pa·s [11]. However, the viscosity must also not be excessively low (< 0.005 Pa·s) otherwise the injection and diffusion of resin will be very quick and there will be the risk of not wetting completely the fibers and having higher void content in the final component.

Another important characteristic of the resin is the *gel time*, which corresponds to the moment when the viscosity increases and the resin becomes solid. After the occurrence of gelation, a further diffusion of the resin inside the preform is impossible [11]. The gel time must be long enough in order to allow the injection and diffusion of the resin when the viscosity is low, but must not be excessively long, otherwise the cycle time will be too long and economically disadvantageous. After gelation, the resin concludes the curing process and finally can be extracted from the mold. Ideally, a good resin for resin infusion processes should have fast curing time for minimizing the cycle time [11, 20].

A consideration must be done on the speed of the resin flow inside the mold. From the point of view of the cycle time, a fast infusion and diffusion would be better. Nevertheless, as it was reported previously, if the flow speed is excessively high, there is the risk of not obtaining proper wetting of the fibers, with high void content and resultant low quality of the part. The flow speed depends on the permeability of the reinforcement, on the viscosity of the resin and the pressure gradient, which can be used as control parameter. When the resin is forced to flow through a layer of unidirectional fibers, there are two types of flow front caused by two different types of channels [11]. The first one is called macro flow front and takes place between the different tows, while the second one is called micro flow front, and is observed between the fibers forming a tow. A representation of the two flows is shown in Figure 23. When the pressure gradient is high, the resin flows faster outside from the tows than inside them. When the resin from the external faster channels penetrates inside the tows, there is the creation of voids that, if they cannot be pushed outside from the tow, will remain in the final component. Instead, if the pressure gradient is low, the flow rate will be also low and the resin flow front will proceed faster inside the fiber bundles than outside from them, reducing the occurrence of voids but causing longer filling time. In general, slow flow rates allow to achieve better overall quality of the components [23]. When the flow rate is moderate it is possible to reach an impregnation almost simultaneous in the channels, with reduced occurrence of voids with respect to fast flow rate and obtaining acceptable filling times. For this reason, it is important to regulate the pressure gradient for achieving a balanced resin flow speed.

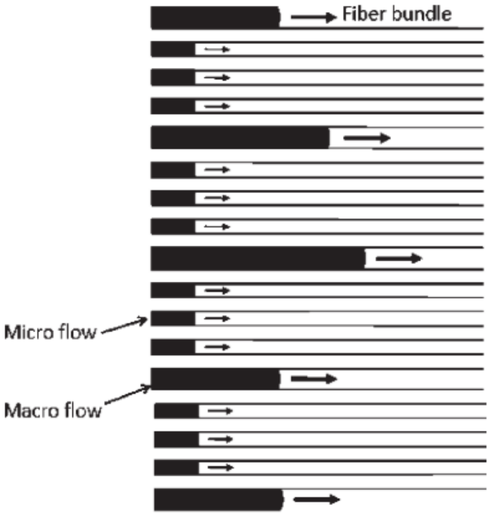

Figure 23. Different flows inside reinforcement channels [11].

In-Mold Curing

The curing of the resin in the LCM methods, as well as in the other closed molding processes, happens inside the mold. When the reinforcement has been wet completely, the curing rate should ideally increase in order to reach the complete curing quickly and increase the productivity. For this reason, the most common objective in the curing optimization is minimizing the time needed for the process [11]. The other factors that are usually considered during the optimization are the minimization of residual stress, warping, void formation and the maximization of the final surface quality.

Delamination is one of the problems that can appear in the curing process and it can be caused by the internal stresses given by the resin shrinkage during solidification. For this reason, a good resin should have low shrinkage properties. Other factors that can contribute to delamination are the fabrication of thick components, using complex geometries or having high gradients of temperature during the process. Apart from using resins with low shrinkage or adding additives in order to limit it, delamination can be avoided by reducing the gradient of temperature of the process, causing a longer curing time, or by increasing the pressure inside the system during curing.

Another problem is the incomplete curing. Usually curing reaches its completion outside from the mold but, if the degree of curing is too low when the part is extracted, the component can be damaged or it can undergo permanent deformations [11]. Possible solutions to the problem can be increasing the temperature, causing an increase of the reactivity of the resin system that reduces the gelation and curing times, or letting the part curing for a longer amount of time inside the mold.

2.3.6.2. Resin Transfer Molding

Resin transfer molding (RTM) is the most utilized LCM process for the production of composites [10]. The dry fibers preform is placed inside the mold and compressed. The resin is injected inside the mold under pressure (200-700 kPa), so it is important that the mold is able to sustain this pressure. Thanks to the high pressure, the resin can be forced to flow through the compacted preform, allowing to obtain high fiber volume fraction (up to 70%) and low void contents (up to 1%). A scheme of the RTM process can be observed in Figure 24.

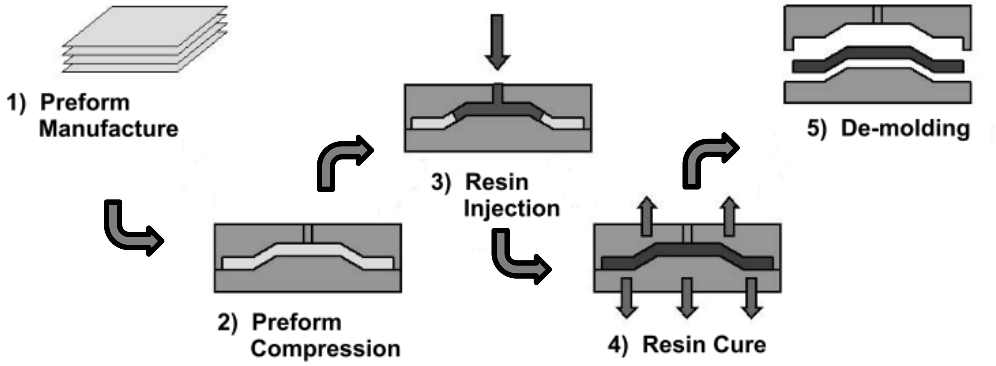

Figure 24. Scheme of Resin Transfer Molding operations [20].

The advantages of this process are the possibility of obtaining components with very high surface finishing (Class-A surfaces), the possibility of manufacturing large parts and complex shapes and the relatively fast cycle time, that can vary between 5 to 150 minutes, making this process applicable also on sectors like the automotive [10, 20].

The infusion of resin under pressure brings advantages, but requires also a complicated infusion system and robust tooling, with the mold usually made in metal since it must resist the load and remain firmly closed. Therefore, this process has a high tooling cost. Another problem is that the resin at high pressure can cause the *fiber wash*, which is a displacement of the preform from its initial correct position and orientation caused by the resin that is entering the mold. In order to reduce this problem and avoid the creation of possible rich resin areas, the preform must fit tightly the mold.

2.3.6.3. Vacuum Assisted Resin Transfer Molding

The VARTM process is a variation of the common RTM, in which the resin infusion is possible thanks to the pressure differential existing between the inside of the mold, under vacuum conditions, and the external environment. One particular aspect of this process is that usually only one side of the mold is rigid. The other side of the mold is composed by a plastic sheet, called vacuum bag, which is pressed on the reinforcement by the atmospheric pressure and keeps it firmly in position.

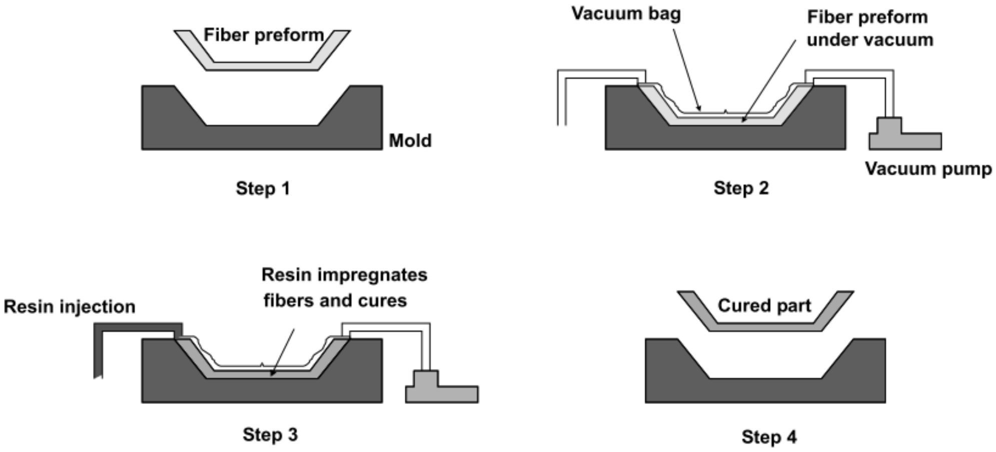

Figure 25. Scheme of VARTM operations [20].

The main advantage of VARTM is that it is a low cost process. Tooling is cheap because only one side of the mold is rigid while a plastic sheet composes the other and, since the pressure involved is just the atmospheric one, there is not the need of high strength materials [11]. The low pressure allows also to use a simple infusion system, which usually is composed by simple plastic hoses and valves. All these aspects make the initial investment of this process considerably lower than that required by RTM, compression molding or processes that make use of autoclave curing [10, 11]. Another factor that helps in keeping the cost low is the possibility of carrying out the curing reaction at room temperature [20]. The infusion of resin at low pressure, together with the action exerted by the vacuum bag on the preform, reduces sensibly the risk of having fiber wash. Then, since the vacuum bag is flexible, when it is pressed on the preform by the atmospheric pressure it adapts to its shape, reducing the risk of having rich resin areas caused by unfitting of the preform in the mold. The transparency of the bag allows also to control the flow of the resin through the preform, understanding if there are problems and adopting countermeasures for the following infusions [20]. Another advantage is the possibility of manufacturing very large components, such as wind turbine blades, that cannot be produced with autoclave methods or RTM due to the high costs required for adapting the processes to the dimensions involved [11, 20].

Nevertheless, VARTM has also disadvantages. The most important is the lower surface quality obtainable with respect to RTM, compression molding and autoclave methods. The problem is evident especially on the side in contact with the flexible bag, which is more irregular since there is not a rigid mold [11, 10]. Since the resin is infused at low pressure, it must have very low viscosity in order to penetrate the preform. Due to the lower pressure involved, the fiber volume fraction is lower and the void content is higher than that obtainable from RTM [10]. Moreover, the infusion process requires longer time to fill the mold, causing an overall longer cycle time [20]. The process is very labor intensive, since it requires skilled operators during the application of the vacuum bag, and for this reason is more difficult to be automated compared to RTM [20]. Finally, the waste of material occurring during VARTM is higher with respect to other processes.

SCRIMP method

SCRIMP, acronym that stands for Seemann Corporation Resin Infusion Molding Process, is a method patented by Seemann Corporation in order to improve the standard VARTM process and overcome the problem of the long filling time of the mold [25]. In SCRIMP method, a layer of porous plastic material called *infusion media* is interposed between the fiber preform and the vacuum bag. The infusion media usually has a permeability 2-3 times higher than the preform, and this cause a rapid flow of the resin through it, since the resistance opposed to the flow is lower. Thanks to this, the resin is quickly spread on the upper surface of the preform and it has to penetrate mainly through the thickness of it, without having to penetrate through the entire cross-section. In this way, the infusion operation is faster and, since the term dz in the Darcy's law is reduced, a lower pressure differential is needed for the infusion [11]. The use of SCRIMP allows to produce larger components than VARTM, with the advantage of having lower cycle times, reducing the quantity of voids and the risk of having short shots. The difference between the two processes is represented in the scheme of Figure 26.

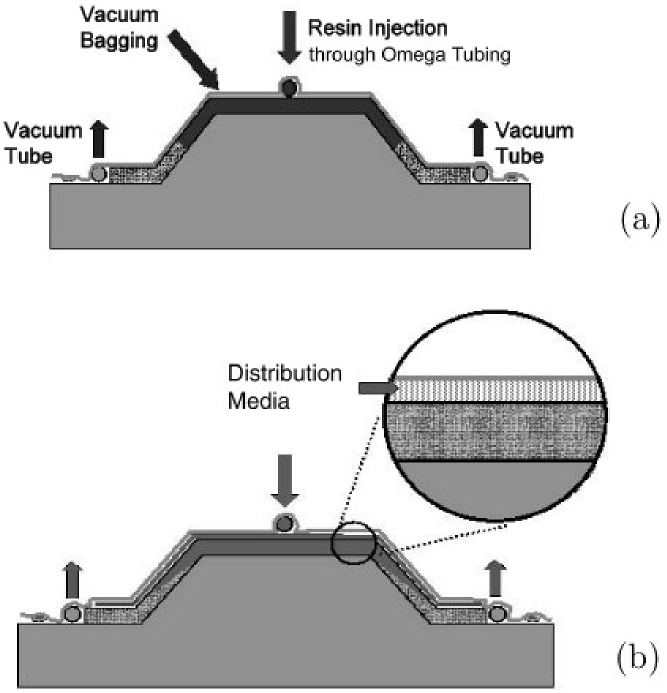

Figure 26. Difference between a VARTM process (a) and a SCRIMP process (b) [20].

2.4. Thermoplastic Composites Manufacturing Processes

As it was already described in Section 2.1, thermoplastic resins have several advantages when compared to thermosetting resins, such as faster mold cycles, absence of shelf life, higher toughness and the possibility of being repaired, welded and recycled. However, their utilization in the composite materials market is limited by the strong disadvantage of having high viscosity, which makes difficult the wetting of the fibers and requires very high processing temperatures, with an increase of the production costs.

For the production of engineering composites with short fibers, it is possible to use the same manufacturing processes of non-reinforced thermoplastic materials with few modifications [10]. The short fibers will be directly mixed with the melted plastic and then processed by injection molding. Another common process is the compression molding of long fiber thermoplastic (LFT) compounds.

Different, instead, is the manufacturing of advanced thermoplastic composites, for which the standard processes employed with thermosetting usually cannot be applied or require heavy modifications.

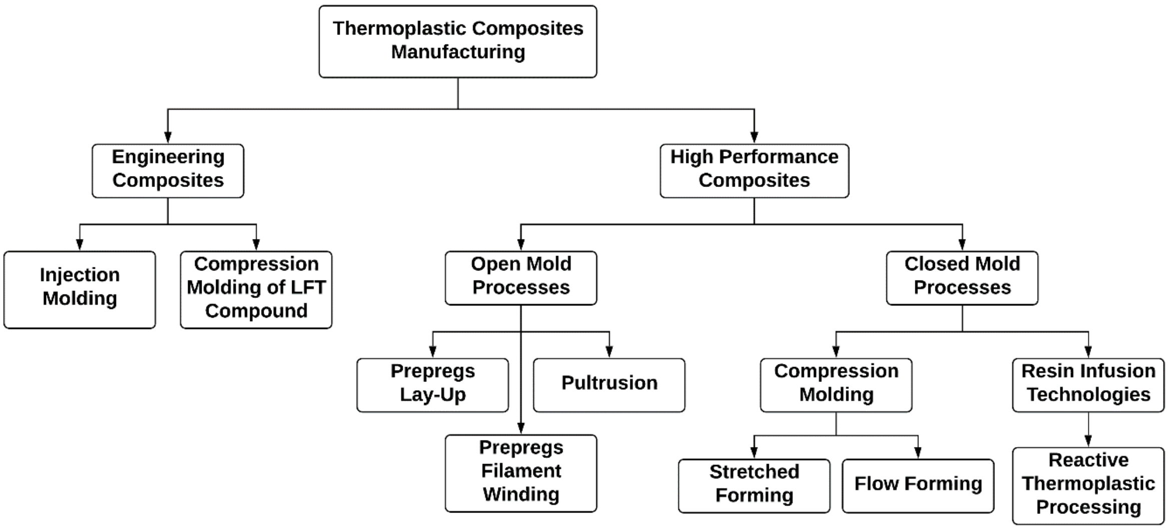

Figure 27. Manufacturing processes for producing thermoplastic composites.

Open Molding Processes

Since the viscosity of thermoplastics is very high, the impregnation of fibers in hand lay-up is difficult and for this reason the process is not used. Open molding of thermoplastic composites is possible using prepregs [10]. Thermoplastic prepregs are solid at room temperature so the laid down operation is performed by heating the layer to the softening temperature of the polymer, allowing the prepregs to be adapted to the shape of the mold. Another possibility is using special prepregs in which polymer fibers are comingled with the reinforcement fibers. The prepregs obtained with this method are flexible, so they can be laid easily on the mold surface. When the prepregs have been laid on the mold in the required orientation, the temperature of the mold is raised to reach the melting point of the plastic and the resin can impregnate the fibers.

Apart from the intrinsic advantages of the material, thermoplastic prepregs do not have shelf life and they do not need to be stored in refrigerators.
However, the processing requires higher temperatures with respect to thermosetting prepregs and usually different materials are needed for constructing the molds, with an overall higher production cost.

Filament Winding

The wetting of the fibers through the resin bath is difficult with thermoplastics, since the viscosity is high even if the resin is at high temperature. In addition, there is the possibility of reaching the material degradation if the plastic is maintained at high temperature for long time. Filament winding therefore must be adapted and preimpregnated tows are used [10]. Prepreg tows are obtained offline by immerging the extended fibers inside the melted thermoplastic or coating the fibers with thermoplastic resin in powder form. When the fibers are wrapped around the mandrel, heat and pressure are applied on them and the thermoplastic material is melted. Since the mandrel of the machine must be modified with respect to the thermosetting processing, the cost of the process is higher.

Pultrusion

The problem of wetting the fibers in the thermoplastic bath is less severe than in filament winding, since the speed of the fibers through the machine is lower and the shearing action of the die, together with the high temperature of it, helps in reducing the viscosity and favoring fibers wetting. However, the continuous heating of the resin inside the bath can cause the degradation of the material. For this reason, a modification of the process has been developed, in which the resin is injected locally on small areas of the fibers [10]. In this way, the resin has to cover a small part of the fibers and the problem of the high viscosity is less effective.

Compression Molding

The compression molding process requires to be modified and takes the name of *stretched forming* [10, 20]. The thermoplastic composite blank, formed by layers of prepregs with fibers arranged in the required direction, is heated to the softening temperature and then placed in a cold mold and clamped in the blank holders. At this point, the press closes the mold, giving the required shape to the thermoplastic composite blank and cooling it down. It is important to notice that, since the blank is clamped in the holders, there is a stretching of the matrix and the fibers. This gives a limitation in the obtainable shapes because the fibers are fragile and cannot be stretched excessively.

If some modifications in the final fibers direction can be accepted, the blank is not clamped in the holders. In this way, when the mold is closed, the blank slips inside the mold and the fibers are not stretched but just bent. This process is called *flow forming*.

Liquid Composite Molding

The viscosity of thermoplastic materials is too high for being used in standard LCM processes. However, in the last decade, a new way of manufacturing thermoplastic materials called *reactive thermoplastic processing* has emerged [20]. In reactive thermoplastic LCM processes, the thermoplastic resin is injected inside the mold when it is in its monomeric form. In this way, the viscosity is low and it is comparable with that of thermosetting resins. Before of being injected, the resin is mixed with the catalyst so that the polymerization reaction starts. When the resin has impregnated the preform, the polymerization will conclude in-situ, in a way analogous to the curing process of the thermosetting resins. Usually, the polymerization is carried out with the applications of heat or radiations, but in the last years, resins that can polymerize at room temperature have been developed.

2.5. Mechanics of Continuous Fiber-Reinforced Composites

The mechanical behavior of composite materials is more complicated than that of traditional materials as metals, ceramics and plastics. Continuous fiber-reinforced plastic composite materials are anisotropic, so their mechanical properties depend on the direction considered [10]. This characteristic can be exploited in order to design composites components that have the maximum mechanical properties along the directions more solicited during service, maximizing the performance. This is obtained by bonding together multiple laminae, also called plies, with the fibers oriented such that the resulting component has the desired mechanical characteristics along the different directions. These types of composites are commonly referred as laminates [6].

In this chapter the mechanical properties of unidirectional composites are initially presented from a micromechanical point of view. Subsequently, the relationship between the mechanical properties of a unidirectional lamina and the ones of a laminate are discussed. Afterwards the failure mechanisms in fiber-reinforced composites are explained and, finally, their behavior under fatigue loading is examined.

2.5.1. Unidirectional Composites Properties

The state of stress and strain in a generic three-dimensional element can be described by six components. In an anisotropic body with no symmetric properties, the stress and the strain are related by 21 independent elastic constants [6]. Consider a composite containing aligned unidirectional continuous fibers, as the one schematically represented in Figure 28. In this kind of material, it is possible to define three orthogonal planes of symmetry, two parallel to the fibers direction and one perpendicular to it, so that the independent elastic constants that relate the stress to the strain are reduced to 9 [6]. The material is called *orthotropic* and its properties differ along three mutually orthogonal axes. Defining the coordinate system 123 oriented along the material principal directions, where axis 1 is parallel to the fibers and the axes 2 and 3 are perpendicular to them, the Hooke's law can be written as:

$$\begin{Bmatrix} \sigma_1 \\ \sigma_2 \\ \sigma_3 \\ \tau_{23} \\ \tau_{13} \\ \tau_{12} \end{Bmatrix} = \begin{bmatrix} C_{11} & C_{12} & C_{13} & 0 & 0 & 0 \\ C_{12} & C_{22} & C_{23} & 0 & 0 & 0 \\ C_{13} & C_{23} & C_{33} & 0 & 0 & 0 \\ 0 & 0 & 0 & C_{44} & 0 & 0 \\ 0 & 0 & 0 & 0 & C_{55} & 0 \\ 0 & 0 & 0 & 0 & 0 & C_{66} \end{bmatrix} \begin{Bmatrix} \varepsilon_1 \\ \varepsilon_2 \\ \varepsilon_3 \\ \gamma_{23} \\ \gamma_{13} \\ \gamma_{12} \end{Bmatrix} \tag{2.1}$$

Then, since in unidirectional composites the fibers are all aligned, the properties are nearly the same in any direction perpendicular to the fibers and the material is called *transversely isotropic* [26]. The number of independent elasticity tensor coefficients that relate the stress to the strain is decreased to 5, since $C_{22} = C_{33}$, $C_{12} = C_{13}$, $C_{55} = C_{66}$ and C_{44} is dependent to the other stiffnesses. The Hooke's law becomes:

$$\begin{Bmatrix} \sigma_1 \\ \sigma_2 \\ \sigma_3 \\ \tau_{23} \\ \tau_{13} \\ \tau_{12} \end{Bmatrix} = \begin{bmatrix} C_{11} & C_{12} & C_{12} & 0 & 0 & 0 \\ C_{12} & C_{22} & C_{23} & 0 & 0 & 0 \\ C_{12} & C_{23} & C_{22} & 0 & 0 & 0 \\ 0 & 0 & 0 & C_{44} & 0 & 0 \\ 0 & 0 & 0 & 0 & C_{55} & 0 \\ 0 & 0 & 0 & 0 & 0 & C_{55} \end{bmatrix} \begin{Bmatrix} \varepsilon_1 \\ \varepsilon_2 \\ \varepsilon_3 \\ \gamma_{23} \\ \gamma_{13} \\ \gamma_{12} \end{Bmatrix} \tag{2.2}$$

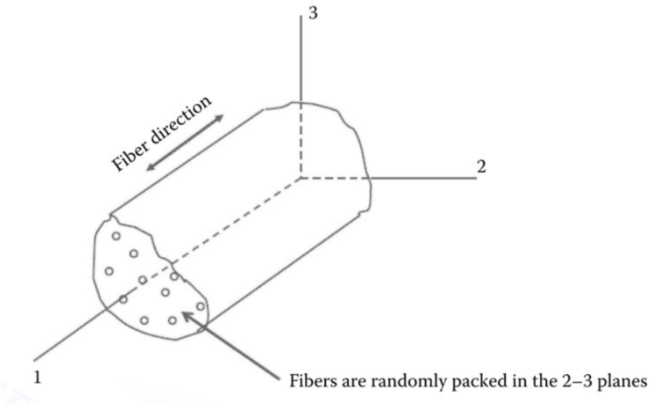

Figure 28. Generic unidirectional composite material with randomly dispersed fibers and the principal coordinate system [26]. Material with this configuration are transversely isotropic.

The elastic properties of unidirectional continuous fiber composites can be defined experimentally or can be predicted knowing the elastic properties of fibers and matrices and their respective volume fractions. The *rule of mixtures* allows to predict quite accurately the longitudinal stiffness and the major Poisson's ratio, but it is not as accurate for the transversal and shear properties. For these ones, the empirically developed *Halpin-Tsai* equations can be used [6]. Considering the reference frame 123 oriented along the material principal directions, the formulas for characterizing the elastic constants of a transversely isotropic unidirectional composite are:

$$E_1 = E_f V_f + E_m V_m \tag{2.3}$$

$$E_2 = E_3 = E_m \left(\frac{1+\xi_1 \eta V_f}{1-\eta V_f}\right) \quad \text{with} \quad \eta = \frac{E_f/E_m - 1}{E_f/E_m + \xi_1} \quad \text{and} \quad \xi_1 = 2\left(\frac{l}{d}\right) \tag{2.4}$$

$$G_{12} = G_{13} = G_m \left(\frac{1+\xi_{12} \eta V_f}{1-\eta V_f}\right) \quad \text{with} \quad \eta = \frac{G_f/G_m - 1}{G_f/G_m + \xi_{12}} \quad \text{and} \quad \xi_{12} = 1 \tag{2.4}$$

$$G_{23} = \frac{E_3}{2(1+\nu_{23})} \tag{2.5}$$

$$\nu_{12} = \nu_{13} = \nu_{12_f} V_f + \nu_m V_m \tag{2.6}$$

$$\nu_{21} = \nu_{12} \frac{E_2}{E_1} \tag{2.7}$$

where E is the tensile modulus, G the shear modulus, ν is the Poisson's ratio, l/d is the aspect ratio of the fibers and the subscripts *m* and *f* represent the matrix and the fibers respectively.

2.5.2. Lamina Properties

A fiber-reinforced lamina, also called ply, is a thin sheet of continuous oriented fibers. Usually the fibers in a ply are unidirectional, as it is represented in Figure 29, but also woven fabric laminae are used depending on the properties required. The laminae are stacked in specific orders of fiber orientation and cured for forming a laminated composite [6]. The properties of the laminate depend on the characteristic and orientation of the single plies, therefore it is important to describe the elastic behavior of a single lamina. A fiber-reinforced lamina is an orthotropic material and, in case it is unidirectional, it is transversely isotropic [6, 26].

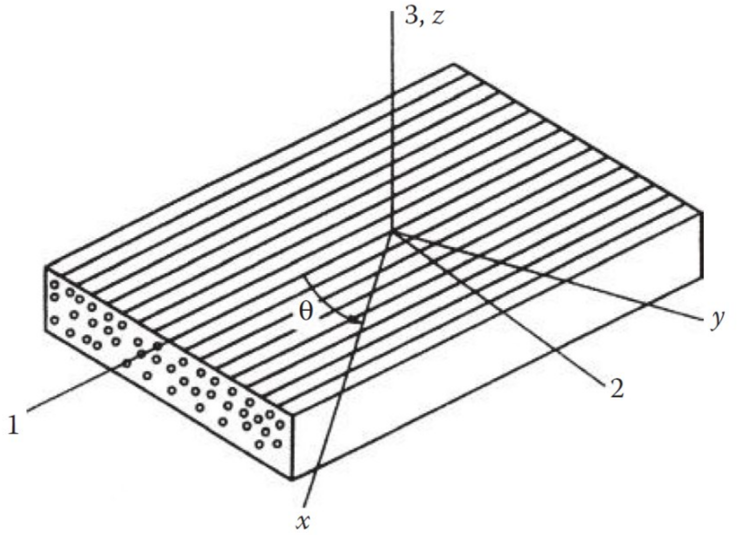

Figure 29. Orthotropic lamina with principal (123) and non-principal (xyz) coordinate systems [26].

Since a lamina is thin, it can be considered in a plane state of stress. With this assumption, considering the case of special orthotropy that verifies when the principal material directions 1 and 2 coincide with the geometric directions x and y, the stress components σ_3, τ_{13} and τ_{23} are all equal to zero. The relationship between strain and stresses in the material principal coordinate system becomes:

$$\begin{Bmatrix} \varepsilon_1 \\ \varepsilon_2 \\ \gamma_{12} \end{Bmatrix} = \begin{bmatrix} S_{11} & S_{12} & 0 \\ S_{21} & S_{22} & 0 \\ 0 & 0 & S_{66} \end{bmatrix} \begin{Bmatrix} \sigma_1 \\ \sigma_2 \\ \tau_{12} \end{Bmatrix} \tag{2.8}$$

where the coefficients S_{ij} are the compliances of the lamina.

The Hooke’s law for the orthotropic lamina becomes:

$$\begin{Bmatrix}\sigma_1\\ \sigma_2\\ \tau_{12}\end{Bmatrix}=\begin{bmatrix}Q_{11} & Q_{12} & 0\\ Q_{21} & Q_{22} & 0\\ 0 & 0 & Q_{66}\end{bmatrix}\begin{Bmatrix}\varepsilon_1\\ \varepsilon_2\\ \varepsilon_{12}\end{Bmatrix} \tag{2.9}$$

where the coefficients Q_{ij} are the reduced stiffnesses and $\varepsilon_{12}=\gamma_{12}/2$.

The reduced stiffnesses are related to the material engineering constants and to the compliances as:

$$\begin{aligned}
Q_{11} &= \frac{S_{22}}{S_{11}S_{22}-S_{12}^2}=\frac{E_1}{1-v_{12}v_{21}}\\
Q_{12} &= -\frac{S_{12}}{S_{11}S_{22}-S_{12}^2}=\frac{v_{12}E_2}{1-v_{12}v_{21}}=Q_{21}\\
Q_{22} &= \frac{S_{11}}{S_{11}S_{22}-S_{12}^2}=\frac{E_2}{1-v_{12}v_{21}}\\
Q_{66} &= \frac{1}{S_{66}}=G_{12}
\end{aligned} \tag{2.10}$$

When the principal material directions of the lamina do not coincide with the geometric axes the condition of special orthotropy is not verified and the stiffness matrix coefficients are all different from zero. This condition is called general orthotropy and the Hooke’s law in the geometric reference frame xyz becomes:

$$\begin{Bmatrix}\sigma_x\\ \sigma_y\\ \sigma_{xy}\end{Bmatrix}=\begin{bmatrix}\bar{Q}_{11} & \bar{Q}_{12} & \bar{Q}_{16}\\ \bar{Q}_{12} & \bar{Q}_{22} & \bar{Q}_{26}\\ \bar{Q}_{16} & \bar{Q}_{26} & \bar{Q}_{66}\end{bmatrix}\begin{Bmatrix}\varepsilon_x\\ \varepsilon_y\\ \gamma_{xy}\end{Bmatrix} \tag{2.11}$$

where the coefficients $\bar{Q}_{ij}$ are called transformed reduced stiffnesses because they are obtained from the reduced stiffnesses Q_{ij} by performing a transformation of coordinate system. Considering the sign convention for the lamina orientation with respect to the geometric directions x and y shown in Figure 30, the transformed reduced stiffness matrix $[\bar{Q}]$ is found as:

$$[\bar{Q}]=[T]^{-1}[Q^*][T]=\begin{bmatrix}c^2 & s^2 & -2cs\\ s^2 & c^2 & 2cs\\ cs & -cs & c^2-s^2\end{bmatrix}\begin{bmatrix}Q_{11} & Q_{12} & 0\\ Q_{21} & Q_{22} & 0\\ 0 & 0 & 2Q_{66}\end{bmatrix}\begin{bmatrix}c^2 & s^2 & 2cs\\ s^2 & c^2 & -2cs\\ -cs & cs & c^2-s^2\end{bmatrix} \tag{2.12}$$

where $[T]$ is the transformation matrix, $c=cos\theta$ and $s=sin\theta$.

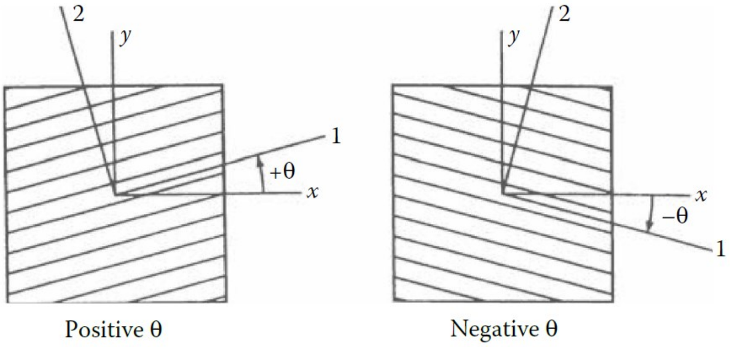

Figure 30. Sign convention for the orientation of the lamina [26].

The transformed reduced stiffnesses can be computed also with the “invariant” method, that has been proposed by Tsai and Pagano [26]. The same coefficients that can be found from Eq. 2.12, by using the “invariant” method can be written as:

$$\begin{aligned}
\bar{Q}_{11} &= U_1 + U_2\cos 2\theta + U_3\cos 4\theta \\
\bar{Q}_{12} &= U_4 - U_3\cos 4\theta \\
\bar{Q}_{22} &= U_1 - U_2\cos 2\theta + U_3\cos 4\theta \\
\bar{Q}_{16} &= \frac{U_2}{2}\sin 2\theta + U_3\sin 4\theta \\
\bar{Q}_{26} &= \frac{U_2}{2}\sin 2\theta - U_3\sin 4\theta \\
\bar{Q}_{66} &= \frac{1}{2}(U_1 - U_4) - U_3\cos 4\theta
\end{aligned} \tag{2.13}$$

where the “invariants” are related to the reduced stiffnesses:

$$\begin{aligned}
U_1 &= \frac{1}{8}(3Q_{11} + 3Q_{22} + 2Q_{12} + 4Q_{66}) \\
U_2 &= \frac{1}{2}(Q_{11} - Q_{22}) \\
U_3 &= \frac{1}{8}(Q_{11} + Q_{22} - 2Q_{12} - 4Q_{66}) \\
U_4 &= \frac{1}{8}(Q_{11} + Q_{22} + 6Q_{12} - 4Q_{66})
\end{aligned} \tag{2.14}$$

2.5.3. Laminates Properties

The properties of a laminate, obtained by stacking together multiple laminae in specific order and fibers direction, can be examined adopting the *Classical Lamination Theory* (CLT) [6, 26]. Thanks to CLT it is possible to analyze laminates composed by arbitrarily oriented plies that can have different coupling effects, which may cause complex combination of extensional, flexural and torsional deformations. The analysis considers the in-plane loading of the laminate caused by axial and shear forces and both bending and torsional moments. Nevertheless, CLT has the limitation of neglecting the interlaminar stresses inside the laminate, since each ply is considered in a plane state of stress. Considering a laminated plate, the coordinate system xyz adopted in the CLT is represented in Figure 31. This coordinate system is assumed to have the origin at the geometric midplane surface of the laminate and u, v and w are the displacements in the x, y and z directions respectively.

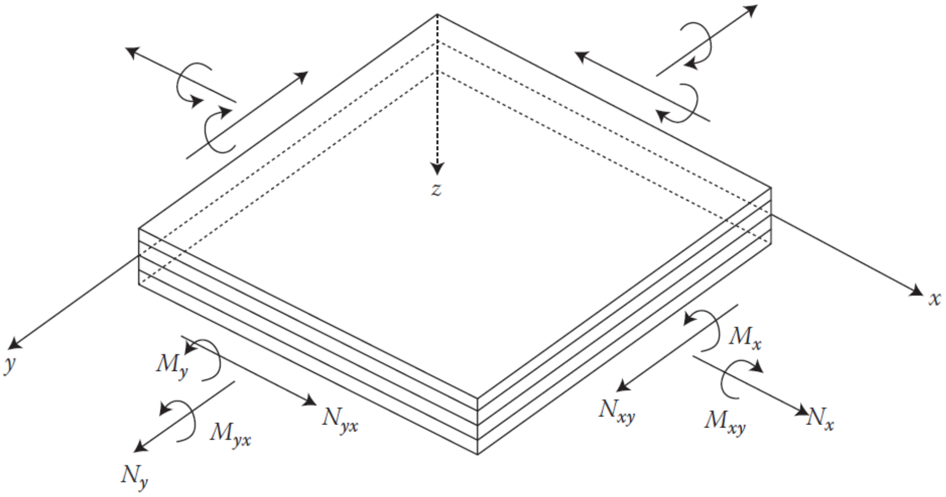

Figure 31. Coordinate system and stress resultants for the laminated plate [26].

In order to apply CLT some assumptions have to be made [26]. These are:

1. The laminated plate is composed by orthotropic laminae bonded together with the principal material axes oriented along arbitrary directions with respect to the x and y axes. The laminae are perfectly bonded and this lead to have no interfacial slip and continuous displacements across the lamina interfaces.
2. The thickness t of the laminate is much smaller than the lateral dimensions.
3. The displacements u, v and w are small compared to the laminate thickness t.
4. The in-plane strains ε_x, ε_y and γ_{xy} are small compared with unity.

5. Transverse shear strains γ_{xz} and γ_{yz} are negligible.
6. The transverse normal strain ε_z is negligible.
7. Tangential displacements *u* and *v* are linear functions of the *z* coordinate.
8. Each lamina obeys to the Hooke's law.
9. The plate thickness *t* is constant.

Assumptions 5 and 7 define the so-called Kirchhoff's deformation hypothesis, which assumes that lines normal to the laminate middle plane remain straight and normal during the deformation. It is possible to demonstrate that, according to the assumptions 6 and 7, the in-plane strains at any distance from the laminate middle surface can be written as:

$$\begin{aligned}\varepsilon_x &= \frac{\partial u}{\partial x} = \varepsilon_x^0 + z\kappa_x \\ \varepsilon_y &= \frac{\partial v}{\partial y} = \varepsilon_y^0 + z\kappa_y \\ \gamma_{xy} &= \frac{\partial u}{\partial y} + \frac{\partial v}{\partial x} = \gamma_{xy}^0 + z\kappa_{xy}\end{aligned} \tag{2.15}$$

where the strains on the middle surface of the laminate are equal to:

$$\varepsilon_x^0 = \frac{\partial u^0}{\partial x}, \qquad \varepsilon_y^0 = \frac{\partial v^0}{\partial y}, \qquad \gamma_{xy}^0 = \frac{\partial u^0}{\partial y} + \frac{\partial v^0}{\partial x} \tag{2.16}$$

The curvatures of the middle surface are:

$$\kappa_x = -\frac{\partial^2 w}{\partial x^2}, \qquad \kappa_y = -\frac{\partial^2 w}{\partial y^2}, \qquad \kappa_{xy} = -2\frac{\partial^2 w}{\partial x \, \partial y} \tag{2.17}$$

Considering a laminate composed by n stacked plies, as the one shown in Figure 32. For each k-th layer it is possible to write the Hooke's law:

$$\begin{Bmatrix}\sigma_x \\ \sigma_y \\ \tau_{xy}\end{Bmatrix}_k = \begin{bmatrix}\bar{Q}_{11} & \bar{Q}_{12} & \bar{Q}_{16} \\ \bar{Q}_{12} & \bar{Q}_{22} & \bar{Q}_{26} \\ \bar{Q}_{16} & \bar{Q}_{26} & \bar{Q}_{66}\end{bmatrix}_k \begin{Bmatrix}\varepsilon_x^0 + z\kappa_x \\ \varepsilon_y^0 + z\kappa_y \\ \gamma_{xy}^0 + z\kappa_x\end{Bmatrix} \tag{2.18}$$

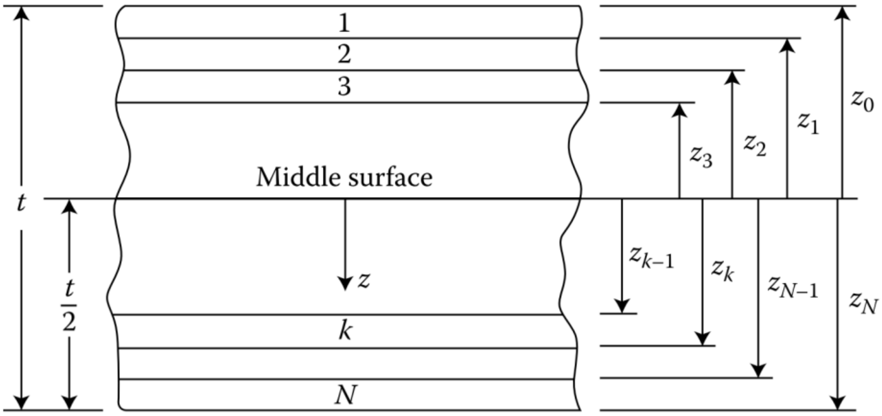

Figure 32. Scheme of a laminate cross section with the relative numbering system [26].

Because the stresses in a laminated composite vary from ply to ply, it is convenient to define the resultants of the stresses and moments *N* and *M*, as it is shown in Figure 31. These stress and moment resultants define a system of equivalent forces and moments acting on the middle plane of the laminate. The stress resultants are defined as:

$$N_x = \int_{-t/2}^{t/2} \sigma_x \, \mathrm{d}z$$
$$N_y = \int_{-t/2}^{t/2} \sigma_y \, \mathrm{d}z \qquad (2.19)$$
$$N_{xy} = \int_{-t/2}^{t/2} \tau_{xy} \, \mathrm{d}z$$

The stress resultants have the dimensions of force per unit of length. The moment resultants are equivalent to the moments produced by the stresses with respect to the middle plane and are equal to:

$$M_x = \int_{-t/2}^{t/2} \sigma_x \mathrm{z} \, \mathrm{d}z$$
$$M_y = \int_{-t/2}^{t/2} \sigma_y \mathrm{z} \, \mathrm{d}z \qquad (2.19)$$
$$M_{xy} = \int_{-t/2}^{t/2} \tau_{xy} \mathrm{z} \, \mathrm{d}z$$

The system composed by three stress resultants and three moment resultants is statistically equivalent to the actual stress distribution through the thickness of the laminate [6].

From Eq. 2.18 it is possible to write the stress resultants as a summation over the *n* plies:

$$\begin{bmatrix} N_x \\ N_y \\ N_{xy} \end{bmatrix} = \sum_{k=1}^{n} \int_{z_{k-1}}^{z_k} \begin{Bmatrix} \sigma_x \\ \sigma_y \\ \sigma_s \end{Bmatrix} \mathrm{dz} = \tag{2.20}$$

$$= \sum_{k=1}^{n} \left(\int_{z_{k-1}}^{z_k} \begin{bmatrix} \bar{Q}_{11} & \bar{Q}_{12} & \bar{Q}_{16} \\ \bar{Q}_{12} & \bar{Q}_{22} & \bar{Q}_{26} \\ \bar{Q}_{16} & \bar{Q}_{26} & \bar{Q}_{66} \end{bmatrix} \begin{Bmatrix} \varepsilon_x^0 \\ \varepsilon_y^0 \\ \gamma_{xy}^0 \end{Bmatrix} \mathrm{dz} + \int_{z_{k-1}}^{z_k} \begin{bmatrix} \bar{Q}_{11} & \bar{Q}_{12} & \bar{Q}_{16} \\ \bar{Q}_{12} & \bar{Q}_{22} & \bar{Q}_{26} \\ \bar{Q}_{16} & \bar{Q}_{26} & \bar{Q}_{66} \end{bmatrix} \begin{Bmatrix} k_x \\ k_y \\ k_{xy} \end{Bmatrix} \mathrm{zdz} \right)$$

Considering that the middle plane stains $\{\varepsilon^0\}$, the curvatures $\{k\}$ and the reduced stiffness matrix $[Q]$ are not functions of the *z*, the previous equation can be simplified as:

$$\begin{Bmatrix} N_x \\ N_y \\ N_{xy} \end{Bmatrix} = \sum_{k=1}^{n} \left(\begin{bmatrix} \bar{Q}_{11} & \bar{Q}_{12} & \bar{Q}_{16} \\ \bar{Q}_{12} & \bar{Q}_{22} & \bar{Q}_{26} \\ \bar{Q}_{16} & \bar{Q}_{26} & \bar{Q}_{66} \end{bmatrix} \begin{Bmatrix} \varepsilon_x^0 \\ \varepsilon_y^0 \\ \gamma_{xy}^0 \end{Bmatrix} \int_{z_{k-1}}^{z_k} \mathrm{dz} + \begin{bmatrix} \bar{Q}_{11} & \bar{Q}_{12} & \bar{Q}_{16} \\ \bar{Q}_{12} & \bar{Q}_{22} & \bar{Q}_{26} \\ \bar{Q}_{16} & \bar{Q}_{26} & \bar{Q}_{66} \end{bmatrix} \begin{Bmatrix} k_x \\ k_y \\ k_{xy} \end{Bmatrix} \int_{z_{k-1}}^{z_k} \mathrm{zdz} \right) \tag{2.21}$$

That finally can be written as:

$$\begin{Bmatrix} N_x \\ N_y \\ N_{xy} \end{Bmatrix} = \begin{bmatrix} A_{11} & A_{12} & A_{16} \\ A_{12} & A_{22} & A_{26} \\ A_{16} & A_{26} & A_{66} \end{bmatrix} \begin{Bmatrix} \varepsilon_x^0 \\ \varepsilon_y^0 \\ \gamma_{xy}^0 \end{Bmatrix} + \begin{bmatrix} B_{11} & B_{12} & B_{16} \\ B_{12} & B_{22} & B_{26} \\ B_{16} & B_{26} & B_{66} \end{bmatrix} \begin{Bmatrix} k_x \\ k_y \\ k_{xy} \end{Bmatrix} \tag{2.22}$$

Where the coefficients A_{ij} are the *laminate extensional stiffnesses* and the coefficients B_{ij} are the *laminate coupling stiffnesses*. They are equal to:

$$A_{ij} = \int_{-t/2}^{t/2} \left(\bar{Q}_{ij}\right)_k \mathrm{dz} = \sum_{k=1}^{N} \left(\bar{Q}_{ij}\right)_k (z_k - z_{k-1}) \tag{2.23}$$

$$B_{ij} = \int_{-t/2}^{t/2} \left(\bar{Q}_{ij}\right)_k z\mathrm{dz} = \frac{1}{2} \sum_{k=1}^{N} \left(\bar{Q}_{ij}\right)_k (z_k^2 - z_{k-1}^2) \tag{2.24}$$

The same can be written for the moment resultants:

$$\begin{Bmatrix} M_x \\ M_y \\ M_{xy} \end{Bmatrix} = \begin{bmatrix} B_{11} & B_{12} & B_{16} \\ B_{12} & B_{22} & B_{26} \\ B_{16} & B_{26} & B_{66} \end{bmatrix} \begin{Bmatrix} \varepsilon_x^0 \\ \varepsilon_y^0 \\ \gamma_{xy}^0 \end{Bmatrix} + \begin{bmatrix} D_{11} & D_{12} & D_{16} \\ D_{12} & D_{22} & D_{26} \\ D_{16} & D_{26} & D_{66} \end{bmatrix} \begin{Bmatrix} k_x \\ k_y \\ k_{xy} \end{Bmatrix} \tag{2.25}$$

where the coefficients B_{ij} are the *laminate coupling stiffnesses*, equal to that of Eq. 2.24, and the coefficients D_{ij} are the *laminate bending stiffnesses*. The laminate bending stiffnesses are defined as:

$$D_{ij} = \int_{-t/2}^{t/2} \left(\bar{Q}_{ij}\right)_k z^2 \mathrm{dz} = \frac{1}{3}\sum_{k=1}^{N} \left(\bar{Q}_{ij}\right)_k (z_k^3 - z_{k-1}^3) \tag{2.26}$$

The Eq. 2.22 and Eq. 2.25 can be combined in a matrix system to form the laminate composite constitutive equations:

$$\begin{Bmatrix} N_x \\ N_y \\ N_{xy} \\ M_x \\ M_y \\ M_{xy} \end{Bmatrix} = \begin{bmatrix} A_{11} & A_{12} & A_{16} & B_{11} & B_{12} & B_{16} \\ A_{12} & A_{22} & A_{26} & B_{12} & B_{22} & B_{26} \\ A_{16} & A_{26} & A_{66} & B_{16} & B_{26} & B_{66} \\ B_{11} & B_{12} & B_{16} & D_{11} & D_{12} & D_{16} \\ B_{12} & B_{22} & B_{26} & D_{12} & D_{22} & D_{26} \\ B_{16} & B_{26} & B_{66} & D_{16} & D_{26} & D_{66} \end{bmatrix} \begin{Bmatrix} \varepsilon_x^0 \\ \varepsilon_y^0 \\ \gamma_{xy}^0 \\ \kappa_x \\ \kappa_y \\ \kappa_{xy} \end{Bmatrix} \tag{2.27}$$

That can also be written in compact form:

$$\begin{Bmatrix} N \\ M \end{Bmatrix} = \begin{bmatrix} A & B \\ B & D \end{bmatrix} \begin{Bmatrix} \varepsilon^0 \\ \kappa \end{Bmatrix} \tag{2.28}$$

In order to understand the meaning of the previous equations, it is useful to analyze the expression for the stress resultant N_x that is equal to:

$$N_x = A_{11}\varepsilon_x^0 + A_{12}\varepsilon_y^0 + A_{16}\gamma_{xy}^0 + B_{11}\kappa_x + B_{12}\kappa_y + B_{16}\kappa_{xy} \tag{2.29}$$

It is possible to notice that the stress resultant N_x depends on the middle plane tensile strains ε_x^0 and ε_y^0, the middle plane shear strain γ_{xy}^0, the bending curvatures κ_x and κ_y and the twisting curvature κ_{xy}. This means that in a laminate there is coupling between tensile and shear, tensile and bending, and tensile and twisting effects [6]. Specifically, the terms A_{16} and A_{26} are responsible for the tension-shear coupling while the terms B_{16} and B_{26} represent the tension-twisting coupling. Considering the expression for the moment resultant M it is possible to see that the coefficients D_{16} and D_{26} represent the bending-twisting coupling while the terms B_{16} and B_{26} couple bending to tension. The different coupling phenomena are schematically represented in Figure 33.

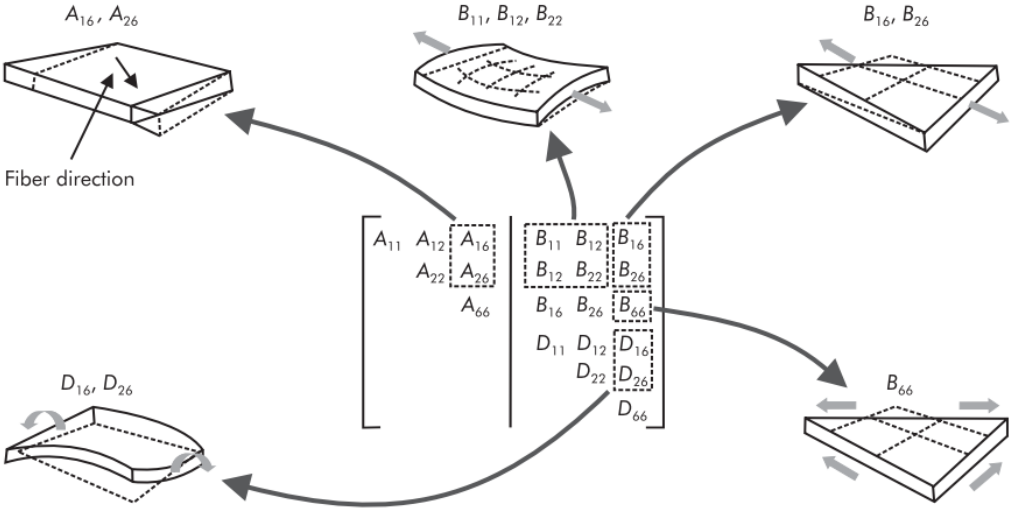

Figure 33. Coupling phenomena of a composite laminate [10].

If certain particular ply stacking orders are respected during the design of a laminate, it is possible to eliminate some of the coupling phenomena [6, 26]. By looking to Eq. 2.23, the terms A_{ij} are obtained from the sum of the $\bar{Q}_{ij}$ of each ply multiplied by the thickness of the ply. The $\bar{Q}_{ij}$ stiffnesses are derived from the orthotropic stiffness applying the transformation of Eq. 2.13 and, because of the form of the transformation, the terms $\bar{Q}_{11}$, $\bar{Q}_{22}$, $\bar{Q}_{12}$ and $\bar{Q}_{66}$ are always positive. This means that the terms A_{11}, A_{22}, A_{12} and A_{66} are always positive as well. The terms $\bar{Q}_{16}$ and $\bar{Q}_{26}$ instead are zero for 0° or 90° oriented plies and can be positive or negative for plies oriented between 0° and 90°. In particular, the terms $\bar{Q}_{16}$ and $\bar{Q}_{26}$ for a ply oriented at $+\theta$ are equal and opposite in sign with respect to the values $\bar{Q}_{16}$ and $\bar{Q}_{26}$ of a ply with $-\theta$ orientation. For this reason, if for each $+\theta$ ply there is another identical ply of the same thickness and with $-\theta$ orientation, the condition of having $A_{16} = A_{26} = 0$ is verified. A laminate realized respecting this stacking sequence is called *special orthotropic* or *balanced*. This condition allows to uncouple the tension effect to the shear one and it is not dependent on the relative position of the opposite oriented plies with respect to the stacking sequence. As it is written in Eq. 2.24, the B_{ij} terms are given by the sum of the ply $\bar{Q}_{ij}$ stiffnesses multiplied by the differences of the square of z coordinate for the top and bottom of each ply. Therefore, the B_{ij} terms are zero if for each ply above the middle plane is present a ply identical in properties and orientation at an equal distance below the middle plane. Laminates of this type are called *symmetric*. Symmetric laminates do not have tension-twisting coupling and bending-tension coupling, meaning that in-plane loads will not produce bending and twisting curvatures that induce out-of-plane warping and bending or twisting moments will not cause stretching of the middle surface. From Eq. 2.26, the D_{ij} coefficients are obtained from the sum of the products between the $\bar{Q}_{ij}$ of the plies and the difference $(z_k^3 - z_{k-1}^3)$, which geometrical contribution is always positive. Being the terms $\bar{Q}_{11}$, $\bar{Q}_{22}$, $\bar{Q}_{12}$ and $\bar{Q}_{66}$ always positive, also D_{11}, D_{22}, D_{12} and D_{66} are always positive. The terms D_{16} and D_{26} therefore will be zero for all plies oriented at 0° or 90°, since the transformed reduced stiffnesses $\bar{Q}_{16}$ and $\bar{Q}_{26}$ are null. Otherwise, D_{16} and D_{26} can be null if, for each ply oriented at $+\theta$ and at a given distance above the middle plane, there is an identical ply at an equal distance below the middle plane but oriented at $-\theta$. This is possible because $\bar{Q}_{16}(+\theta) = -\bar{Q}_{16}(-\theta)$ and $\bar{Q}_{26}(+\theta) = -\bar{Q}_{26}(-\theta)$, while the difference $(z_k^3 - z_{k-1}^3)$ is the same for both plies. Laminates realized with this stacking order are called *anti-symmetric* and do not have coupling phenomenon between bending and twisting, as well as tension-shear coupling since also $A_{16} = A_{26} = 0$. A schematic representation of the three special stacking sequence discussed can be observed in Figure 34.

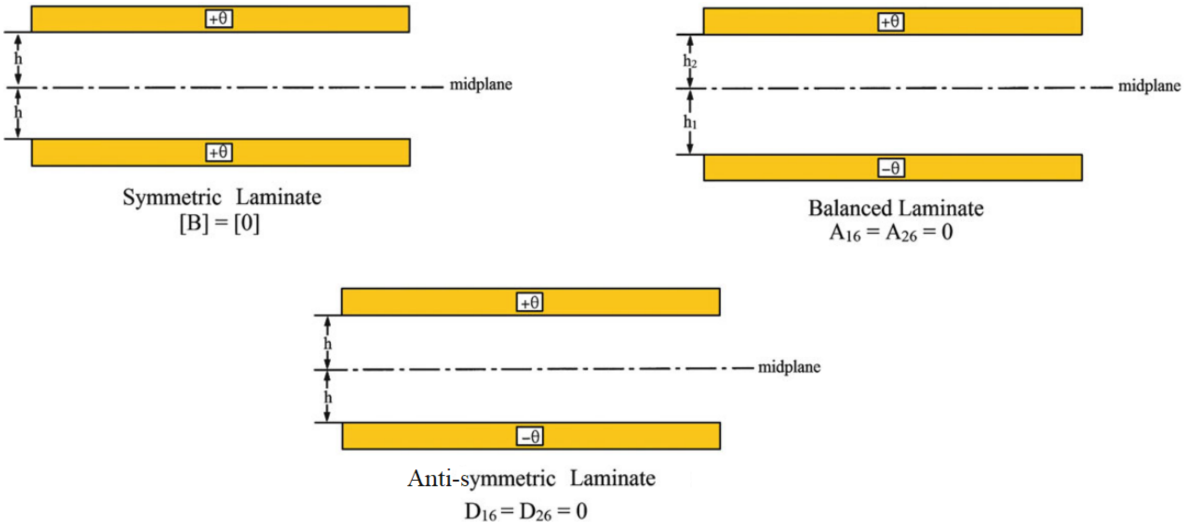

Symmetric Laminate
$[B] = [0]$

Balanced Laminate
$A_{16} = A_{26} = 0$

Anti-symmetric Laminate
$D_{16} = D_{26} = 0$

Figure 34. Example of special stacking sequences for laminates design [6].

2.5.3.1. Interlaminar Stresses

One of the main limitations of the CLT is that it assumes each ply of the laminate in a plane state of stress in the xy plane, neglecting the interlaminar stresses. However, the interlaminar stresses are present and they may cause delamination, leading the laminate to failure [26]. The assumption of generalized plane state of stress is actually valid in the region sufficiently far from geometric discontinuities such as the free edges of the laminate. Nevertheless, as it was demonstrated by Pipes and Pagano, even in a laminate under simple uniaxial loading conditions as the one represented in Figure 35, there is a "boundary layer" region along the free edges where a three-dimensional stress state exists [6, 26]. The dimensions of this boundary layer was discovered to be approximately equal to the laminate thickness.

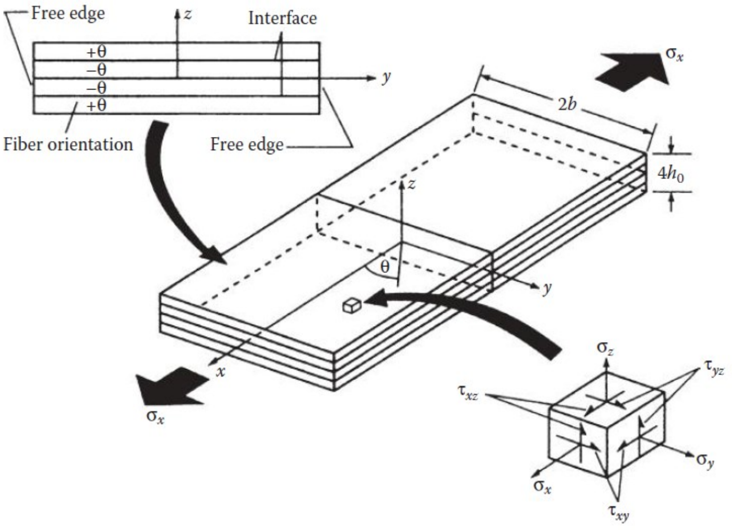

Figure 35. Model utilized by Pipes and Pagano for the analysis of interlaminar stresses in a laminate under uniaxial extension [26].

Consider the three stress equilibrium equations from the theory of elasticity:

$$\begin{aligned}
&\frac{\partial \sigma_x}{\partial x} + \frac{\partial \tau_{xy}}{\partial y} + \frac{\partial \tau_{xz}}{\partial z} = 0 \\
&\frac{\partial \tau_{yx}}{\partial x} + \frac{\partial \sigma_y}{\partial y} + \frac{\partial \tau_{yz}}{\partial z} = 0 \qquad (2.30) \\
&\frac{\partial \tau_{zx}}{\partial x} + \frac{\partial \tau_{zy}}{\partial y} + \frac{\partial \sigma_z}{\partial z} = 0
\end{aligned}$$

Taking into account a region near the free edges of the uniaxially loaded laminate shown in Figure 35, where $y = \pm b$, and assuming that the stresses do not vary along the loading direction x.

It follows that $\partial\sigma_x/\partial x = 0$ and the interlaminar stress is given by:

$$\tau_{xz}(z) = -\int_{-t/2}^{z} \frac{\partial\tau_{xy}}{\partial y}\,\mathrm{d}z \tag{2.31}$$

In the interior region of the laminae, the in-plane shear stress τ_{xy} is assumed to have a constant value. However, moving toward a free edge along the y-direction, τ_{xy} must decrease and become zero at the stress-free surfaces, where $y = \pm b$. Thus, approaching $y = \pm b$, the term $|\partial\tau_{xy}/\partial y|$ increases. This means that the interlaminar shear stress τ_{xz} must increase from zero in the interior region of the laminate to a very large value for $y \to \pm b$. The region of the laminate where there are these changes is the boundary layer region. The other interlaminar stresses are equal to:

$$\tau_{yz}(z) = -\int_{-t/2}^{z} \frac{\partial\sigma_y}{\partial y}\,\mathrm{d}z \tag{2.32}$$

$$\sigma_z(z) = -\int_{-t/2}^{z} \frac{\partial\tau_{yz}}{\partial y}\,\mathrm{d}z \tag{2.33}$$

The behavior of the stresses of the uniaxially loaded lamina studied by Pipes and Pagano is represented in Figure 36. It is important to notice that the in-plane stress state predicted by CLT is valid in the interior region of the laminate, since the interlaminar stresses σ_z, τ_{yz} and τ_{xz} are all zero. In the boundary layer region, the in-plane stresses σ_x and τ_{yx} drop and the interlaminar stresses rapidly grow. The shear stress τ_{xz} is the largest of the interlaminar stresses. It was demonstrated by numerical results on laminates with different cross sectional aspect ratios that the dimension of the boundary layer region from the free edge is approximately equal to the laminate thickness [26]. Moreover, it was discovered that the ply stacking sequence in a laminate affects the magnitude and the sign of the interlaminar stresses, affecting the mechanical performance of the laminate [6].

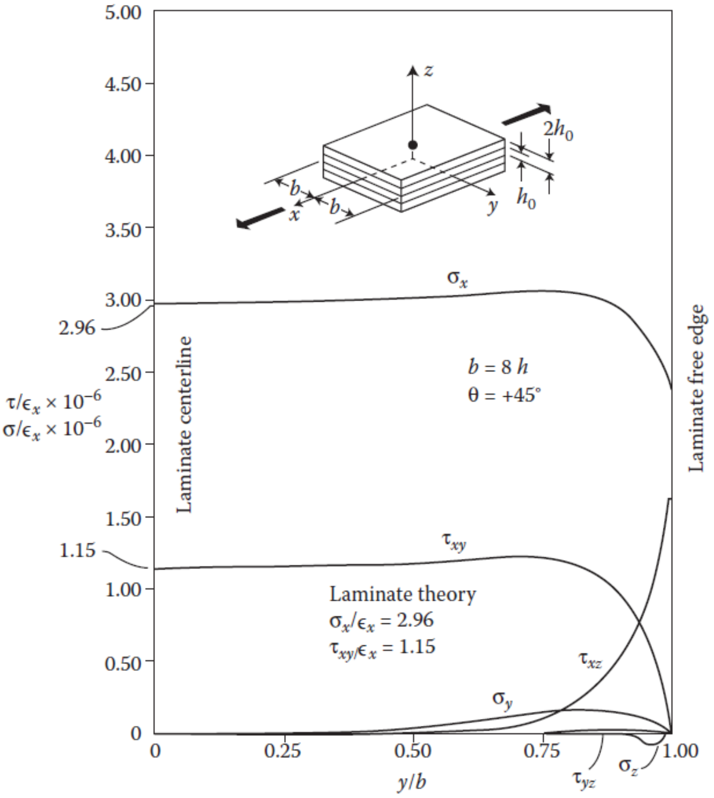

Figure 36. Distribution of all the stresses from the Pipes and Pagano analysis [26]. The interlaminar stresses are present only in the boundary layer region near the free edge of the laminate.

2.5.4. Damage of Composite Materials

The heterogeneous microstructure and anisotropic properties of composite materials result in damage mechanisms and failure behavior different from those of conventional homogeneous materials such as metals and ceramics [6, 27]. Failure in composites is not a sudden process caused by a localized concentration of the stress, but it is a progressive process during which different damage mechanisms can appear simultaneously and interact between each other. As loading increases, the composite material accumulates damages that eventually leads to failure [27]. Damage mechanisms in FRP composites occur at different length scales, from microscopic such as fiber breakage and fiber/matrix debonding, to macroscopic such as ply cracks and delamination [28]. In the following, the damage mechanisms occurring in FRP composites are discussed.

2.5.4.1. Interfacial Debonding

The adhesion bond at the interface between the fibers and the matrix affects strongly the properties of a composite. A strong bond between the fibers and the matrix is fundamental for obtaining high performance. However, during thermomechanical loading, debonding between the fibers and the matrix in certain regions of the composite can occur. Generally, debonding can be caused by two types of loading, which are load perpendicular to the fibers direction and load parallel to it [28]. When a load is applied transversely to the fibers, the load is mainly supported by the matrix. The deformation induced in the matrix can induce debonding in some of the fibers and, in case of coalescence of the debonded fibers, generate a ply crack. This effect is shown in Figure 37.

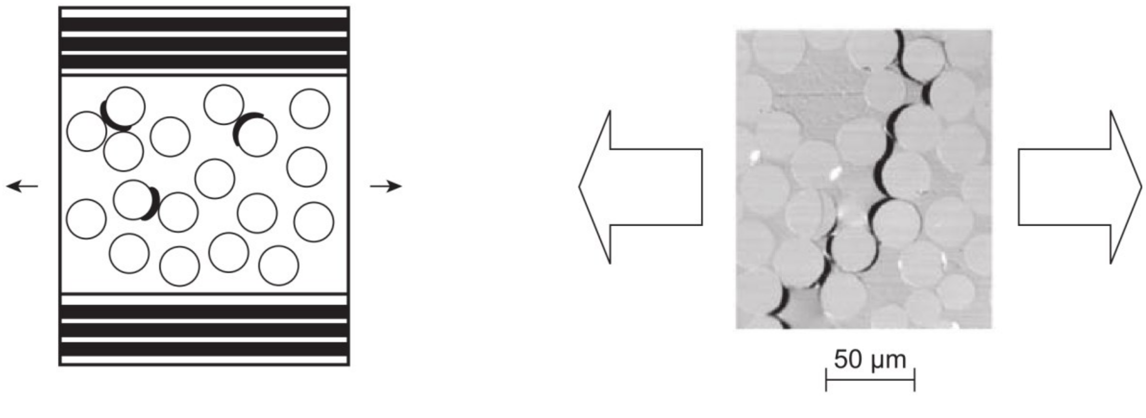

Figure 37. Schematic of fiber matrix debonding in a transversely loaded ply (left image) and coalescence of fiber-matrix debonding in a ply-crack (right image) [28].

Fiber-matrix debonding can occur also in fibers oriented parallel to the loading direction. Considering a crack that propagates perpendicularly to the fibers, as represented in Figure 38, which can be caused by a point of stress concentration, such as a void. When the crack arrives at the fiber-matrix interface, it may either arrest at the fiber if the stress is not high enough, or it may pass around the fibers without damaging the interface bond. As the applied longitudinal load increases, the deformations of fibers and matrix are different and this generates large local stress in the fiber. This causes local Poisson contraction and, if the shear stress developed at the interface exceeds the interfacial shear strength, debonding of the fiber from the matrix happens [27]. Another condition that can induce longitudinal debonding verifies when a continuous fiber breaks inside the matrix. The shear stress generated between the free ends of the fiber and the matrix can result in local interfacial debonding [28].

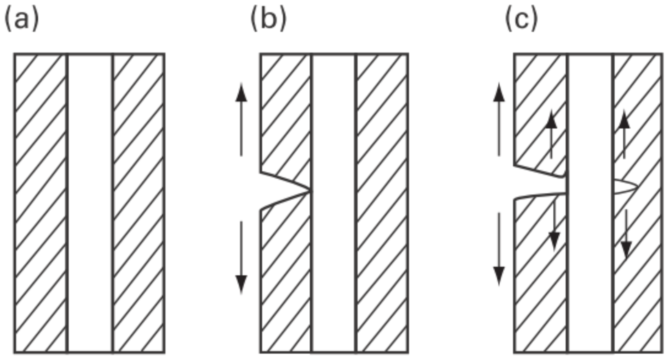

Figure 38. Mechanics of interfacial debonding in a continuous fiber composite: (a) perfect laminate; (b) differential deformation of fiber and matrix crack causes high stress at the fiber/matrix interface; (c) when the shear stress exceeds the interfacial shear strength debonding is nucleated [27].

2.5.4.2. Matrix Intralaminar Cracking

Matrix intralaminar cracks, also called ply cracks, are caused by transverse tension/compression and shear stresses acting in a lamina under thermal mechanical loading. In laminates with differently oriented plies, they can originate from transversal fiber-matrix debonding or manufacturing defects such as voids and inclusions, and grow extending across the entire thickness of the ply and running parallel to its fibers [27]. Ply cracks do not cause structural failure by themselves, thus are referred as sub-critical damage mechanisms. However, they can cause degradation of the laminate stiffness and induce more severe forms of damage, such as fiber breakage and delamination [27].

2.5.4.3. Interlaminar Cracking (Delamination)

Interlaminar cracking is a crack that generates at the interface between two adjacent plies, causing the separation of them, and is referred as delamination. Delamination can occur at the free edges of a laminate, where shear and normal interlaminar stresses are present. Delamination can also be caused in the internal region of a laminate by stress concentrations at the tip of a ply crack or during low velocity impact loading [27]. The growth of delamination under the application of external loads induces a rapid deterioration of the mechanical properties and can cause catastrophic failure of the composite. Delamination initiation and propagation are determined by the interlaminar strength and by the fracture toughness respectively, which are both properties depending on the matrix. Delamination can be reduced by improving these two properties acting on the matrix material or by selecting particular plies stacking sequences that allow to reduce the interlaminar stresses [27].

2.5.4.4. Fiber Breakage

The strength of the fibers inside a bundle is not constant but changes for every fiber, since it depends on the diameter and on the presence of defects caused by the fiber manufacturing process or during the composite production. Due to the variability in strength between the fibers of a same bundle, when a composite is loaded in tension along the fibers, individual fibers may fail at their weak point at different values of stress. This causes a redistribution of the stress between the matrix and the fibers that increases the stress in the local vicinity of the broken fiber. Increasing the load, the localized stress concentrations caused by isolated fiber fractures can induce failure in adjacent fibers that can lead to an accumulation of fiber fractures and failure of the composite [27, 28]. The fracture of multiple fibers is considered a critical damage. Studies have demonstrated that in composite laminates composed by unidirectional plies, the stress on the fibers of a lamina is enhanced in proximity of ply cracks in the adjacent plies, and this causes a concentration of the fiber failure sites [27].

2.5.4.5. Void Growth

Voids are one of the most common and primary types of defects in composite materials. Their presence inside a composite is due to the manufacturing process parameters, such as infusion pressure and vacuum level in LCM processes, curing temperature, curing pressure and resin viscosity. The presence of voids has a significant detrimental effect on the composite performance even for low volume fractions, and affects most the flexural, transverse and shear properties of the material [27]. Voids can cause local inelastic deformations in the material, which can initiate other damage processes as crazing, shear yielding and local fractures of the matrix. These damage processes may influence the deformation response and failure properties of the composite material [27].

2.5.5. Fatigue in Composites

When a component is subjected to a cyclic loading condition, it undergoes a degradation of the mechanical properties that will finally lead to its failure. This phenomenon is called fatigue and understanding the behavior of composite materials when they are subjected to cyclic loads is fundamental in order to design components that will ensure the required working lifetime. When subjected to cyclic loading, materials experience microscopic damages during each cycle that deteriorate their mechanical properties. The damage propagates as the number of cycles increases, and the speed of propagation depends on the value of the stress applied to the material. The closer the applied stress is to the ultimate strength of the material, the faster will be the propagation of damage and therefore the shorter will be the lifetime of the component. On the contrary, under a certain magnitudes of stress, no damage is induced in the material or the damage propagates with a slow rate. In this case, the lifetime of the component under this cyclic loading is considered infinite and the value of the stress that allows this condition is called fatigue limit.

The fatigue behavior of composite materials is very different from that of conventional homogeneous and isotropic materials as metals. In metals subjected to fatigue loading for example, a single damage mechanism appears under the form of a crack. The crack is generally started in regions where there is a concentration of the stress, which can be caused by a defect in the material or a particular shape of the component (notch). During each cycle, the crack propagates of a certain length, until it reaches a critical length at which the uncracked area is not able anymore to sustain the applied stress and there is a catastrophic failure of the component. The facture behavior of composites instead, as it was described in the previous chapter, is characterized by the occurrence of multiple damage mechanisms. Which of the different damage mechanisms appear in the material and lead the component to failure depend on the direction of the application of load with respect to the fibers orientation.

2.5.5.1. Unidirectional Composites Longitudinally Loaded

Consider a unidirectional composite subjected to cyclic tension in the fiber direction. The behavior of the composite material depends on the entity of the load applied. When the maximum load is such that the strain of the composite reaches the failure strain of the fibers, the component will fail suddenly in few cycles due to fiber breakage. In this case, the component does not undergo strength degradation and this failure mechanism can be described as non-progressive [27]. When the applied load is such that the strain of the component is lower than the failure strain of the fibers, the composite will experience fatigue cracking of the matrix. Increasing the number of cycles, cracks in the matrix propagate perpendicularly to the fibers. When the crack front arrives at the fiber-matrix interface, the crack progresses by breaking the fiber or by debonding and going around the fiber. This kind of cracks is called fiber-bridged matrix cracking [27]. These damages accumulate in the component through the cycles, deteriorating its mechanical properties as the stiffness, until one of the cracks grows unstably causing the failure. Finally, if the maximum load applied during the cycles causes stress below the fatigue limit, the matrix undergoes cracks, but the driving force for the cracks is insufficient to make them propagate by breaking or debonding the fibers. In this case, the cracks remain confined between the fibers and the component will not have fatigue failure. Another possibility is that since the load is low, the fiber-bridging cracking progressing rate is very low and the failure will happen after an extremely high number of cycles [27]. The three different cases are schematically represented in Figure 39.

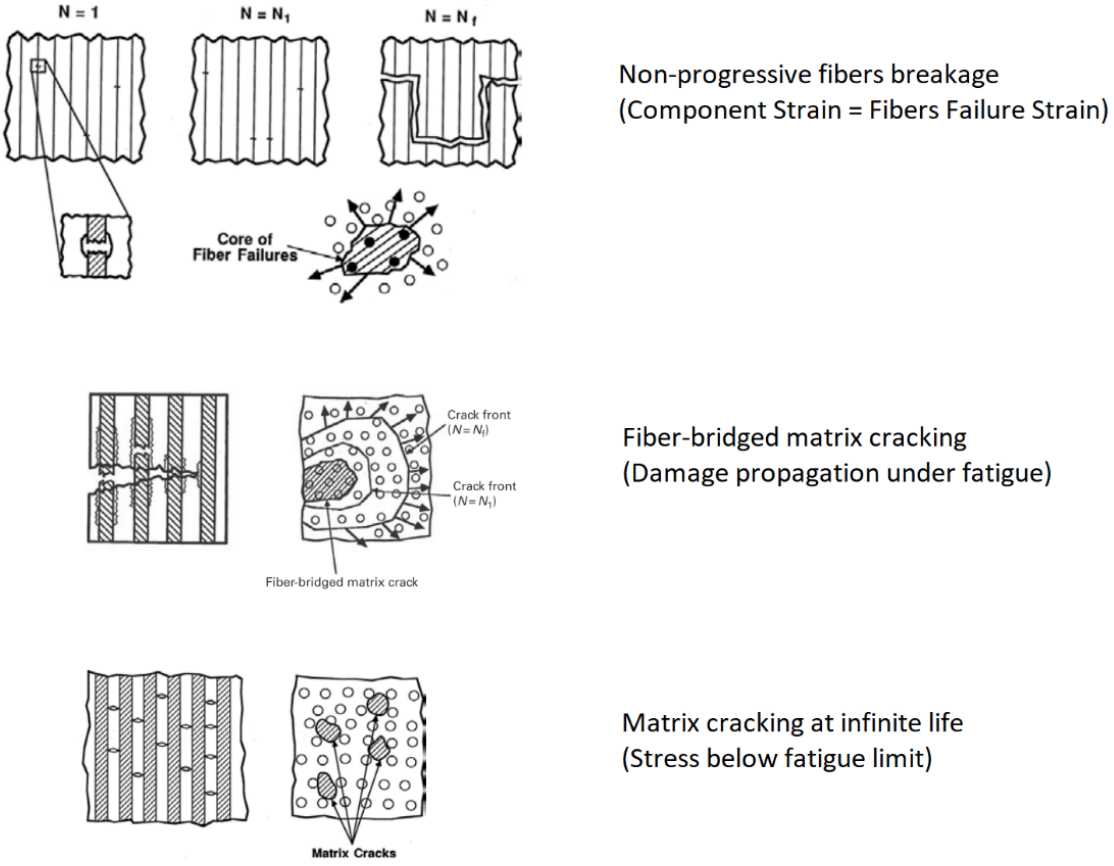

Figure 39. Fatigue behavior of a unidirectional composite subjected to longitudinal tension [27].

2.5.5.2. Unidirectional Composites Loaded Inclined to the Fibers

When a unidirectional composite is cyclically loaded in a direction inclined with respect to the fibers, cracks are initiated along the fibers, either at the matrix-fiber interface or in the matrix. At the beginning, the cracks can start from defects in the matrix material, such as voids, or at the fiber-matrix interface from debonding, and grow with cycles through the thickness and proceeding parallely to the fibers. At a certain point in the damage accumulation process, one of the cracks may reach unstable growth conditions and quickly propagate through the entire cross-section, breaking the composite in two pieces [27]. The failure mechanism is represented in Figure 40. It must be underlined that the maximum performance of unidirectional continuous fiber composites in terms of stiffness, strength and fatigue resistance are attained when the component is loaded longitudinally. In case of inclined loads, the role of the matrix becomes more important in the deformation and failure processes and the performance decrease [6].

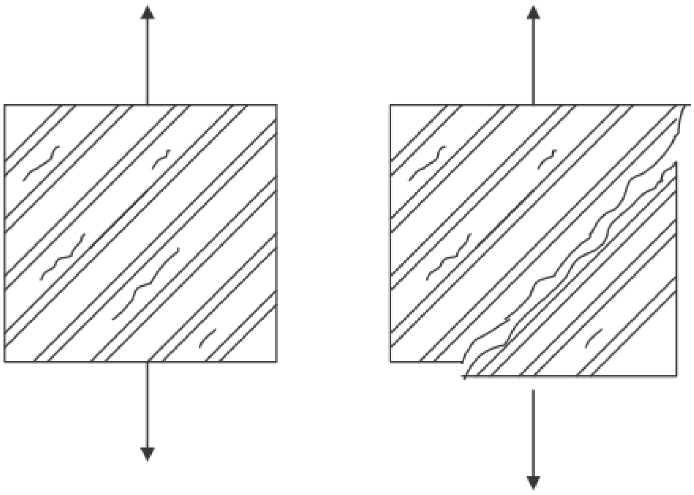

Figure 40. Schematic fracture in a unidirectional composite under inclined cyclic load. Fracture happens when one of the cracks present in the matrix grows unstably propagating in the entire cross-section [27].

2.5.5.3. Fatigue in Laminates

Being composed by plies stacked in different directions, laminates show a complex damage behavior when they are subjected to cyclic loadings. In FRP laminates subjected to cyclic loading, damages start in the plies that are loaded off-axis, similarly to what happens in unidirectional composites subjected to inclined load [27]. Ply cracks generate from voids in the matrix or fiber-matrix debonding, growing rapidly through the entire thickness of the ply and propagating parallel to the ply fibers direction as the number of cycles increases. As it is shown in Figure 41, the ply cracks usually grow until they span through the entire width of the lamina and, because of this, they are also referred as tunneling cracks [28]. However, differently from what happens in unidirectional composites loaded off-axis, when a ply crack propagates through the entire cross-section of the lamina, it does not cause the failure of the laminate. In fact, the presence of the other plies act as a constraint and allows the ply to continue to sustain the load, leading to the occurrence of multiple ply cracks in the same lamina [27]. Meanwhile, as the front of a ply crack encounters the interface between two adjacent plies, the intense stress state ahead of the crack front debonds the interface, causing small local interlaminar cracks. Increasing the number of cycles, ply cracks multiplies inside the laminae and this affects the mechanical properties. The most evident result is a degradation of the stiffness of the laminate. As the number of cracks inside the ply increases, the spacing between adjacent cracks diminishes. In this way, different interlaminar cracks can merge together, causing major delamination and leading to separation of the plies. This causes a redistribution of the stress inside the laminate, which can overload individual plies causing their failure. Finally, further development of damage involves extensive and localized fiber breakage that leads to the fracture of the specimen [27]. Thus, a laminate subjected to fatigue loading undergoes a process of damage accumulation during the cycles. Different damage mechanisms appear and they can be distinguished between critical and sub-critical damages. The sub-critical damages consist of all the events until fiber breakage, which is the ultimate damage mechanism. An example of the development of the damage of a laminate under fatigue loading can be observed in Figure 42. As it was said previously, during continued cycling, a multiplication of the number of cracks within the plies occurs and this causes a reduction of the overall stiffness of the laminate. For this reason, a measurement of the stiffness loss as a function of the number of cycles has shown to be a useful technique for assessing the level of fatigue damage in composite laminates [6].

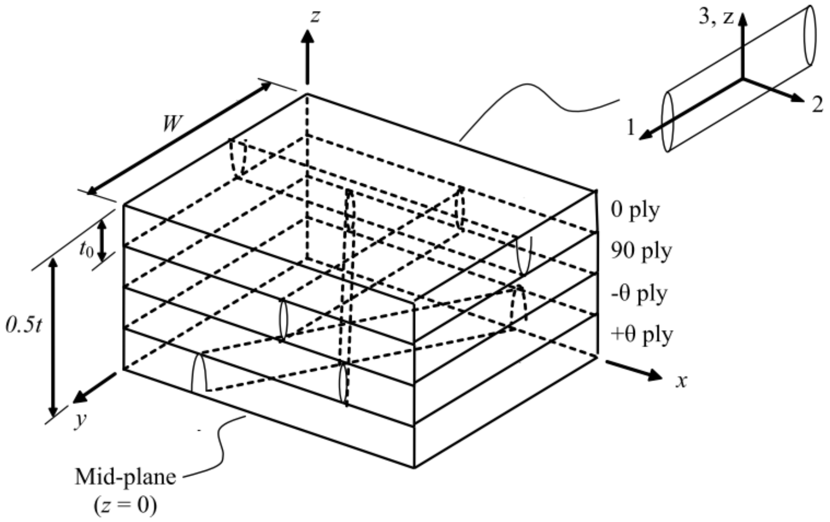

Figure 41. Schematic of multiple ply cracks inside a laminate [29]. The ply cracks grow through the entire cross-section of the ply propagating along the fibers direction.

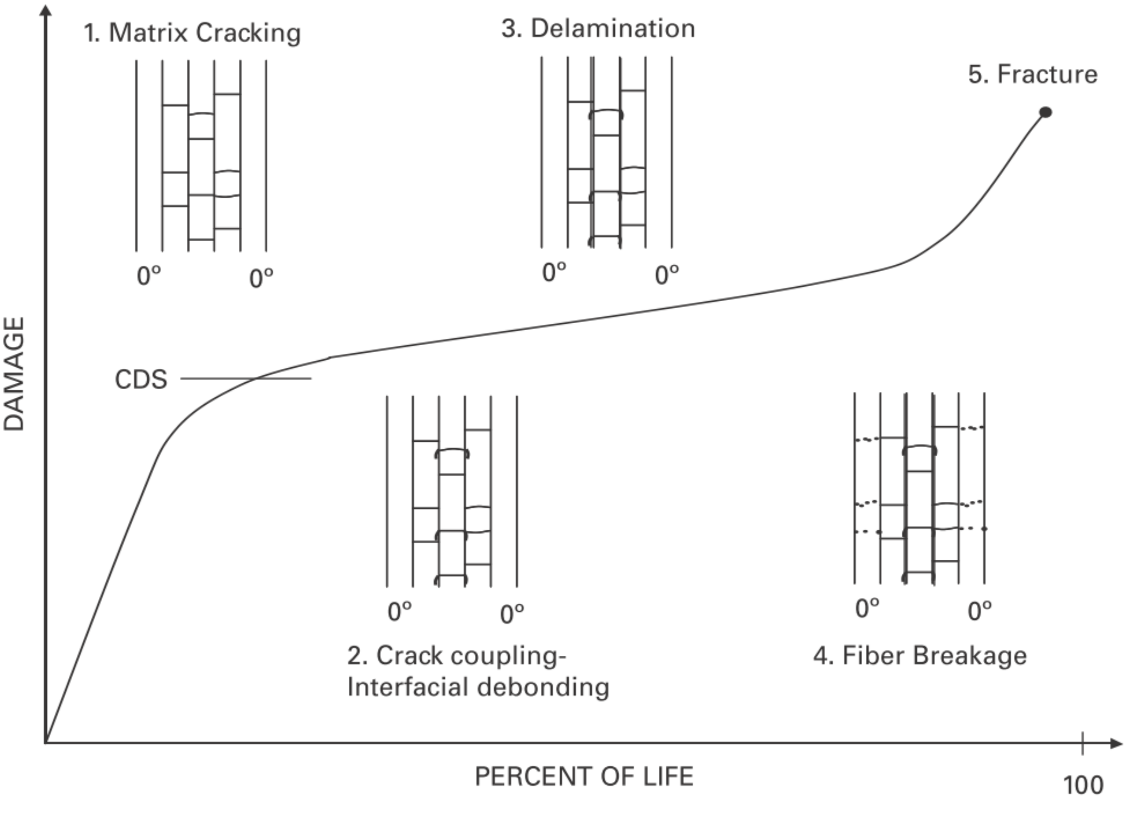

Figure 42. Development of damage in a composite laminate subjected to tension [27].

3. Literature Review

In this chapter, a brief overview of the publications consulted for developing the work described in this thesis is presented.

3.1. Thermoplastic GFRP Panels Manufacturing

VARTM Process

As already described in Chapter 2, Seemann [25] patented an improvement of the classic VARTM process, called SCRIMP, in which a resin distribution media is interposed between the vacuum bag and the fiber reinforcement preform. The infusion media has a permeability higher than that of the reinforcement and, in this way, it allows the resin to spread quickly on the top surface of the preform. Therefore, the resin has only to penetrate through the thickness of the fibers and not through the cross-section for the entire length of the preform. This allows to reduce the time required for the infusion and full wet out of the fibers, with benefits on the overall cycle time.

Menta [30] described the advantages of VARTM over autoclave processes, and then explained the application of it for the processing of composites CFRP epoxy panels with curing performed at high temperature. Similar setups for manufacturing panels with SCRIMP process were described by Torkamani et al. [31] and Nagabhushana et al. [32], that produced CFRP panels in order to investigate the damage behavior of laminated composites.

Naik et al. [23] explained the various parameters affecting the preform permeability in RTM and VARTM processes, basing the research on state of art literature review covering experimental studies. The discussion on how the porosity of the preform, which depends on the fiber volume fraction and compaction pressure, affects the permeability, and how the flow rate affects the presence of voids in the final components are useful suggestions in order to increase the final quality of the parts.

Polowick [24] developed numerical studies to simulate the mold filling in a VARTM process. Various process parameters were studied and, in particular, the effect of the vacuum bag on the preform permeability was investigated. It was described how the compaction pressure exerted by the vacuum bag on the preform causes a reduction of its permeability. The factors affecting the final quality of the part were studied experimentally and an optimization of the VARTM infusion process parameters was carried out, with the final purpose of producing high quality CFRP components for an UAV vehicle at low cost.

A modification of the VARTM process was studied by Yokozeki et al. [33]. In the research, a porous mold was used in a SCRIMP-like process in order to force the vacuum inside the bag. In this way, the outlet portion dimensions have a remarkable increase with respect to using pipes and valves. Panels of different size and thickness were produced with this method and the results showed that the components had very low void content (about 1.5 %).

Thermoplastic Composites Infusion Processes

Recently the possibility of manufacturing thermoplastic composites with the resin infusion processes employed for thermosetting has been taken into consideration thanks to the reactive thermoplastic processes. Two examples of the works developed in this field are the researches of Ben et al. [34] and Louisy et al. [35]. In these studies, composites laminates comprised of lamina with thermoplastic matrix and glass fiber or carbon fiber reinforcements were manufactured with a VARTM technique. However, both resins utilized, which were ε-caprolactam [34] and poly-L-lactide [35], were heated to temperatures higher than 100 °C before the infusion and the in-situ polymerization reaction was carried out with molds heated at temperatures around 200 °C.

For this reason, the real turning point was reached when Arkema introduced on the market a novel family of methyl methacrylate (MMA) thermoplastic resins called Elium®. The major advantage of this family of liquid resins with respect to the other thermoplastic resins for liquid infusion methods is that they can be infused and polymerized at room temperature [18, 36].

Kazemi et al. [37] produced VARTM laminates with Elium® 188 resin and polyethylene (UHMWPE) fibers, carbon fibers or hybrid of the two fibers as reinforcement. The laminates were tested to characterize the performance in tensile, compression and shear loadings. The results showed that the mechanical properties were comparable with the thermosetting-based panels adopting the same type of reinforcement, but the thermoplastic laminates had higher toughness. In a different work, Kazemi et al. [38] tested polyethylene fiber-reinforced with

Elium® 188 resin specimen at low velocity impact and compared the results with two different epoxies based composites specimen with the same reinforcement. The results of the impact tests on the three materials showed that the thermoplastic composites had a ductile behavior with elevated plasticity. Elium® based specimen were able to sustain higher impact loads than epoxies ones.

Barbosa et al. [39] studied the out of plane properties of CFRP laminates manufactured with VARTM using Elium® 150 resin. The objective of this work was to investigate the interlaminar fracture behavior of the novel resin and compare it with that of epoxy based CFRP. The results from the test showed how the thermoplastic composites had higher resistance to crack propagation and higher resistance to Mode II interlaminar fracture with respect to the epoxy counterpart.

Obande et al. [40] performed a benchmarking between an Elium® 188-based glass fiber-reinforced composite and an epoxy-based counterpart. The specimen were produced by VARTM and transverse tensile test, longitudinal and transverse flexural tests, short beam shear test and Mode I fracture toughness test were performed on them. The results showed how the thermoplastic-based specimen had higher transverse tensile strength and Mode I fracture toughness compared to the epoxy composites, with the flexural properties and short beam shear strength comparable between the two materials.

VARTM processing with Elium® resins was employed also by Khalili et al. [41], whom produced flame retarded natural fiber-reinforced panels, and for the production of sandwich fiber metal laminates by Kazemi et al. [42] and Mamalis et al. [43].

3.2. Multiaxial Fatigue Characterization of Laminates

Usually, composite materials employed in structural applications are subjected to complex multiaxial states of stress during service, which can be caused by loading in multiple directions or by the coupling phenomena characteristic of multidirectional laminates. Therefore, understanding the fatigue behavior of composite laminates when they are subjected to multiaxial stress states has crucial importance for designing structural components.

Quaresimin and Carraro [44] studied the fatigue behavior of GFRP tubular specimens under multiaxial cyclic loading. Tubular composite laminates with layup $[0_F/90_{U,3}/0_F]$ were subjected to combined cyclic tension/torsion loads and the initiation and propagation of matrix cracks in the 90° layers was investigated. The multiaxial state of stress in the 90° plies was composed by transverse tension and in-plane shear. Different biaxiality ratios, defined as the ratio between the shear stress and the transverse stress applied on the tube, were tested in order to investigate the effect of shear on the fatigue behavior. During the tests, multiple cracks occurred in the specimens and caused a progressive decrease in the axial and torsional stiffnesses. The results showed that the presence of shear stress has a strong detrimental effect. Increasing the biaxiality ratio, so increasing the tangential stress on the specimen, resulted in a reduction of the life spent for the initiation of the first transverse crack for a given value of transverse stress. After crack initiation, the crack was propagating along the circumference under mixed Mode I and Mode II. Higher values of biaxiality ratio resulted in higher Crack Growth Rate. A following study of the same research group [45] investigated the influence of the load ratio and biaxiality ratio on the biaxial fatigue behavior and damage evolution. $[0_F/90_{U,3}/0_F]$ GFRP tubular specimen were tested under combined cyclic tension/torsion loadings with different values of biaxiality ratio and fatigue load ratio ($R = \sigma_{min}/\sigma_{max}$). A strong influence of the load ratio R and the biaxiality ratio was found on both crack initiation and propagation. As in the previous study, higher shear stress led to lower fatigue life. Lower values of the load ratio R caused a decrease of the number of cycles needed for first crack initiation with the same amount of maximum transverse stress. In particular, a synergistic detrimental effect of the combination of transverse compressive and shear stresses in the case of alternate cyclic loads was highlighted for crack initiation and propagation.

Schmidt et al. [46, 47] developed studies aimed on investigating the effect of manufacturing defects on the biaxial fatigue performance of GFRP tubular specimens. In the first work [46], a comparison of the damage development and final failure process of glass fiber winding specimens was performed between defect-free tubes and tubes presenting fiber waviness. Fiber waviness is a manufacturing problem that can be caused by changes in thread tension of the roving during filament winding process or by fiber washing effect in resin infusion processes. The tubular specimens were subjected to cyclic combined axial and torsion loads, with load ratio $R = -1$. During the tests, an increase of crack density and related stiffness degradation caused by cyclic loading were observed equally for specimen with and without fiber waviness. However, specimens with fiber waviness presented early formation of delamination during the fatigue life. Local fiber waviness resulted in considerably lower fatigue strength of the composites. In the second study [47], the effect of evenly distributed voids and regions of large accumulated voids on damage evolution and fatigue life during biaxial cyclic loadings was investigated. Tubular GFRP specimens were produced with RTM, varying the process parameters in order to control the distribution and the quantity of voids inside the material. The tubes were tested under cyclic combined axial and torsion loads, with load ratio $R = -1$. During the tests, the presence of voids and their distribution seemed to not influence the increase in crack density and the stiffness degradation, which was observed equal in all the test specimens. However, the presence of porosities caused by voids had a detrimental effect on the damage propagation, with an early onset of delamination especially in the tubes with large accumulated voids. Both evenly distributed and accumulated voids resulted in lower multiaxial fatigue strength with respect to the defect-free composite.

Capela et al. [48] studied the fatigue behavior of CFRP tubular specimens under cyclic combined bending/torsion loadings. Thin tubes with [90/0] layup were tested adopting different torsional/bending stresses ratio λ. The results showed that increasing the torsional stress had a detrimental effect on the fatigue strength of the material, with the lifetime of the specimens that was strongly reduced. In particular, a change in the final failure modes was discovered during the tests. When subjected to pure bending the tubes were failing for compressive buckling, while for $\lambda = 0.25$ the effect of torsional stress caused a crack growing in planes inclined of about 45°. Finally, adopting $\lambda = 0.5$, torsional buckling failure was noticed.

McLeave [19] investigated the cracking behavior of E-glass/epoxy laminates subjected to cyclic multiaxial loading. Multiaxial laminates with generalized layups $[0_2/\theta_2/0_2/-\theta_2]_S$ and tubular laminates with layup $[0_F/90]_S$ were produced and tested under transverse compression and shear loads. The multidirectional laminates were loaded in cyclic compression only, and the multiaxial state of stress was obtained thanks to the shear coupling effect. The tubular laminates were loaded cyclically in combined compression and torsion. During the tests, three ratios of ply-level shear stress to transverse compressive stress (biaxiality ratio equal to 0.00, 0.21 and 0.40) were considered and crack initiation and propagation were studied. During the study it was discovered that compressive cracks can be visualized in-situ, even if the crack does not cause crack opening displacement. The experimental results showed that, as subcritical cracks appeared inside the specimens, the stiffness of the laminates under compression gradually decreased over the lifetime. The presence of shear was detrimental on the fatigue strength of the components, since increasing the shear stress caused a decrease in the lifetime of a ply. In the tubular specimens subjected to compression/torsion loads, failure was caused by a single dominant crack in the 90° plies. The crack was inclined of about 55° with respect to the plane perpendicular to the loading direction, and it was propagating along the circumference. This type of cracks is characteristics of the transverse compression failure mode. This particular damage mechanism is different from the one that can be observed in tensile failure, where many cracks appear in the off-axis plies and start propagating.

Regarding the characterization of the composite materials subjected to fatigue, there are some areas in the literature where the number of publications is limited. While numerous studies have been conducted in order to investigate the behavior of composites under cyclic tensile, shear or bending loadings and multiaxial tensile-shear loadings, few studies have characterized the transverse compressive fatigue performance. In particular, the area of studying the damage characteristics of composites under compressive fatigue has not yet been investigated rigorously.

Characterization of Damage in Composite Laminates during Fatigue

When composite laminates are subjected to cyclic loading, they undergo a process of damage accumulation that causes a degradation of the mechanical properties and leads to the final failure of the component. The damages occur in the form of ply cracks that appear in the matrix and start propagating along the fiber direction. Therefore, studying the damage mechanics of composites is necessary for understanding their complex fatigue behavior. The most important tool to this purpose is the finite element analysis, which allows to characterize numerically the phenomenon of cracking inside the material. Thanks to FEM in fact, it is possible to replicate the cracks observed in experimental tests and extract data through simulations or, by applying suitable damage models, predict the appearance of cracks and their propagation in the laminates.

One of the main parameters for characterizing the propagation of cracks in a material is the strain energy release rate (SERR), which is defined as the amount of energy dissipated at the crack tip during propagation divided by the new surface that is formed by the damage process. The method that is usually employed for computing the SERR at crack tip is the Virtual Crack Closure Technique (VCCT), that was developed by Rybicki and Kanninen [49] for two dimensional-cracks and was adapted on three-dimensional cracks by Shivakumar et al. [50]. The method is based on the assumption that the energy released when a crack extends of a small amount is equal to the work required to close the crack to its original length.

Xie and Biggers [51, 52] performed numerical studies on the problems of progressive two-dimensional crack growth and three-dimensional delamination growth. An interface element able to compute the SERR as the crack extends was developed, and the results were used in the numerical simulations to determine the direction of crack growth. The interface element used the VCCT method for computing Mode I and Mode II SERR.

In the study of Quaresimin and Carraro [44] on the fatigue behavior of tubular GFRP laminates subjected to multiaxial cyclic loading, the crack initiation and propagation in the 90° plies was numerically investigated. The crack observed in the experimental test was replicated in the model and the Mode I and Mode II SERR were computed with a manual VCCT-based method. The results of the SERR were correlated with the crack grow rate (CGR) and showed the detrimental effect of the presence of shear on the fatigue strength of the material. In fact, the higher was the Mode II contribution, the lower was the Mode I SERR necessary to reach a certain CGR.

Investigating the literature, it was found a substantial lack in the study and characterization of crack propagation under mixed Mode II and III, which has particular relevance to this study. Most of the publications in fact, analyze the propagation of cracks due to pure Mode I, pure Mode II or by mixed Mode I and Mode II contributions.

4. Thermoplastic GFRP Panel Manufacturing

In this chapter, the manufacturing of glass reinforced thermoplastic composites through a VARTM process is presented. The materials employed and the setup adopted are described, with a discussion on the problems encountered and the solutions applied for optimizing the process. Finally, the testing procedure for validating the process is explained and the results are presented and discussed.

As it was described previously, the objective of the manufacturing part of the project is to setup the VARTM process for thermoplastic resins that will be used in the future for producing components for the wind energy sector. The components produced during the setup were flat square panels from which the specimens utilized for the following testing procedures were obtained.

4.1. Materials

4.1.1. Elium® 188 XO acrylic resin

Elium® resins are an innovative family of liquid thermoplastic acrylic resins recently developed by Arkema Inc. (France). Elium® resins are specifically formulated for in-situ polymerization-based fabrication of FRP components using liquid composite molding processes that are typically reserved for fabrication of FRP components with thermosetting resins. The mechanical properties of polymerized Elium 188 XO are similar to that of cured epoxies [18] (see Table 3).

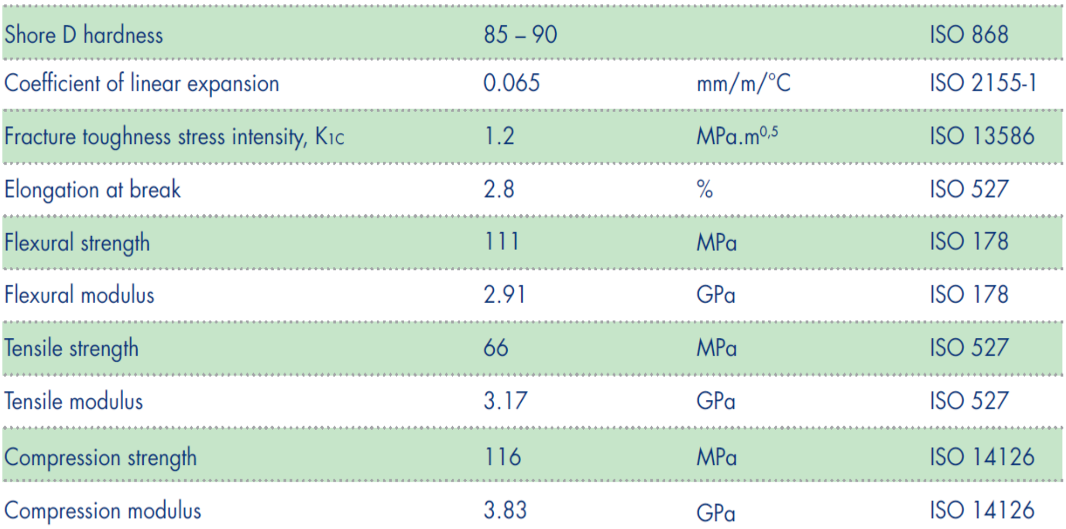

Shore D hardness	85 – 90		ISO 868
Coefficient of linear expansion	0.065	mm/m/°C	ISO 2155-1
Fracture toughness stress intensity, K_{IC}	1.2	$MPa.m^{0,5}$	ISO 13586
Elongation at break	2.8	%	ISO 527
Flexural strength	111	MPa	ISO 178
Flexural modulus	2.91	GPa	ISO 178
Tensile strength	66	MPa	ISO 527
Tensile modulus	3.17	GPa	ISO 527
Compression strength	116	MPa	ISO 14126
Compression modulus	3.83	GPa	ISO 14126

Table 3. Mechanical properties of non-reinforced cured Elium 188 XO resin [36].

From the manufacturing point of view, Elium® 188 XO resin monomer has a very low viscosity, equal to 0.1 Pa·s [36]. This value is within the range of viscosity of thermosetting resins, that is usually between 0.05 and 0.5 Pa·s, and makes this resin suitable for resin infusion technologies. The resin has a liquid density of 1.01 g/cm^3, while after polymerization the density increases to 1.19 g/cm^3 [53]. The processing temperature range of the resin is between 20 and 60 °C. Initially, the thermoplastic resin is in its monomeric form, which is methyl methacrylate (MMA), and before processing is mixed with a dibenzoyl peroxide initiator. In this way, it undergoes addition polymerization and becomes poly-methyl methacrylate (PMMA), also known as acrylic (see Figure 43). In this study, the dibenzoyl peroxide used was Luperox® AFR40 (Arkema Inc., France), which was mixed with the resin in a quantity equal to 2-3 % of the resin mass.

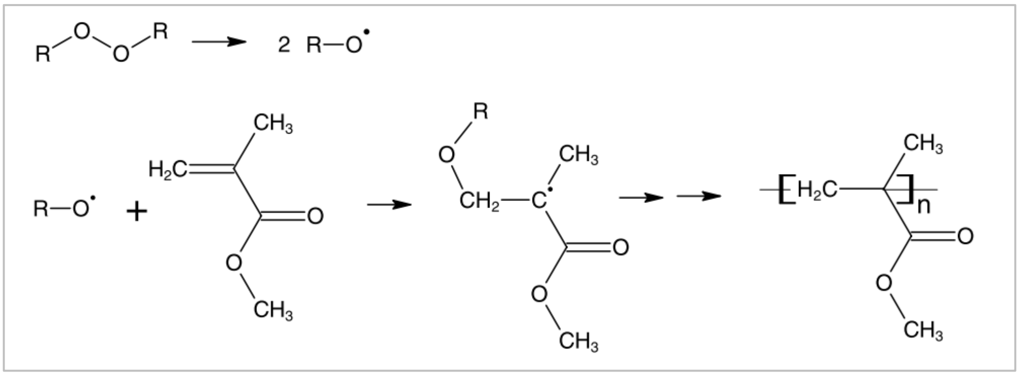

Figure 43. Addition polymerization of poly methyl methacrylate from methyl methacrylate monomer [54].

Polymerization of PMMA resin is an exothermic process, therefore care must be taken during the production of the components [54]. When the parts are thin, as in the case of the panels produced in this project, the heat can be dissipated easily but, for the production of thick parts, the process parameters must be controlled carefully and the heat generated must be dispersed in a proper way. If the temperature increases too much, there is the risk that the resin starts boiling inside the mold and this causes severe problems in the final quality of the component, which will be affected by a high amount of voids. Elium® 188 XO has been specifically designed to achieve low exothermic temperature during the polymerization, and this makes this resin more suitable for infusion of thick parts with respect to the other Elium® resins.

4.1.2. Glass Fiber Reinforcement

The reinforcement used in this study for producing flat laminated composite panels was an E-glass unidirectional non-crimp fabric supplied by V2 Composites (Auburn, AL, US). The E-glass fiber rovings coated with sizing compatible with the Elium 188 XO resin were provided by Johns Manville (Littleton, CO, US), and were comprised of filaments with a density of 2.55 g/cm^3 and a tensile strength of approximately 3450 MPa [10]. A light polyester stitching in a tricot pattern was used to bond the aligned fiber rovings and a polymeric veil was used on the upper surface to aid with resin infusion during GFRP panel processing. The non-crimp fabric is shown in Figure 44 and Figure 45.

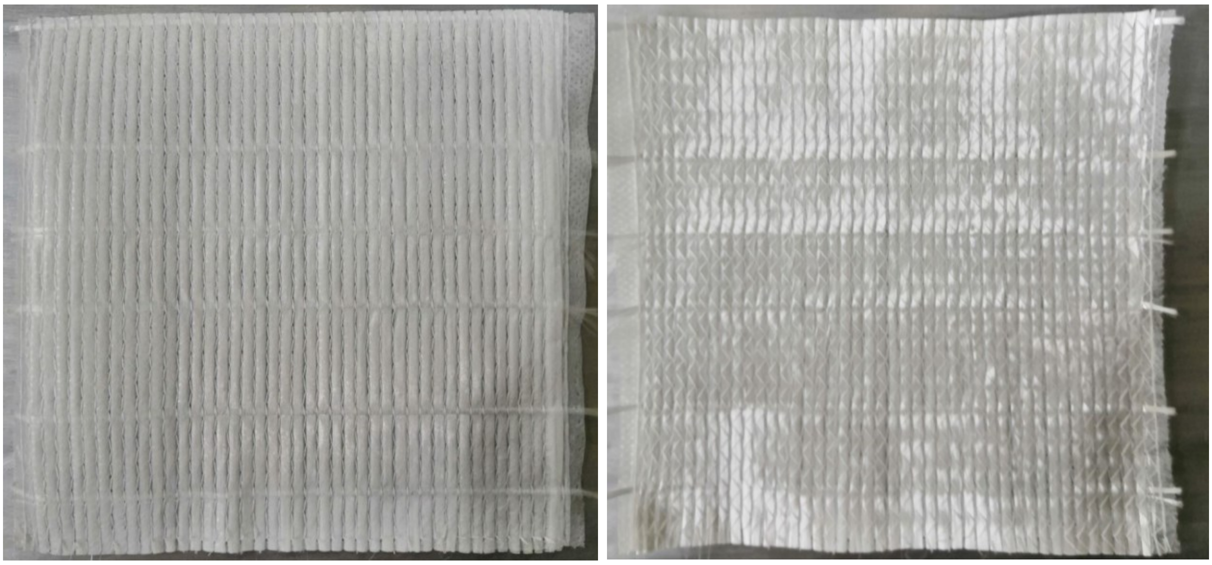

Figure 44. Images of the E-glass non-crimp fabric utilized for the panels: top surface or veil side (left) and bottom surface or stitching side (right)

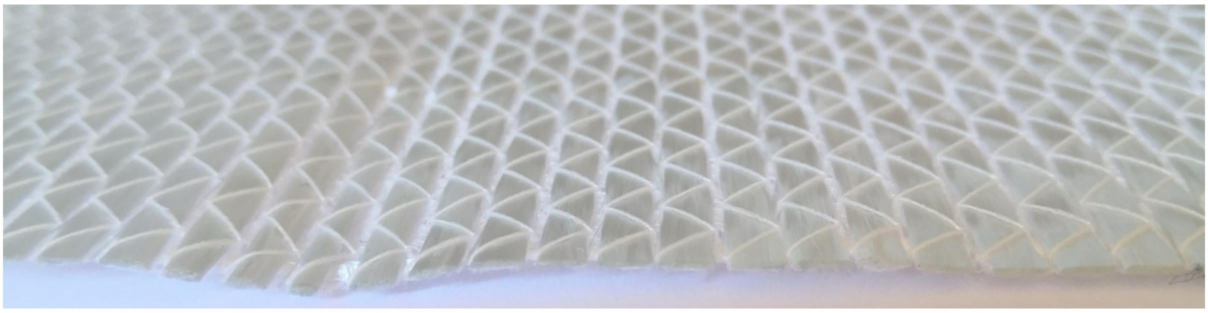

Figure 45. Magnified image of the E-glass fiber rovings and stitching on the bottom surface of the fabric.

The dimensions characterizing the fabric layers are the following:

- Supplied fabric width = 15 cm
- Average thickness = 0.600 mm
- Average roving width = 2.85 mm
- Average fiber diameter = 16 µm
- Stitching pitch distance = 7.50 mm
- Roving linear density value (TEX number) = 1100 g/km

4.1.3. VARTM Process Equipment

The equipment and tools that were utilized for setting up the VARTM process are listed and described in the following.

1. **Rigid mold lower side.** Since the components produced were flat panels, a flat aluminum plate (6.4 mm thick) was utilized as mold lower side.

2. **Peel ply.** The peel ply adopted in this project is the Airtech Econostitch®, which is a polyester tightly woven fabric that is laid on the reinforcement and allows an easy release of the final part. This layer can be crossed by the resin but, thanks to its design, it can be easily detached from the final component surface by peeling. The peel ply leaves a texture on the component surface.

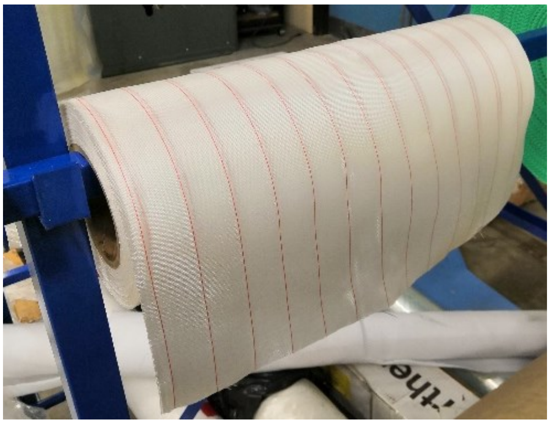

Figure 46. Airtech Econostich® peel ply.

3. **Resin distribution mesh.** As it was already described previously, use of the infusion media differentiates the SCRIMP process from a traditional VARTM process. The infusion media allows spreading of the resin on the upper surface of the component in order to facilitate the impregnation of the fibers reinforcement. In this project the Airtech Greenflow 75 distribution mesh was employed, which is a high permeability polypropylene net.

Figure 47. Airtech Greenflow 75 resin distribution mesh.

4. **Vacuum bag.** It is a plastic sheet that forms the flexible side of the mold. Thanks to the vacuum inside the mold, the plastic bag is compressed on the layers below by the atmospheric pressure.

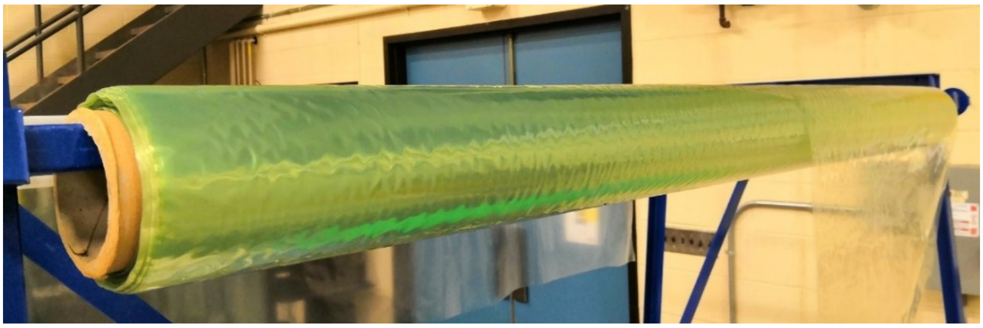

Figure 48. Vacuum bag.

5. **Sealant tape.** It is a roll of special tacky synthetic rubber that is used to ensure sealing between the rigid mold and the vacuum bag. The sealant tape used for the project is the Airtech AT-200Y.

6. **Transparent plastic hoses.** The hoses were used at the inlet of the mold as infusion system and at the outlet for applying the vacuum. Transparent hoses allowed for observation of the resin flow during the process.

7. **Clamps.** Used for closing/sealing the plastic hoses at the mold inlet and outlet.

8. **Funnel.** It was connected to the inlet hose and used as resin reservoir before the infusion.

9. **Catch pot.** It is a metallic container designed specifically for resin infusion processes. The internal circumference of the lid is covered by rubber for ensuring a proper sealing and, on the top of the lid, there are threaded connections for the hose fittings. The function of the catch pot is to prevent excess resin that may escape from the infusion from reaching the vacuum pump.

10. **Vacuum pump.** A pump was used for forcing vacuum inside the mold. A pressure gauge was mounted downstream of the pump, after the on/off ball valve, and allowed to measure the pressure in the catch pot.

11. **Mold cleaner.** In order to clean the mold during the preparation for the infusion, the solvent-based Loctite Frekote® PMC cleaner was employed.

12. **Release agent.** The solvent-based Loctite Frekote® 44-NC release agent was applied on the surface of the mold before of laying down the reinforcement plies on it. The function of the release agent is to facilitate the detachment of the final part from the mold surface, reducing the risk of damaging the component during its release.

4.2. VARTM Setup

In this section the description of the procedure employed for manufacturing the composite material panels is reported, from the preparation of the mold to the release of the final component.

The first operation consisted in carefully cleaning the rigid surface of the mold. This was performed by wiping a solvent-based cleaner on the aluminum sheet, in order to ensure that all the possible residuals from previous infusions, such as cured resin and release agent, were removed. At this point, it was possible to apply the release agent on the mold surface. The release agent must be wiped uniformly on the region where the fibers were applied. Four layers were applied, one perpendicular to the other, and 15 minutes were waited between the coats in order to make the release agent dry on the mold as it was suggested by the producer. After the last coat, it was necessary to wait 30 minutes for allowing the final curing of the release agent. Subsequently, 4 fiber reinforcement layers were stacked on the mold. The fabric was cut from the roll and 15x15 cm squared plies were obtained. All fabric layers were positioned on the mold with the same unidirectional orientation. To obtain symmetric [0_4] panels, the two lower layers had the veil downwards while the two upper layers had the veil upwards.

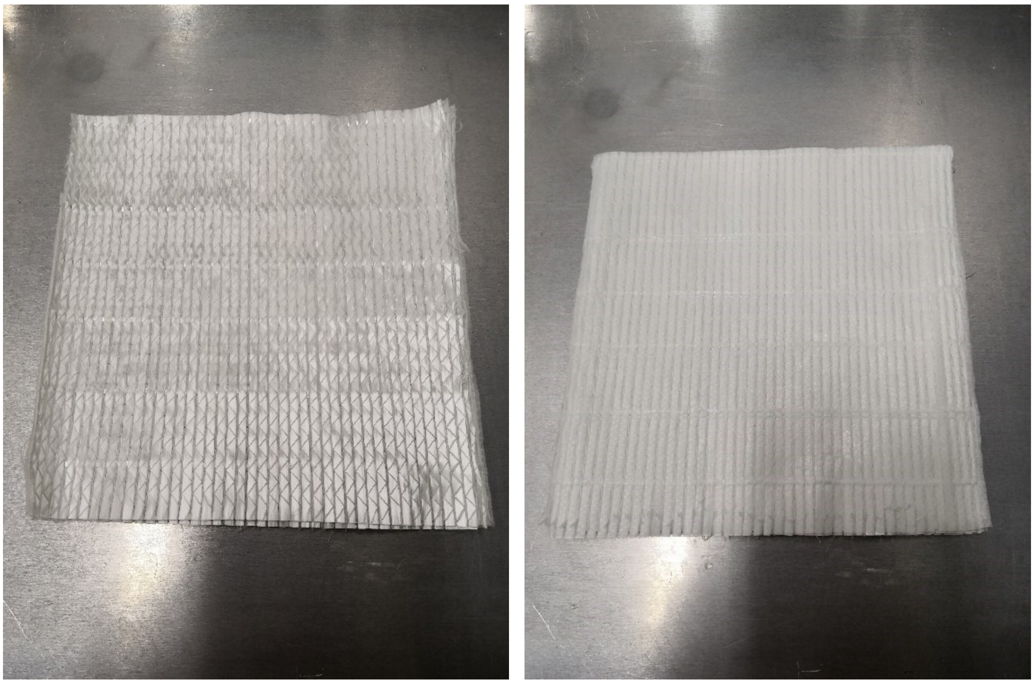

Figure 49. Disposition of the four fiber reinforcement plies on the mold. The two bottom layers (left image) had the veil facing the mold while the two upper layers (right image), stacked on the two bottom layers, had the veil facing upward.

The peel ply was laid on the reinforcement, covering it completely, so that the infusion mesh and the vacuum bag were not in contact with the reinforcement and an easy detachment of the panel was ensured. The peel ply was fixed on the mold with masking tape in order to keep it tight on the fiber plies and maintain them in the correct position.

Figure 50. Peel ply covering the reinforcement layers.

The infusion mesh was positioned on the top of the peel ply. The function of the infusion mesh, as it was explained previously, is to quickly spread the resin on the upper surface of the preform and, for this reason, it was cut slightly larger than the fibers ply in order to transport the resin uniformly on the entire surface. However, as it is possible to observe in Figure 51, the infusion mesh was not covering completely the reinforcement but it was interrupted, leaving uncovered 0.5-1 cm of fibers, and applied again in contact with the outlet side. This was done in order to stop the quick spreading of resin near the end of the preform and allows it to penetrate through the thickness before of being captured by the suction hose. If the infusion mesh were running continuously from the inlet hose to the outlet hose, since its permeability is much higher than that of the fabric, the resin would run mostly inside it and it would start flowing out from the mold before of penetrating completely through the preform. This issue could cause bad fibers wetting and high waste of material. The infusion mesh was folded on itself at the inlet and outlet sides in order to create a channel in which the hoses were inserted, and it was kept in the correct position by masking tape.

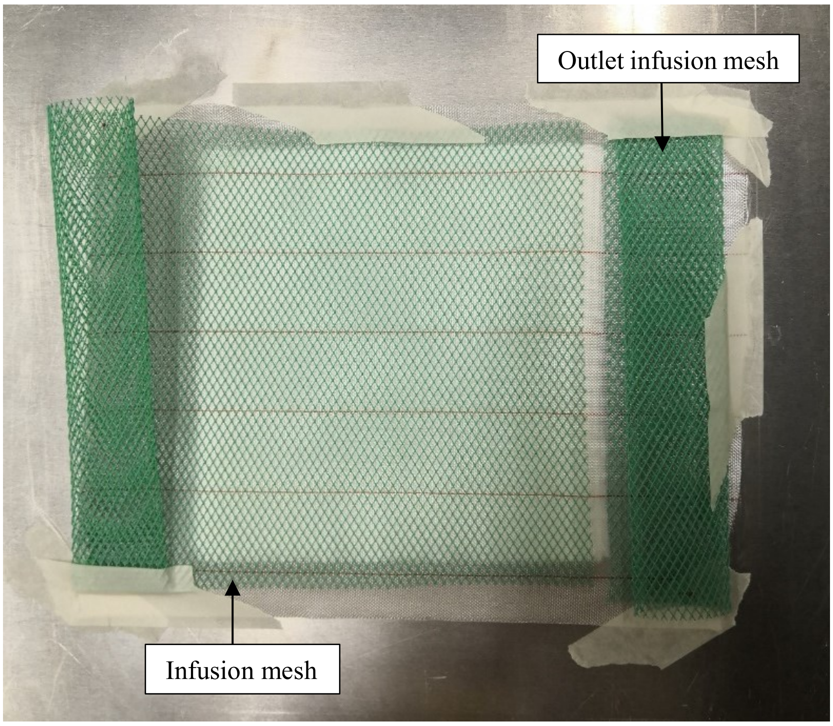

Figure 51. Infusion mesh applied on the top of the peel ply. Note the uncovered portion of reinforcement near the outlet side (on the right) to interrupt the quick spreading of the resin toward the suction hose.

The sealant tape was applied on the mold, along the contour of the layers laid previously, and the hoses were placed inside the channels of the infusion mesh. With the hoses completely surrounded by infusion mesh, as soon as the resin started flowing out from the tube, it was captured by the distribution media and quickly spread on the surface of the reinforcement. Some sealant tape was attached around the hoses in order to obtain a proper sealing with the vacuum bag. The position of the inlet and outlet hoses with respect to the preform influences the flow of the resin inside it, and it must be chosen carefully. In the next chapter, a discussion on the different configurations considered for the pipes position will be presented. After different trials, the final setup chosen is the one shown in Figure 52, where the inlet and outlet hoses are placed near the middle of the reinforcement plies.

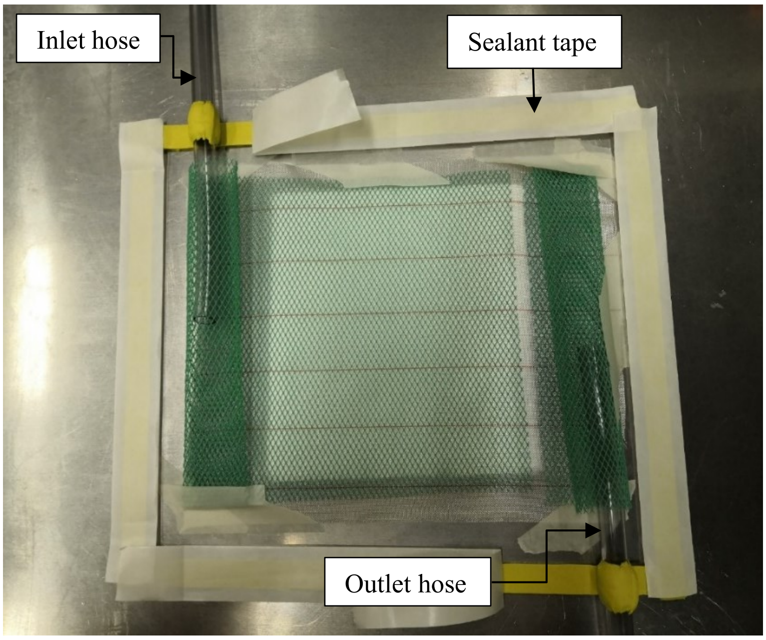

Figure 52. In the picture is shown how the sealant tape and the inlet and outlet hoses were positioned.

The mold was ready for sealing with a sheet of vacuum bag, which was cut from a roll and applied on the sealant tape. The bagging operation is the most important operation during the preparation of the mold, since from it depends the capacity of maintaining the vacuum for the entire process. The application of the vacuum bag must be done carefully, paying particular attention to follow the contour of the hoses and stretching the plastic sheet before of laying it on the sealant tape, in order to avoid folds that can cause leakages. At the end of the operation, the vacuum bag was pressed on the tape to close all the gaps and ensure the sealing of the mold.

Figure 53. The vacuum bag is laid on the sealant tape to close the mold.

When the mold was finally closed, it was possible to apply a vacuum using a suitable vacuum pump. As it can be observed in Figure 54, the vacuum pump was connected to the catch pot, then the outlet hose was connecting the catch pot to the mold. As it was explained previously, the function of the catch pot is collecting the resin in excess and avoiding that this can reach the pump, causing damages to it.

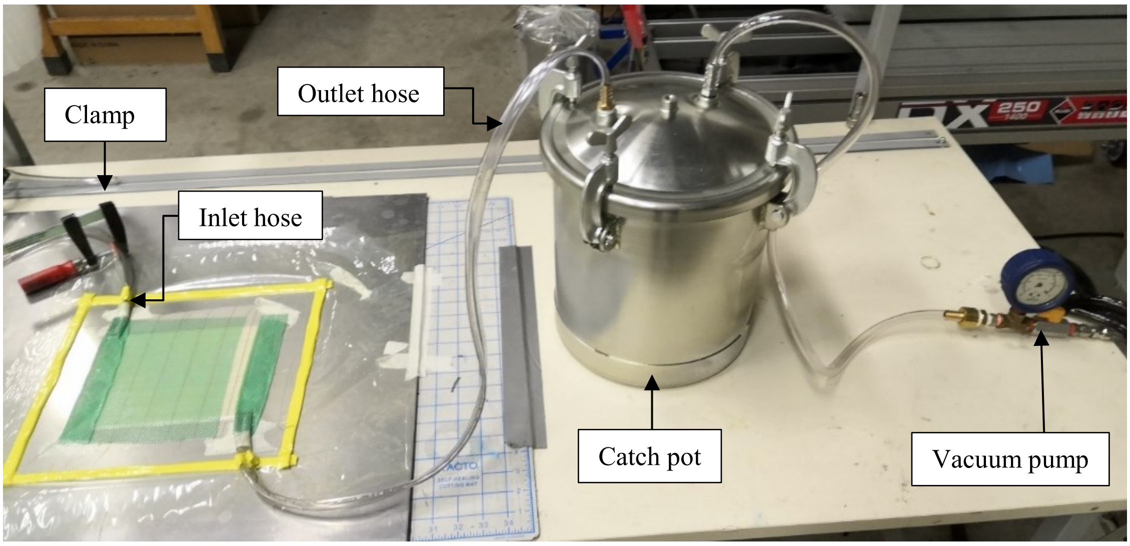

Figure 54. Series of hoses connecting the mold, the catch pot and the vacuum pump.

For applying vacuum, the inlet hose was closed with a clamp and the vacuum pump was started. As soon as the air was removed from the mold, the vacuum bag was compressed on the layers below, adhering tightly to the preform, as it is shown in Figure 55. The constant pressure inside the mold during all the infusions was approximately 95 kPa below the atmospheric pressure. When the minimum pressure inside the mold-catch pot system was achieved, the pump became idle and the on/off ball valve downstream from the pressure gauge was closed. At this point, the mold and the catch pot were isolated from the vacuum pump. Since the vacuum is the most important parameter in the VARTM process, the capability of maintaining it for the entire duration of process must be verified. This was done by monitoring the pressure inside the mold-catch pot system, which did not change for at least 20 minutes. If during this time a variation of the vacuum pressure from the gauge was noticed, the vacuum bag was pressed strongly on the sealant tape to close any leakages. Instead, when the pressure was maintained for the entire control time, the mold was finally ready for the infusion of the resin.

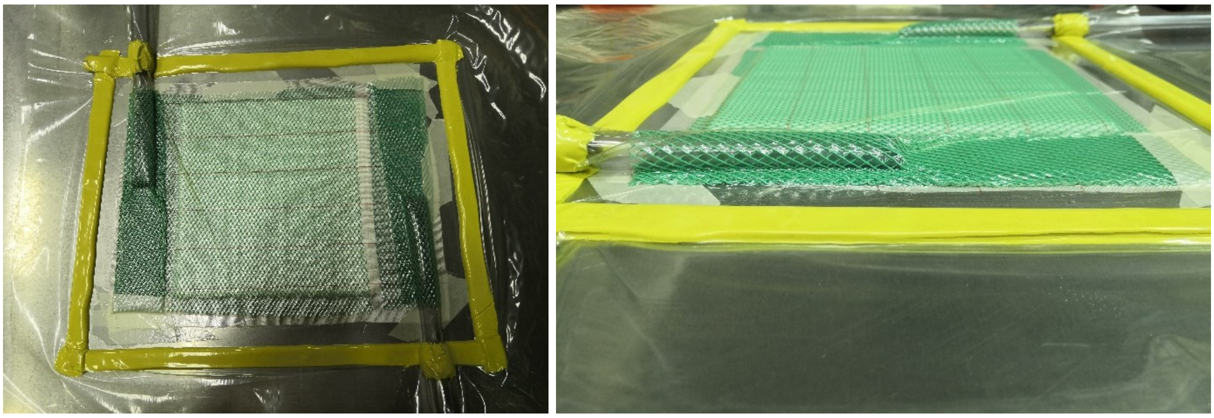

Figure 55. When vacuum is applied inside the mold, the vacuum bag is pressed on the layer below by the atmospheric pressure.

For preparing the infusion, the Elium® resin was extracted from the drum using a bulb dispenser, poured inside a mixing container and weighted on the weight scale. The Luperox® AFR40 peroxide was added to the mixing container in a quantity equal to 2-3% of the resin mass. It was very important to respect the ratio indicated by the supplier, otherwise it was not possible to obtain a correct and complete polymerization. Afterwards, the resin and the peroxide were mixed using a stirring stick for obtaining a uniform mixture. During all these operations it was necessary to wear a respirator and safety glasses, since the Elium® resin emits vapors that can cause serious respiratory problems and eyes irritations.

Figure 56. Luperox® AFR40 peroxide is added to the Elium® resin and mixed in order to obtain a uniform mixture.

Once the peroxide was mixed with the resin, the polymerization reaction was activated and the mixture had to be infused inside the mold before that the viscosity started increasing. The mixture was poured inside a reservoir (i.e. a funnel) that was connected to the inlet hose, which was closed by the clamp. The mixture sat for approximately two minutes in order to allow the small air bubbles that formed during mixing of the resin to reach the surface of the mixture, thus reducing the possibility of void formation during processing.

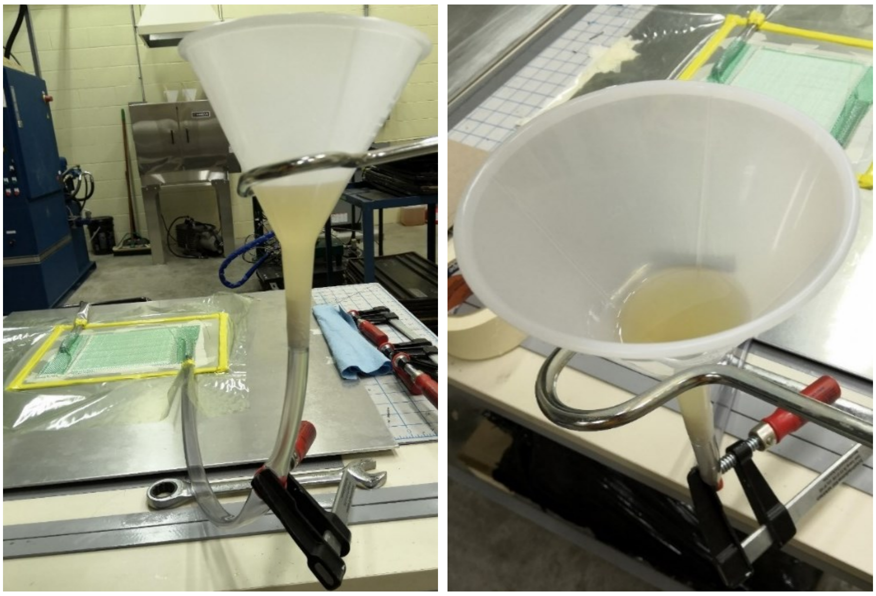

Figure 57. Funnel used as resin reservoir during the infusions.

When no air bubbles were visible in the resin inside the inlet hose, it was possible to proceed with the infusion. The inlet clamp was opened and the resin started flowing toward the mold. The clamp at the inlet was opened partially and used as a nozzle, limiting the speed of the resin flow toward the mold. The inlet clamp also enabled closure of the inlet tube at the appropriate moment, thus preventing the air above the resin in the tube from entering the mold. The infusion mesh directed the resin flow in the mold, which quickly spread on the upper surface of the fiber layers before permeated through the fabric thickness. The diffusion of the resin inside the infusion mesh can be observed in Figure 58. During the entire infusion operation, the pump was switched on again, since it was necessary to have a suction force that allowed the resin to diffuse toward the outlet once the inlet hose was closed and the atmospheric pressure was not pushing anymore the resin inside the mold. When the resin was reaching the part of preform left uncovered from the infusion mesh, the flow speed decreased. The resin started to penetrate through the thickness of the plies and it was possible to observe the phenomenon because the preform was becoming darker. Once the resin had penetrated through all the thickness of the preform covered by the infusion mesh, it started flowing toward the outlet, wetting the remaining 0.5-1 cm of fiber plies left uncovered. When the resin reached the infusion mesh positioned at the outlet, the outlet tube was closed with a clamp and the pump switched off. At that point, the mold was isolated and the stationary resin was allowed to polymerize in situ. The total time of the process, from the start of the infusion process to the moment when the preform was completely wet, was about 300-360 seconds. The diffusion of resin through the last part of preform can be observed in Figure 59.

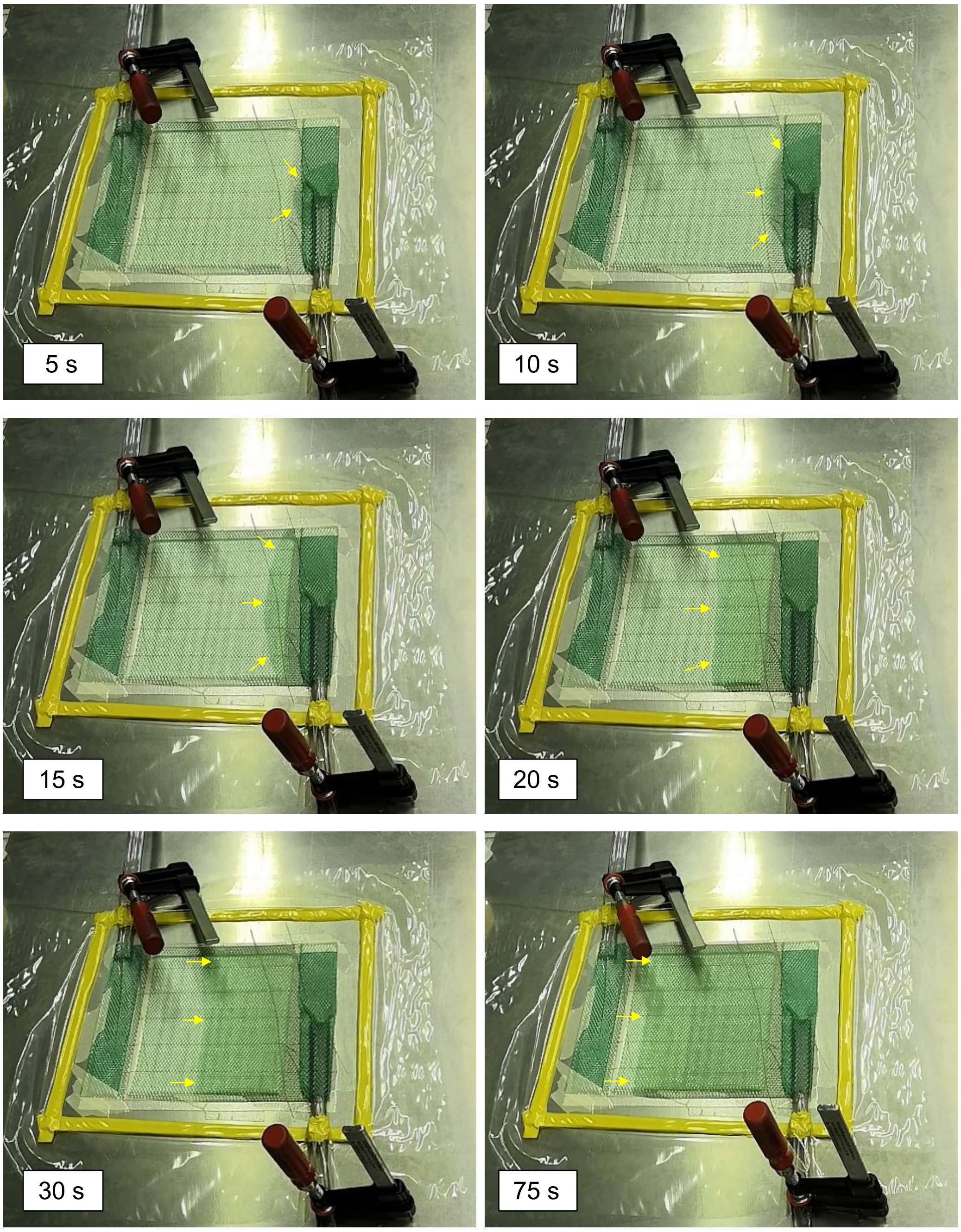

Figure 58. Diffusion of the resin inside the infusion mesh. The seconds passed since the start of the infusion process are reported in each frame. The yellow arrows indicate the position of the flow front in the infusion mesh.

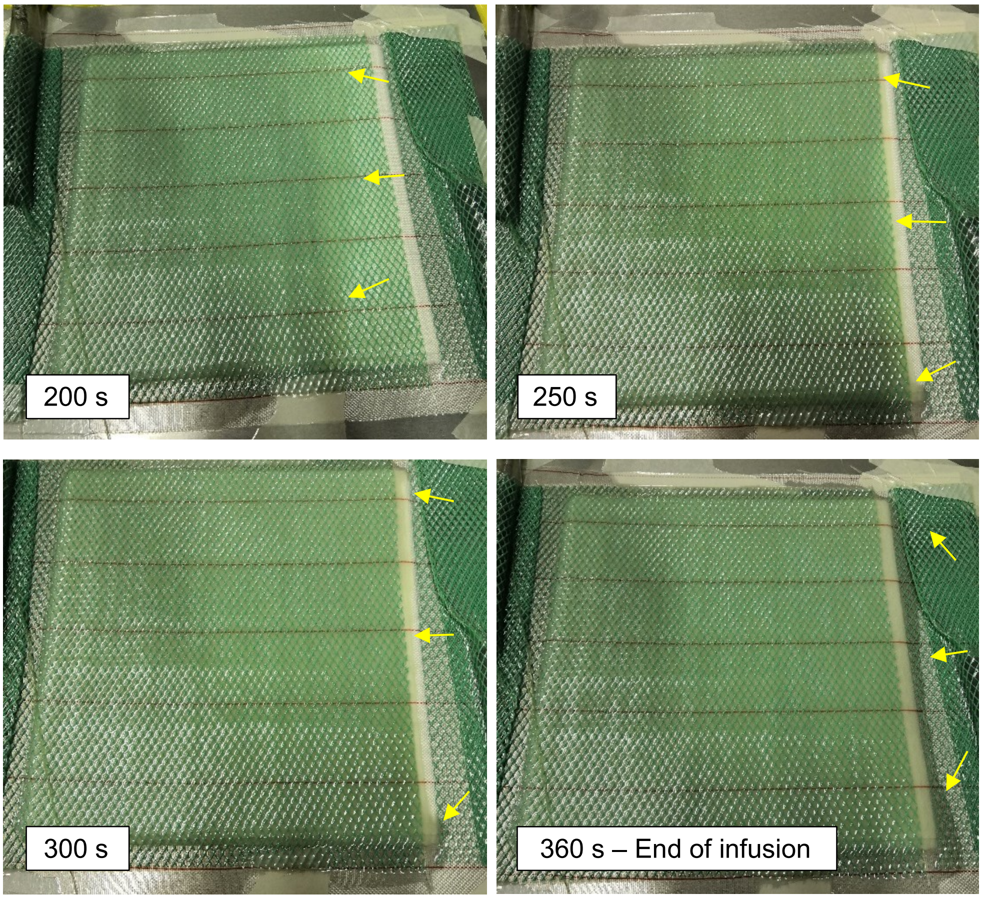

Figure 59. Diffusion of the resin through the thickness of the plies and in the last portion of preform, left uncovered from the infusion mesh. The seconds passed since the start of the infusion process are reported in each frame. The yellow arrows indicate the flow front of the resin inside the preform.

The producer of the resin suggested a processing time of 60 minutes, but in the current work the time needed for obtaining rigid panels that could be extracted from the mold without being damaged was 90-120 minutes. During the entire polymerization process it was fundamental that the vacuum remained constant inside the mold. When leakages were detected, even if very small, the polymerization did not complete and the panel remained soft. After completion of polymerization, the panels were demolded and the peel ply was removed. Finally, the contour of the panels was trimmed.

4.3. Results and Process Improvements

During the production of the first panels, multiple quality issues were encountered. Some possible solutions were applied and the results obtained are discussed in the following paragraphs.

For the first infusion, the quantity of monomeric resin extracted from the storage drum was computed considering the volume of a panel and the target fiber volume fraction of 50%. The dimensions of the 0.600 mm thick fabric layers cut from the roll were 18x18 cm, and along with the density of the liquid resin of 1.01 g/cm^3, it was possible to compute the mass of the resin that had to be infused in the mold. The volume of the panel was equal to:

$$V_{panel} = l \cdot l \cdot t_{hyp} = 18 \cdot 18 \cdot 0.2 = 64.8\, cm^3$$

Where t_{hyp} is the hypothetical thickness of the panel, that was assumed equal to 2 mm by considering four plies 0.6 mm thick laid one on top of the other and compacted by the vacuum bag. Assuming no voids inside the panel, the volume of resin should be:

$$V_{resin} = V_{panel} \cdot (1 - v_f) = 64.8 \cdot 0.5 = 32.4\, cm^3$$

Knowing the resin liquid density ρ_{r_l} , the mass of resin inside the panel should be:

$$m_r = V_{resin} \cdot \rho_{r_l} = 32.4 \cdot 1.01 = 32.7\, g$$

In order to take into account possible waste of resin inside the infusion system and in the mixing container, in total 55 g of resin were extracted from the drum for the first infusion. However, as it is possible to observe in Figure 60, the resin was not able to wet completely the preform and a short shot was obtained.

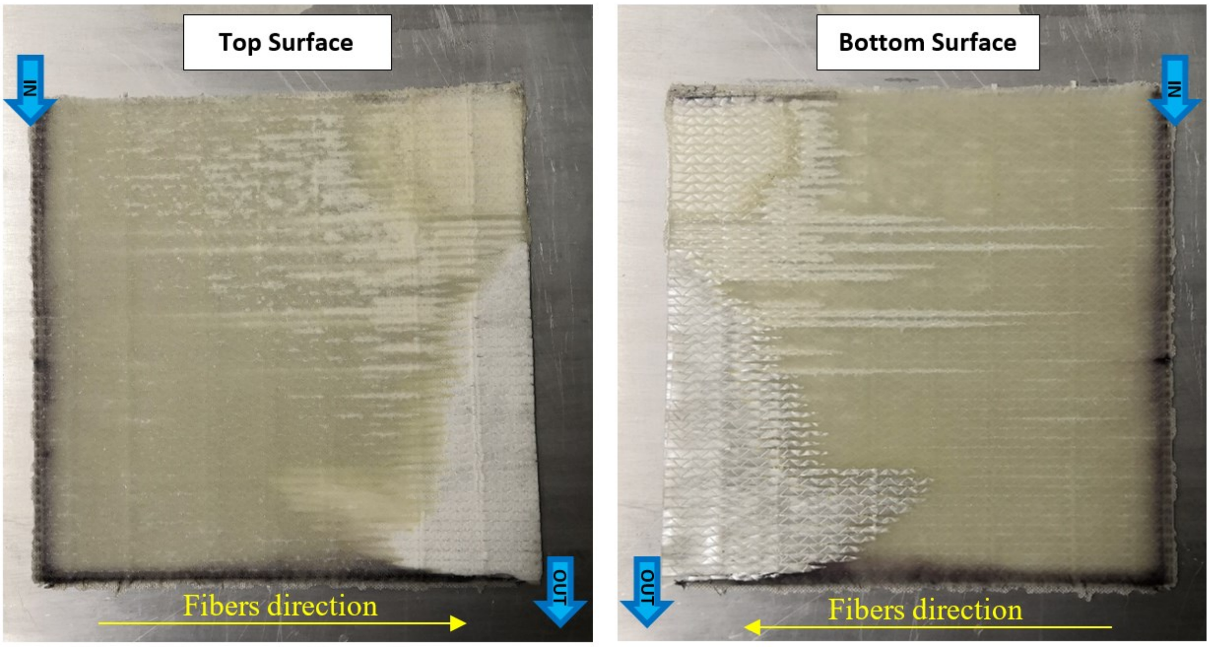

Figure 60. In the first panel produced the resin was not able to wet completely the plies. In the picture, the position and direction of the inlet and outlet hoses are indicated with blue arrows on the top and on the bottom surfaces.

During the first infusions, the inlet and outlet hoses were positioned at the corners of the preform, as it is indicated in Figure 60, and the fibers were positioned parallel to the theoretical resin flow, that should go horizontally from the inlet side to the outlet side.

With the goal of obtaining full fiber wetting, 85 g of resin were used for the second attempt. This time, the resin was able to completely wet the preform, but a high quantity of resin remained inside the inlet and outlet hoses, and also inside the resin reservoir. This caused an unnecessary excessive waste of material. Regarding the quality of the panel produced, undesired grooves running along the locations of the stitching between the fiber rovings were observed on the lower surface of the panel (see Figure 61). This phenomenon was surprising since on the rigid mold side a good surface finish was expected. It is possible that the high speed of resin diffusion in the mold caused poor fiber wetting, as it was explained in Section 2.3.6.1.

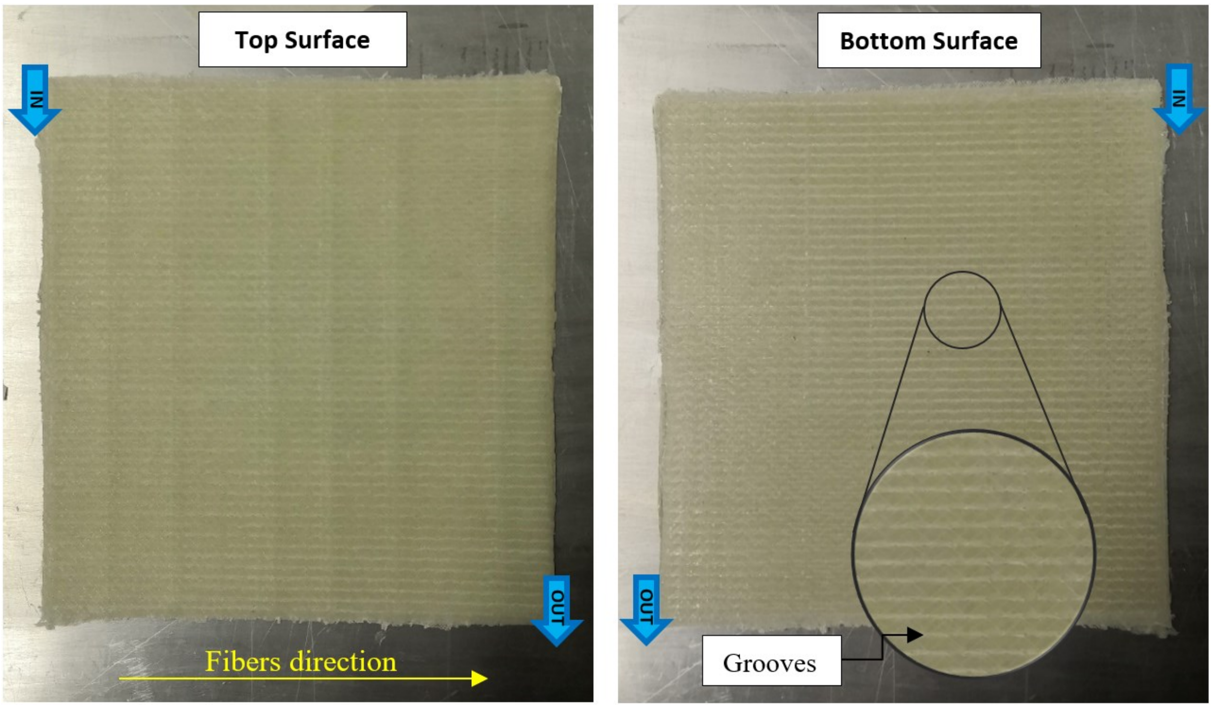

Figure 61. The top and bottom surfaces of the second panel. On the bottom surface it is possible to observe many white horizontal lines, that are the grooves running between the fiber rovings.

A different problem occurred in the fabrication of the third panel. When the panel was released from the mold after polymerization was complete, some non-wetted regions were observed on the upper surface. The dry regions, shown in Figure 62, were all inclined and parallel between each other. The dry regions were running from the top left corner, where the inlet hose was positioned, to the bottom right one, where the outlet hose was placed. This problem was likely caused by the asymmetry in the disposition of the hoses with respect to the plies, and by the speed of infusion of the resin that, as in the previous infusion, was too high.

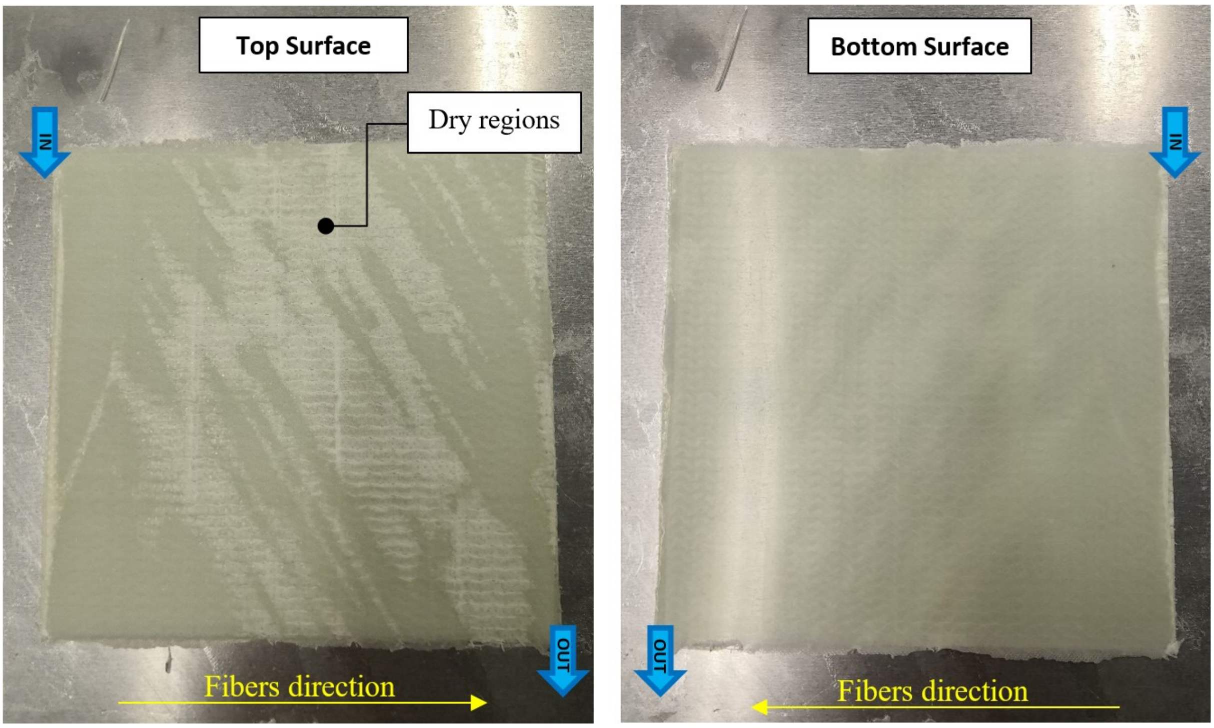

Figure 62. Inclined non-wetted regions on the upper surface of the third panel produced.

The low quality of the first panel produced, together with some difficulties encountered during resin infusion, revealed the need to improve the process. A summary of the problems encountered are as follows:

- Air entering the mold during resin infusion: In fact, during the first infusions, the mixing container was used as resin reservoir and the inlet hose was positioned inside it. In this configuration, the resin was at the bottom and the hose was entering in the liquid approaching from the top. As soon as the inlet clamp was opened, the resin was sucked inside the inlet hose at high speed and, as the resin level inside the container was going to be low, the hose started capturing air. The air was entering the mold in the form of bubbles of different dimensions, and this probably caused many voids inside the preform. Moreover, this configuration caused also a high waste of resin, since a portion of it was remaining inside the mixing container because infusing it would have meant introducing excessive quantity of air, with the consequent loss of vacuum in the mold.

- Rapid diffusion of resin inside the preform: During fabrication of the initial panels, the duration of the entire infusion process was about 180 seconds, from the moment when the resin was going out from the inlet hose to the one when the resin was starting to flow inside the outlet hose after having covered the preform. It was already explained that in a VARTM process, if the flow speed is too high, there is the risk of not obtaining good penetration of the resin inside the rovings and having many voids in the final component.

- Grooves developed on the bottom surface of some panels: The grooves were running along the stitching lines between the fibers rovings, as shown in Figure 61, and resulted in poor surface quality.

- Inclined non-wetted regions on the top surface of the third panel.

- Uncertainty in the quantity of resin to be infused in the mold in order to obtain a desired fiber volume fraction.

- High waste of resin inside the mixing container and inlet and outlet hoses: This problem was a consequence of the uncertainty on the quantity of resin needed for producing a panel with a certain fiber volume fraction. Starting from the production of the second panel in fact, a higher quantity of resin was extracted from the drum because, adopting the quantity obtained from the computation based on the panel volume, a short shot was obtained. Moreover, the resin left inside the mixing container was related to the difficulty in avoiding injecting air together with the resin that forced to close the inlet clamp before that all the resin could had been captured.

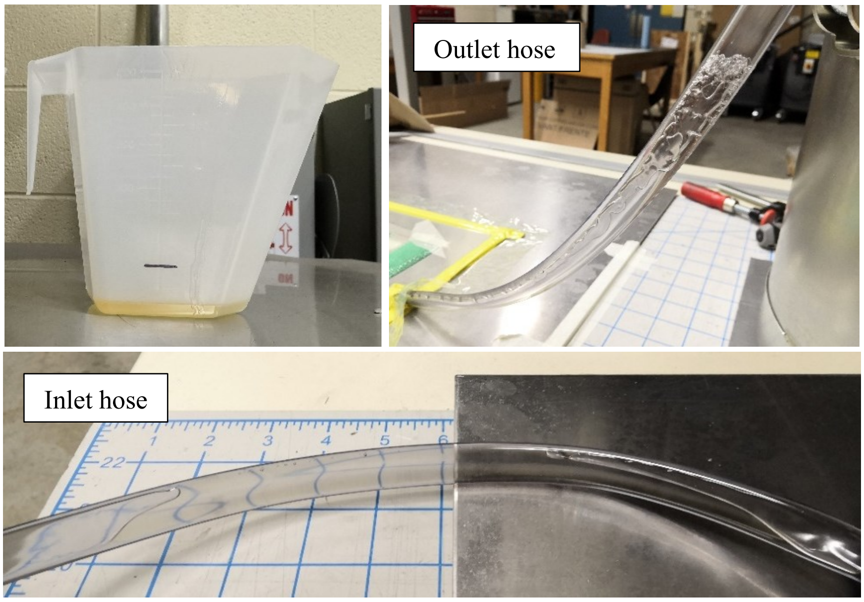

Figure 63. Excessive waste of resin inside the mixing container, inlet and outlet hoses was obtained.

Possible solutions were applied on the process and the effects of them were observed during the production of new panels.

To minimize the amount of air inside the mold during resin infusion, the setup described by Torkamani et al. [31] was considered and a funnel was used as resin reservoir instead of the mixing container. The funnel was fixed on the working bench and the inlet hose was connected to the lower end (see Section 4.2, Figure 57). When the clamp was opened, the resin was sucked inside the hose and its surface was moving toward the pipe entrance. This made possible to better control the infusion, closing the inlet clamp before that the external air could enter inside the hose and reducing the quantity of resin wasted.

A further improvement in the resin flow control was the application of two clamps in series at the inlet hose. Looking at Figure 64, the clamps were open partially during the infusion so that they were acting as nozzles. By changing their opening, it was possible to control the speed of the resin inside the hose. This had two beneficial effects, since it was possible to slightly reduce the speed of diffusion inside the preform and minimize the waste of resin inside the inlet hose.

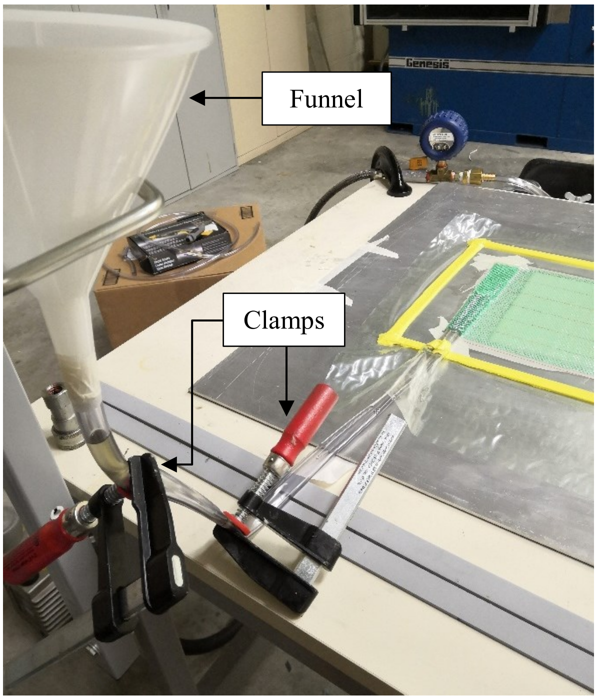

Figure 64. New inlet configuration, with the utilization of a funnel as resin reservoir and two clamps in series for controlling the flow of resin.

The following effort was dedicated in improving the position of the inlet and outlet hoses with respect to the mold. The configuration adopted at the beginning had the hoses placed at the corners of the plies. Observing Figure 65, assuming that when the resin goes out from the mold it expands with a circular flow front (yellow arrows), with the adopted setup the top left corner was immediately filled by resin while the bottom left corner was reached by resin with a certain delay. The resin advanced in the infusion mesh expanding along the diagonal direction of the plies and, as it was penetrating through the thickness, started also flowing inside the channels between the fibers rovings (orange arrows), which were oriented horizontally. These resulted in an asymmetric filling of the preform that probably caused the problem of the inclined dry-regions of the third panel.

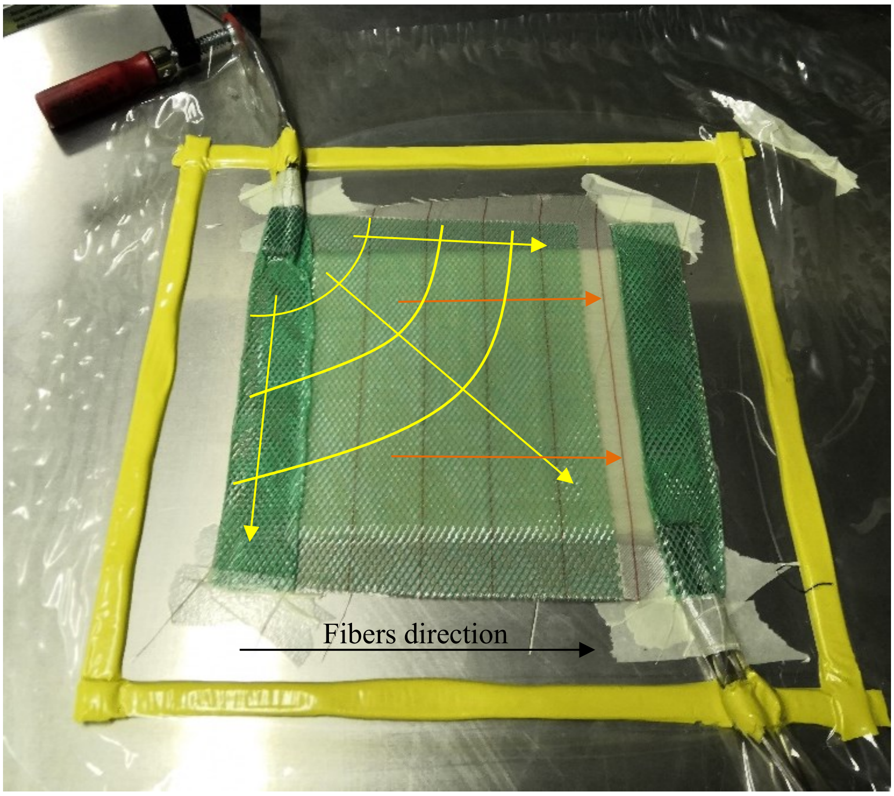

Figure 65. Initial hoses configuration. The inlet was placed at the top left corner of the plies, while the outlet was at the bottom right corner of them. The yellow arrows indicate the direction of the resin flow front inside the infusion mesh, while the orange arrows indicate the direction of the resin flow inside the channels between the fiber rovings.

The first alternative configuration considered had the hoses positioned at the horizontal middle line of the preform and parallel to it, as shown in Figure 66. The fibers were positioned parallel to the hoses. Adopting this setup allowed to obtain a symmetrical flow front with respect to the preform. However, some difficulties in the preparation of the process were encountered, with the need of cutting a hole in the infusion mesh in order to place the hoses inside it and with a more difficult bagging operation. After having failed three times in maintaining the vacuum inside the mold due to problems during the application of the vacuum bag, the setup was abandoned.

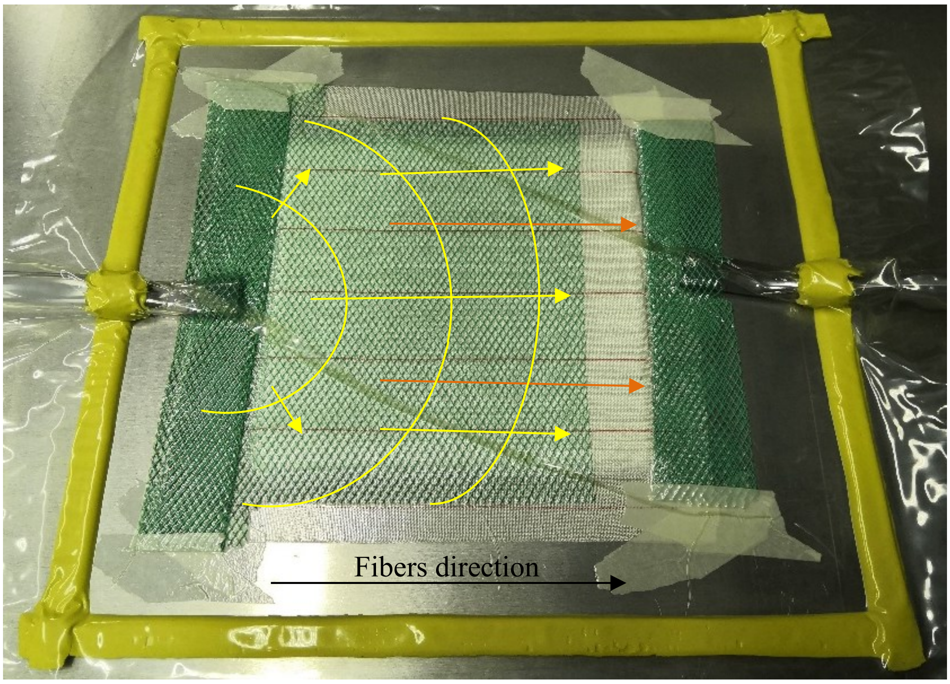

Figure 66. Alternative configuration of the inlet and outlet hoses position. The yellow arrows indicate the direction of the resin flow front inside the infusion mesh, while the orange arrows indicate the direction of the resin flow inside the channels between the fiber rovings. This setup allowed to obtain a symmetric flow front but caused some difficulties in the application of the vacuum bag, therefore it was abandoned.

A new configuration was attempted. The idea of placing the hoses near the horizontal middle line of the preform was maintained but, instead of being parallel to it, they were perpendicular, as it was in the first configuration. Moreover, as it can be observed in Figure 67, the hoses were farther from the fabric reinforcement when compared to the first configuration. This setup allowed to obtain a symmetric flow front inside the mold, as it was in the previous alternative setup but, differently to this last one, the bagging operation was easier. For this reasons, as it was explained in chapter 4.2., this configuration of the hoses was adopted for the production of all the subsequent panels.

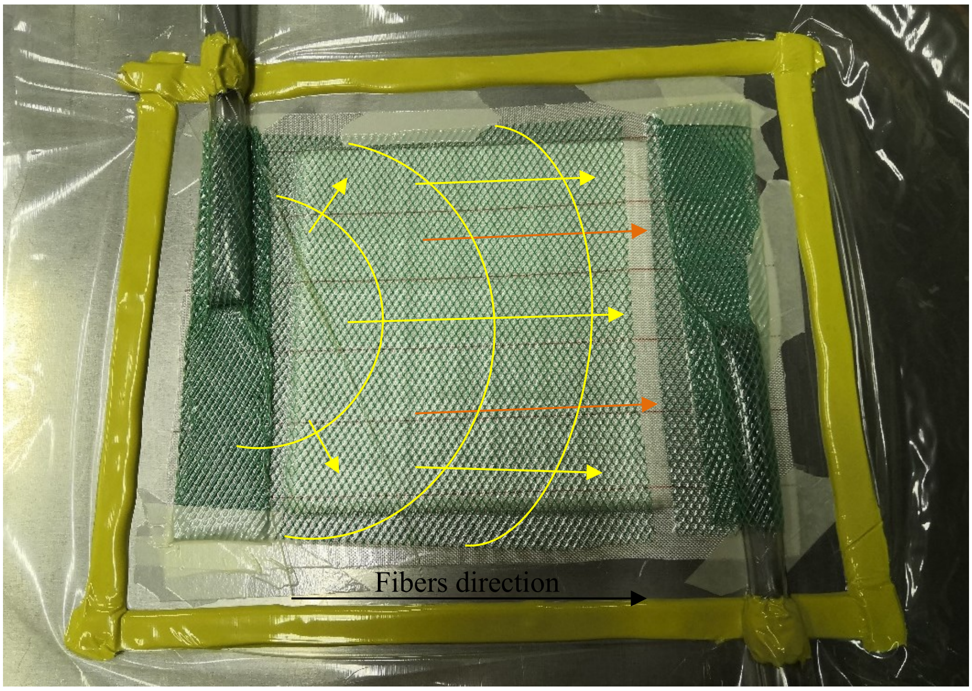

Figure 67. Final configuration adopted for the hoses position. The hoses were placed near the horizontal middle line but they were parallel to the vertical symmetry line. The yellow arrows indicate the direction of the resin flow front inside the infusion mesh, while the orange arrows indicate the direction of the resin flow inside the channels between the fiber rovings.

Despite of the improvement of the flow front inside the mold, grooves running between the fibers rovings were still observed on the lower surface of the components produced. The speed of resin diffusion was still excessive. Searching in the literature, it was found that the resin moves easily along the direction of the fibers because it flows inside the channels generated by the gaps between the rovings. For this reason, it is advisable to interrupt these preferential paths to force the resin to flow throughout the preform [10]. Therefore, the plies were laid on the mold with the unidirectional fibers perpendicular to the flow of resin and not parallel as it was previously. The result of the change in the direction of the fibers with respect to the resin flow was immediately noticeable, with the flow front that became more regular, as it was shown in Figure 58, and with the speed of diffusion that decreased sensibly. In fact, in the first infusions, about 180 seconds were needed from the moment when the resin was exiting from the inlet hose to the one when the preform was wet and the resin started flowing inside the outlet hose. Instead, after having applied two clamps at the inlet to regulate the flow and having changed the direction of the fibers, about 300-360 seconds were needed to complete the infusion process.

The outlined improvements applied to the process enabled the fabrication of panels with improved quality. The new infusion system configuration allowed to minimize the waste of resin inside the hoses and made possible to decrease the quantity of resin extracted from the drum for obtaining a full wetting of the preform. Nevertheless, the exact quantity of resin needed for obtaining full wetting of the preform and obtaining a precise fiber volume fraction was still uncertain. For example adopting 15x15 cm glass fiber plies, assuming an average panel thickness of 2 mm and aiming to a desired fiber volume fraction equal to 60%, about 20 g of resin should be extracted from the drum but this quantity was not enough for having a full preform wetting. For this reason, different panels were produced varying the amount of resin extracted between 60 to 46 g. The objective was to have many panels in which the only difference was the mass of resin employed and, by performing the matrix acid digestion test on them, discover which was the correct quantity needed to obtain the desired fiber volume fraction of 60 %.

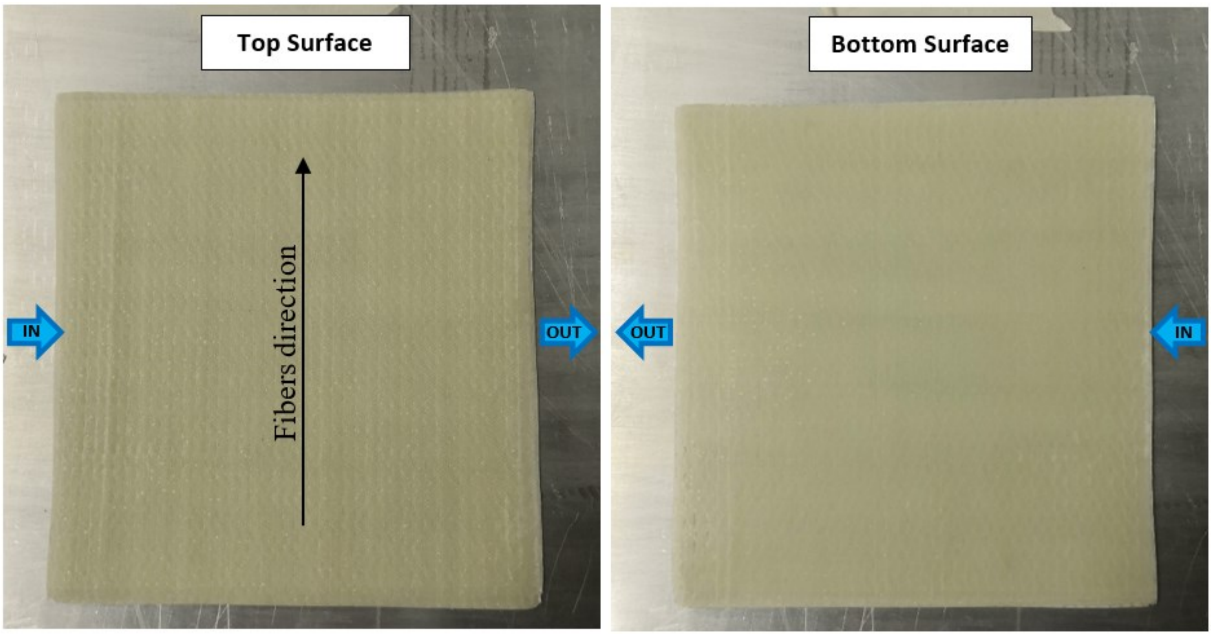

Figure 68. Panel produced with 54 g of resin.

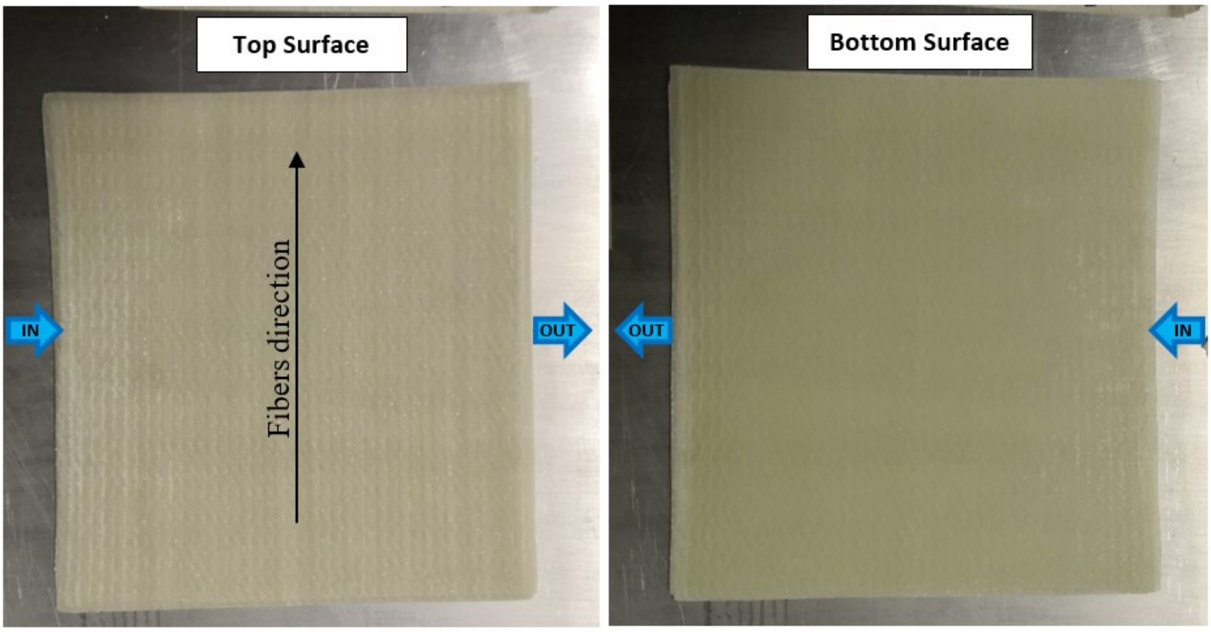

Figure 69. Panel produced with 50 g of resin.

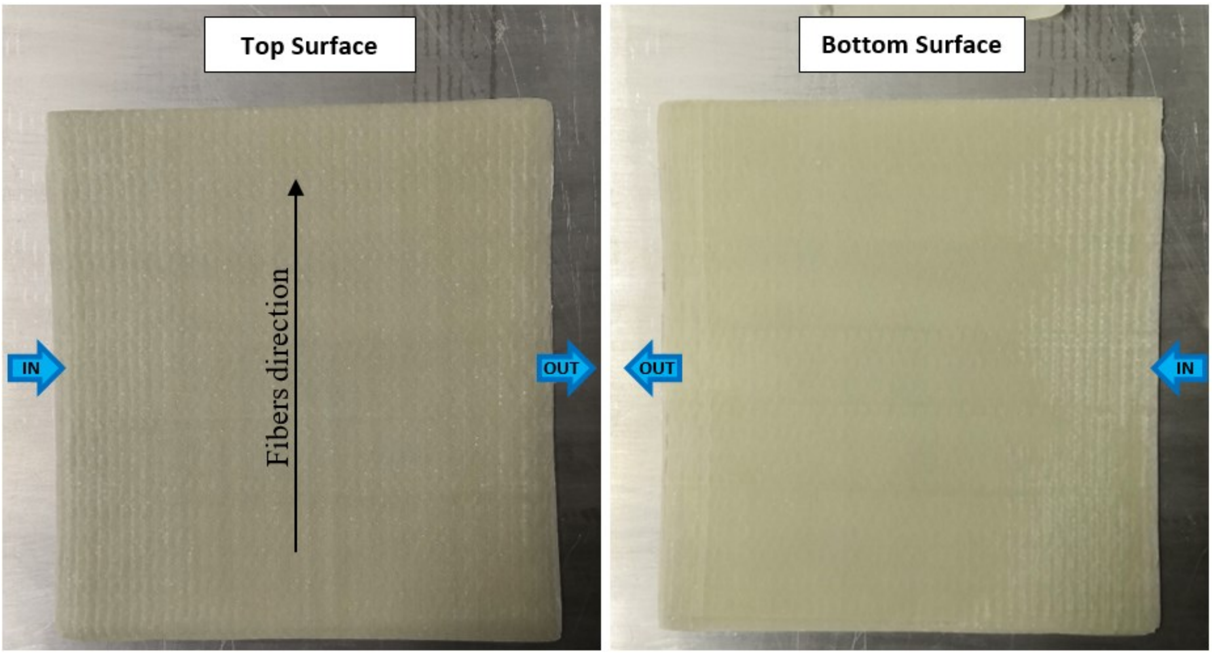

Figure 70. Panel produced with 46 g of resin.

Three examples of panels produced with different quantities of resin are reported in the previous figures. It can be observed that the quality of these panels, produced applying all the improvements described before, was better than that of the second panel that was shown at the beginning of the chapter in Figure 61. The resin seemed to be distributed evenly through the panel. As it was expected from a VARTM process, the top surface of the panels was not perfectly flat but it had the texture left from the peel ply and many small waves following the rovings of the fibers. This was caused by the vacuum bag that was compressing the fiber plies and was adhering tightly to them. This intrinsic disadvantage of the VARTM process caused a continuous variation on the thickness of the panel that, depending on the point where the measuring faces of the micrometer were touching, was in the range 2.000 ± 0.150 mm. Compared to the first panels produced, the bottom surface of the last panels was flat and very smooth, with few grooves observed. However, near the inlet side, some marks running along the stitching lines between the fibers rovings were still present. This problem for example, was particularly evident on the bottom surface of the panel produced with 46 g of resin, shown in Figure 70, which had many white lines only near the inlet side. The grooves were less deep than those obtained in the first panels, but they were still representing a quality issue and therefore it was investigated a possible solution. Observing Figure 71, a portion of the resin was remaining attached to the mold near the inlet side after the release of the part, and this left the marks on the bottom surface.

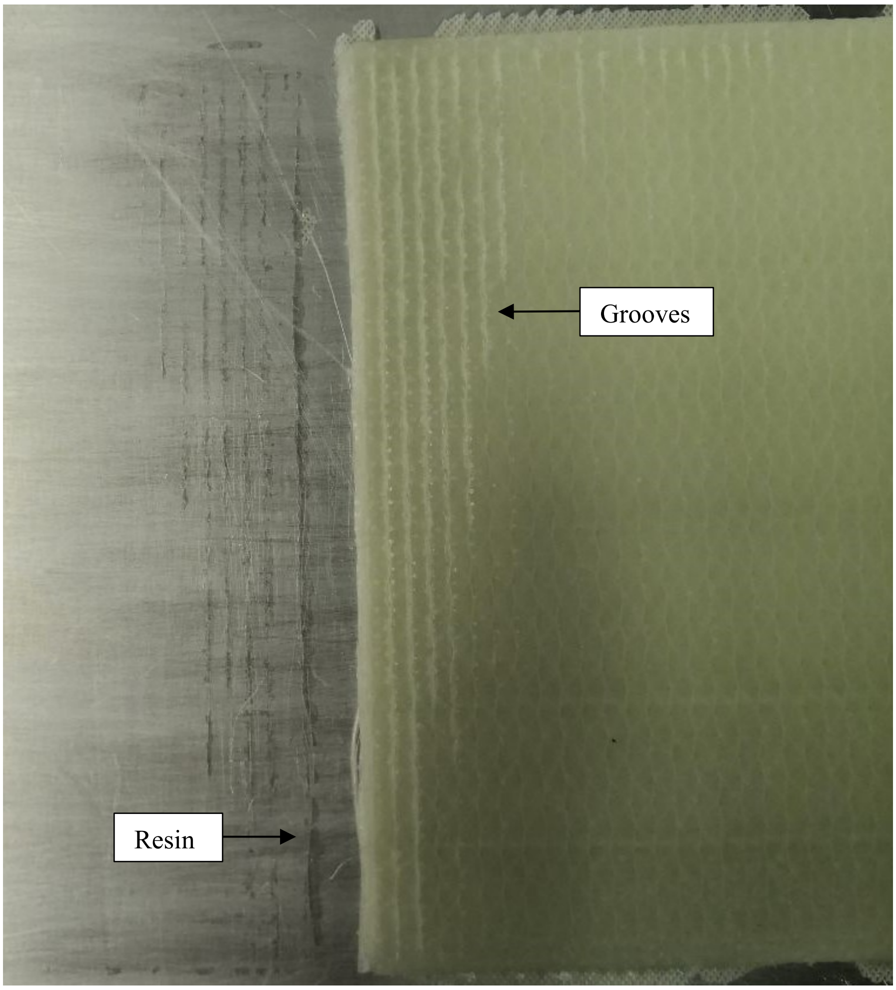

Figure 71. Grooves near the inlet side on the bottom surface of the panels. The problem was caused by some resin that was remaining attached to the mold during the part release, causing a damage on the component.

The problem was noticed on almost all the panels produced, despite of the quantity of resin utilized, therefore this last aspect probably was a non-influencing factor. Since the issue was related to a not complete detachment of the resin from the mold, the investigation was focused on the release agent utilized. The first idea was to apply six layers of release agent instead of four, but the resulting panels did not show any substantial difference. The second possible solution was to let the release agent cure for a longer time, increasing from the 30 minutes suggested by the producer to 3 hours. Also this time, the panels were still presenting some marks at the inlet side. Asking for advice to an expertise on the thermoplastic resin infusion processes, it was suggested that the fact that the resin does not detach completely only near the inlet side could be caused by the washing effect of the release agent under the action of the resin that enters in the mold. If the release agent is not compatible with the resin utilized, the resin can dissolve it as it flows on the surface of the mold. In a SCRIMP process the resin is mainly spread on the upper surface of the preform by the infusion mesh and then it starts penetrating through the thickness but at the inlet side, where the quantity of resin arriving is high, it starts also penetrating through the cross section of the preform. As the resin penetrates through the cross section of the initial part of the panel, it flows also inside the channels between the fibers rovings on the mold surface, probably dissolving the release agent. In the remaining part of the panel instead, since the resin penetrates mainly through the thickness without flowing on the mold surface, the washing effect is less strong and the release agent is not dissolved, therefore allowing an easy release of the final part. For this reason, a possible solution to the problem can be changing the release agent employed, adopting one that is compatible with the Elium® resin.

4.4. Process Validation

In order to validate the quality of the process, three different tests were performed on samples cut from the panels produced:

- Acid digestion of the matrix, aimed in discovering the fiber volume fraction of the panels produced.
- Optical microscopy analysis, for investigating the microstructure of the material.
- Dynamic mechanical analysis (DMA), for finding the glass transition temperature of the material.

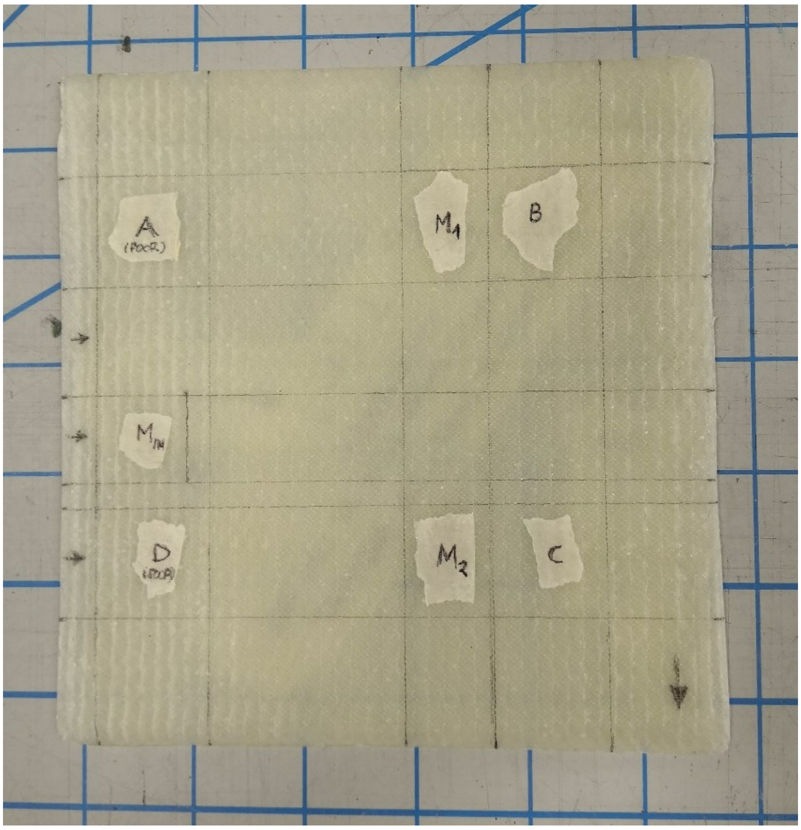

Figure 72. Example of samples of different dimensions cut from the panel produced using 46 g of resin.

4.4.1. Acid Digestion Test

The acid digestion of the matrix, described in the ASTM D3171 standard [55], is a test that allows to find the content of the constituents of a composite material. The test specimens were cut from three panels produced with different quantity of resin (54 g, 50 g and 46 g), since the final purpose of this test was discovering which was the quantity of resin that allowed to produce panels with the fiber volume fraction closer to the target of 60 %. The samples were cut from different regions of the panel, in order to have a wider representation of the material distribution throughout the component. The procedure adopted was the following:

1. Computation of the specimen volume. The length of the specimen sides was measured with a micrometer by taking the dimensions on three different points. The values were used for computing the average lengths of the samples. The same procedure was applied for obtaining the average thickness of the specimen, which was computed using the values of the thickness measured in four different points of the sample. The average values of the lengths of the two sides and of the thickness were multiplied for obtaining the volume of the sample.

2. Measurement of the specimen mass to the nearest 0.0001 g.

3. Dissolution of the matrix. The samples were placed inside a beaker containing 100 ml of 70 % nitric acid solution that was constantly heated using a hot plate. For safety reasons, the operation was performed under a fume hood, and it was important to maintain the acid below 80 °C in order to avoid dangerous splashes caused by its boiling. The dissolution of the matrix was favored by mixing with a glass stirring stick.

4. Filtering and washing the fibers. When the matrix had been clearly dissolved, the fibers were separated from the solution by using a system with a sintered glass filter. When the fibers were finally separated from the nitric acid solution, they were washed using distilled water and acetone.

5. Drying the fibers.

6. Measurement of the fibers mass to the nearest 0.0001 g.

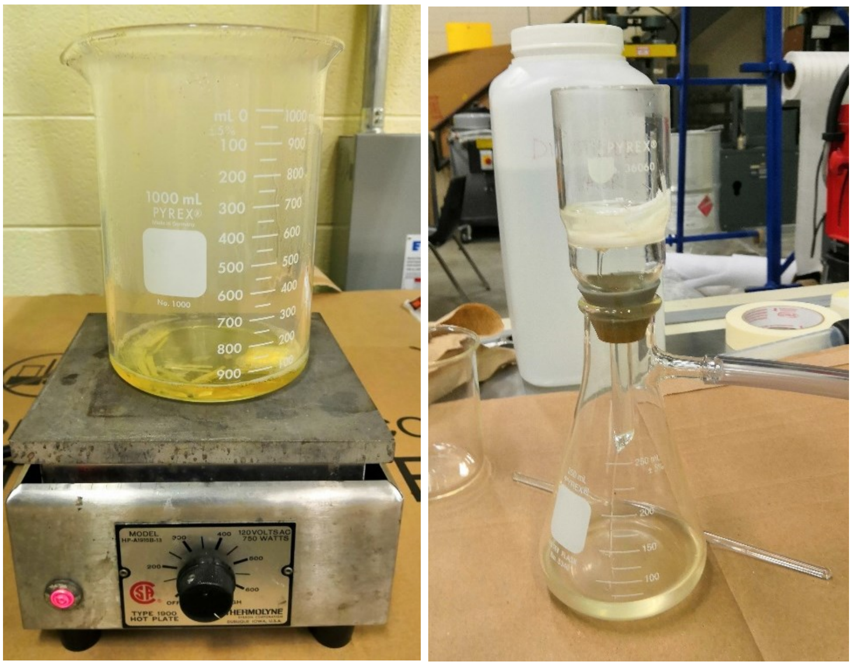

Figure 73. The left image shows the operation of dissolution of the matrix inside the nitric acid solution heated by the hot plate. The right image shows the filtering system utilized for separating the fibers from the solution.

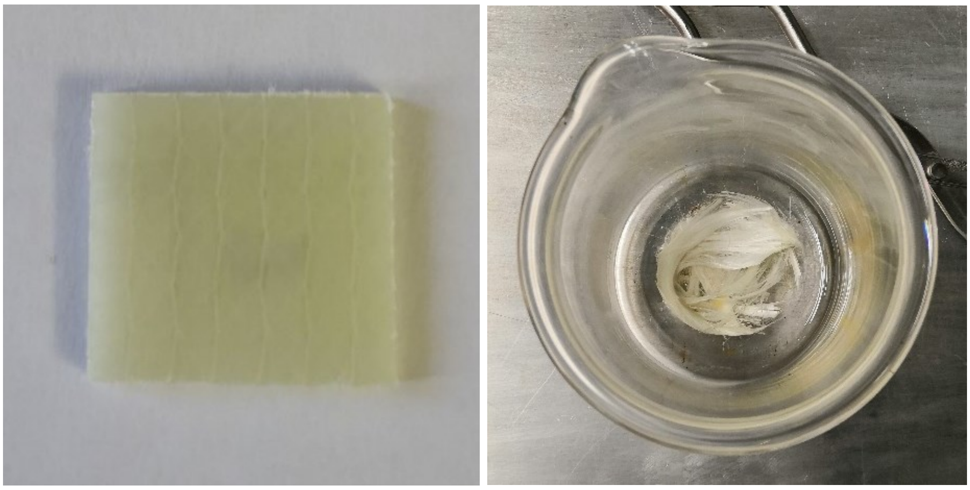

Figure 74. Initial specimen (left image) and glass fibers obtained from the matrix digestion (right image).

Knowing the density of the E-glass fiber reinforcement ρ_f, equal to 2.55 g/cm^3, the initial mass of the sample M_i and the final mass of the fibers M_f, it was possible to compute the fiber volume fraction as:

$$V_{f\%} = \frac{M_f}{M_i} \cdot 100 \cdot \frac{\rho_c}{\rho_f} \tag{4.1}$$

where the density of the specimen was equal to:

$$\rho_c = \frac{M_i}{V} \tag{4.2}$$

Also the void content inside the specimen was computed. Assuming an ideal situation in which no voids are present inside the sample, the theoretical volume of the matrix was found as:

$$V_{m\,th} = V - V_f \tag{4.3}$$

where V_f was the volume of the fibers, computed as:

$$V_f = \frac{M_f}{\rho_f} \tag{4.4}$$

Assuming the density of the solid Elium® resin ρ_m equal to 1.19 g/cm^3 [53], it was possible to find the theoretical mass of the matrix:

$$M_{m\,th} = V_{m\,th} \cdot \rho_m \tag{4.5}$$

The actual mass of the matrix was equal to:

$$M_m = M_i - M_f \tag{4.6}$$

From which it was computed the actual mass of the matrix as:

$$V_m = \frac{M_m}{\rho_m} \tag{4.7}$$

The volume occupied by the voids inside the sample it was equal to:

$$V_v = V_{m\,th} - V_m \tag{4.8}$$

Finally, the void content of the sample was computed as:

$$V_{v\%} = \frac{V_v}{V} \cdot 100 \tag{4.9}$$

4.4.1.1. Results

The results obtained from the acid digestion test are reported in Table 4.

	46 g				50 g		54 g		
	A	B	C	D	A	B	A	B	C
V [mm^3]	1083,536	1034,264	1018,437	1028,940	1000,594	1055,033	1130,060	1007,519	1155,836
Mi [g]	1,6930	1,6235	1,5756	1,5600	1,5788	1,6670	1,7914	1,6600	1,8248
Mf [g]	1,4483	1,3738	1,3377	1,3448	1,2742	1,2888	1,4013	1,2463	1,4217
ρ_c [g/cm^3]	1,562	1,570	1,547	1,516	1,578	1,580	1,585	1,648	1,579
Vf	0,5680	0,5387	0,5246	0,5274	0,4997	0,5054	0,5495	0,4887	0,5575
Vm th [cm^3]	0,516	0,496	0,494	0,502	0,501	0,550	0,581	0,519	0,598
Mm th [g]	0,6135	0,5897	0,5877	0,5969	0,5961	0,6540	0,6908	0,6173	0,7120
Mm actual [g]	0,2447	0,2497	0,2379	0,2152	0,3046	0,3782	0,3901	0,4137	0,4031
Vm actual [cm^3]	0,206	0,210	0,200	0,181	0,256	0,318	0,328	0,348	0,339
Vv	0,3099	0,2857	0,2939	0,3207	0,2449	0,2318	0,2527	0,1711	0,2596
Vf [%]	52,4	52,1	51,5	51,3	49,9	47,9	48,6	48,5	48,2
Vv [%]	28,6	27,6	28,9	31,2	24,5	22,0	22,4	17,0	22,5

Table 4. The table contains the measurements and the results of the acid digestion test.

4.4.1.2. Discussion

The results from the acid digestion test performed on the samples showed that the quantity of resin that allowed to reach the fiber volume fraction closest to the target of 60 % was 46 g. All the samples cut from different regions of the panel produced with 46 g, in fact, showed a fiber volume fraction higher than 51 % while the other panels had a value lower than 50%. Nevertheless, the value was still lower than the required one, therefore a quantity of resin lower than 46 g should be infused in the preform in order to reach a fiber volume fraction of 60 %.

It is important to notice that the void content resulting from the computation is very high on all the samples (>20 %), and it is not in correspondent with the void content that a good quality component should have. The values can be excessive also considering low quality parts and it may mean that an error in the test have been committed. A possible mistake could have been made during the computation of the specimen volume. The procedure utilized consisted in measuring with a micrometer the lengths and the thickness of the samples. Four measurements of the thickness were taken on four different points of the specimen, and the average value was computed. The approximation of considering an average value for the thickness of the sample could have been excessively rough, since the upper surface of the panels was presenting many undulations and the value of thickness depended on which points the micrometer faces were touching. A small variation in the volume computed can affect strongly the void content results and modify the fiber volume fraction. For this reason, the optical microscopy analysis of the samples cut from the same panels utilized during this test was important in order to verify the quality of the panels produced, understanding if the high void content was due to an error in the test procedure or due to a problem of the process.

4.4.2. Optical Microscopy Analysis

The optical microscopy analysis was performed for studying the microstructure of the material. The samples were cut from the same panels utilized for the acid digestion test, and they were prepared for the microscope. The preparation consisted in polishing the specimen section perpendicular to the fibers direction. The polishing was performed in five steps, using wet silicon carbide discs of increasing grit (from 180 to 1200) and finishing the surface using diamond paste and extender fluid applied on a felt polishing disc.

4.4.2.1. 54 g of resin Panel

From the panel produced with 54 g of resin two samples were cut. The position of the samples inside the panel is represented in Figure 75, where also the position of the samples used for the acid digestion test is reported.

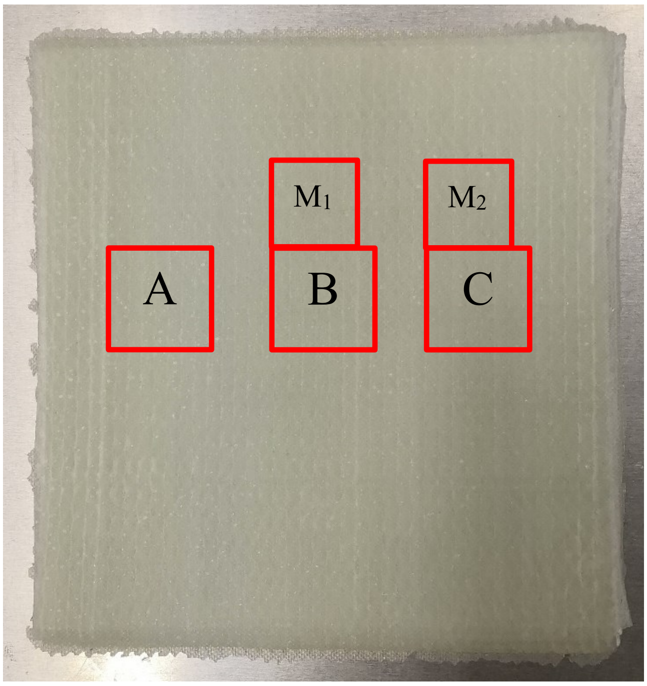

Figure 75. Position of the samples cut from the 54 g panel. The panels A, B and C were utilized for the acid digestion test while M_1 and M_2 were analyzed with the optical microscope.

Sample M_1

The sample M_1 was approximately located at the middle of the panel. Referring to Figure 75, the surface of the sample M_1 analyzed was the one perpendicular to the fiber directions and in contact with the sample B. The images are reported in Figure 76.

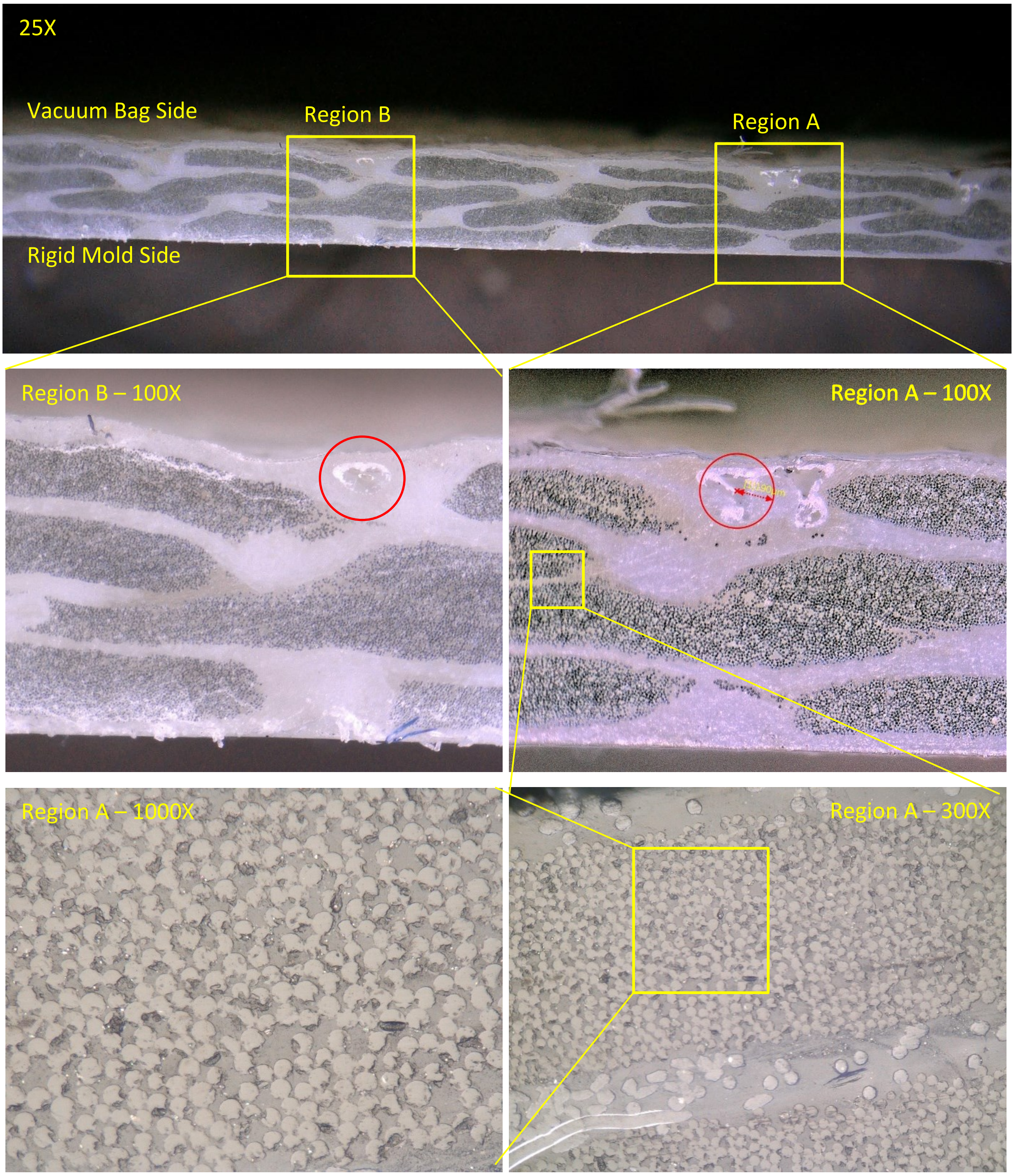

Figure 76. Microscope images of sample M1 cross-section.

Observing the images of the sample M_1 cross-section it is possible to notice that the resin had penetrated completely through the preform. Micro voids are not present and, as shown in the 500X image of the region A, the fibers have been completely wetted. In regions A and B some voids are present near the upper surface, that are highlighted by a red circle. As it can be observed in the 25X image of the cross-section, the surface of the panel that was in contact with the vacuum bag has very high roughness.

Sample M_2

The sample M2 was located near the outlet side of the panel. The cross-section analyzed with the microscope was the one in contact with the sample C utilized in the acid digestion test.

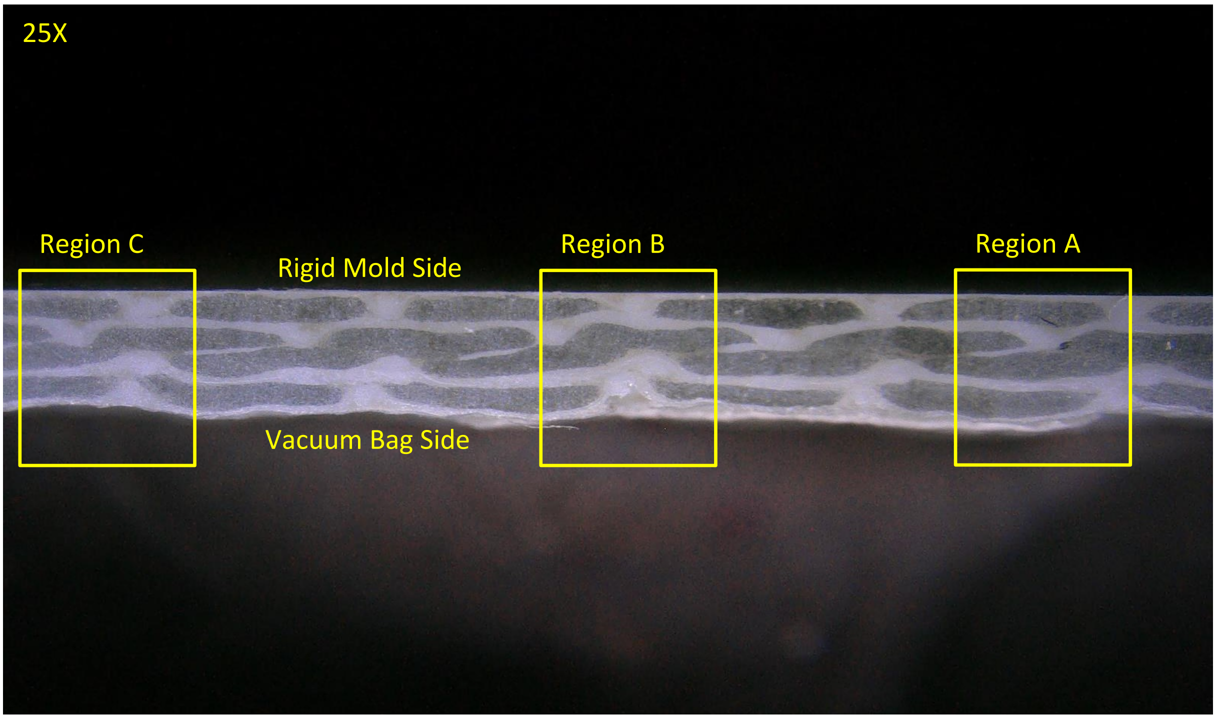

Figure 77. 25X image of the sample M2 cross-section.

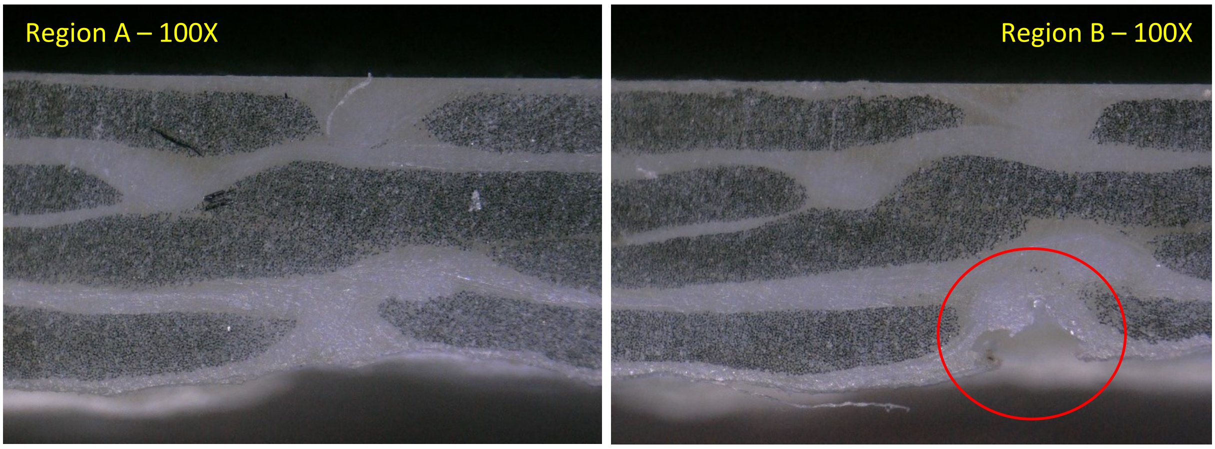

Figure 78. 100X images of region A (left image) and region B (right image). The red circles highlights the presence of a void on the vacuum bag side surface.

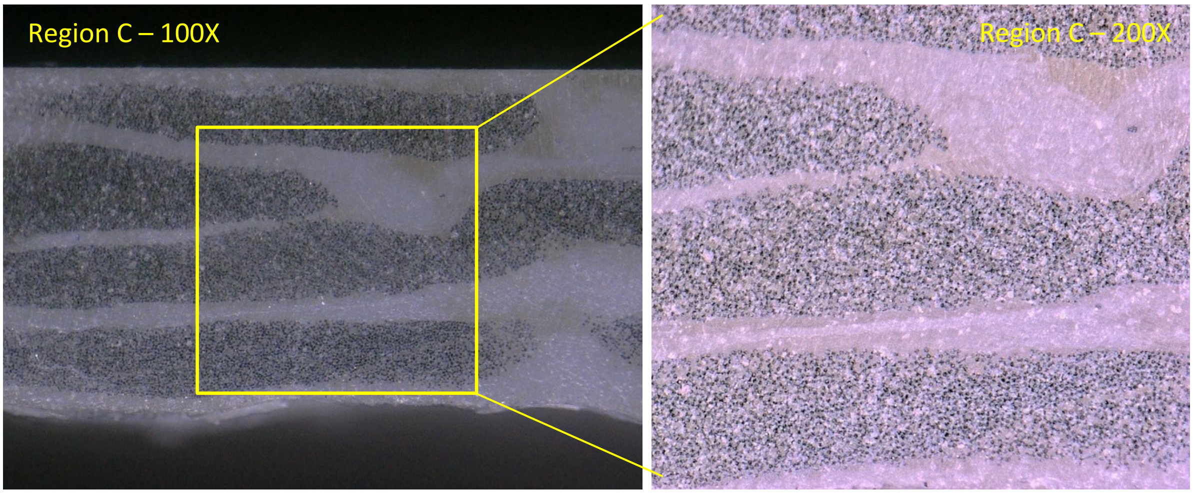

Figure 79. 100X (right) and 200X (left) images of region C.

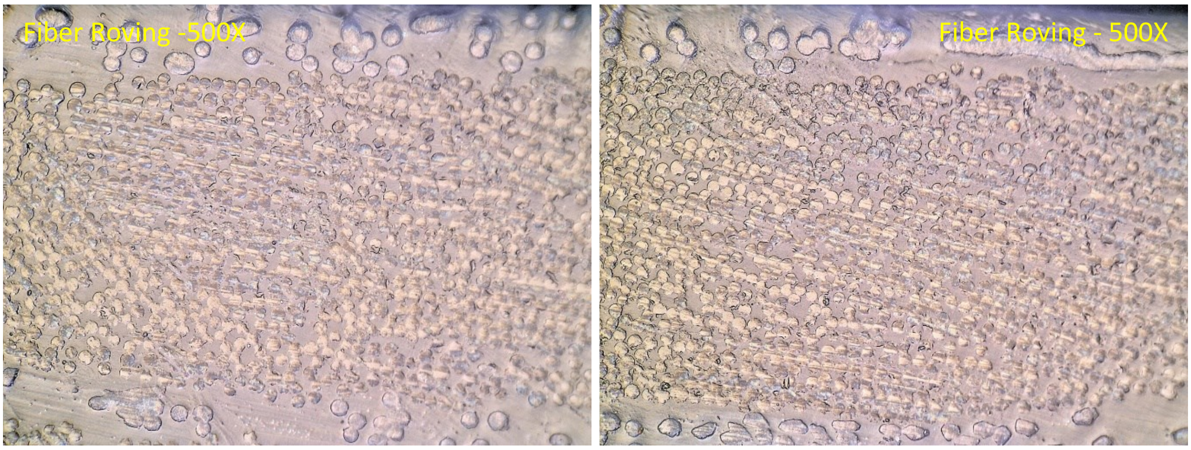

Figure 80. 500X images of two tow of fibers of sample M2.

The images from M2 sample show how the fibers had been completely wetted by the resin. There are no micro voids neither between the fibers rovings (Figure 79) nor within them (Figure 80). As it is highlighted in Figure 78, a void is present on the surface that was in contact with the vacuum bag. The 25X and 100X cross-section images show how the surface that was in contact with the rigid side of the mold is very flat, while the roughness of the opposite side is high and the surface has many undulations. From the 200X image of Figure 79 it is possible to observe that the area around the fiber rovings presents regions of two different colors. It is probable that the brighter white regions are showing the cross-sections of the polyester stitching yarns and of the polymeric veil that was covering the fiber plies, impregnated by the resin. Instead, the regions that have a more yellowish color are composed by pure polymer.

4.4.2.2. 50 g of resin Panel

From the panel produced using 50 g of resin two samples were cut, one near the inlet side and one near the outlet. The position of the two samples, shown in Figure 81, was chosen in order to study the differences between the quality of the region near the outlet side and the quality of the region near the inlet side.

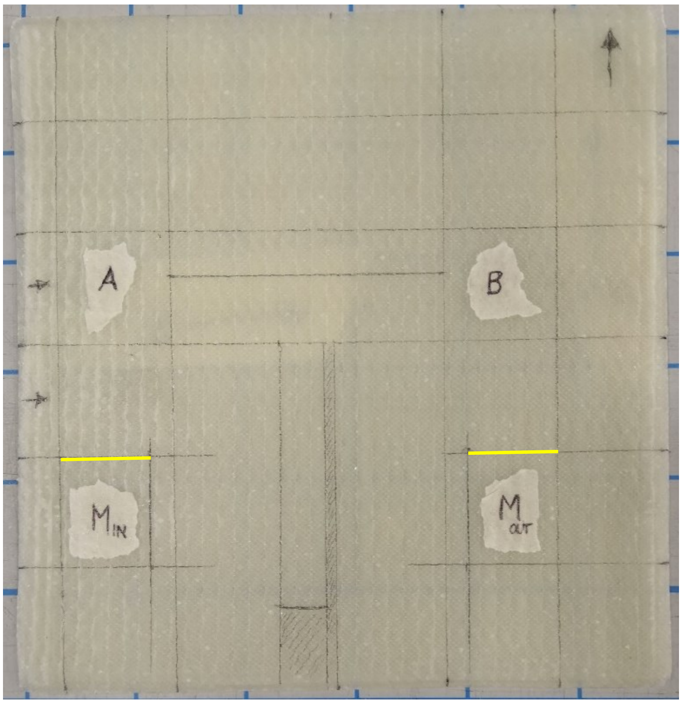

Figure 81. Position of the samples cut from the 50 g panel. The panels A and B were utilized for the acid digestion test while M_{IN} and M_{OUT} were analyzed with the optical microscope. A yellow line highlights the cross sections of the samples that were analyzed with the microscope.

Sample M_{IN}

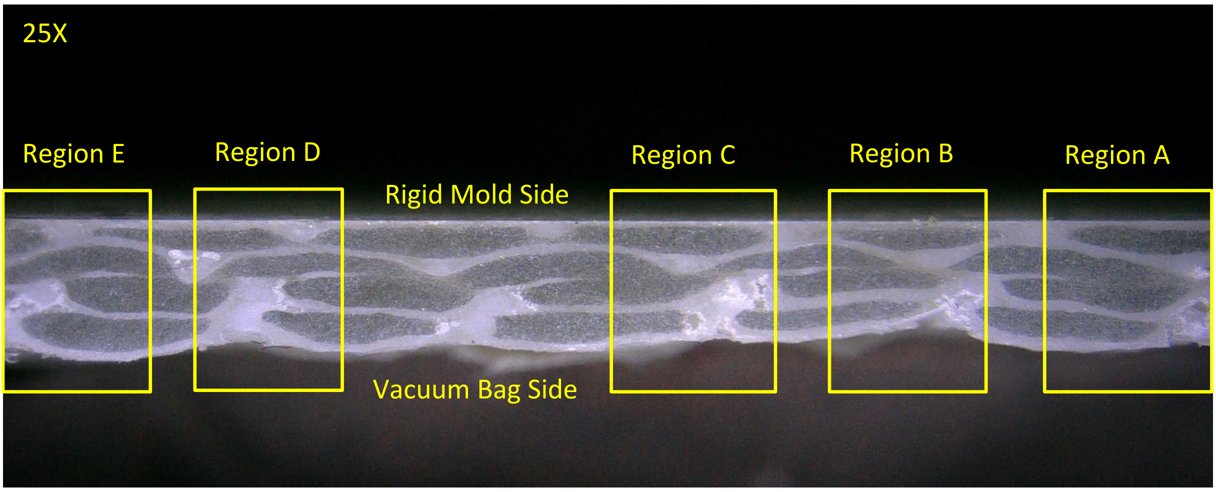

Figure 82. 25X image of the sample M_{IN} cross-section.

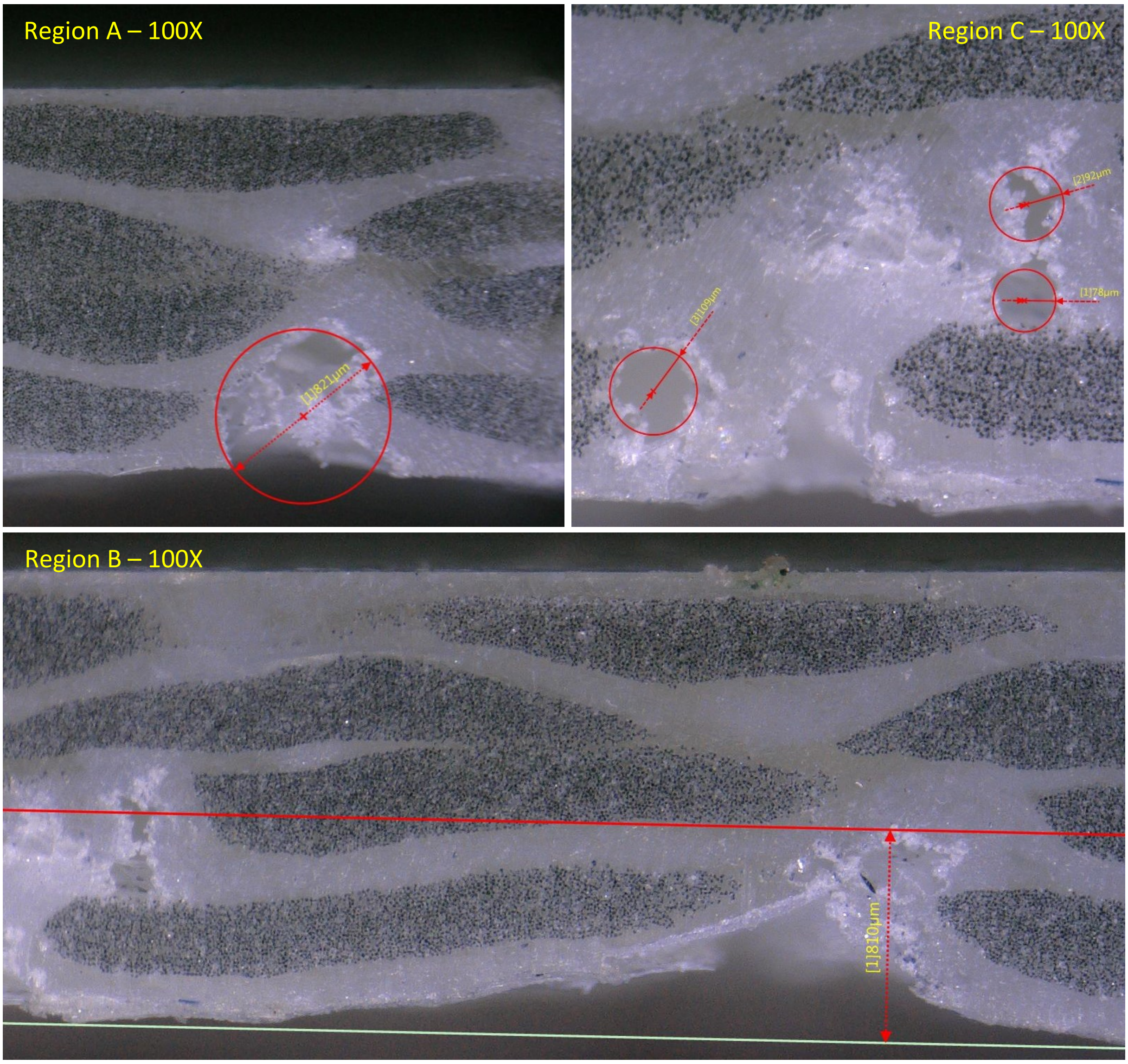

Figure 83. 100X images of regions A (top left image), B (bottom image) and C (top right image). The red circles highlight the voids. The bottom image shows a deep valley caused by a void on the surface that was in contact with the vacuum bag.

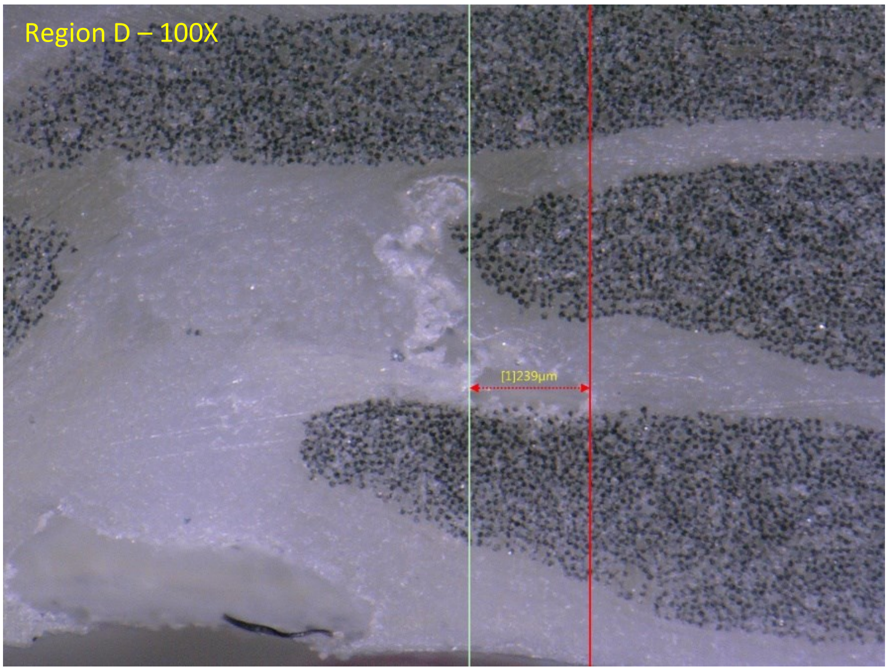

Figure 84. 100X image of the region D of the cross-section. The dimension of a void have been measured.

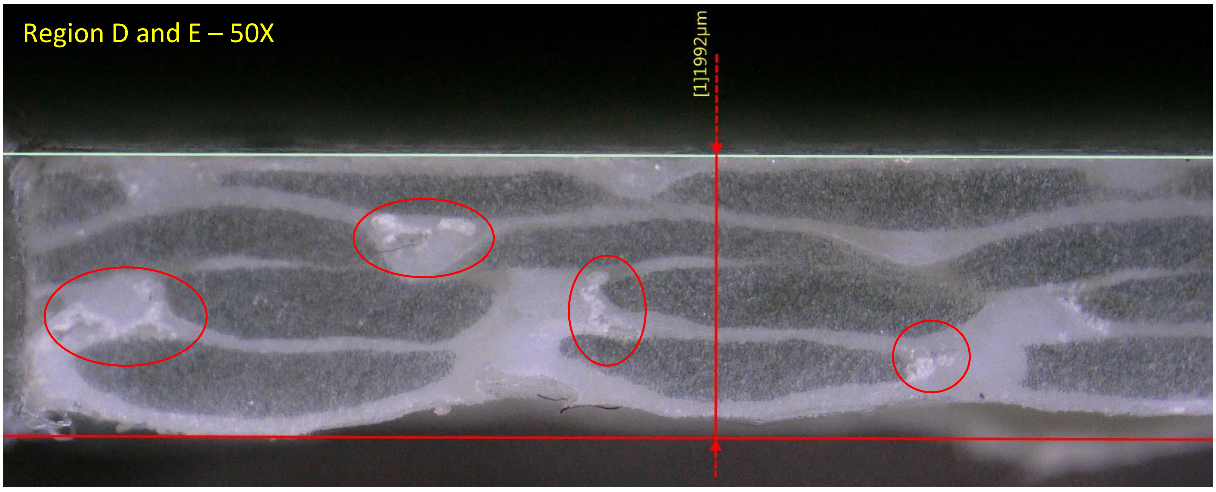

Figure 85. 50X image of the regions D and E of the cross-section. The red line placed on the higher crest highlights the variation in the thickness of the sample. Voids are highlighted by the red circles.

The optical microscopic images obtained from the sample M_{IN} show that the panel presents many quality problems near the inlet side. Many voids of dimensions included between 100 and 200 µm are visible inside the matrix material. Moreover, voids of greater dimensions (about 800 µm) are present on the vacuum bag side surface, which has also an evident variation of the thickness along the length.

Sample MOUT

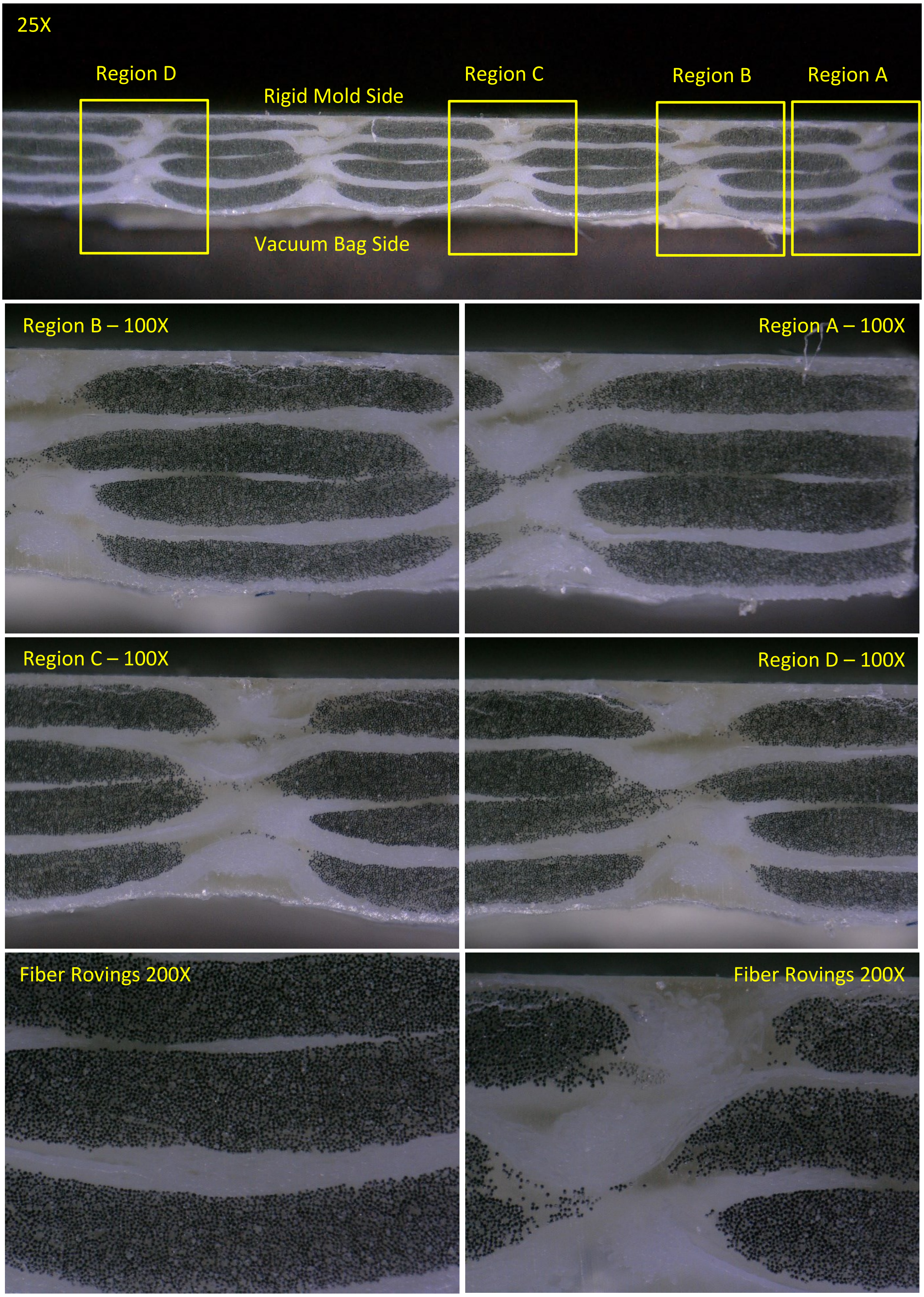

Figure 86. Sample MOUT cross-section images with different levels of magnification (25X, 100X and 200X).

Observing the images of the sample M_{OUT} cross-section it is possible to notice that the quality is higher with respect to the sample M_{IN}. The sample do not present any void inside the matrix material or on the vacuum bag side surface. The resin had wetted completely the fibers within the rovings and no micro voids are present. The thickness of the sample is still varying along the length, but the absence of superficial voids gives a better surface quality with respect to the sample MIN. In this sample it is evident the distribution of the materials: the brighter white regions around the rovings are given by the cross section of the stitching yarns and of the veil, in fact they are always on the top of the fiber plies; the yellowish color regions instead are given by pure thermoplastic polymer. The same yellowish color is found inside the fiber rovings, meaning that they are impregnated by resin.

4.4.2.3. 46 g of resin Panel

From the panel produced using 46 g of resin three samples were cut. As shown in Figure 87, the first sample M_{IN} was taken at the inlet side of the panel, where there was the problem of the grooves caused by incorrect release of the panel from the mold. The other two samples M_1 and M_2 were cut near the outlet side, in order to make a comparison between the quality of different regions of the panel.

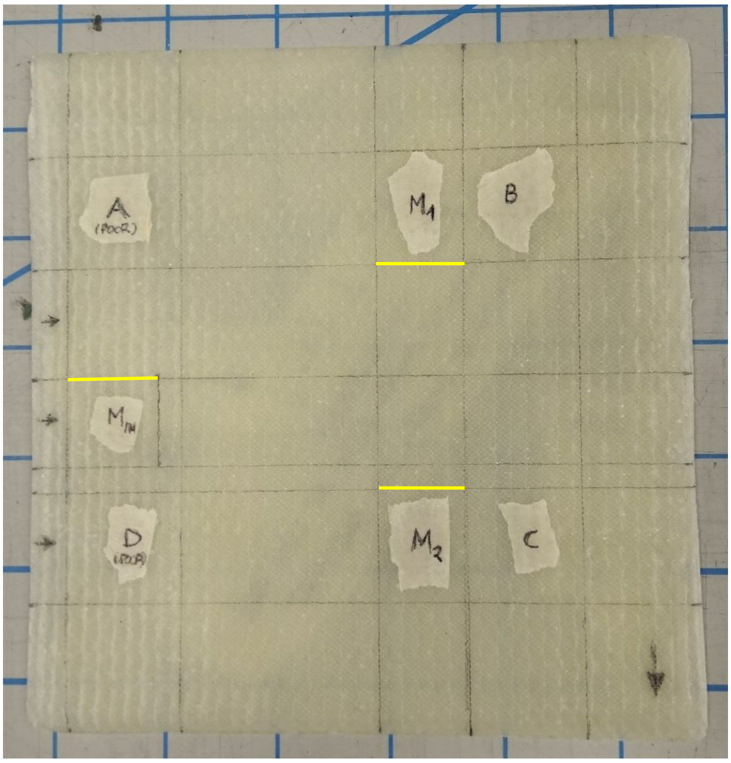

Figure 87. Position of the samples cut from the 46 g panel. The panels A, B, C and D were utilized for the acid digestion test while M_{IN}, M_1 and M_2 were analyzed with the optical microscope. A yellow line highlights the cross section of the samples that was analyzed with the microscope.

Sample MIN

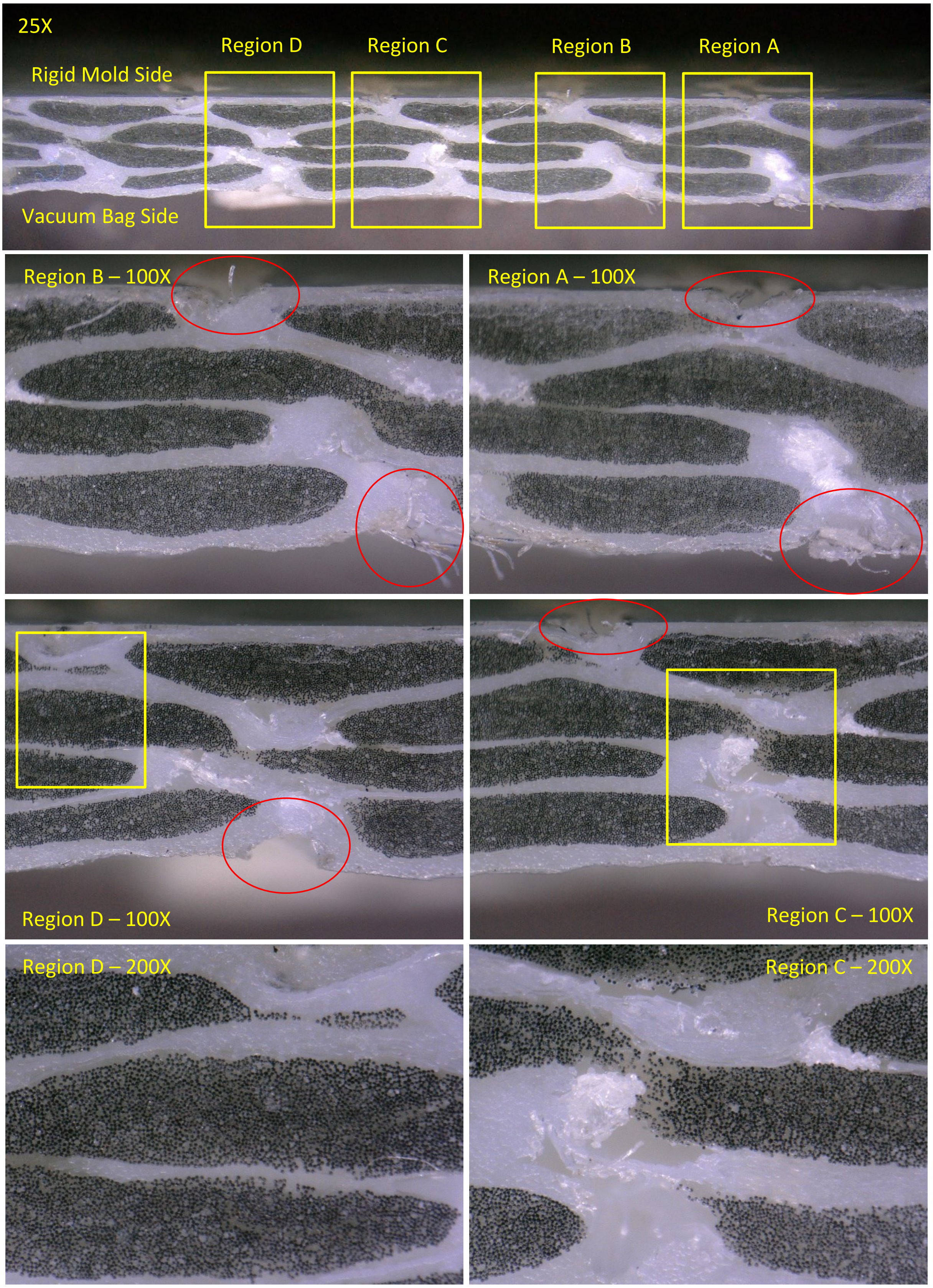

Figure 88. Sample MIN cross-section images with different levels of magnification (25X, 100X and 200X). Defects are highlighted by red circles.

Observing the images of the sample M_{IN} cross-section it is possible to notice many defects. The rigid mold side surface has grooves between the fiber rovings, which were caused by the portion of resin that remained attached to the mold during the release of the panel. Moreover, voids are present also on the surface that was in contact with the vacuum bag.

Sample M_1

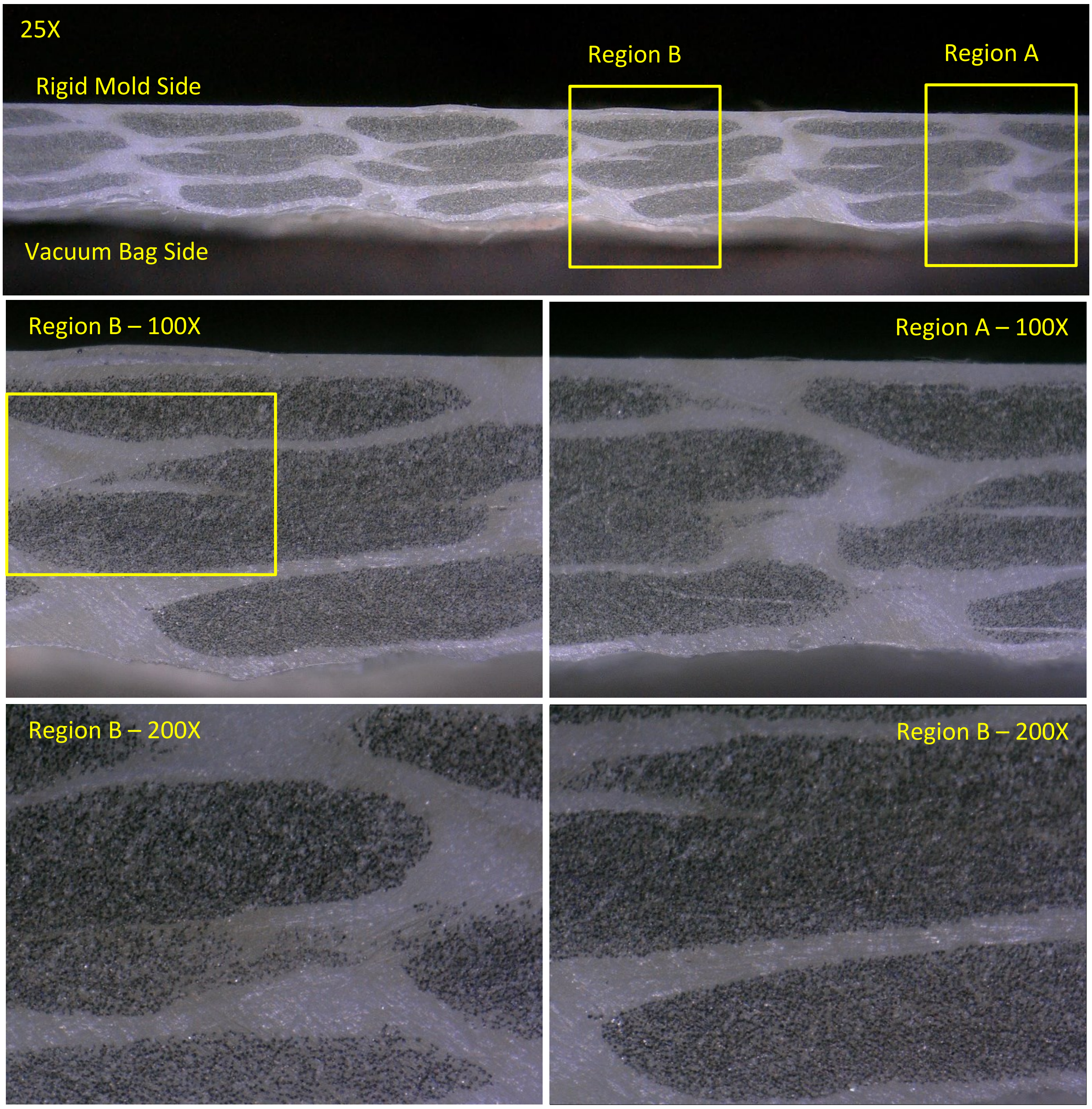

Figure 89. Sample M_1 cross-section images with different levels of magnification (25X, 100X and 200X).

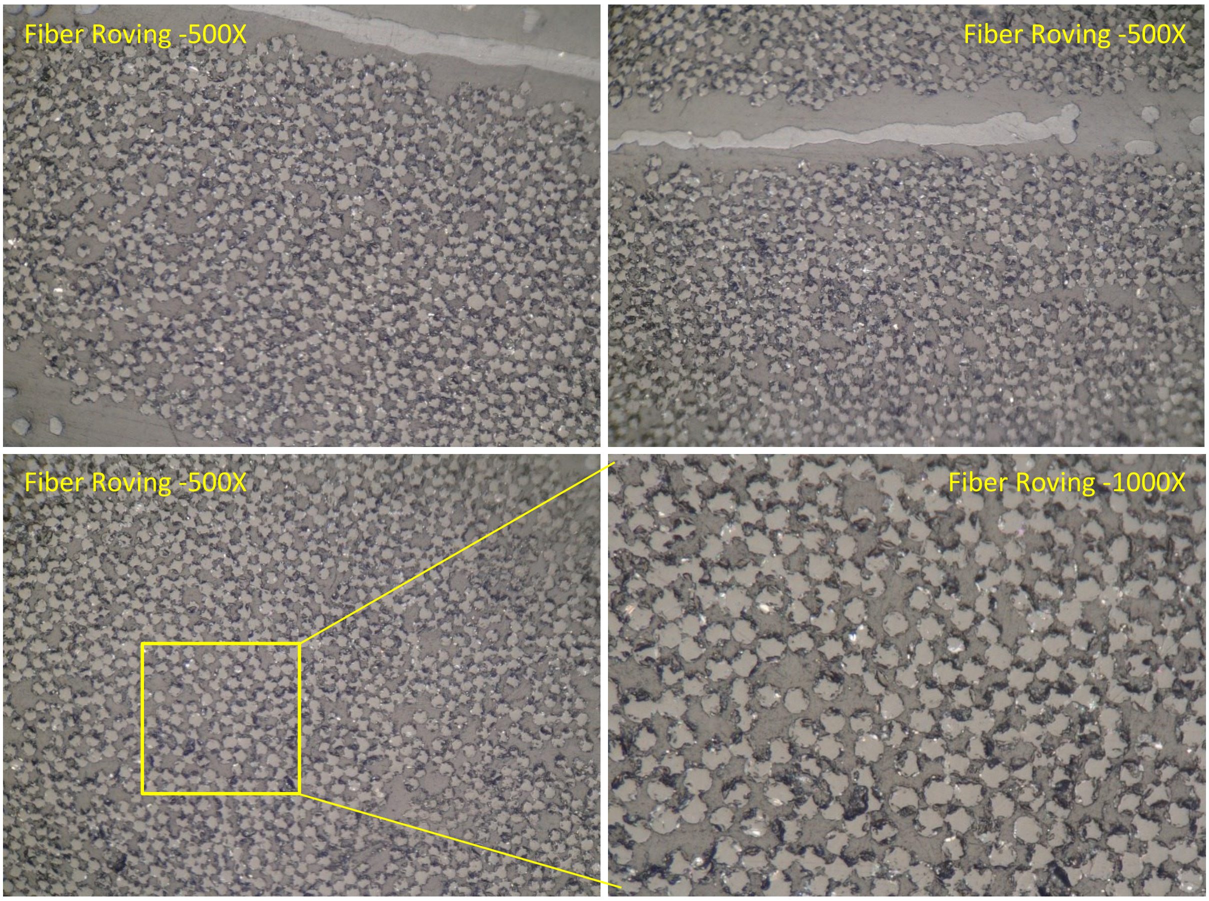

Figure 90. Images of fiber rovings (500X and 1000X)

The sample M_1, which was cut near the outlet side of the panel, does not have the quality problems that are affecting the sample M_{IN}. The surface that was in contact with the rigid side of the mold is flat, with very low roughness and without any groove. Also the opposite surface is free from voids. Considering Figure 90, it is possible to notice that the resin had completely wetted the fibers and there is total absence of micro voids.

Sample M$_2$

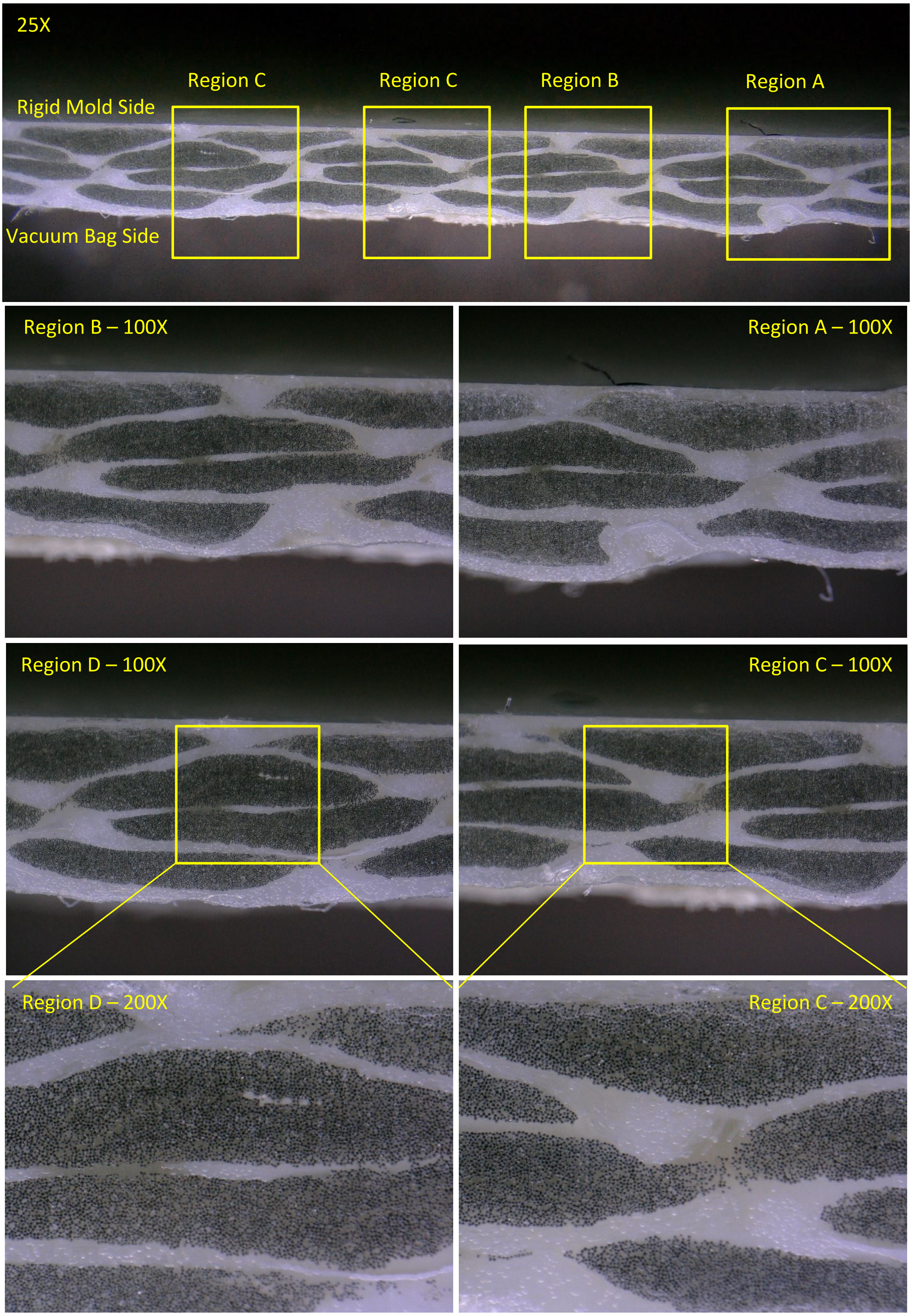

Figure 91. Sample M$_2$ cross-section images with different levels of magnification (25X, 100X and 200X).

The sample M2, similarly to the sample M1 analyzed before, does not have particular defects. The sample is free from voids inside the material or grooves on the rigid mold side surface. The only quality issue, also encountered on all the other specimens, remains the variability of the thickness caused by the undulations of the surface that was in contact with the vacuum bag.

4.4.3. DMA Test

The dynamic mechanical analysis (DMA) was used in order to find the glass transition temperature of the thermoplastic matrix and understand if the in-situ polymerization have been completed correctly.

During the test, the testing machine applies a small cyclic deformation to a specimen of known dimensions meanwhile the temperature is increased. The machine measures the stiffness and damping of the material and how they change with the variation of temperature [56].

Four specimens with dimension 60 x 10 mm were cut from two different panels, with the longer side parallel to the fibers direction. The panels considered were produced using 48 g and 50 g of resin. The testing machine applied a three-points bending deformation to the samples.

4.4.3.1. Results

The results obtained from the DMA machine are shown in the figures below. In the graphs it is represented the variation of Storage Modulus, Loss Modulus and Tan Delta with the increase of temperature.

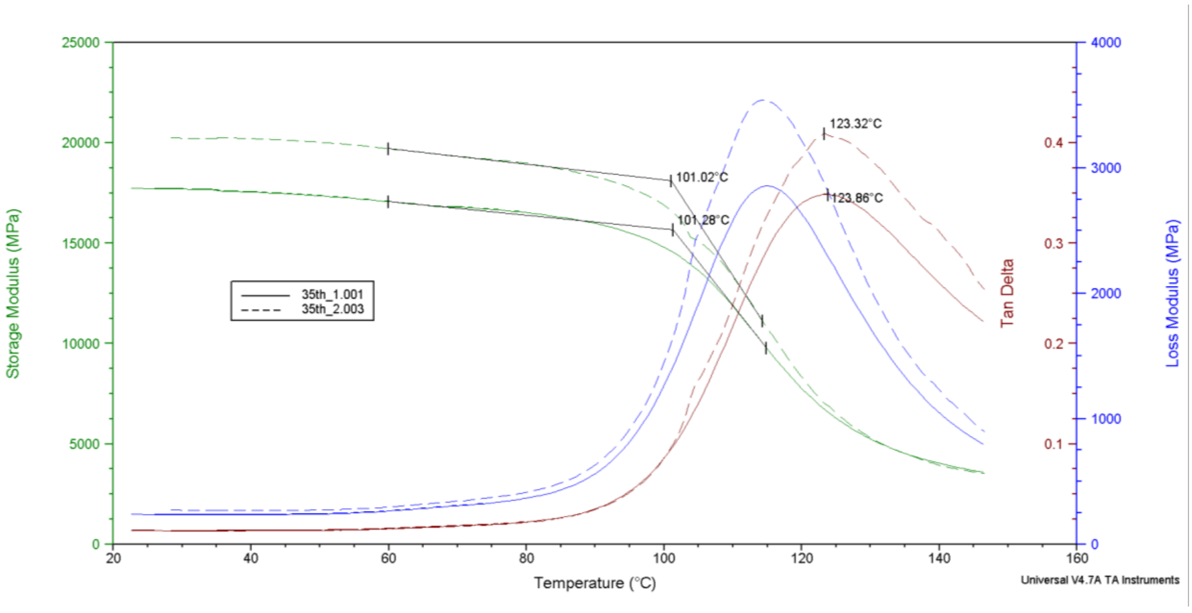

Figure 92. DMA test results of the samples cut from the panel produced using 48 g of resin.

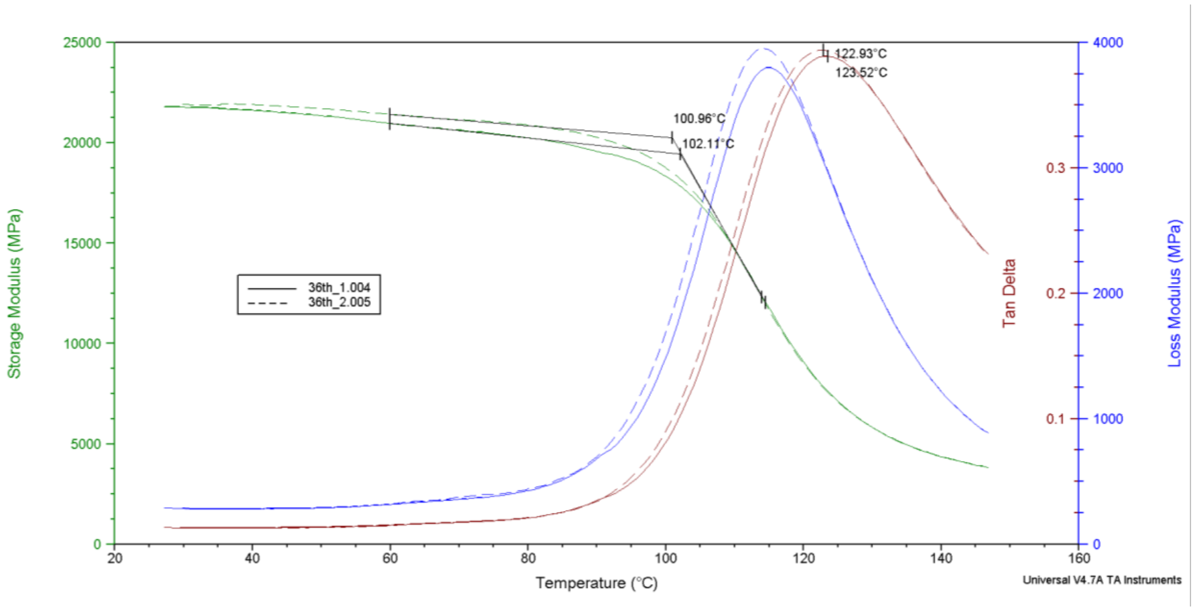

Figure 93. DMA test results of the samples cut from the panel produced using 50 g of resin.

4.4.3.2. Discussion

The glass transition temperature determined from the peak of Tan Delta was around 123 °C for all the samples. These values have been compared with the DMA glass transition temperature declared by the producer. For the Elium® resin, Arkema stated a glass transition temperature obtained from the Tan Delta peak equal to 107 °C [53]. The glass transition temperature of a thermoplastic material increases as the molecular weight increases [10]. As the polymerization proceeds, monomers connect together forming long chains and the average molecular weight of the material increases. Having a glass transition temperature equal or, as in this case, higher than that indicated by the producer, means that the polymerization was completed correctly. If the glass transition temperature were lower than the one declared by Arkema, it would have meant that there was an excessive quantity of residual monomers inside the plastic and, therefore, the polymerization was not completed successfully.

4.5. Discussion

In this chapter, the main results obtained from the manufacturing of thermoplastic GFRP panels through VARTM process will be discussed.

4.5.1. Manufacturing Process Setting Up

During the setting up of the VARTM process for manufacturing the composite panels it was confirmed that this is a low cost manufacturing method, which is the main advantage of this process. It was possible to produce GFRP components adopting a simple infusion system, composed by plastic hoses, a funnel and a vacuum pump. Moreover, the Elium® resin in monomeric form has very low viscosity and it allowed to easily produce thermoplastic components by infusion at room temperature. Finally, Elium® resin allowed to perform the polymerization at room temperature, decreasing further the cost of the entire process.

The quality of the panels depended mainly on the ability of infusing resin without air and on the resin flow speed inside the distribution mesh and preform. The first aspect can be achieved by optimizing the infusion system. In fact, the improvements performed on the infusion system layout, described in chapter 4.3, allowed to minimize the air injected in the mold and decrease the scrap of resin. If the resin flow speed in the preform is too high, the quality of the components produced can be easily affected by voids. This was noticed during the fabrication of the first panels, which were presenting many defects on the surfaces. The two factors that were affecting most the speed of the resin flow inside the mold were the vacuum pressure and the orientation of the plies fibers with respect to the flow. From Darcy's Law (Eq. 2.2), the higher is the pressure gradient ∇P, the higher will be the fluid velocity. Unfortunately, the pump utilized in this experience did not allow to regulate the vacuum level inside the mold, so it was not possible to optimize the resin flow speed acting on the pressure. Modifying the plies fibers orientation with respect to the flow allowed to interrupt the preferential paths inside the preform, created by the channels formed between the fibers rovings, and it reduced the speed of the resin. Most of the resin was distributed on the preform by the infusion mesh and it had only to penetrate through the thickness. This helped also in reducing the release agent washing effect caused by the resin that was flowing on the mold surface, decreasing the problem of the grooves on the bottom surface of the panels and improving the overall quality. The problem was still encountered in the region of the panels near the inlet. Probably, at the inlet side, the resin that was arriving in high quantity from the infusion system started flowing both inside the infusion mesh and directly through the cross-section of the preform. By flowing through the cross-section of the plies, the resin washed the release agent from the mold. Since the permeability of the plies with the fibers oriented perpendicularly to the flow is much lower than that of the infusion mesh, the flow of resin through the cross-section was considerably slower than the one inside the infusion media. For this reason, most of the panel was filled by the penetration of the resin through the thickness and the release agent washing was limited to the inlet region. Adopting a different release agent, compatible with the resin utilized, could solve the problem.

The main disadvantage of the process was the high amount of manual skills requested for preparing the infusion and setup a vacuum proof mold. Small differences in laying the plies on the mold, cutting and positioning the infusion mesh and placing the hoses could result in variation of the quality between panels, affecting negatively the process repeatability. The time required for preparing the mold for the infusion summed with the time required for completing the polymerization resulted in a total cycle time of at least 3 hours per panel. In case components bigger or with more complicated shape have to be manufactured, the time required for preparing the infusion can increase further. For this reason, this manufacturing method is suitable for low-medium production volumes, as the ones characterizing the wind energy sector, but can find difficult application for higher production volumes, as the ones required for mass produced vehicles. Nevertheless, in the automotive sector this process can be applied for manufacturing composites components for niche applications, such as race, high performance or high-end luxury cars.

4.5.2. Process Validation Tests

The quality of the panels was investigated in order to validate the process. Three different tests were performed. The first test was the acid digestion of the matrix, that was conducted for finding the fiber volume fraction of the panels and understand which was the right amount of resin needed to achieve the target of $V_f = 60\ \%$. The results showed that the lowest quantity of resin employed to manufacture the panels, equal to 46 g, allowed to obtain only $V_f \cong 52\ \%$. This would mean that a lower quantity of resin should be adopted for increasing the fiber volume fraction. However, it is important to underline that the results of the void content obtained from the computations were excessively high, all between 20 and 30 %. Considering that in case of high performance applications the tolerable void content is lower than 1 %, while for common applications the tolerable content should not overcome 5 % [57], it was likely that an error during the test was committed. The results from the optical microscopy analysis were useful to solve this question. In fact, the images of the microstructure of the samples cut from the same panels used for the acid digestion test showed that the resin have completely wetted the fiber rovings. Some of the samples cut near the inlet side presented some small voids inside the matrix, while some other samples cut near the outlet had some rare and small voids on the upper surface. However, the quality of the samples was much higher than the one that should have been discovered in case of an effective void content around 30 %. For this reason, the results obtained from the acid digestion test were assumed wrong. One error that could have been committed in the test procedure was the method employed for calculating the volume of the samples. For the computation, an average value of the thickness was assumed but, as it is possible to see in the microscope images of the sample cross-section (Section 4.4.2), the thickness had a high variability. Measuring directly the volume, for example by immersion, in order to obtain a more precise value would have been more correct. The value of the volume affects both the void content and the fiber volume fraction. For example, by reducing the volume of 5 %, the fiber volume fraction increases of about 5 % while the void content decreases of about 13 %. Another possible factor that could have affected the results was that during the computations of void content and fiber volume fraction, only fibers and matrix were considered as materials composing the sample. However, as it is possible to observe in the microscope images, some regions of the cross-section were occupied by the veil covering the plies and by the stitching yarns, which can have different densities with respect to fibers and matrix. Therefore, these regions with different densities could have increased the resulting value of void content.

The results from the optical microscope analysis showed that there was a discrepancy in the quality between the inlet side and outlet side of the panels. The samples cut near the inlet side had more voids inside the material and more surface defects. The samples cut in the middle or near the outlet side were free from voids inside the matrix and some of them presented few voids on the surface on which the infusion mesh was placed. A possible explanation of this phenomenon was that the resin was not subjected to degassing after having been poured inside the mixing container. Micro voids can be created due to entrapment of air during resin mixing operations [57]. During the pouring operation in fact, some small air bubbles were forming inside the resin that subsequently was mixed with the catalyst and transferred inside the funnel. Despite the fact that some minutes were waited before of starting the infusion, exactly with the purpose of allowing the small bubbles of air to reach the surface of the liquid, some air could have remained trapped inside the resin and injected in the mold. These small bubbles of air, transported with the resin by the infusion mesh, could have caused the small voids on the upper surface of the panel. Moreover, since at the inlet side the resin was probably penetrating through the cross-section of the preform, some air bubbles could have created the small matrix voids between the fiber rovings that were observed only in the samples cut near the inlet side. Degassing the resin prior to the mixing operation could improve the quality of the panels. Another possible aspect that may have affected the void content inside the panels could have been the speed of the resin flow that, despite the improvements applied, was still fast. As it was reported previously, one of the main factors that influences most the resin flow speed is the pressure gradient. Kedari et al. [58] studied the effect of the vacuum pressure, the inlet pressure and the mold temperature on the void content and fiber volume fraction of polyester resin GFRP panels manufactured with VARTM process. In the study emerged how, by using strong vacuum level for increasing the preform compaction and high mold temperature (30 °C) for decreasing the viscosity of the resin, it was possible to obtain high fiber volume fraction inside the panels. However, with these process parameters, the void content was higher. In order to decrease the void content it was discovered that the inlet pressure had to be decreased, so that the pressure gradient was reduced and the resin flow slowed down according to the Darcy’s Law. The matrix material employed in the study was polyester resin, which at 30 °C had a viscosity of 0.3 Pa·s. The Elium® resin has a viscosity of 0.1 Pa·s at room temperature, so the situation can be similar to the one described in Kedari’s study. Therefore, decreasing the pressure gradient by decreasing the vacuum level inside the mold or decreasing the pressure at the inlet could be a solution for the problem.

The upper surface of the panels had many undulations, corresponding to the profile of the fiber rovings. This caused a continuous variation of the panel thickness. The lower quality of the surface in contact with the vacuum bag is an intrinsic disadvantage of the VARTM process. Nevertheless, it is possible that the high vacuum pressure employed may have caused an excessive compression of the vacuum bag on the fabric layers, which could have caused greater surface roughness and undulations. Therefore, decreasing the vacuum pressure could improve also the surface quality of the panels. Despite these issues, the overall quality of the panels from the microstructural point of view was good. The resin had clearly wetted the preform, penetrating inside the rovings and surrounding each single fiber.

The last test performed was the DMA. From this test emerged that the polymerization of the Elium® resin was completed correctly, since the glass transition temperature of the material was higher than the minimum declared by the producer of the resin.

5. Ply Crack Growth in GFRP Composites

In this chapter the numerical characterization of the growth of intra-laminar ply cracks in GFRP laminated tubular specimens subjected to combined transverse compression and shear stresses is described. This multiaxial state of stress is relevant in the fatigue loading of wind turbine blades, since one of the most common failure modes of the blades is due to a combination of transverse matrix compression and shear stresses [59]. In fact, wind turbine blades are laminated composites subjected to bending caused by the aerodynamic load that, due to the coupling phenomena of laminates, generates a combined compression-shear stress state in the plies of one side.

The computational study was based on previous experimental work performed by McLeave [19], and had the objective of integrating the existing experimental results with the computational study of the material microscopic fracture behavior. In the study performed by McLeave, the evolution of ply cracks in E-glass/epoxy plies subjected to multiaxial loading was investigated. GFRP tubular laminates with layup $[0_F/90]_S$ were manufactured and tested under combined cyclic transverse compression and shear stresses. The multiaxial stress state in the 90° ply of the tubular specimen was obtained by applying axial compressive and torsion loads through a testing machine. The specimens were subjected to compression-compression fatigue cycles. The tests were performed by imposing different minimum transverse compressive stress and shear stresses in the 90° ply, in order to investigate how these factors affected the evolution of ply cracks. The tubular specimens presented a single dominant ply crack in the 90° plies inclined at about 55° with respect to the horizontal plane, which propagated with increasing cycles along the circumferential direction of the tube. A schematic of the crack encountered in the tubular specimen is shown in Figure 94. This kind of crack is characteristic of transverse compressive failures, where a distinct inclined fracture plane is observed.

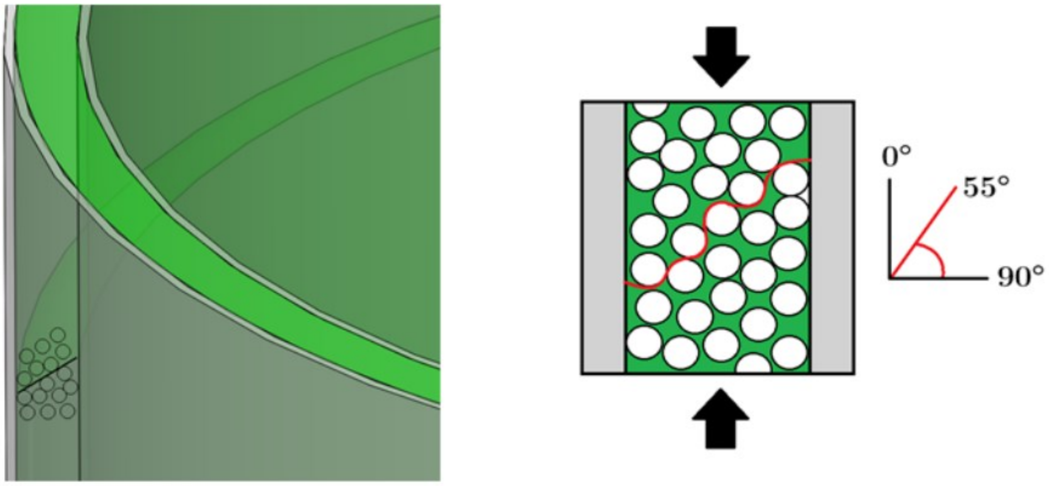

Figure 94. Schematic representation of the circumferential propagation of transverse compressive cracks in the tubes [19].

In the current work, the fracture behavior encountered in the experimental tests was modelled using the commercial finite element software Abaqus CAE. The propagation of the ply crack was simulated, with the objective of studying the corresponding strain energy release rate (SERR).

5.1. Energy Release Rate

Before describing the numerical model, it is necessary to briefly introduce some concepts of the fracture mechanics theory that are useful for understanding the computational work explained afterwards.

When a crack initiates inside a solid material, a discontinuity inside the material is formed. The crack will be characterized by two surfaces, separated from the uncracked region of the material by the crack front [60]. Considering the arbitrarily shaped three dimensional crack represented in Figure 95, at any point along the crack line a local coordinate system can be defined. The local coordinate system can be oriented with the x_1 axis orthogonal to the crack front, the x_2 axis perpendicular to the crack surface and the x_3 axis tangential to the crack front.

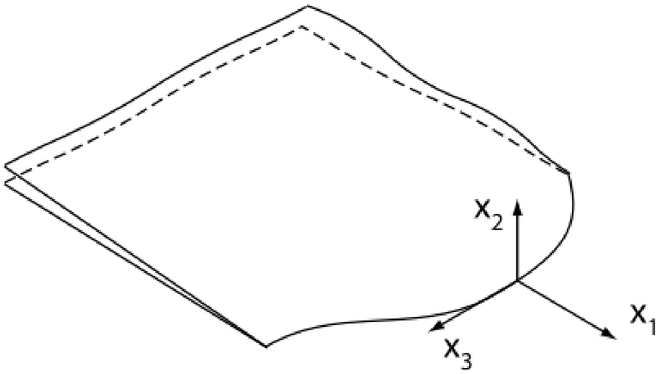

Figure 95. Schematic of a 3D crack in a solid material with the local reference system defined along the crack line [60].

At the crack tip, the stress field can be decomposed into three components that can act to drive crack propagation based on three crack surface displacement modes, namely Mode I, Mode II and Mode III [60]. Mode I, also called opening mode, causes the crack to open orthogonally to the local fracture surface under the effect of forces with direction along the x_2 axis. Mode II, called sliding mode, causes a relative sliding between the crack surfaces in the x_1 direction. Finally, Mode III, also called tearing mode, causes the crack surfaces to slide relative to each other in the x_3 direction. The three fracture modes are shown schematically in Figure 96.

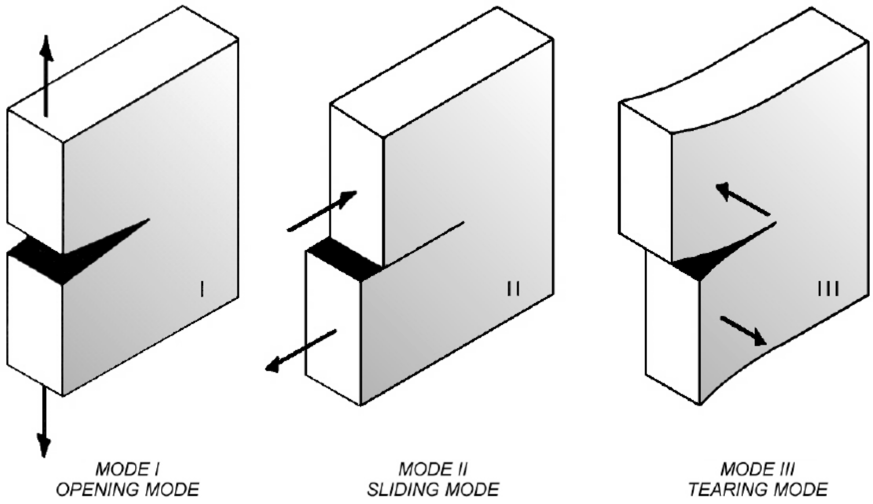

Figure 96. The three modes of crack surface displacement [61].

In order to propagate a crack, energy has to be supplied to the crack tip. The energy flows to the crack tip through the elasticity of the body and then it is dissipated in the form of irreversible deformation, heat, sound and surface energy. The energy release rate, indicated as G, is defined as the energy dissipated during the fracture propagation per unit of new fracture surface area ds [60]. It is possible to demonstrate that the energy release rate can be mathematically defined as the change of potential energy per unit crack area:

$$G \equiv -\frac{\partial \Pi}{\partial s} \tag{5.1}$$

where Π is the total potential energy.

The energy release rate of a fracture that is propagating can be computed with several different methods, both analytical and computational. Computational methods such as FEM analysis allow to study fracture of real problems and, therefore, they are tools of extreme importance. One of the most utilized computational method is the Virtual Crack Closure Technique (VCCT), that was first introduced by Rybicki and Kanninen [49] for two-dimensional problems and later adapted for three-dimensional problems by Shivakumar et al. [50]. The method is based on the Irwin's Crack Closure Integral and therefore is also called Modified Crack Closure Integral (MCCI). According to Irwin, the change of total potential energy is equal to the energy released during the crack propagation [60]. Irwin's assumption states that the energy released during a small crack extension is equal to the work required to close the crack to its original length [49]. The VCCT method then makes the further assumption that when a crack extends of a small amount, the state at the crack tip is not significantly altered. Observing the schematic 2D model of a meshed crack shown in Figure 97, the meaning of the previous assumption is that, when the crack extends of Δa and the crack tip that moves from the node j to the node j+1, the displacements at node j are approximately equal to the displacements at node j-1 when the crack tip was located at node j [60]. In this configuration, the work required to close the crack between the nodes j and j-1 is equal to:

$$\Delta E = \frac{1}{2} \boldsymbol{F}^{j^T} \Delta \boldsymbol{u}^{j-1} \tag{5.2}$$

where $\boldsymbol{F}^j$ is the vector of nodal forces at node j and $\Delta \boldsymbol{u}^{j-1}$ is the vector of distances between the crack surfaces at node j-1. Thanks to the assumptions of the VCCT method, it is possible to compute the SERR for the three fracture modes by dividing the energy obtained from 5.2 by the area of crack increment Δa as:

$$G_I = \frac{1}{2\Delta a} {F_2}^j \Delta {u_2}^{j-1}$$

$$G_{II} = \frac{1}{2\Delta a} {F_1}^j \Delta {u_1}^{j-1} \tag{5.3}$$

$$G_{III} = \frac{1}{2\Delta a} {F_3}^j \Delta {u_3}^{j-1}$$

where the subscripts of the nodal forces and displacements are given according to a reference system positioned at the crack tip and oriented as shown in Figure 95. The relative displacement between the nodes on the crack surface is equal to $\Delta u_i = {u_i}^{(+)} - {u_i}^{(-)}$, where ${u_i}^{(+)}$ is the absolute displacement of the node on the upper crack surface and ${u_i}^{(-)}$ is the absolute displacement of the node on the lower crack surface.

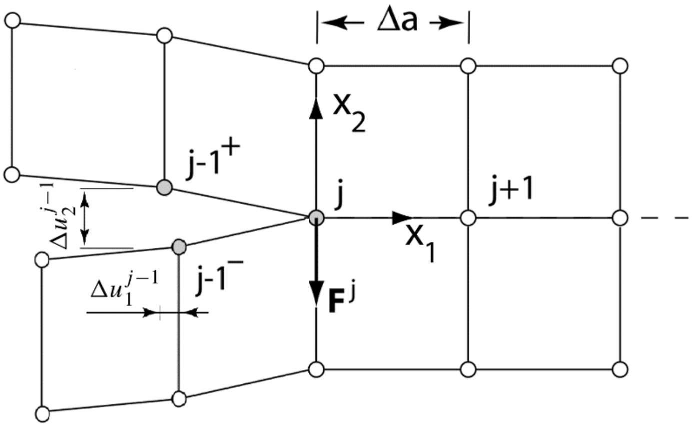

Figure 97.Schematic of VCCT procedure for computing the SERR [60].

5.1.1. Manual VCCT Method

A computational method based on VCCT for finding the SERR of tubular laminate specimen subjected to multiaxial state of stress was presented by Quaresimin and Carraro [44]. $[0_F/90_{U,3}/0_F]$ layup tubular laminates were tested experimentally and subjected to cyclic traction and torsion stresses and Mode I and Mode II SERR were computed from the FE model. The tubes were modelled using 360 elements along the circumference and 8 through the thickness. Only one half of the tube was modelled, since the crack was symmetric. The uncracked region was simulated by constraining the nodes axial and tangential displacements, while the crack was simulated by a non-constrained area on the 90° plies.

According to the definition, Mode I and Mode II SERR were equal to:

$$G_I = \frac{dU_\sigma}{d(2A)}$$

$$G_{II} = \frac{dU_\tau}{d(2A)} \qquad (5.4)$$

Here, the subscript σ refers to the traction loading condition, τ refers to the torsion one and $2A$ is the total area of the crack. U is the energy released during crack propagation, equal to:

$$U_\sigma = \frac{1}{2}\int_{2A} \sigma_2 \cdot \Delta u \cdot d(2A)$$

$$U_\tau = \frac{1}{2}\int_{2A} \sigma_6 \cdot \Delta v \cdot d(2A) \qquad (5.5)$$

where σ_2 and σ_6 are the transverse and the in-plane shear stresses acting on the 90° plies in the uncracked condition. Δu and Δv are the relative transverse and tangential displacements between the two surfaces of the crack. Since the tubular specimen was thin, the stresses before crack nucleation varied slightly through the thickness of the 90° ply and therefore they were considered constant and equal to their average value. With this assumption, the stress was removed from the integrals of Eq. 5.5, which became:

$$U_\sigma = \frac{1}{2}\sigma_{2_{avg}} \int_{2A} \Delta u \cdot d(2A) = \sigma_{2_{avg}} \cdot \Delta u_{avg} \cdot A$$

$$U_\tau = \frac{1}{2}\sigma_{6_{avg}} \int_{2A} \Delta v \cdot d(2A) = \sigma_{6_{avg}} \cdot \Delta v_{avg} \cdot A \qquad (5.6)$$

The average stresses were determined from the FE model of the uncracked specimen, while the average displacements were evaluated by changing the crack extension. The crack was manually extended by removing the constraints from the nodes on the crack surface and the nodal displacements were obtained from the FE simulation and averaged over the entire crack area. Finally, the SERR was computed with the Eq. 5.4. G_I and G_{II} were evaluated with maximum applied tension and shear stresses equal to 1 MPa. Since the system was supposed to behave in linear elastic way, it was possible to obtain the SERR for every value of nominal transverse and shear stress by multiplying the results obtained from 1 MPa by the square of the applied stress [44].

This method was adopted in the current project for computing the Mode II and Mode III SERR related to the crack initiation and propagation in the tubular specimen subjected to cyclic compressive and torsion stresses. Nevertheless, as it will be described carefully in the following chapters, the FE model and the formulas had to be adapted in order to take into account that the multiaxial state of stress was caused by compression and torsion and not traction and torsion as it was in the Quaresimin and Carraro's work.

5.2. FE Model

The computational work was developed using the commercial finite element software Abaqus CAE. The model was completely created within the Abaqus CAE environment and its definition was done carefully in order to replicate as close as possible the experimental conditions.

5.2.1. Parts Definition

The tubular laminates used in the experimental tests were manufactured with two hoop-wound E-glass fibers/epoxy unidirectional plies supported internally and externally by thin woven glass fabric plies [19]. The resulting layup was $[0_F/90]_S$. The internal and external fabric plies were adopted in order to constrain the cracking inside the 90° plies during cyclic loading, so that the propagation of cracks could be studied. The tubes length was 100 mm, with gauge length equal to 50 mm and two 25 mm areas for end tabs. The nominal inner radius of each tube was 9.5 mm, while the nominal outer radius was 10.23 mm.

The tubular specimens were modelled using different parts representing the plies, and were assembled together adopting the suitable boundary conditions, described in order to make them behave as a single component. The composites plies were modelled as effectively homogeneous orthotropic materials. The asymmetric 90° ply crack surfaces were explicitly accounted for, thus both the upper and lower halves of the tubes were modelled. The parts created for defining the tubes model were:

- Upper and lower halves of the unidirectional plies layer;
- Upper and lower halves of the external woven fabric ply;
- Upper and lower halves of the internal woven fabric layer.

Unidirectional plies

The upper and lower halves of the unidirectional 90° plies were created with the bottom and top surfaces inclined of 55° with respect to the horizontal plane, as it is show in Figure 98. The two surfaces were representing the upper and lower crack surfaces obtained from the experimental tests. Only one layer was created taking into account the presence of two 90° plies. Since the plies were assumed to deform in a linear elastic manner, only a 9 mm long portion of the tubes were modelled. In this way, it was possible to reduce the computational effort required from the simulations. The dimensions of the 90° upper and lower halves were:

- Outer radius $Re = 10.13\ mm$
- Inner radius $Ri = 9.60\ mm$
- Height $h = 5\ mm$

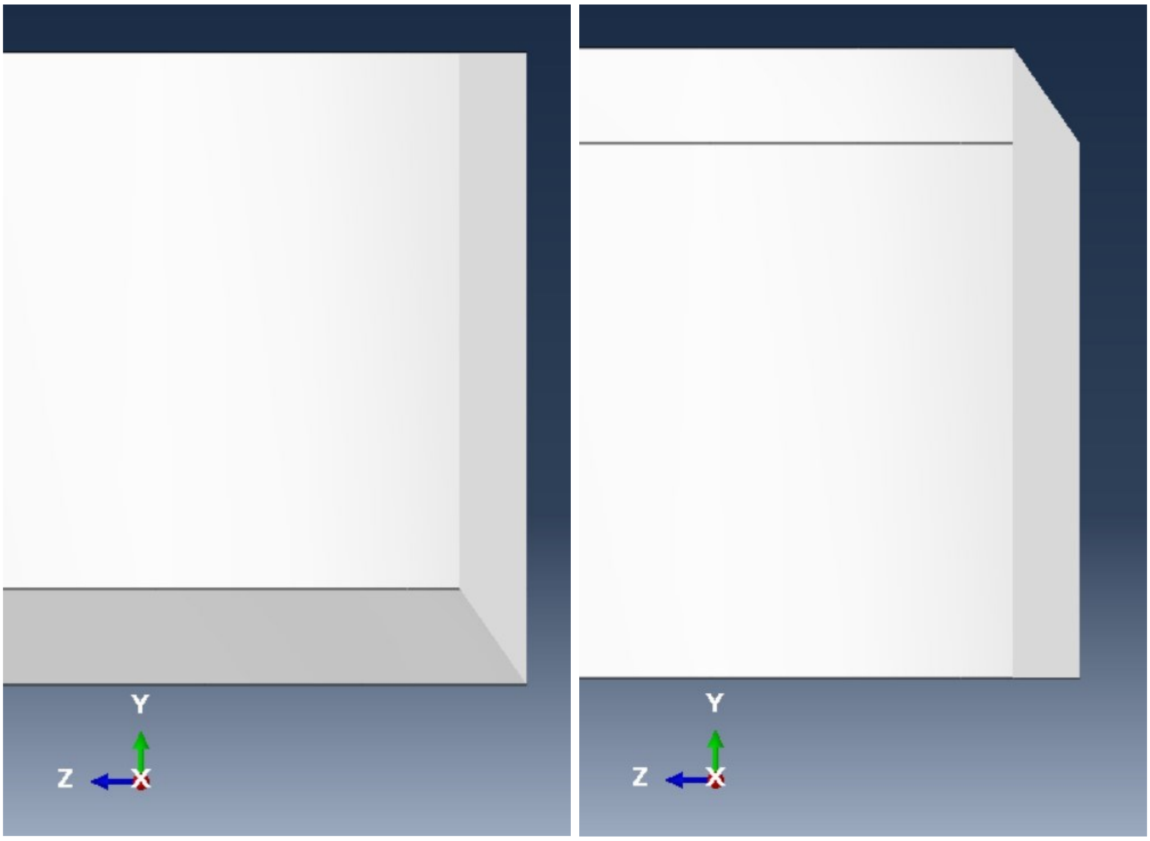

Figure 98. Upper (left image) and lower (right image) halves of the unidirectional layers. It is possible to notice the inclined surfaces defined for modelling the crack surface.

Woven fabric plies

The internal and external woven fabric plies were modelled as thin cylinders with thickness equal to 0.1 mm. Four cylinders were created, two for the internal ply and two for the external one. The height of the cylinders was assigned in order to match the height of the internal and external surfaces of the unidirectional layers.

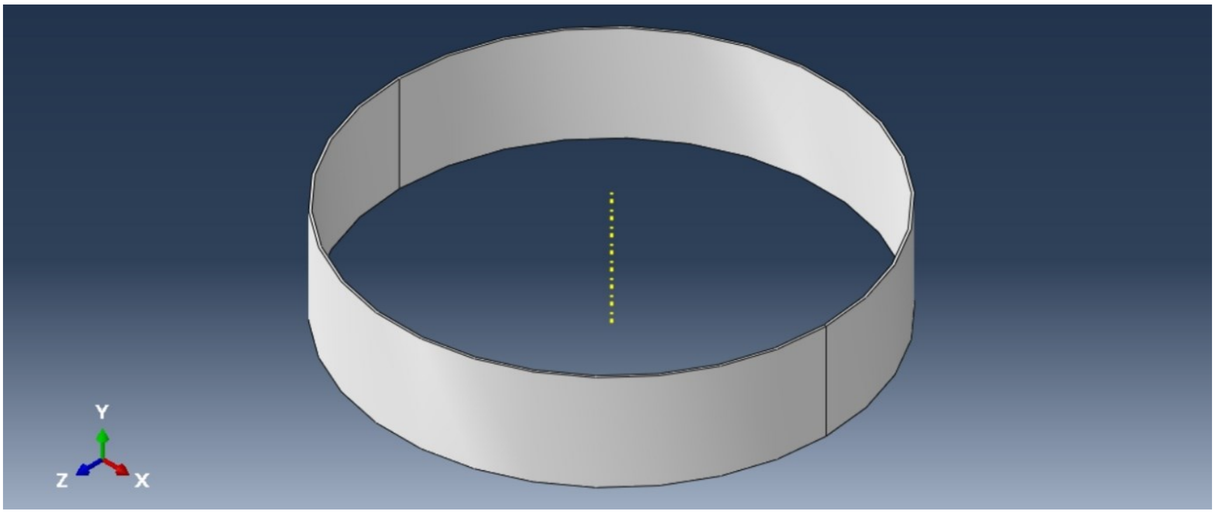

Figure 99. Example of cylinder used for modelling the internal and external woven plies.

Assembly

The various parts were assembled together in the *Assembly Module* of Abaqus in order to build the tubular specimen. The parts were still free to move the one with respect to the others, since no constraints were applied up to now.

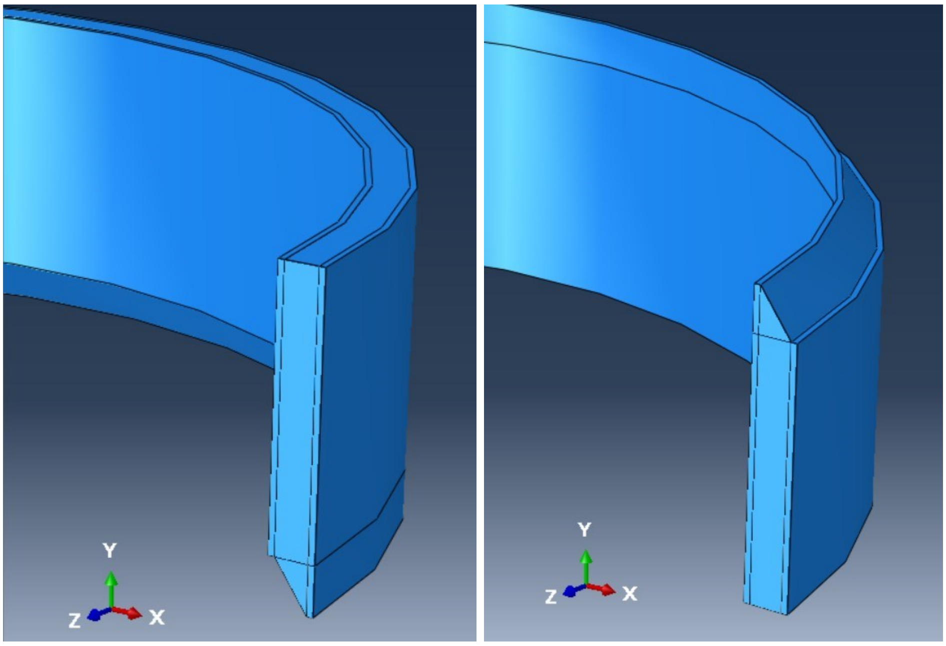

Figure 100. Upper (left image) and lower (right image) halves of the tubular specimen.

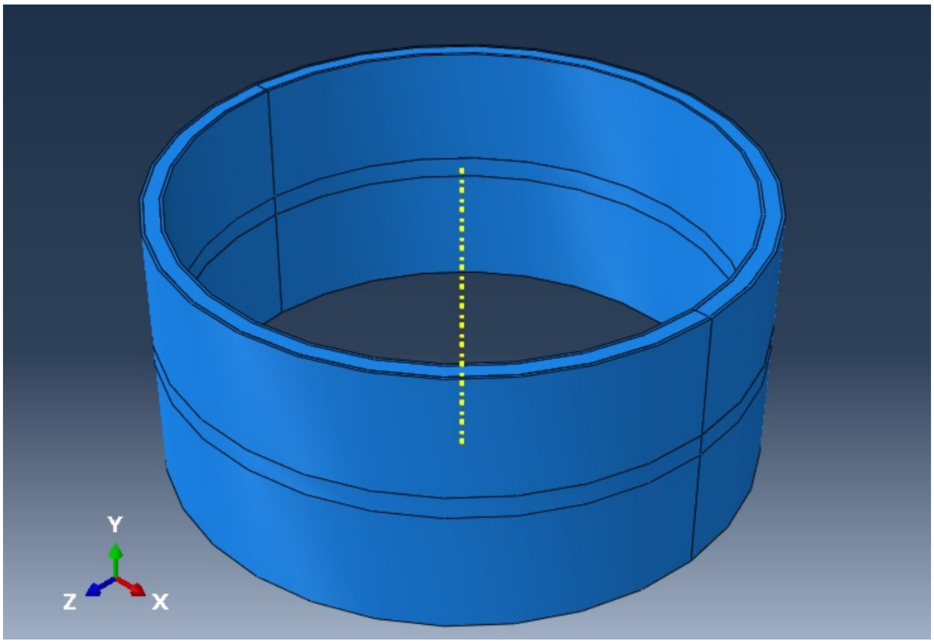

Figure 101. Tubular specimen obtained from the assembly of the various parts.

5.2.2. Mesh

The following step was meshing the parts defining the tubular specimens. The parts were meshed using quadratic elements, which allow to obtain more accurate results but require a higher computational effort.

Unidirectional layer

The unidirectional layers were created with an inclined surface that made impossible to obtain regular shaped elements by using only hexagonal elements in all the volume. For this reason, a partition was created inside the layers. The partition created two regions inside the parts that were meshed separately:

- Regular cylindrical region. It was meshed using hexagonal quadratic C3D20R elements;
- Ring with triangular section. It was meshed using wedge quadratic C3D15H elements.

The seed assigned to the cylindrical region, meshed with hexagonal elements, made use of 6 element divisions through the thickness of the layer and 360 element divisions along the circumference. Biased seed was assigned along the height, with quadratic increase of the elements size that was changing from 0.00013 near the crack surface to 0.001 far from it. This was done in order to have a very fine mesh near the crack surface and a coarser mesh distant from it, which allows to obtain accurate results while reducing the computational effort required. The wedge elements region were meshed assigning 6 elements along the sides of the triangle. The mesh seed can be observed in Figure 102, while the upper unidirectional layer is represented in Figure 103.

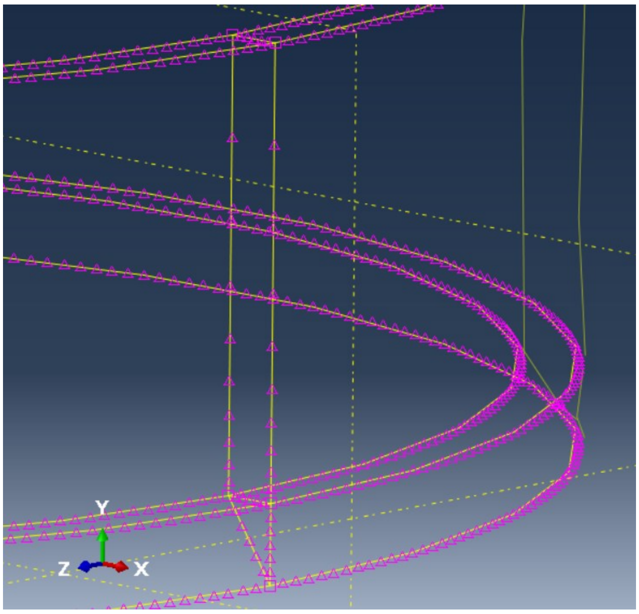

Figure 102. Seed applied on the upper unidirectional layer.

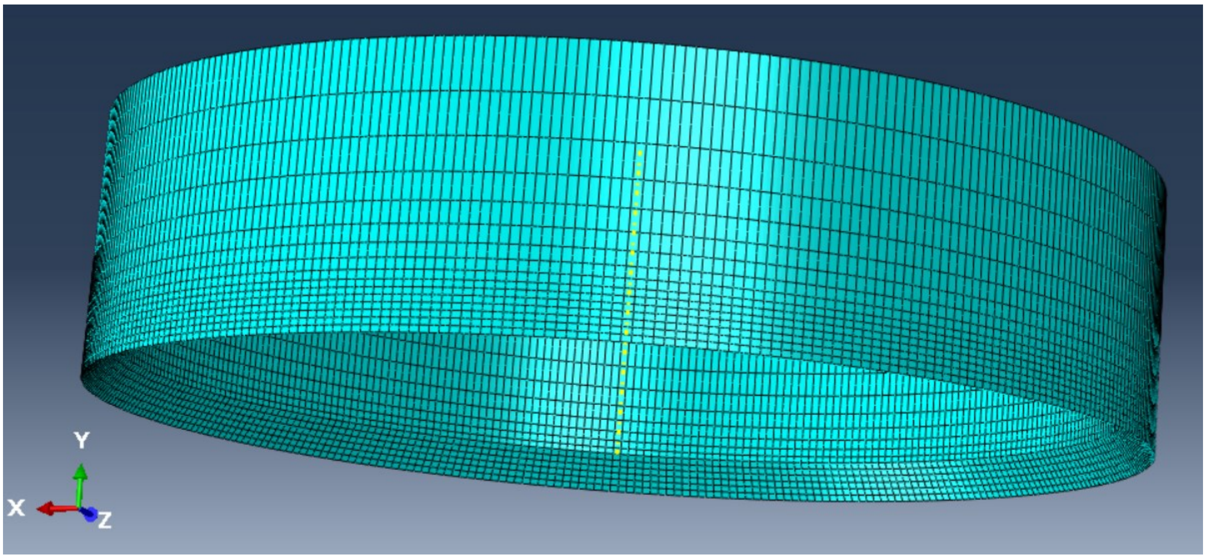

Figure 103. Upper unidirectional layer meshed.

Woven fabric layers

The four woven fabric layers were meshed adopting 1 element on the thickness and 360 element divisions along the circumference. A biased seed equal to that of the unidirectional layers was assigned to the height of the parts, with quadratic increase of the element size from 0.00013 near the crack to 0.001 far from it. The mesh was assigned so that the nodes of the surfaces of the woven layers and unidirectional layers that were in reciprocal contact were coincident.

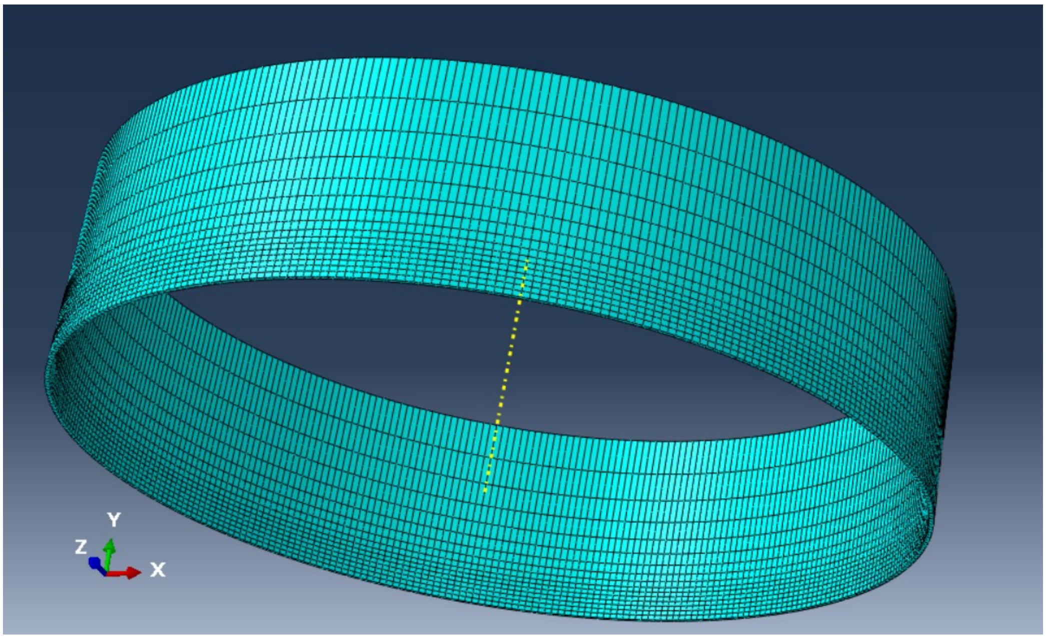

Figure 104. External upper woven layer meshed.

5.2.3. Parts Merging

Even if the tubes were formed by four different plies, after the curing of the epoxy resin a single component was obtained. The same behavior had to be replicated in the FE model. In order to obtain this, the command *Merge* was used in the *Assembly Module*. This command allowed to merge together the nodes of the unidirectional and woven fabric plies surfaces that were in contact. Merging the coincident nodes of two different parts means substituting the nodes with only one node, belonging to both the elements. In this way, two different parts can behave as if they were a single body, while maintaining the possibility of having different properties assigned. After having merged the layers, two different new meshed parts were created, one for the upper half and one for the lower half of the tubular specimen.

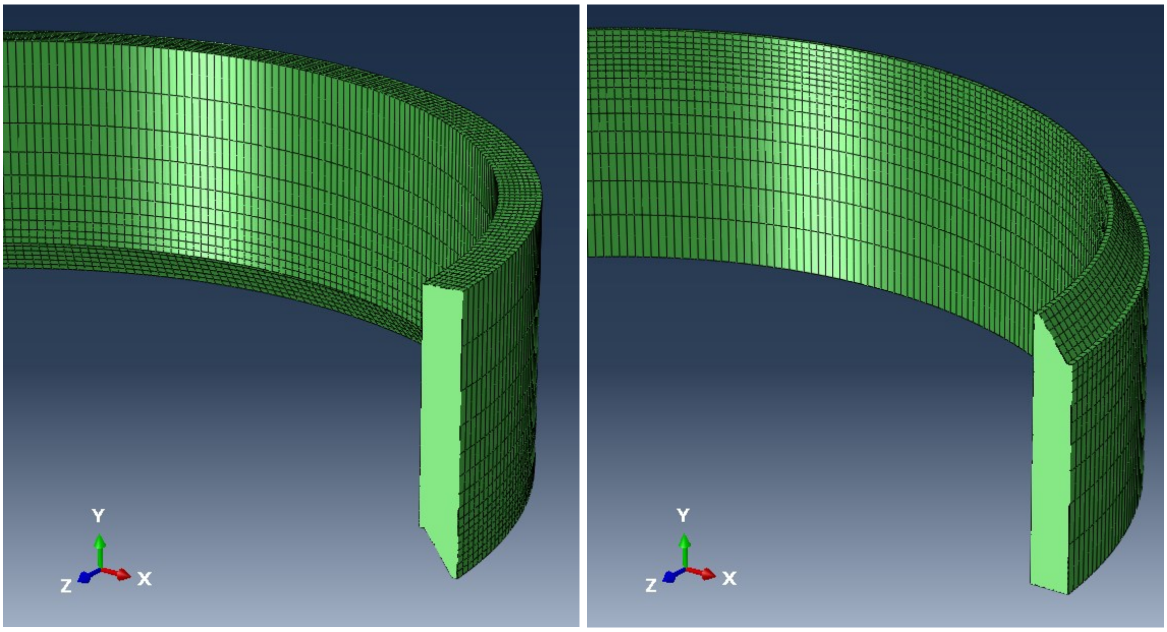

Figure 105. New meshed parts obtained from merging the nodes of the unidirectional and woven fabric layers.

In order to obtain a single tube, also the upper and lower halves obtained from the merging operation had to be united together. Nevertheless, the technique of merging the nodes could not be adopted, otherwise the inclined fracture surfaces would have disappeared. Hence, a different method had to be used. In the *Interaction Module*, *Tie Constraints* were employed for connecting the nodes of the crack surfaces. Tie constraints are a special boundary condition that forces adjacent nodes to have the same translational and rotational displacements, making them behave as if they were a single node.

To apply this boundary condition, three sets of nodes were created on the surfaces that were in contact:

- External woven fabric layers surfaces nodes;
- Internal woven fabric layers surfaces nodes;
- Unidirectional layers surfaces nodes.

Since the woven fabric plies were not subjected to cracks, they had to be completely connected in all the simulations. For this reason, the sets of nodes used for defining the tie constraints for the internal and external woven fabric layers were including all the nodes along the circumference. Crack initiation and propagation had to be simulated on the unidirectional layers. This was carried out by defining a set of nodes on the inclined surfaces on which tie constraints were applied. The set of nodes was initially including all the surfaces nodes along the circumference for simulating an uncracked specimen and obtaining the stresses needed for the computation. Subsequently, the set of nodes was progressively reduced in dimensions by removing one radial row of nodes for each simulation performed in order to reproduce the crack propagation. In this way, the tie constraints were applied only on the nodes representing the uncracked region of the tubular specimen, while the nodes excluded from the set were let free to move with respect to each other for simulating the crack surfaces. The tie constraints applied on the set of nodes can be observed in Figure 106. On Figure 107 is given an example of how the crack was propagating by progressively excluding rows of nodes from the set.

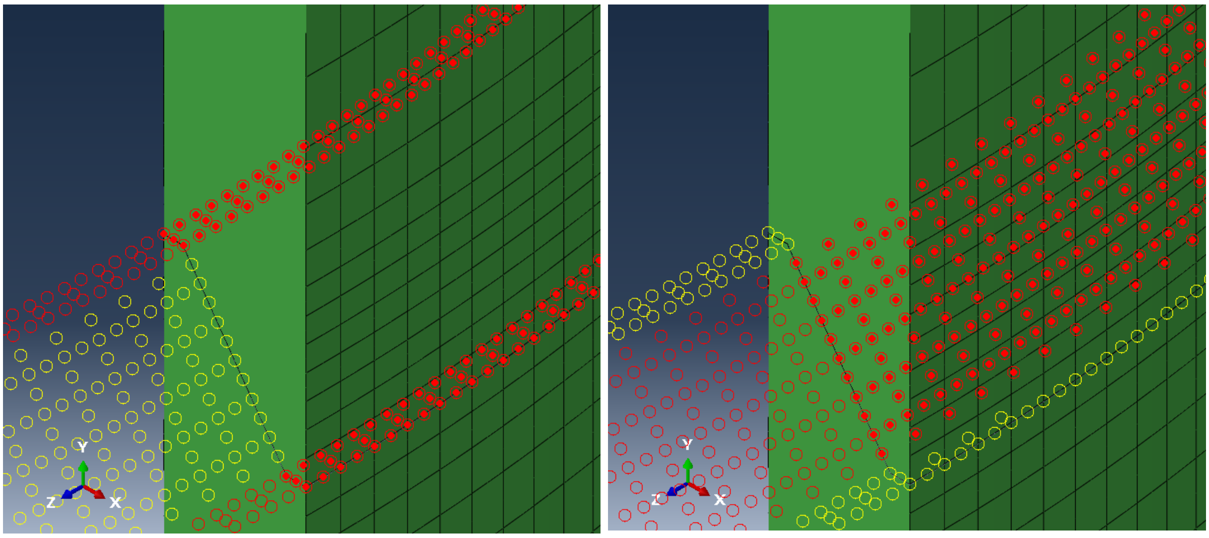

Figure 106. Set of nodes utilized for applying the tie constraints of the woven fabric layers (left image) and unidirectional layers (right image).

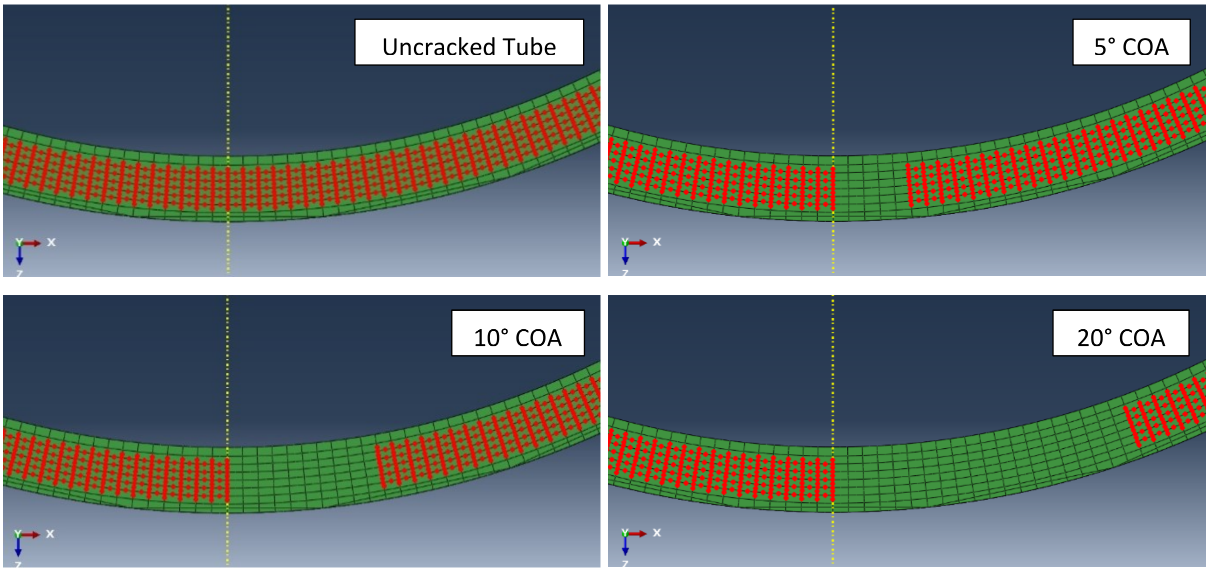

Figure 107. The crack surfaces were simulated by unconstrained regions (regions of nodes excluded from the tie constraint). The crack was expanded by removing radial row of nodes from the set. In the example, it is possible to observe the set of nodes for the uncracked specimen and for increasing crack opening angles (COA).

5.2.4. Material Properties Definition

The composites properties were simulated using homogeneous orthotropic materials for the different plies. The properties of the unidirectional fibers GFRP plies and of the woven glass fabric plies were defined and assigned to the respective layers.

Unidirectional layer

The properties of the transversely isotropic unidirectional 90° GFRP plies were taken from the study by McCleave [19] and are summarized in Table 5.

E_1	43.61 GPa
E_2	15.43 GPa
E_3	15.43 GPa
G_{12}	4.92 GPa
G_{13}	4.92 GPa
G_{23}	5.51 GPa
v_{12}	0.323
v_{13}	0.323
v_{23}	0.4

Table 5. Elastic properties of the unidirectional GFRP plies [19].

The 90° ply was oriented such that the fibers were aligned with the tube circumferential direction. For assigning the orientation, a local cylindrical reference frame was created (fiber direction 1) as shown in Figure 108.

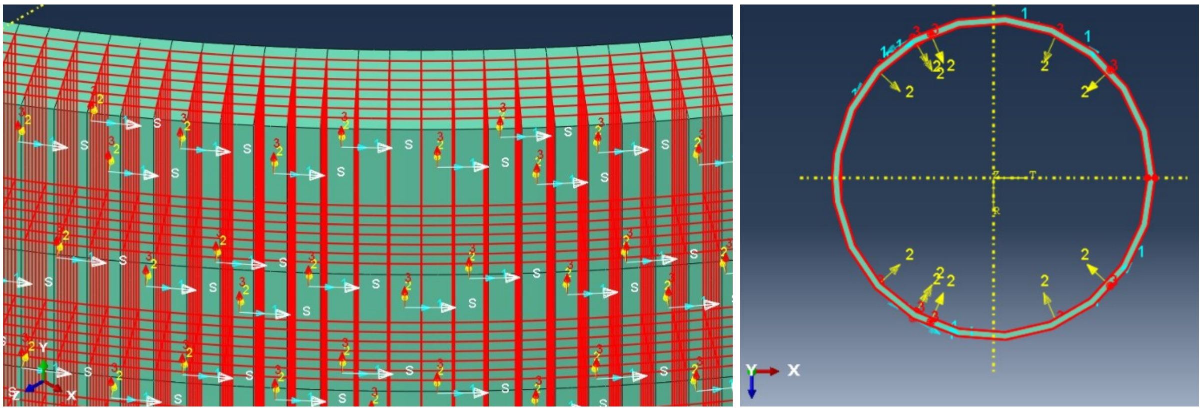

Figure 108. Orientation of the material properties in the unidirectional plies.

Woven fabric layers

The material properties of the woven fabric plies were also taken from the study by McCleave [19]. The material elastic properties are collected in Table 6.

E_1	17.03 GPa
E_2	16.54 GPa
E_3	8.20 GPa
G_{12}	3.03 GPa
G_{13}	3.03 GPa
G_{23}	3.03 GPa
v_{12}	0.159
v_{13}	0.159
v_{23}	0.159

Table 6. Elastic properties of the woven fabric GFRP plies [19].

The material properties were assigned to the internal and external woven fabric layers of the merged parts. The properties were oriented adopting the same cylindrical reference system defined for the orientation of the unidirectional layer. The orientation can be observed in Figure 109.

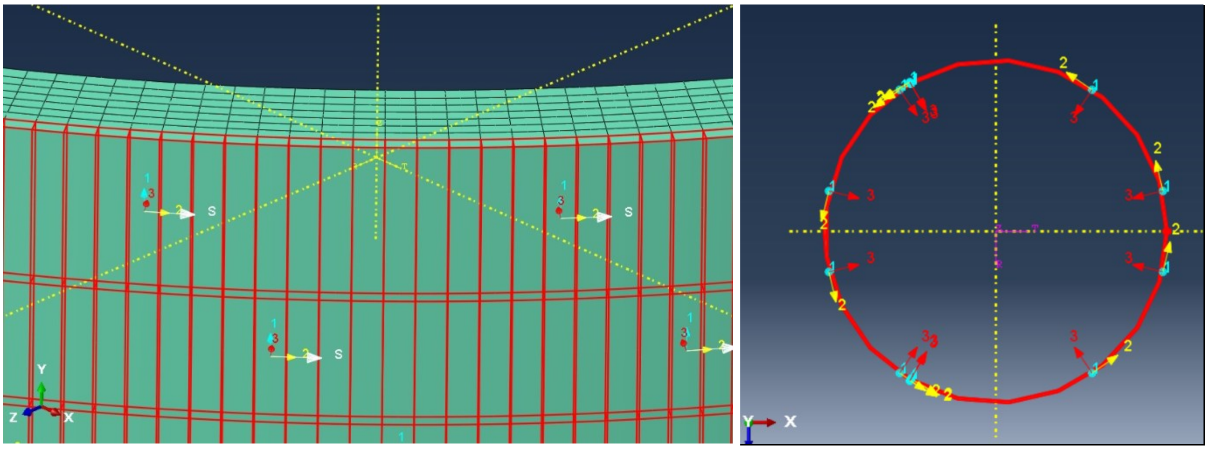

Figure 109. Orientation of the material properties in the woven fabric plies.

5.2.5. Boundary Conditions

The boundary conditions were applied to the tubular specimen model in order to replicate as close as possible the loading conditions imparted by the gripping fixtures during the experimental tests.

The lower part of the tube was clamped by a cylindrical testing fixture, therefore the tangential and transversal displacements of the tube in the model were constrained. The displacements constraints, shown in Figure 110, were assigned with respect to the local cylindrical reference frame.

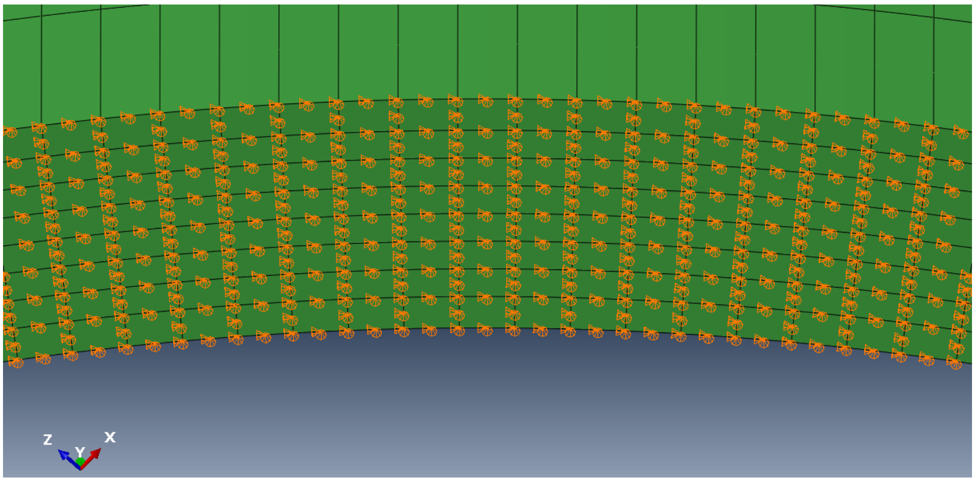

Figure 110. Displacement constraints on the lower surface of the tubular specimen model.

The upper end of the tube was also clamped in a cylindrical testing fixture and subjected to combined axial compressive load and torsion. Thus, in the model the transverse compressive stress in the 90° unidirectional plies was induced by applying a compression stress on the upper surface of the unidirectional layer. The loading condition is represented in Figure 111.

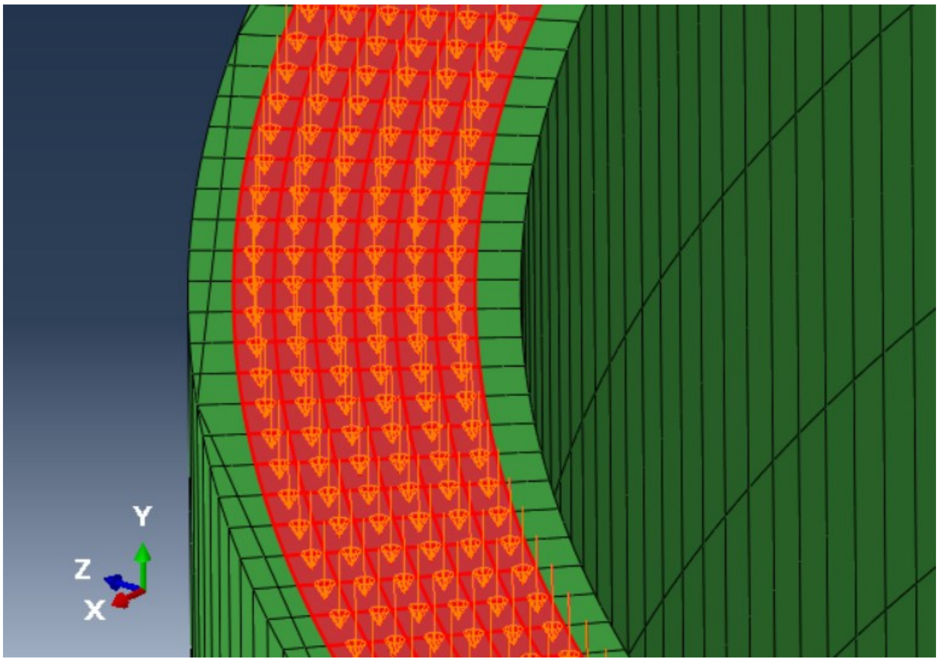

Figure 111. Compressive stress applied on the upper surface of the unidirectional layer.

The torsion was applied to the upper part of the tubular specimen in the model by creating shell cylindrical elements connected to the external first row of elements of the tube model with tie constraints. Boundary conditions were applied on the shell element, which is represented in Figure 112. The displacements along the X and Z axes were constrained, as well as the rotations around X and Z axes. The torsional stress on the specimen was induced by applying a torque to the shell element. The complete boundary conditions implemented on the tubular specimen model can be observed in Figure 113. The local effects due to the application of nodal forces disappear after one element division from the loaded point [44].

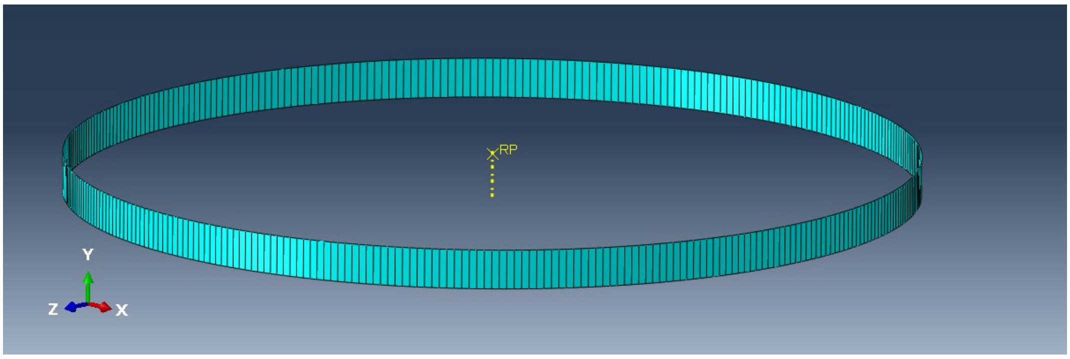

Figure 112. Shell element used for simulating the aligning fixtures on the upper side of the tubular specimen.

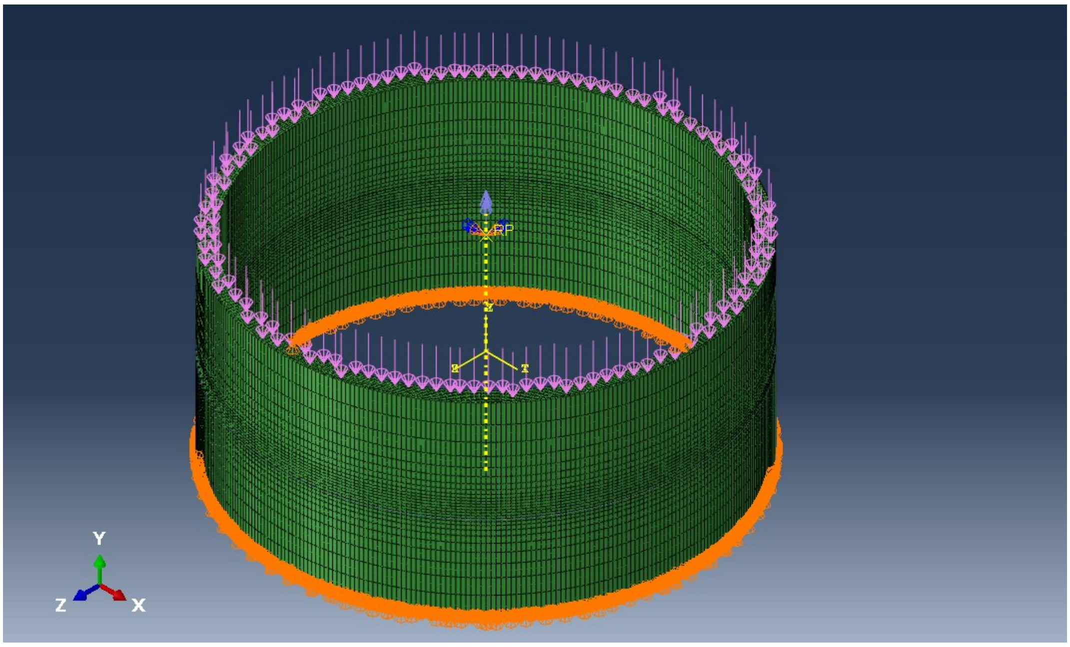

Figure 113. Boundary conditions applied on the tubular specimen model.

5.2.6. Modelling Contact

Differently from a fracture caused by tensile stress, the crack surfaces of a fracture caused by compressive stress do not separate but remain in contact between each other. For this reason, the contact between the two crack surfaces had to be modelled. There are two different algorithms for defining contact in Abaqus CAE, which are *Contact Pairs* (Surface to Surface Contact) and *General Contact* [62]. In the *Contact Pairs* algorithm, the surfaces that will be in contact together must be defined and the contact properties specified exclusively for this pair. If multiple surfaces of the model enter in contact during the simulation, a contact pair must be defined for each one of the contacts. In the *General Contact* algorithm instead, it is enough to define the general contact properties for all the model. During the simulation, the software will automatically detect when two or more surfaces come into contact and will apply the properties previously defined to the interaction. If two surfaces need specific contact properties different from the general ones, they have to be excluded when the *General Contact* is defined and a *Contact Pairs* interaction must be applied to them.

A comparison between the two algorithms was carried out in order to study the differences between them. Simulations with different crack opening angles (COA) were performed with both *Contact Pairs* and *General Contact* methods. Both frictionless and friction ($f = 0.3$) cases were considered. The results of stress and displacements on the crack surfaces obtained from the two different methods were compared, as well as the time required to complete the simulations. Examples of stresses and displacements on the upper crack surface obtained from simulation with friction are reported for two different crack opening angles in Figure 114 and Figure 115. As it is also possible to observe from the example, the results obtained from the two different methods were almost identical for all the crack opening angles considered both for frictionless and friction cases. The main difference between the two algorithms was the simulation time. Considering the friction case that has a higher computational cost, the simulations with *General Contact* required about 1 hour to be completed while those with *Contact Pairs* required about 1 hour and 50 minutes. For this reason, considering that the numerical results were almost identical, General Contact algorithm was adopted for all the following simulations.

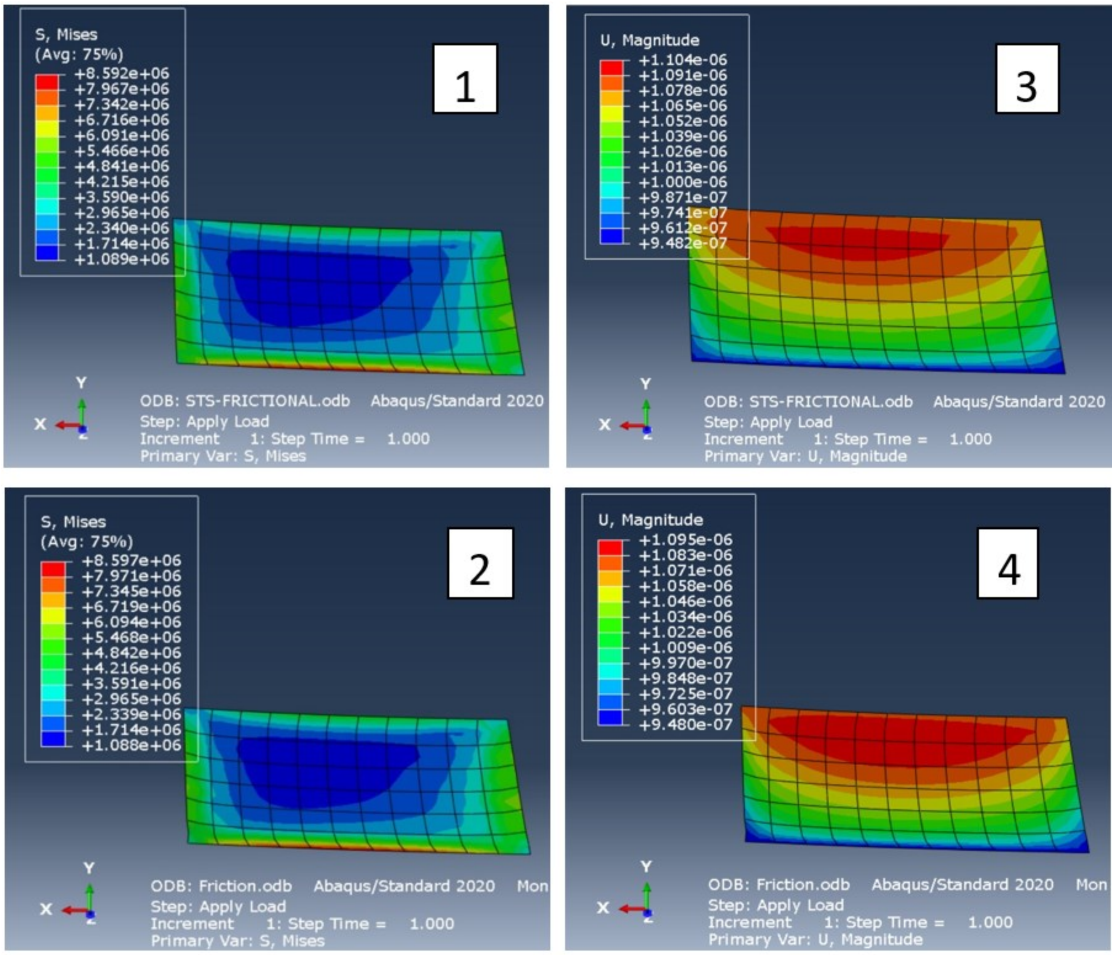

Figure 114. Mises stress and total displacement on the upper crack surface for 11° COA. Contact Pairs algorithm stress and displacement (images 1 and 3 respectively) are compared with those obtained with General Contact algorithm (images 2 and 4 respectively).

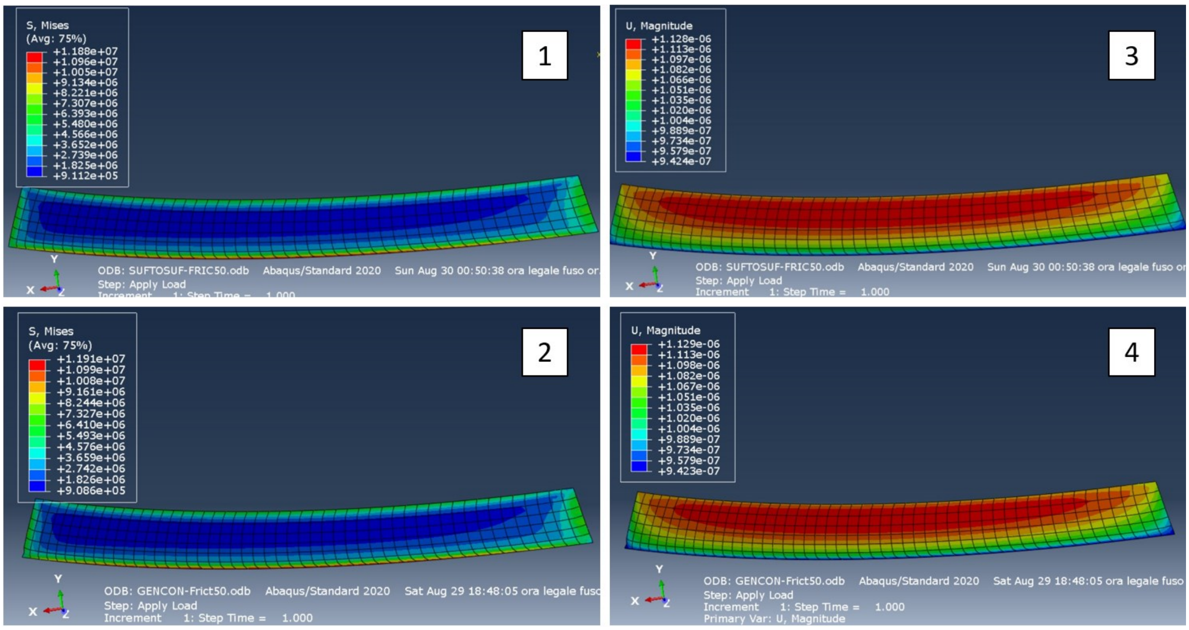

Figure 115. Mises stress and total displacement on the upper crack surface for 50° COA. Contact Pairs algorithm stress and displacement (images 1 and 3 respectively) are compared with those obtained with General Contact algorithm (images 2 and 4 respectively).

5.3. Post-Processing

The Mode II and Mode III SERR related to the crack propagation were computed applying the manual VCCT method described in Section 5.1. In order to compute the energy released during crack propagation with the Eq. 5.6, it was necessary to extract the stress of the uncracked tubular specimen and the average crack surfaces nodal displacements. The procedure adopted for obtaining the required data is described in this chapter.

5.3.1. Uncracked Specimen Stress

For obtaining the uncracked specimen stress, the simulation was performed with the two halves of the tube model completely connected together by tie constraints. The uncracked specimen stress state was extracted on the inclined surfaces of the tube model. The values of the stresses were represented in a cylindrical reference frame. An example of the shear stress on the unidirectional layer of the tubular specimen can be observed in Figure 116. The values of the stresses were acquired by using circular path of nodes created on the inclined surface, as the one represented in Figure 117.

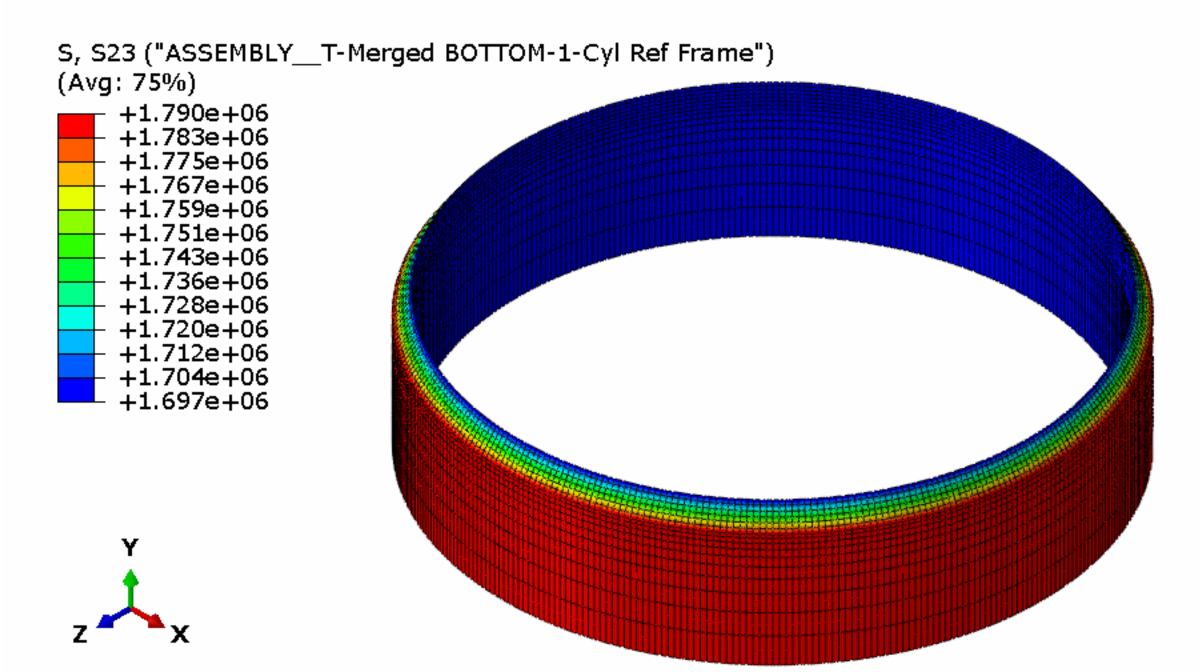

Figure 116. Shear stress S23 induced by the torsion load represented in the cylindrical reference frame.

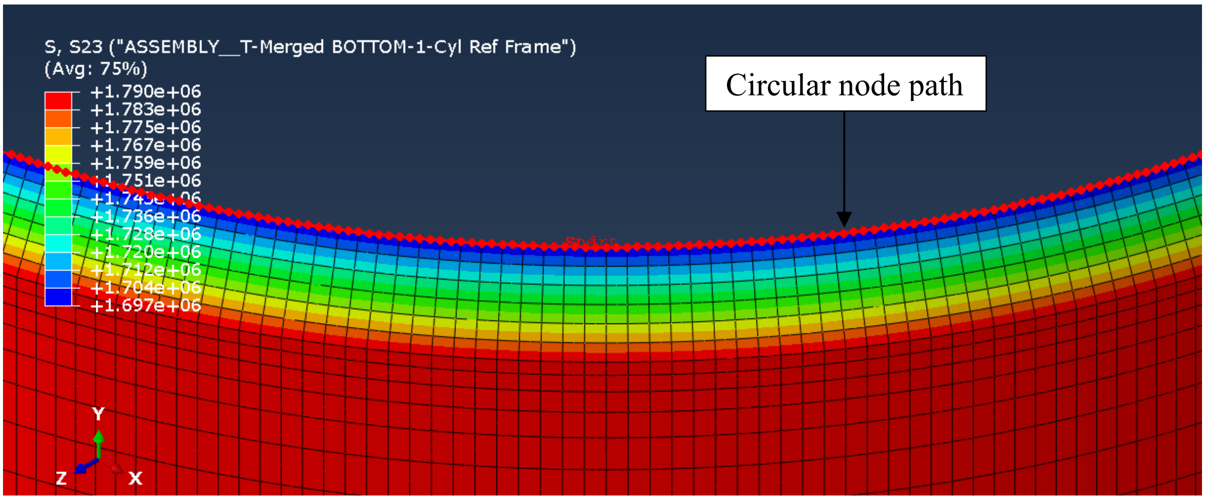

Figure 117. Example of circular path of nodes utilized for extracting the values of the stress on the inclined surface of the tubular specimen model.

In order to compute the Mode II and Mode III SERR, the shear stresses acting on the surface inclined of 55° were needed. However, the values of the stresses extracted from Abaqus CAE were oriented in the cylindrical reference frame. For this reason, a stress transformation was applied. A second reference frame lying on the crack surface was defined, obtained by rotating the cylindrical reference frame of 55° with respect to the tangential axis. The stress values, extracted in the cylindrical reference frame, were transformed in the crack surface local reference frame. The two reference frame are represented in Figure 118.

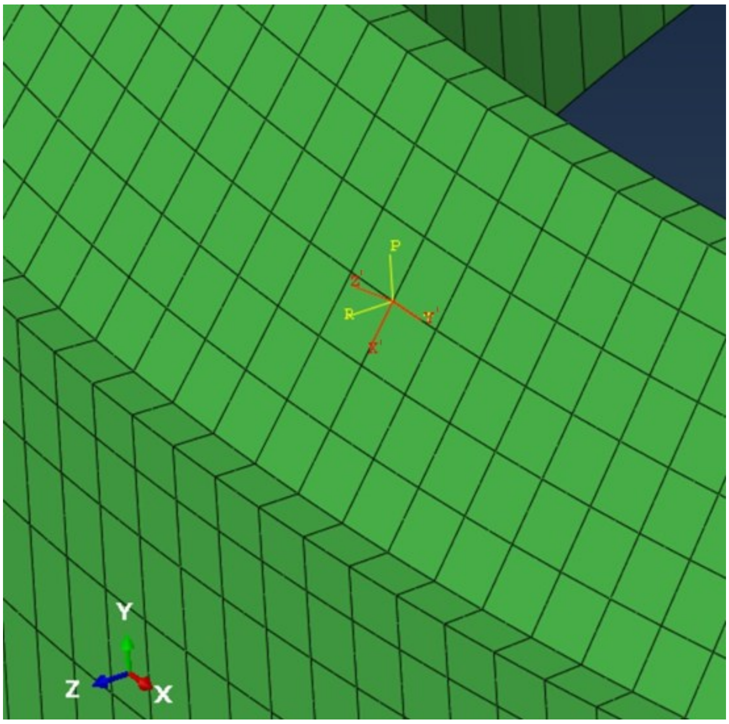

Figure 118. The stress values extracted were referring to the cylindrical reference frame (yellow) and subsequently transformed in the reference frame laying on the crack surface (red).

Making reference to Figure 118, the local cylindrical reference system has axes RTP while the local crack surface reference system has axes $x'y'z'$. Knowing the stress tensor of the cylindrical reference frame, denoted with $[\sigma]$, it is possible to obtain the stress tensor of the new reference frame $[\sigma']$ as:

$$[\sigma'] = [q][\sigma][q]^T \tag{5.7}$$

Where $[q]$ is the transformation matrix, defined as:

$$[q] = \begin{bmatrix} \cos(x', R) & \cos(x', T) & \cos(x', P) \\ \cos(y', R) & \cos(y', T) & \cos(y', P) \\ \cos(z', R) & \cos(z', T) & \cos(z', P) \end{bmatrix} \tag{5.8}$$

The terms inside the brackets are equal to the angle between the axes considered. Considering that the crack surface local reference frame was obtained from the cylindrical reference frame by rotating it of 55° about the tangential axis T, the transformation matrix $[q]$ became equal to:

$$[q] = \begin{bmatrix} \cos(55) & 0 & -\sin(55) \\ 0 & 1 & 0 \\ \sin(55) & 0 & \cos(55) \end{bmatrix} \tag{5.9}$$

The stress components on Abaqus CAE are denoted with numerical subscripts. Taking into account this factor and making reference to the local cylindrical reference frame, the subscript 1 represented the direction of the R axis, the subscript 2 represented the T axis direction and subscript 3 represented the P axis direction. Considering the local crack surface reference frame instead, x' axis direction was denoted with $1'$ subscript, y' axis direction was denoted with $2'$ subscript and z' axis direction was denoted with $3'$. After having developed the matrix calculation of Eq. 5.7, the stress component causing the Mode II and Mode III fracture modes were obtained:

- Mode II: $\tau_{2'3'} = \tau_{23}\cos(55) + \tau_{12}\sin(55)$ (5.10)

- Mode III: $\tau_{1'3'} = (\sigma_1 - \sigma_3)\, cos(55) + \tau_{13}[cos^2(55) - sin^2(55)]$ (5.11)

Since the unidirectional layer was thin, the stress values were varying slightly through the thickness of the specimen. For this reason, the assumption of utilizing an average value for the computation of the SERR through Eq. 5.6 was reasonable. The compression stress and torque values to be applied on the tubular specimen model for the first simulation were chosen in order to have an average shearing stress $\tau_{1'3'}$ and average tearing stress $\tau_{2'3'}$ equal to 1 MPa after the stress transformation. The reason of this choice was that, assuming to have a linear elastic system, it is possible to obtain the SERR values for any nominal applied stress by multiplying the results obtained from 1 MPa of stress for the square of the effective stress on the crack surface [44]. The displacements corresponding to the effective surface stresses of 1 MPa were obtained through simulations and the SERR computed. Subsequently, the nominal stress adopted during the experimental fatigue tests were applied on the tubular specimen models for computing the effective stress in the uncracked conditions and the values obtained were used in the calculations of the effective SERR related to the experimental tests. In order to obtain $\tau_{1'3'}$ and $\tau_{2'3'}$ equal to 1 MPa, the compressive stress applied on the unidirectional layer upper surface was equal to 2.473 MPa and the torque applied to the fixture shell element was equal to 0.697 Nm.

The assumption of computing an average value of the stress on the crack region of the uncracked specimen and using this value for the computations of all the SERR values after the crack initiation and propagation is a reasonable approximation. In fact, the stress results obtained from the simulations showed that the stress values on the uncracked region remained equal even after the introduction of the crack. An example of this can be observed in Figure 119, where the compressive stress S33 (in the cylindrical reference frame) on a circular path is represented for the uncracked specimen and for the specimen with a 90° ply crack with a circumferential length spanning an angle of 120° in the tube (i.e., crack opening angle). The stress value of the uncracked region of the specimen that presents the crack was practically the same that was obtained from the uncracked specimen simulation. As it is possible to observe in Figure 120, this value of stress was constant until the last element before of the crack region, therefore utilizing it for the SERR calculation is a reasonable approximation.

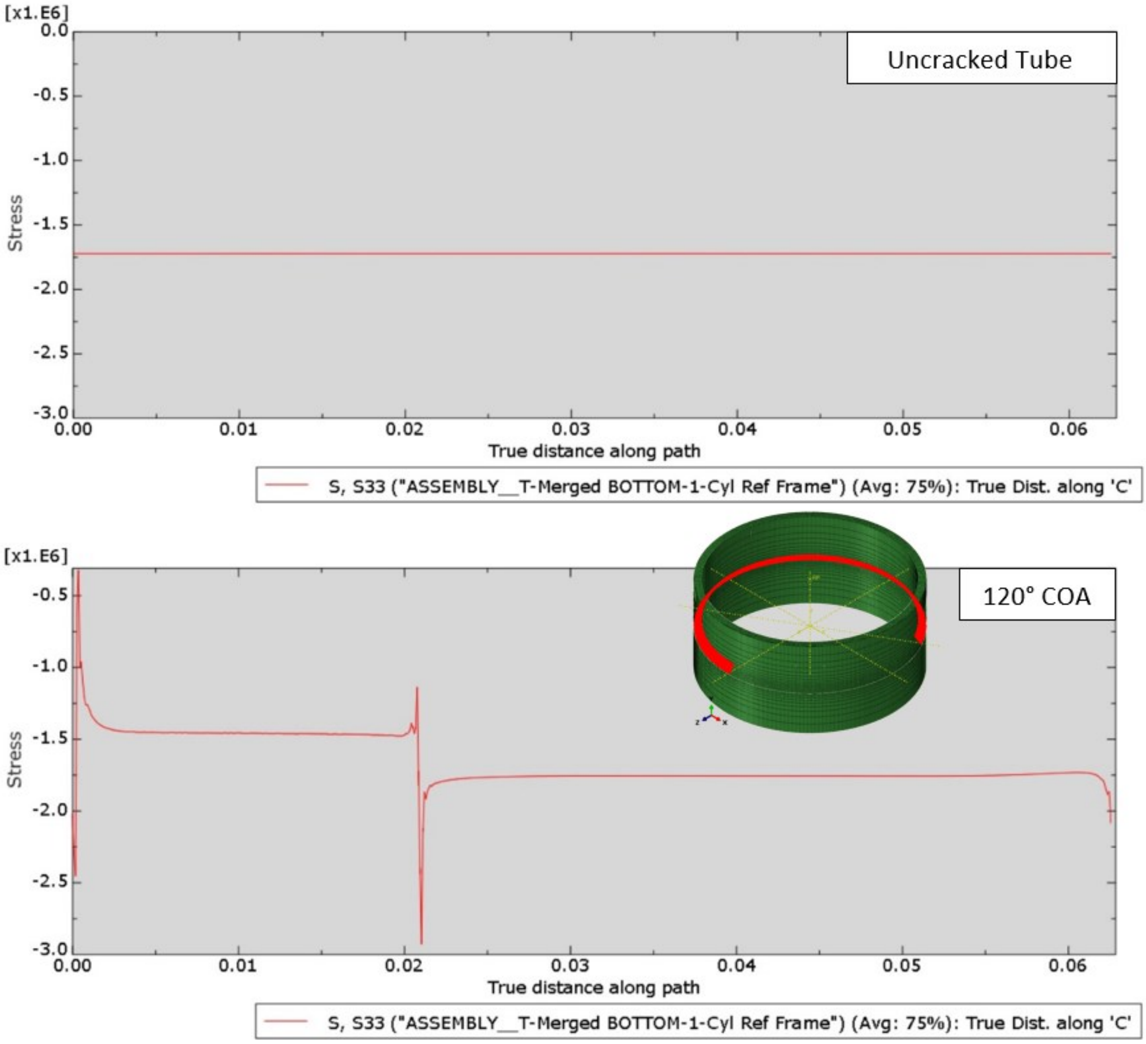

Figure 119. Values of the compression stress S33 along one circular path of nodes on the inclined surface for the uncracked specimen (top image) and for a specimen with 120° COA (bottom image). The stress values of the uncracked specimen and of the uncracked region of the specimen with the crack are the same.

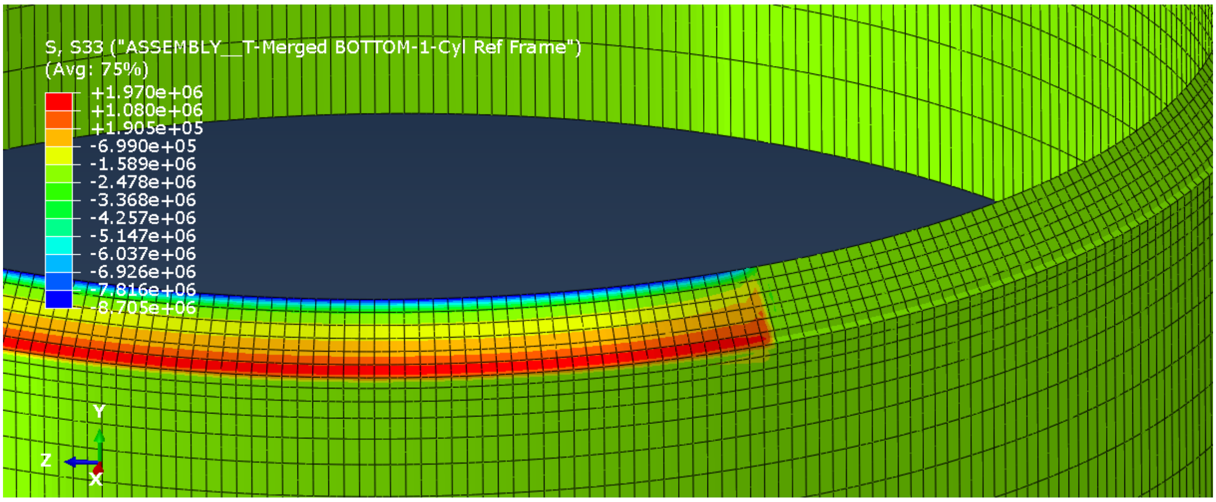

Figure 120. Compression stress S33 (cylindrical reference frame) for a specimen with 120° COA. The color pattern shows how the stress remains constant until one row of elements before the crack surface.

5.3.2. Crack Surface Displacements

For computing the SERR the average relative displacements between the two crack surfaces were needed. The nodal displacements were obtained by running different simulations, changing the 90° ply crack circumferential length span from angles in the range of 1° to 180° (i.e., crack opening angle) as it was explained in chapter 5.2.3. An example of the upper and lower crack surfaces nodal displacement can be observed in Figure 121. The nodal displacements were extracted from the two crack surfaces using a path of nodes that was selecting all the rows of nodes along the thickness, going from the external to the internal sides of the tubular specimen. The path of nodes is represented in Figure 122. Two identical path of nodes were defined on the upper and lower crack surfaces, both starting from the same node. This method allowed to ease the computation of the relative displacements of the nodes that before of the crack propagation were connected together.

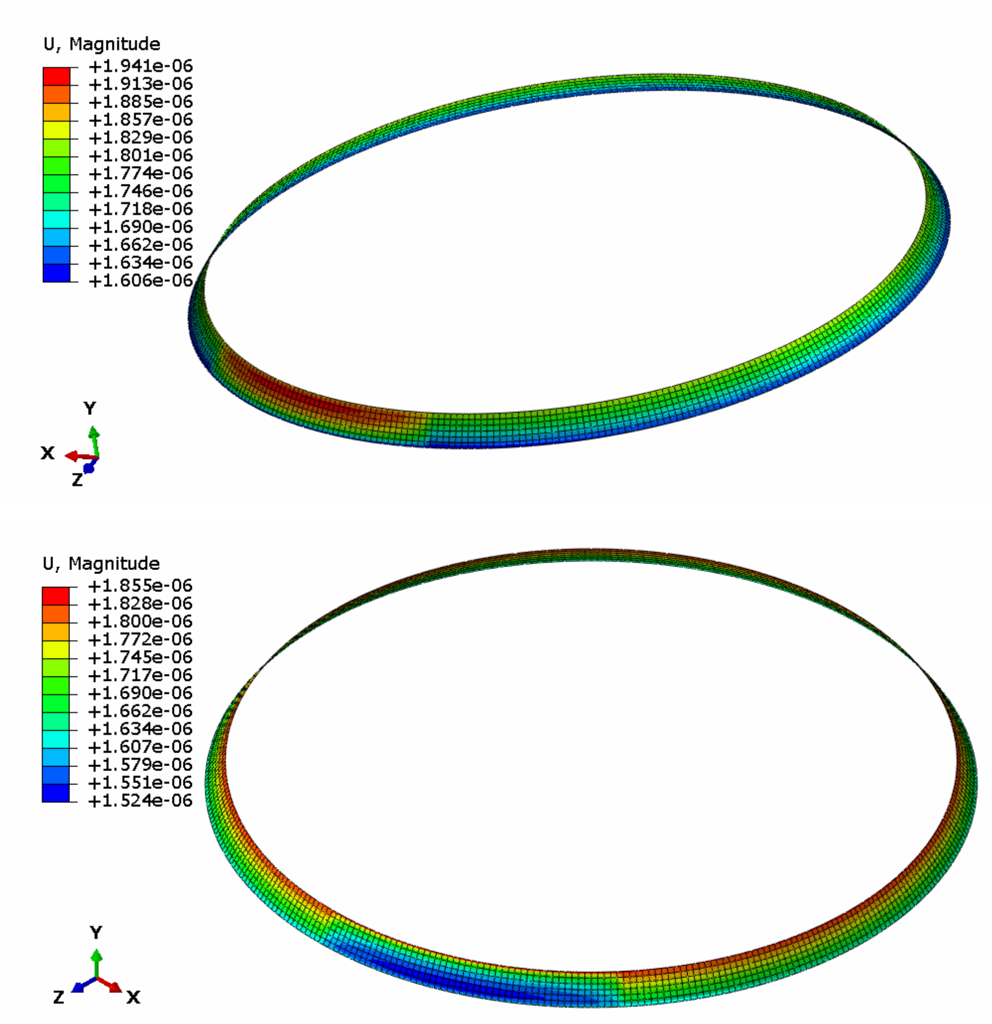

Figure 121. Magnitude of the displacements on the upper (top image) and lower (bottom image) inclined surfaces for 50° COA. The crack surfaces can be recognized by the different color distributions.

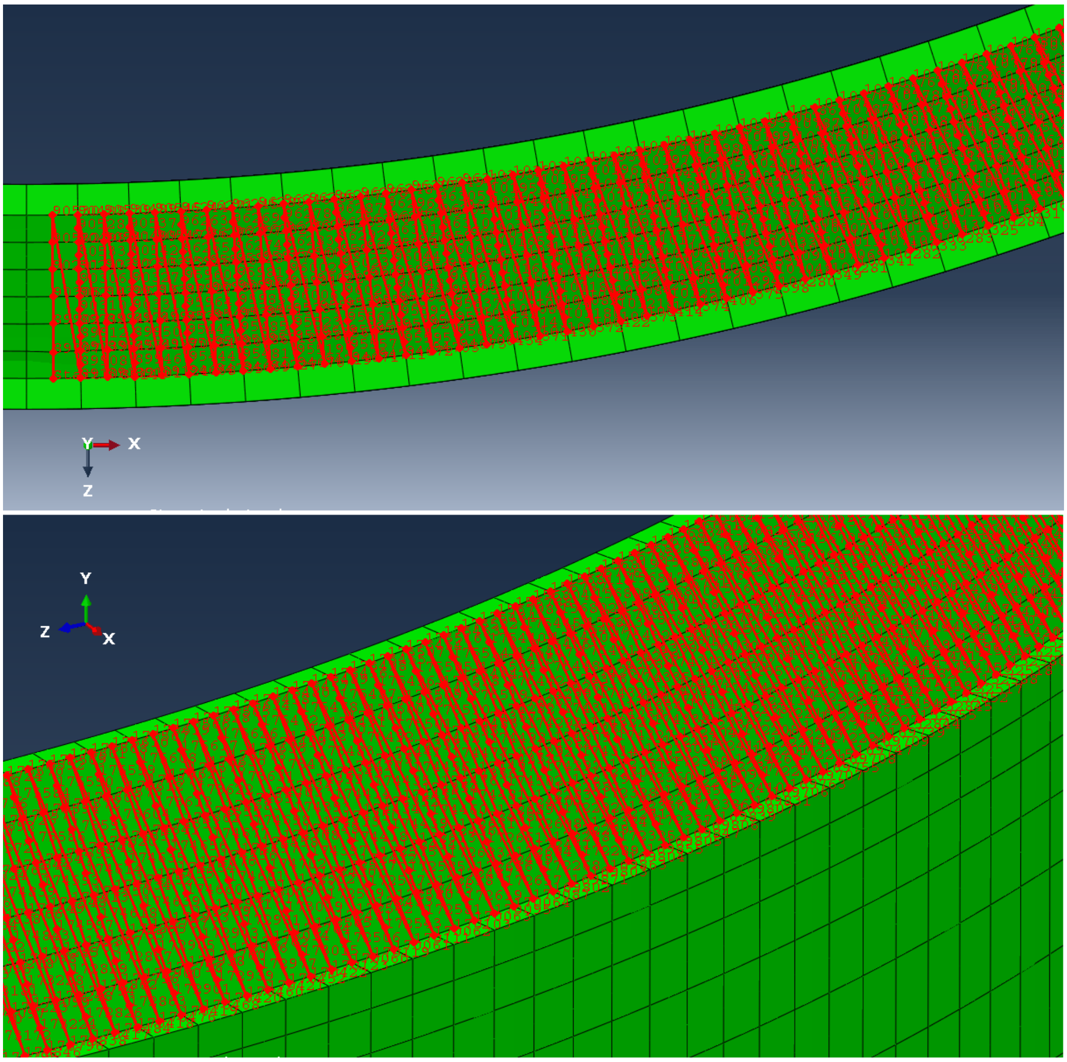

Figure 122. Path of nodes utilized for extracting the nodal displacements on the crack surfaces.

The displacements extracted from the path of nodes were referring to the local cylindrical reference frame. Therefore, a transformation of the displacements from the cylindrical reference frame to the crack surface local reference frame was necessary. The relative displacement caused by the Mode II crack surface displacements was along the y' direction and it was called Δv. The relative displacement caused by the Mode III crack surface displacement was along the x' direction and it was called Δu. The two relative displacement were equal to:

$$\Delta u = \left(U_{1_{TOP}} - U_{1_{BOT}}\right)\cos(55) - \left(U_{3_{TOP}} - U_{3_{BOT}}\right)\sin(55) \tag{5.11}$$

$$\Delta v = U_{2_{TOP}} - U_{2_{BOT}} \tag{5.12}$$

where U_1 is the displacement in the radial direction R of the cylindrical reference frame, U_2 is the displacement along the tangential direction T and U_3 is the displacement along the vertical direction P. The subscripts TOP and BOT are indicating the upper and lower crack surfaces, respectively. The relative displacement had to be averaged on the crack area:

$$\overline{(\Delta u)}_{surf} = \frac{1}{A}\int_A \Delta u(x', y')dA \tag{5.13}$$

$$\overline{(\Delta v)}_{surf} = \frac{1}{A}\int_A \Delta v(x', y')dA \tag{5.14}$$

The double integrals reported in Eq. 5.13 and 5.14 were approximated by two subsequent summations. Considering the relative displacement Δu, first the value of the average relative displacement for each i-th radial row of nodes of the crack surface was computed as:

$$\overline{(\Delta u)}_{(\mathrm{i-th\ row})} = \frac{1}{t_\alpha}\sum_{i=1}^{n_{nodes}} \Delta u_{\mathrm{j}} \cdot \frac{t_\alpha}{n_{nodes}-1} \tag{5.15}$$

where t_α is the unidirectional layer thickness, n_{nodes} is the number of nodes in the row and Δu_{j} is the relative nodal displacement between the j-th nodes.

After having computed the average relative displacement for all the row of nodes of the crack surface, the average relative displacement of the entire crack area was calculated as:

$$\overline{(\Delta u)}_{(\mathrm{surf})} = \frac{1}{\alpha \cdot r_{avg}}\sum \overline{(\Delta u)}_{(\mathrm{i-th\ row})} \cdot \Delta\alpha \cdot r_{avg} \tag{5.16}$$

Where α is the crack opening angle, r_{avg} is the mean radius of the unidirectional layer and $\Delta\alpha$ is the angular distance between two consecutive rows of nodes.

5.3.3. Strain Energy Release Rate Calculation

Once the average stresses and average crack surfaces relative displacements were obtained respectively from the uncracked specimen and crack propagation simulations, it was possible to compute the Mode II and Mode III SERR. As a first step, the energy released during crack propagation was calculated as:

- Mode II: $$U_{\tau_{2'3'}} = \tau_{2'3'_{avg}} \cdot \overline{(\Delta v)}_{(\text{surf})} \cdot A \tag{5.18}$$
- Mode III: $$U_{\tau_{1'3'}} = \tau_{1'3'_{avg}} \cdot \overline{(\Delta u)}_{(\text{surf})} \cdot A \tag{5.19}$$

where $\tau_{2'3'_{avg}}$ is the average tangential shear stress on the uncracked inclined surface, $\tau_{1'3'_{avg}}$ is the average tearing shear stress on the uncracked inclined surface and A is half of the total crack surface. The energy released during crack propagation were calculated for every crack opening angle between 0° and 180°.

Finally, with the results of the energy released $U_{\tau_{2'3'}}$ and $U_{\tau_{1'3'}}$, it was possible to compute the Mode II and Mode III SERR:

$$\begin{aligned} G_{II} &= \frac{dU_{\tau_{2'3'}}}{d(2A)} = \frac{U_{\tau_{2'3'i}} - U_{\tau_{2'3'i-1}}}{2A_i - 2A_{i-1}} \\ G_{III} &= \frac{dU_{\tau_{1'3'}}}{d(2A)} = \frac{U_{\tau_{1'3'i}} - U_{\tau_{1'3'i-1}}}{2A_i - 2A_{i-1}} \end{aligned} \tag{5.20}$$

where $2A$ is the total crack area.

5.4. Results

The Mode II and Mode III SERR for the frictionless case with effective stresses on the crack region of 1 MPa were calculated in MS Excel and plotted against the crack opening angle, as it is represented in Figure 123 and Figure 124.

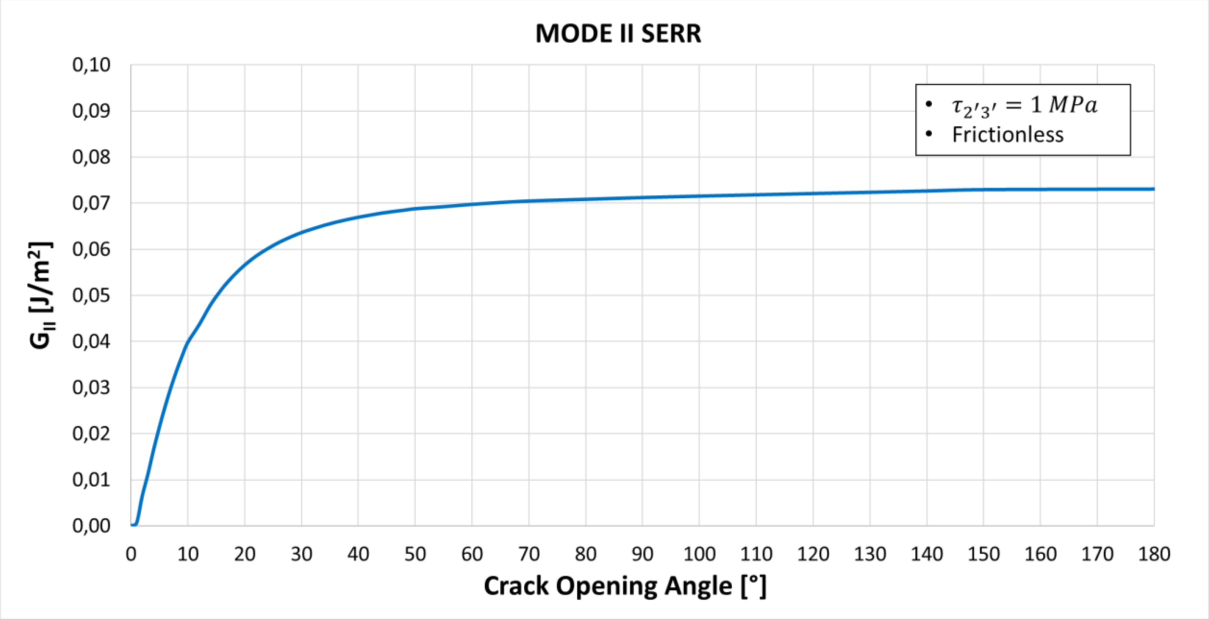

Figure 123. Mode II SERR for frictionless compression-torsion crack propagation. Results obtained with effective stress on the crack surface equal to 1 MPa.

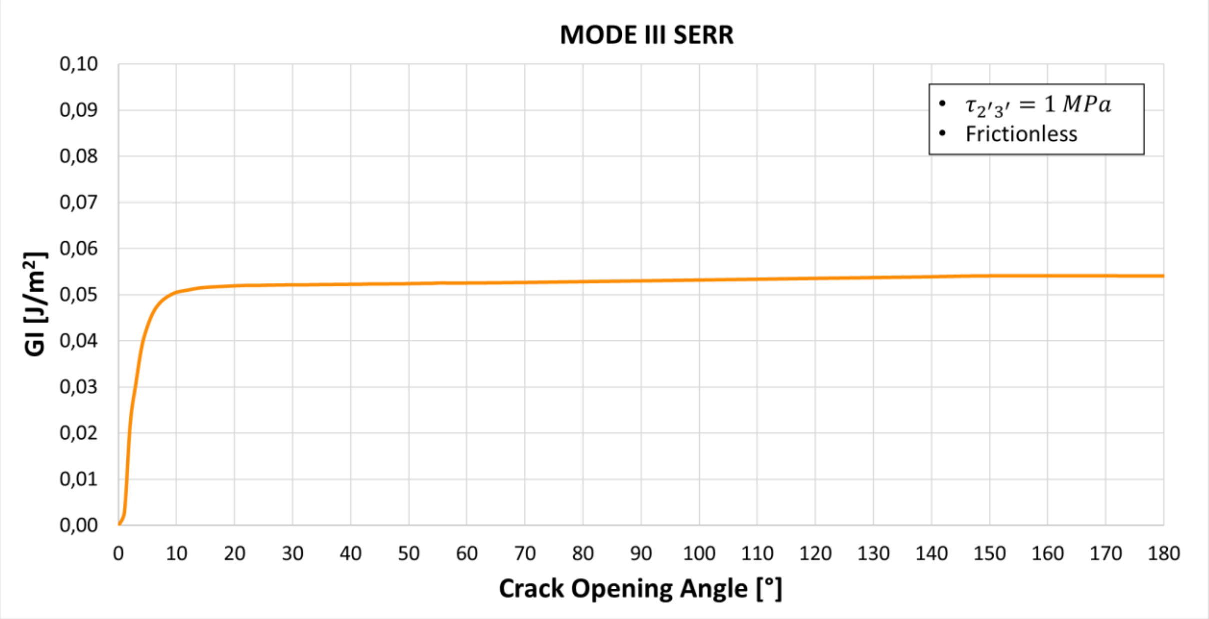

Figure 124. Mode III SERR for frictionless compression-torsion crack propagation. Results obtained with effective stress on the crack surface equal to 1 MPa.

The curves of Mode II and Mode III SERR have a similar behavior, with the SERR value that increases almost linearly with the crack opening angle in the initial phase and then stabilizes reaching a plateau region. The plateau region can be approximated by a steady state condition, in which the SERR remains constant as the crack propagates. Mathematically it means that, since the increment of crack surface during the simulations was constant, the energy released during crack propagation had an initial quadratic increase followed by a linear increase. The Mode II SERR reaches the steady state condition at about 50° COA, while the increment of the Mode III SERR is steeper and the steady state condition is reached after about 15° COA.

5.4.1. Fatigue Tests

The experimental fatigue tests performed by McCleave [19] applied different combinations of compressive and torsional stress in order to study how the variation of the multiaxial stress state affected 90° ply crack growth. The different load cases considered during the tests were:

- $Minimum\ compression\ stress = 0.8\ F_{2C}$; $\lambda_{12} = 0.4$
- $Minimum\ compression\ stress = 0.8\ F_{2C}$; $\lambda_{12} = 0.21$
- $Minimum\ compression\ stress = 0.75\ F_{2C}$; $\lambda_{12} = 0.4$
- $Minimum\ compression\ stress = 0.75\ F_{2C}$; $\lambda_{12} = 0.21$
- $Minimum\ compression\ stress = 0.7\ F_{2C}$; $\lambda_{12} = 0.4$
- $Minimum\ compression\ stress = 0.7\ F_{2C}$; $\lambda_{12} = 0.21$

Where F_{2C} is the unidirectional ply transverse compressive strength and λ_{12} is the biaxiality ratio, defined as the ratio between the shear stress and the transverse compression stress in the 90° ply.

Since the system was assumed to behave in linear elastic way and the friction effect between the crack surfaces was neglected, the results of SERR related to the experimental tests were calculated starting from the results obtained from the simulations with 1 MPa of effective tangential and tearing shear stresses on the crack surface (Figures 124 and 125). Initially, the effective stress state of the uncracked specimens was computed performing simulations applying the loading conditions of the experimental tests. Once the effective tangential shear stress and tearing shear stress acting on the crack region were calculated, the effective SERR values were obtained as:

$$G_{II_{eff}} = G_{II|1MPa} \cdot {\tau_{2'3'}}_{eff}^{\ 2}$$

$$G_{III_{eff}} = G_{III|1MPa} \cdot {\tau_{1'3'}}_{eff}^{\ 2} \tag{5.21}$$

Where ${\tau_{2'3'}}_{eff}$ and ${\tau_{1'3'}}_{eff}$ are the effective uncracked specimen shear stresses acting on the inclined surface.

The loads applied on the tubular specimen model are reported in Table 7. The compressive stress σ_2 applied on the unidirectional layer of the specimen was equal to the minimum stress applied during the fatigue cycle. The unidirectional ply ultimate compressive strength was equal to $F_{2C} = -163.58\ MPa$. The tangential stress σ_6 caused by the torsion was computed from the biaxiality ratio. The torque that had to be applied on the fixture shell element was computed assuming to have the value of tangential stress σ_6 on the external surface of the unidirectional ply. The results of the effective tangential shear stress and tearing shear stress obtained from the simulation of the uncracked specimen are reported in Table 8.

	$\lambda_{12} = \sigma6/\sigma2 = 0,4$			**$\lambda_{12} = \sigma6/\sigma2 = 0,21$**		
% F_{2C}	**Normal stress σ2 [Mpa]**	**Tangential stress σ6 [Mpa]**	**Torque [Nm]**	**Normal stress σ2 [Mpa]**	**Tangential stress σ6 [Mpa]**	**Torque [Nm]**
0,8	-130,86	52,35	16,53	-130,86	27,48	8,68
0,75	-122,69	49,07	15,50	-122,69	25,76	8,14
0,7	-114,51	45,80	14,47	-114,51	24,05	7,59

Table 7. Loading conditions of the tubular specimen during the simulations for finding the uncracked specimen stress state.

	$\tau_{2'3'eff}$	**$\tau_{1'3'eff}$**
Load Case	[MPa]	[MPa]
0,8 F_{2C} - λ_{12}=0,4	23,65	52,66
0,8 F_{2C} - λ_{12}=0,21	12,41	52,71
0,75 F_{2C} - λ_{12}=0,4	22,14	49,50
0,75 F_{2C} - λ_{12}=0,21	11,63	49,43
0,7 F_{2C} - λ_{12}=0,4	20,69	46,17
0,7 F_{2C} - λ_{12}=0,21	10,86	46,15

Table 8. Effective Mode II tangential shear stress and Mode III tearing shear stress on the inclined surface of the model.

The validity of the computational method for calculating the effective SERR was verified performing a comparison between the SERR results obtained applying the formulas of Eq. 5.21 and those obtained from simulating the crack propagation for acquiring the crack surfaces relative displacements. The case selected for the comparison was $0.8\,F_{2C} - \lambda_{12} = 0.4$. The simulations were performed for crack opening angles between 0° and 90°. The results for Mode II and Mode III are shown in Figure 125 and Figure 126. The charts show that the results obtained calculating the SERR with Eq. 5.21 were almost identical to those obtained from the crack propagation simulations. The slightly difference between the two curves in the initial phase was mainly due to the fact that a lower number of simulations were performed with respect to the original 1 MPa stress case on which the calculated results were based. The orange curves for this reason were built on a lower number of points. What is important to observe is that the steady state value of the two curves is identical in both Mode II and Mode III cases. For this reasons, the method for calculating the SERR starting from the results of 1 MPa was assumed to be valid.

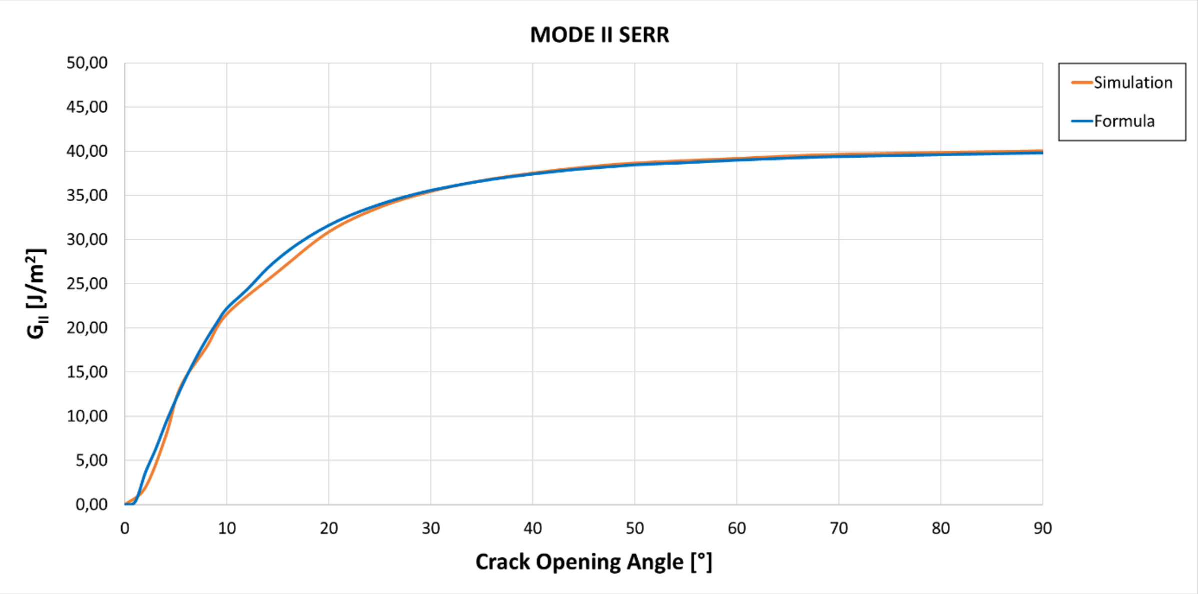

Figure 125. Mode II SERR comparison between the results obtained from the simulation procedure and those calculated starting from the results of 1 MPa stress case.

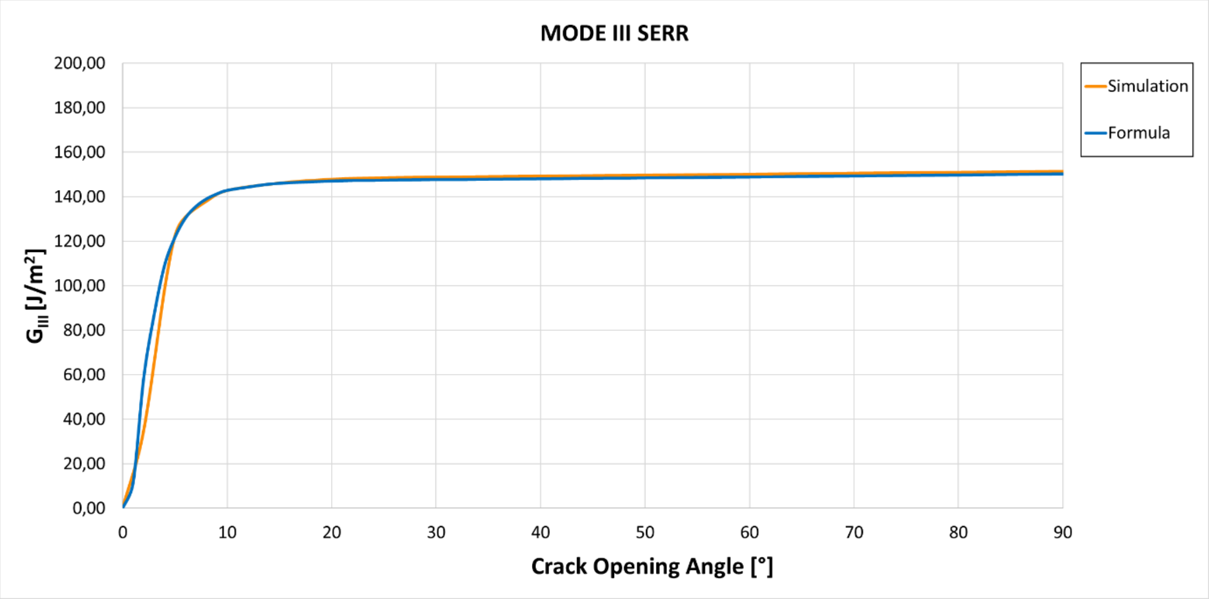

Figure 126. Mode III SERR comparison between the results obtained from the simulation procedure and those calculated starting from the results of 1 MPa stress case.

The results obtained from the different load cases were represented on the same chart in order to compare them. The Mode II SERR are represented in Figure 127. From the chart it is possible to notice that the results obtained from the cases with biaxiality ratio $\lambda_{12} = 0.4$ have higher Mode II SERR with respect to the cases with $\lambda_{12} = 0.21$. Considering the same axial loading condition in fact, by decreasing the torsional load of about 50 % the steady state value of the SERR decreases of about 70 %.

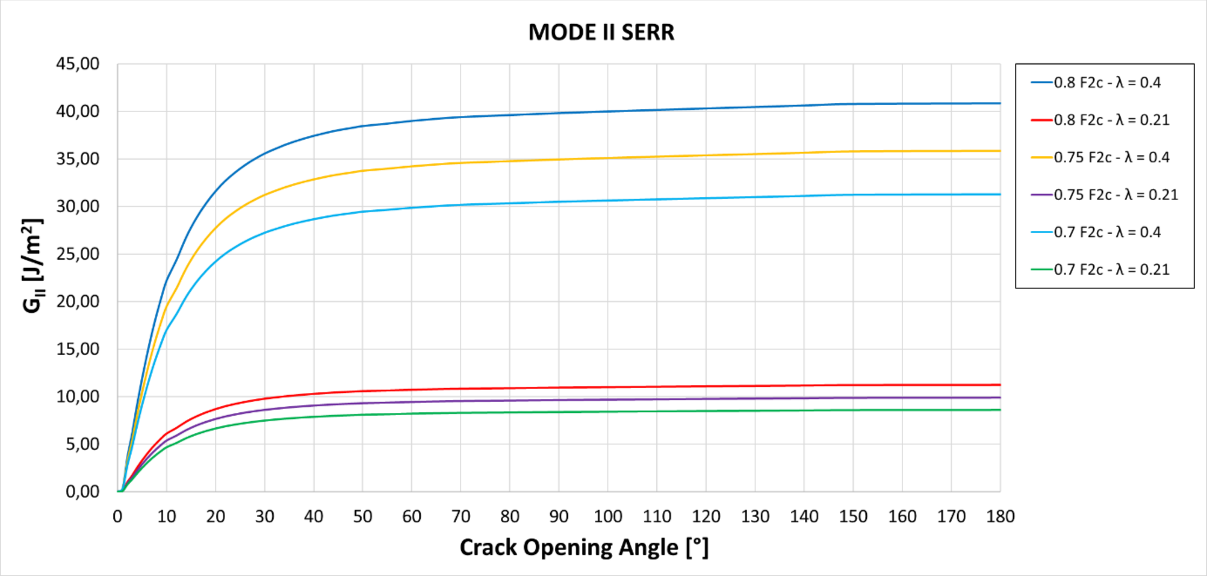

Figure 127. Mode II SERR results for the different load cases.

The Mode III SERR results for the different load cases are represented in Figure 128. From the chart, it is possible to observe that, by decreasing the axial compressive stress applied on the unidirectional ply of about 6 %, the Mode III SERR steady state value decreases of about 12 %. Since the system is linear and elastic, the curves obtained from the load cases that have the same compression stress applied are superimposed because the effective tearing stresses on the crack surfaces were equal.

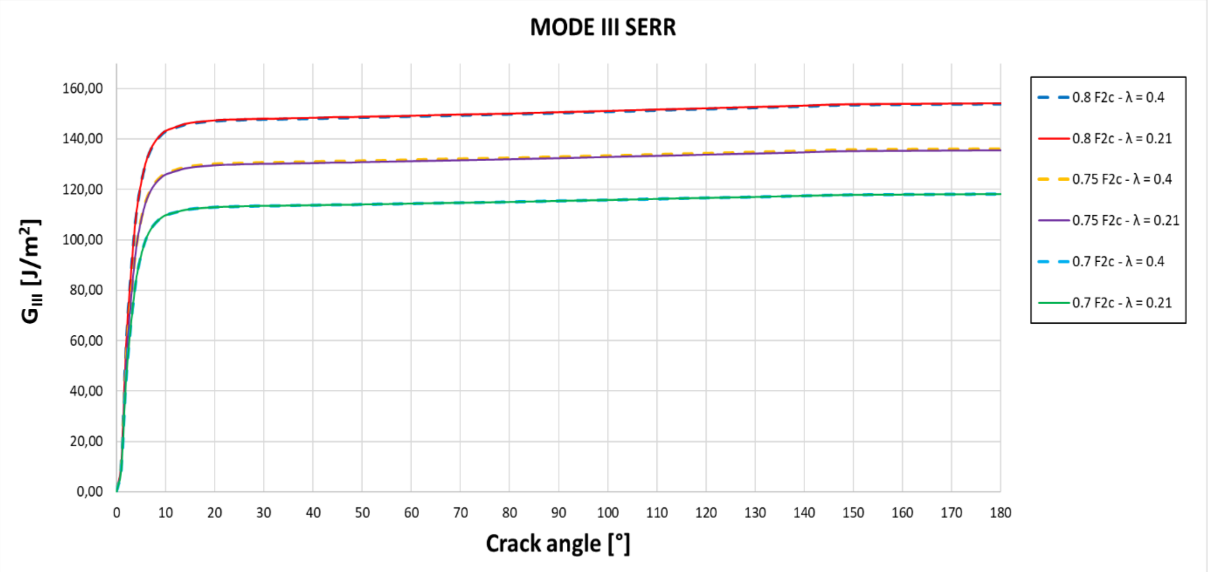

Figure 128. Mode III SERR results for the different load cases.

The results of the total SERR, defined as $G_{TOT} = G_{II} + G_{III}$, are represented in Figure 129. The higher were the values of the stress components of the multiaxial state of stress, the higher was the SERR related to the crack propagation. Considering the same compressive load, the total SERR of the cases with $\lambda_{12} = 0.4$ is about 15 % higher than that of cases with $\lambda_{12} = 0.21$.

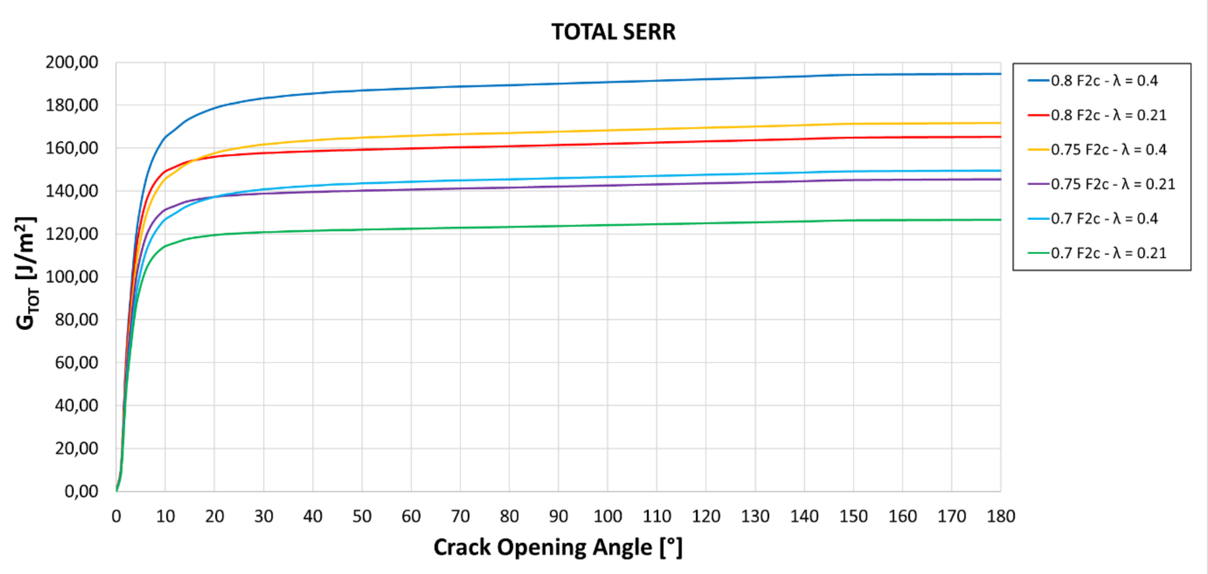

Figure 129. Total SERR results for the different load cases.

5.4.2. Friction Effect on SERR

In the case of cracks induced by a compression state of stress, the crack surfaces do not separate but remain in contact between each other. The results presented previously were assuming a linear elastic system and were neglecting the friction between the crack surfaces. Obviously, this was an ideal case and therefore the effect of the friction between the crack surfaces on the SERR had to be investigated. Searching in the literature, the value of the friction coefficient characterizing the sliding between two glass fiber/epoxy surfaces was not discovered. Different studies reported that the friction coefficient value of glass fiber/epoxy material sliding on steel is about 0.3-0.5 [63, 64, 65] and depends on fibers orientation, vertical load, sliding distance and sliding speed. For this reason, different values of friction coefficient, between $f = 0.1$ and $f = 1.2$, were assumed during the simulations. Initially, the effect of the presence of friction on the trend of the SERR with respect to the crack opening angle was studied. For this purpose, the crack propagation was simulated adopting friction coefficient $f = 0.3$ and 1 MPa of effective shear stresses on the crack surface. The results were compared with the frictionless case and they are shown in Figure 130 and Figure 131.

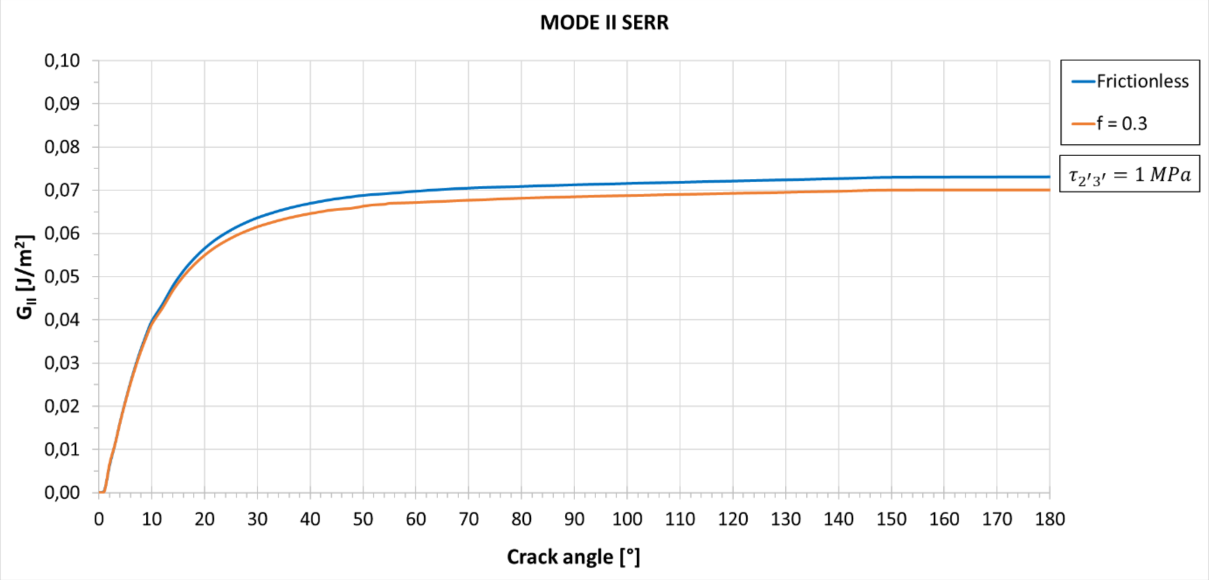

Figure 130. Comparison of the Mode II SERR between the frictionless case and the friction f = 0.3 case for 1 MPa of effective tangential shear stress.

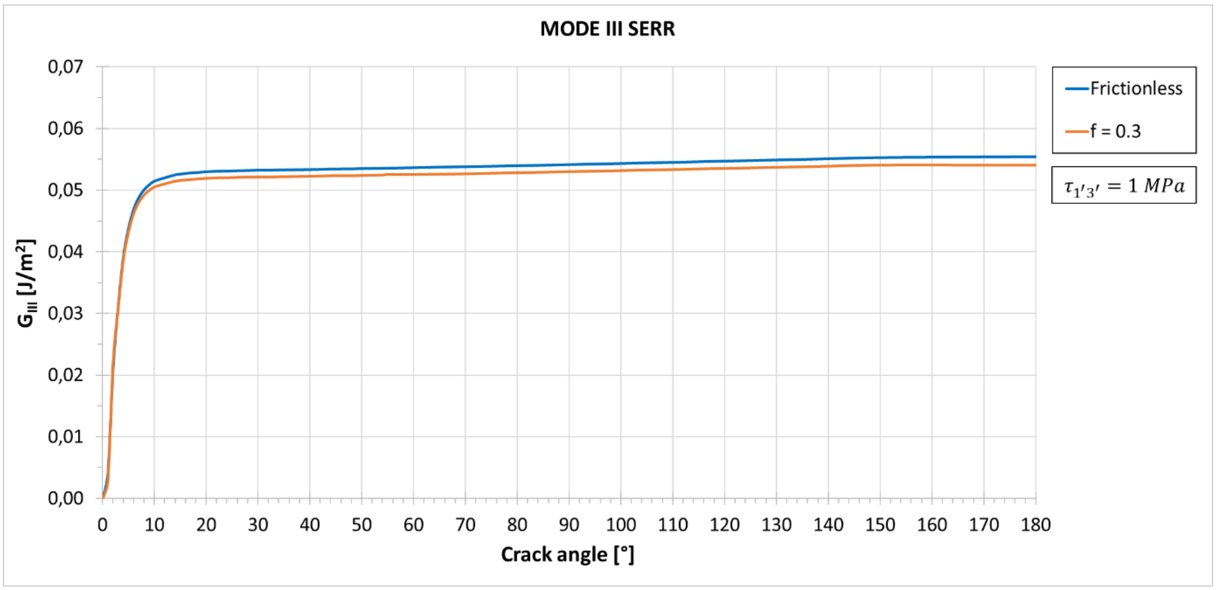

Figure 131. Comparison of the Mode III SERR between the frictionless case and the friction f = 0.3 case for 1 MPa of effective tearing shear stress.

It is possible to notice that the effect of friction is only to decrease the SERR steady state value. For small crack opening angles, the friction effect is negligible, with the curves that are perfectly superimposed. When the curves start approaching the plateau region, the SERR values for the friction case become slightly lower than those of the frictionless case. Due to this aspect, the effect of the different friction coefficient values on the SERR results was evaluated at steady state conditions. Considering the compression and torsional loads that were giving effective shear stresses equal to 1 MPa, crack propagation simulations were performed between 55° and 70° of crack opening angle assuming friction coefficients between $f = 0.1$ and $f = 1.2$. The results are reported in Figure 132 and Figure 133.

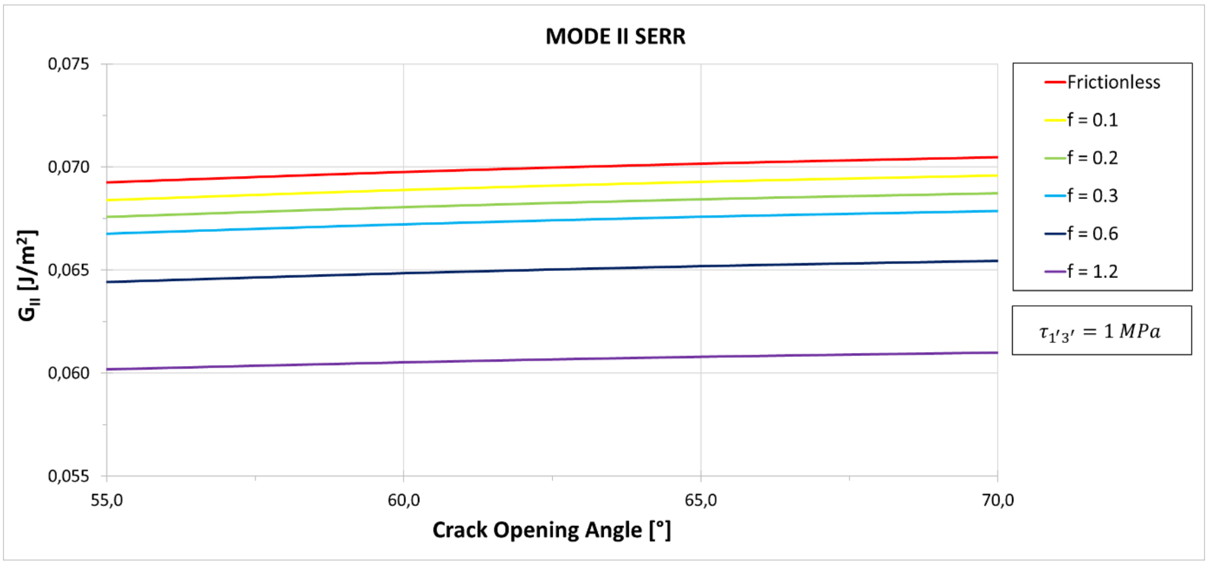

Figure 132. Comparison of the Mode II SERR between different friction coefficients for 1 MPa of effective tangential shear stress.

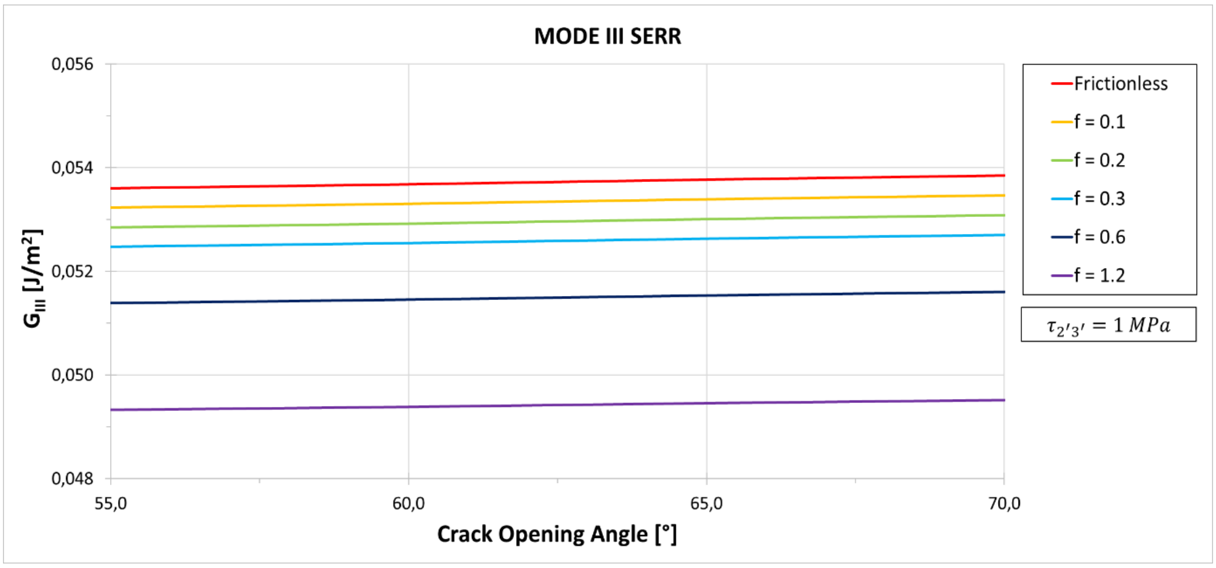

Figure 133. Comparison of the Mode III SERR between different friction coefficients for 1 MPa of effective tearing shear stress.

The results obtained from the simulations show that, by increasing the friction coefficient, the Mode II and Mode III SERR decrease. For low vertical loads, as in this case, the model seems to be not too much sensitive to the effect of friction. The Mode II SERR is more sensitive to the friction coefficient value than the Mode III SERR. Considering the results with friction coefficient $f = 0.3$, the Mode II SERR is about 3,6 % lower than the frictionless case while the Mode III SERR is only 2 % lower than it. By doubling the friction coefficient, so considering $f = 0.6$, the difference becomes even larger. Compared to the frictionless case, the Mode II SERR is about 7 % lower while the Mode III is only 4 % lower.

By increasing the compressive load, the friction force becomes larger. Therefore, the effect of the presence of friction with real loading conditions was investigated. For this purpose, the crack propagation was simulated between 55° and 70° COA considering the load case $0.8\ F_{2C} - \lambda_{12} = 0.4$. Two friction coefficients, equal to $f = 0.3$ and $f = 0.6$, were applied and the results were compared with the frictionless ideal case. The results are reported in Figure 137 and Figure 138.

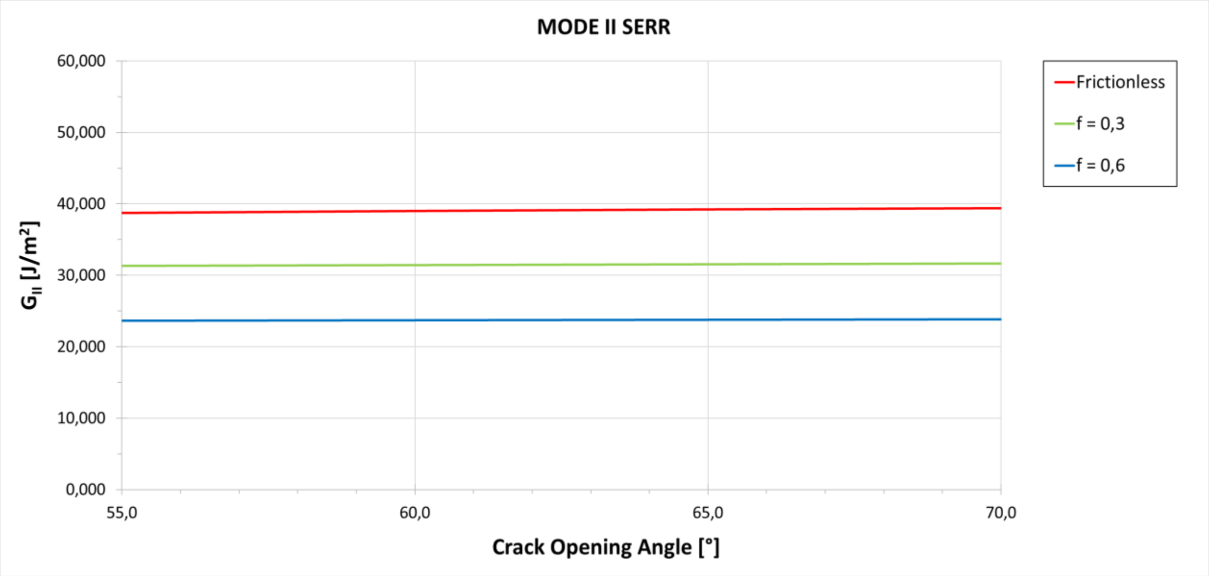

Figure 134. Comparison of the Mode II SERR between different friction coefficients for the load case $\mathbf{0.8\,F_{2C} - \lambda_{12} = 0.4}$.

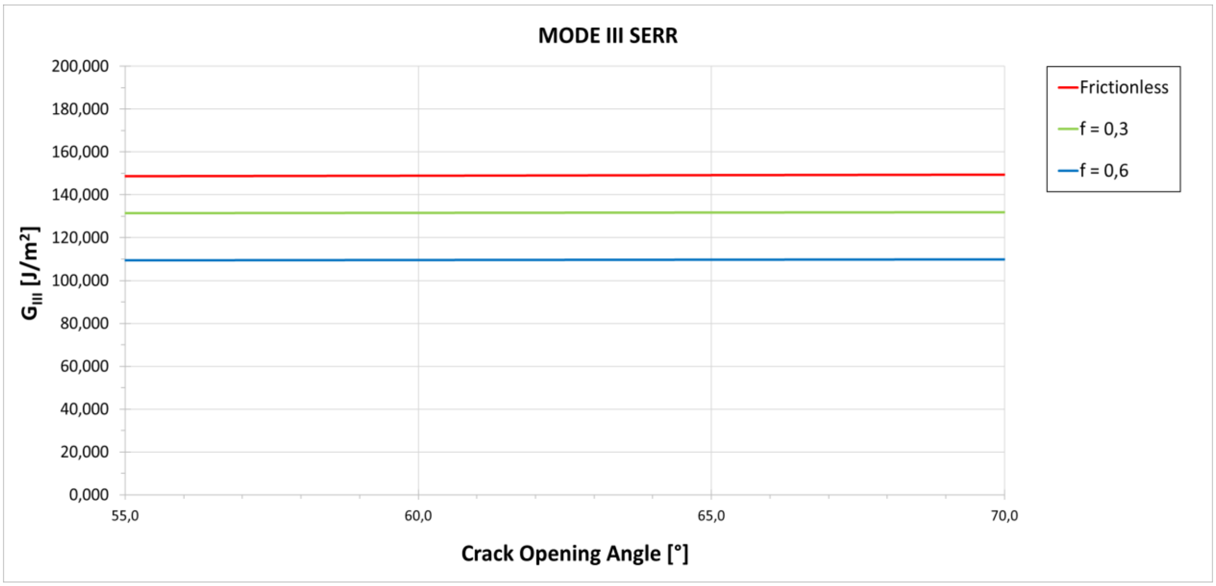

Figure 135. Comparison of the Mode III SERR between different friction coefficients for the load case $\mathbf{0.8\,F_{2C} - \lambda_{12} = 0.4}$.

From the results of the $0.8\,F_{2C} - \lambda_{12} = 0.4$ load case, it is possible to observe that the model is not anymore low sensitive to the effect of friction as it was in the case with 1 MPa of effective shear stresses. With a real loading condition, being the compression stress applied higher, also the friction force increases and, consequently, its effect on the SERR values does the same. The Mode II SERR confirms the trend of being more sensitive to the value of friction coefficient employed. Considering $f = 0.3$, the Mode II SERR steady state value is 24 % lower than the frictionless case while the Mode III SERR is only 11 % lower than it. Increasing the friction coefficient to $f = 0.6$, the Mode II SERR becomes about 50 % lower than the frictionless case and the Mode III SERR only 26 % lower than the ideal case value.

5.5. Discussion

The FE model developed allowed to numerically characterize the propagation of the intra-laminar ply cracks observed in GFRP laminated tubular specimens during the experimental tests performed by McLeave [19]. The crack propagation in the tubular specimens subjected to combined transverse compression and shear stresses was performed manually, and the SERR was computed with a VCCT-based method. The results showed that the SERR of both Mode II and Mode III increase rapidly after the crack initiation and, after the initial growth, stabilize for assuming an almost constant value as the crack continues to propagate. The Mode II SERR reaches the steady state condition at about 50° COA, while the Mode III SERR reaches the steady state condition around 15° COA. It is interesting to notice that the trend of the Mode II and Mode III SERR is similar to that encountered in the Mode I and Mode II SERR of $[0_F/90_{U,3}/0_F]$ GFRP tubular specimens subjected to combined tension and torsion in the Quaresimin and Carraro's study [44]. As it is represented in Figure 136, the Mode I SERR and Mode II SERR were initially growing quickly and then they were reaching a plateau region at similar crack opening angles. The steady state conditions in that case were assumed after 30° COA. The trends of the SERR for mixed Mode II/Mode III and Mode I/Mode II can mean that the way with which the material releases energy during the crack propagation is similar despite the different fracture modes involved.

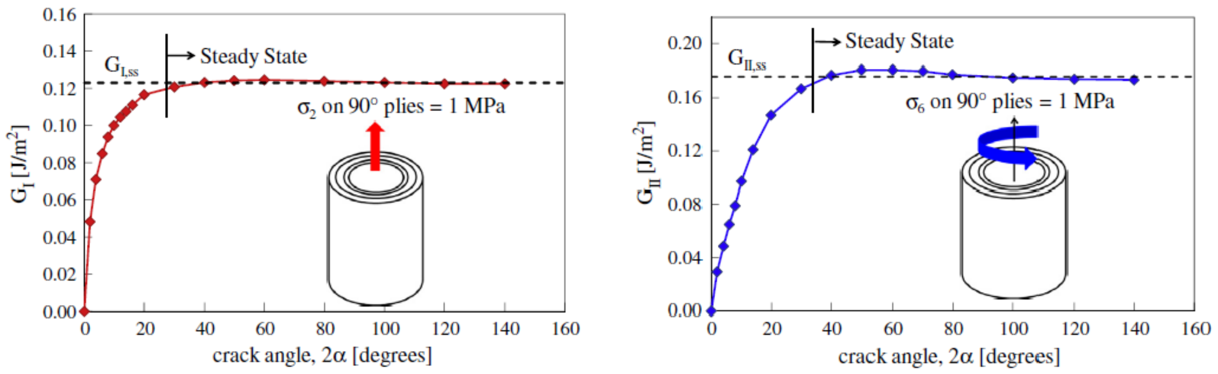

Figure 136. Mode I and Mode II SERR related to the crack propagation of a GFRP tubular specimen subjected to combined tensile and torsion loads [44]. The trend is similar to those of the Mode II and Mode III SERR in this thesis.

One of the major conclusion drawn in the experimental work of McLeave [19] was that the presence of shear stress on the specimens loaded in compression has a detrimental effect on the components lifetime. As it can be observed in the S-N data resulting from the fatigue tests, shown in Figure 137 and Figure 138, the crack initiation lifetime of the plies was decreased of approximately one order of magnitude when changing from biaxiality ratio $\lambda_{12} = 0.21$ to $\lambda_{12} = 0.4$. From a fracture mechanics point of view, the effect of the shear on the lifetime of the specimen can be explained by looking at the results of the SERR obtained from the simulations. Considering the same compressive stress and crack opening angle, the Mode II SERR values obtained from the simulations with biaxiality ratio equal to $\lambda_{12} = 0.4$ were about 70 % higher than those obtained with $\lambda_{12} = 0.21$ (Figure 127). This gave a higher total SERR, meaning that a higher amount of energy was released at the crack tip considering the same crack extension. According to the energetic approach, a certain amount of energy per unit of area is required at the crack tip in order to propagate the crack [60]. The criterion for having fracture propagation is:

$$G \geq G_C$$

where G is the total energy release rate available at the crack tip and G_C is the fracture toughness of the material. G depends on the applied load, on the crack length and on the geometry of the body, while G_C is considered a property of the material. According to this failure criterion, if G is lower than G_C, the crack cannot grow. If instead G becomes equal to G_C, the crack can propagate. When G overcomes G_C, the crack will become unstable and will grow rapidly until the body is completely fractured [60]. The higher is G, the more rapidly the fracture will propagate. This can explain the influence of the shear load on the lifetime of the compressed tubular specimens. By increasing the shear load in fact, the Mode II SERR was increasing. Therefore, the total SERR for the cases with biaxiality ratio $\lambda_{12} = 0.4$ was higher, causing a more rapid crack propagation and a reduction in the tubular specimens lifetime.

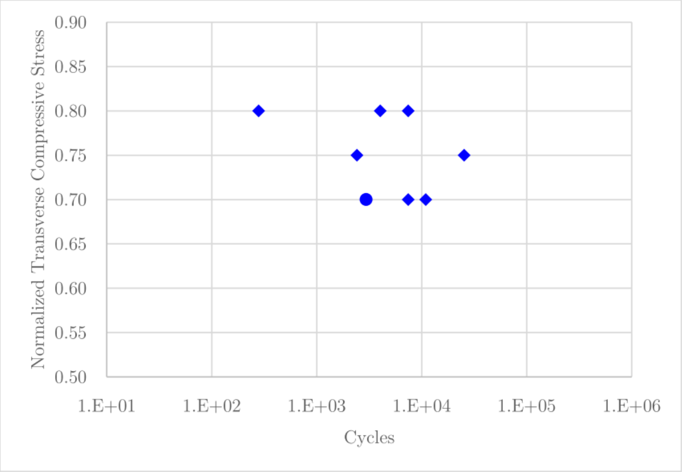

Figure 137. S-N data for $\lambda_{12} = 0.21$. Diamond markers represent data points obtained at 10 Hz, while circle markers represent data points obtained at 5 Hz [19].

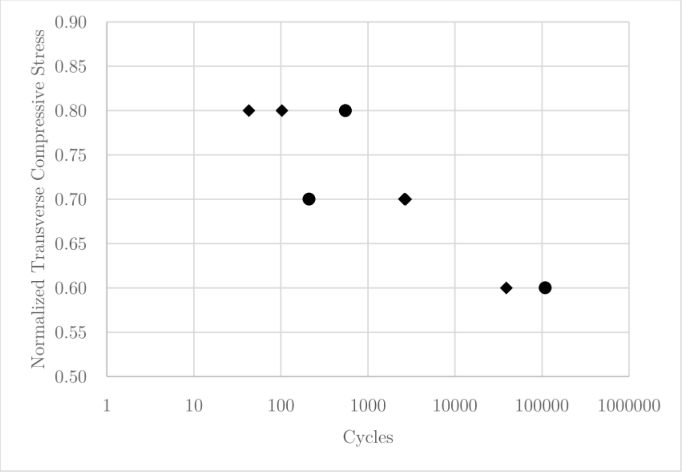

Figure 138. S-N data for $\lambda_{12} = 0.4$. Diamond markers represent data points obtained at 10 Hz, while circle markers represent data points obtained at 5 Hz [19].

The effect of friction between the crack surfaces on the final SERR results was studied. Since the real friction coefficient present between the two surfaces was not available, a general investigation was developed considering different friction coefficient values and studying their effect on the SERR results. The presence of friction decreased the steady state value of the SERR for both Mode II and Mode III. The Mode II SERR was more sensitive to the friction coefficient value, since its reduction with respect to the ideal frictionless case SERR was higher than that observed in the Mode III SERR. A possible explanation on the effect of the friction on the SERR can be found in the definition of the energy release rate. The energy release rate is defined as the ratio between the energy dissipated during the fracture propagation and the new fracture surface generated during the crack extension [60]. The energy considered is the one dissipated at the crack tip in the form of irreversible deformation, heat, sound and surface energy. Being friction a source of energy dissipation, it is probable that when the two surfaces are in contact the friction force dissipates part of the energy of the system. In this way, the amount of energy that is dissipated at the crack tip is reduced and, therefore, the strain energy release will be lower. Increasing the compression load, the friction force increased and therefore the difference in the SERR between the ideal case and the friction case became larger. For this reason, the model with the real loading conditions was more sensitive to the presence of friction with respect to the case with only 1 MPa of effective stresses.

6. Conclusions

6.1. Thermoplastic GFRP Panels Manufacturing

The main objective of this project was setting up a VARTM process for producing GFRP panels utilizing an innovative thermoplastic resin for the matrix material. The setup was completed successfully after having applied several improvements to the process. The thermoplastic Elium® resin demonstrated to be suitable for infusion processes at low pressure, such as the VARTM, thanks to its low viscosity. The main outcome of the experimental procedure was that the quality of the panels was strongly dependent on the direction and on the speed of the resin flow inside the mold. The speed of the resin flow was influenced by the direction of the preform fibers with respect to the flow and by the vacuum pressure inside the mold, which had a predominant effect. While the effect of the fibers direction was studied and improved, it was not possible to act on the pressure due to a technical limitation of the pump utilized. The validity of the process was confirmed by the quality tests performed on the panels.

The overall quality of the panels produced was good. Thanks to the optical microscopy analysis of the microstructure, it was possible to observe that a full wetting of the preform and low void content were obtained during the production. Nevertheless, a quality difference between the region of the panels near the inlet hose and the region near the outlet hose was noticed. While the microstructure of the material in the samples cut near the outlet side of the panels was uniform and almost completely free from voids, the microstructure of the samples cut near the inlet side was presenting defects. Small voids were noticed inside the material and on the upper surface of the sample. Moreover, most of the panels showed defects also on the lower surface at the region near the inlet side. The defects, observable in the form of grooves running parallel to the fiber rovings, were related to the resin that was dissolving the release agent. This washing effect was causing difficulties during the release of the part from the mold. Unfortunately, due to time limitations, it was not possible to investigate further and try to solve these problems. In general, the surface of the panels that was in contact with the rigid side of the mold had good surface finishing. On the opposite, the surface of the panels that was in contact with the vacuum bag had the texture left by the peel ply and it was presenting small undulations that were causing small thickness variation. This last is an intrinsic disadvantage of the VARTM process with flexible mold side, which allows to obtain a high surface quality only on one side of the components. The DMA test confirmed that the polymerization of the resin, carried out at room temperature inside the mold, was completed correctly and no residuals monomer were obtained.

6.1.1. Recommendations and Areas of Future Investigation

Additional testing is necessary in order to complete the validation and optimization of the process. In this section the main recommendations for going forward with the research are discussed.

One of the main aspects that must be investigated deeply in the future is the quality difference between the inlet side region and the remaining part of the panels. As it was discussed previously, the region of the panels near the inlet side was showing a higher amount of voids inside the matrix and on the upper surface. A possible improvement to the process could be utilizing a lower vacuum level inside the mold (higher pressure), which would slow down the resin flow in the infusion mesh and in the preform. The pressure inside the mold utilized during the panels production was 95 kPa below the atmospheric pressure. In order to decrease the vacuum level, the use of a less powerful pump or of one that can be regulated is recommended. Another option for reducing the speed of the resin flow would be infusing the resin at a pressure lower than the atmospheric one, as it was described in the study of Kedari et al. [58], but this would complicate the infusion system. Another recommendation aimed in eliminating or reducing the quantity of small voids inside the matrix material and on the upper surface of the panels is performing the degassing of the resin after that it is transferred inside the mixing container. This action would remove the small air bubbles that were forming during the pouring operation and could increase the quality of the panels. Another problem that must be solved is the presence of the grooves on the lower surface of the panels in the region near the inlet side. The issue was related to the washing effect of the release agent employed that, due to an incompatibility with the resin, was dissolved and it was not allowing the complete releasing of the part. For this reason, in order to improve the quality of the future components, a different release agent compatible with the Elium® resin should be utilized.

A further aspect that must be investigated is finding the relationship between the quantity of resin utilized for producing a panel and the resulting fiber volume fraction. As it was described previously, the acid digestion test was performed with this purpose but an error in the procedure led to incorrect results. For this reason, it is recommended to perform again the test by measuring directly the volume of the samples in order to obtain accurate results.

Once the validation of the process and its optimization will be completed, the following step will be the mechanical characterization of the novel GFRP material. It is important to obtain the longitudinal and transverse tensile and compression strengths of the material, as well as its fracture toughness and resistance to delamination. The mechanical characterization of the material is useful in order to compare its properties with similar glass fiber/epoxy materials. The final step of the research will be adapting the process that was setup in this work for manufacturing thermoplastic GFRP wind turbine blades.

6.2. Ply Crack Growth in GFRP Composites

In the computational part of the project, a model able to simulate the fracture behavior observed in experimental tests on tubular GFRP specimen with layup $[0_F/90]_S$ subjected to multiaxial state of stress was developed. The multiaxial state of stress was composed by combined transverse compression and shear loads. The model simulated the presence of the crack inside the unidirectional 90° plies by leaving unconstrained the region corresponding to the crack surface. The crack propagation was simulated by extending manually the unconstrained region. The procedure was manual because the final objective was to replicate exactly the fracture encountered during the experimental tests and compute the strain energy release rate related to the crack propagation using a modified VCCT method.

The main result emerged from the simulations was that the SERR of both Mode II and Mode III increases quickly at the beginning of the crack propagation, when the crack surface is small, and then stabilizes reaching a steady state condition. The Mode III SERR reached the steady state condition almost immediately, after only 15° COA, while the Mode II SERR growing rate was slower and reached the steady state conditions at about 55° COA.

The presence of a higher shear load gave higher total SERR. It was noticed how, by considering the same compressive load and halving the shear load, the Mode II SERR was decreasing of about 70 % and the total SERR of about 15 %. These results matched the experimental results obtained from the fatigue tests on the tubular specimen [19], where it was observed that, by doubling the shear load, the lifetime of the plies was decreasing of almost one order of magnitude. When the SERR is higher in fact, the crack propagation is faster and this leads to a shorter lifetime of the components that reach failure sooner.

The effect of the presence of friction between the crack surfaces that are pressed one against the other was investigated. The study was performed considering different friction coefficients because the real value characterizing the contact between the 90° plies surfaces was missing. The results showed that the SERR decreases as the friction coefficient increases. The higher is the compressive load, the lower are the Mode II and Mode III SERR, because the friction force becomes higher and its dissipation effect increases. The Mode II SERR demonstrated to be more sensitive to the presence of friction with respect to the Mode III SERR.

6.1.2. Recommendations and Areas of Future Investigation

The manual procedure employed for simulating the crack propagation and computing the SERR was extremely time consuming. The crack had to be displaced manually simulation by simulation, removing the boundary conditions from the nodes that were belonging to the crack surfaces. The simulations were lasting about 1 hour and the computation of the average surface displacement was done manually on MS Excel since Abaqus CAE does not include an option for obtaining directly the result from the post processing. For this reason, in case of future applications of this method, it is recommended to try to automate the process of crack propagation, simulations and extraction of data on Abaqus CAE through a Python script.

A possible work that could be developed in the future is the correlation of the SERR profiles obtained with the data of the crack length versus the number of cycles of the tubular specimens. Another area of investigation could be the study of the effective friction coefficient that characterizes the contact between the two surfaces of continuous glass fibers/epoxy material, in order to find the effective values of SERR related to the crack propagation in the 90° plies.

References

[1] *Regulation (EU) 2019/631 of the European Parliament and of the Council,* 2019.

[2] W. Joost, "Reducing Vehicle Weight and Improving U.S. Energy Efficiency Using Integrated Computational Materials Engineering," *JOM,* vol. 64, no. 9, p. 1032–1038, 2012.

[3] J. Hofer, E. Wilhelm and W. Schenler, "Optimal Lightweighting in Battery Electric Vehicles.," *World electric vehicle journal,* vol. 5, no. 3, p. 751–762, 2012.

[4] G. Belingardi, G. Genta and P. Campagna, "Hybrid composite technology for automotive drive shaft: a computer aided optimization," in *Proc. ISATA 85 Conference*, Graz, Austria, 1985.

[5] A. Elmarakbi, Advanced Composite Materials for Automotive Applications : Structural Integrity and Crashworthiness, Chichester, West Sussex, United Kingdom: John Wiley & Sons Inc., 2014.

[6] K. K. Chawla, Composite Materials Science and Engineering, 3rd ed., New York: Springer, 2012.

[7] Y.-J. Lee, Y.-T. Jhan and C.-H. Chung, "Fluid–structure Interaction of FRP Wind Turbine Blades Under Aerodynamic Effect," *Composites: Part B, Engineering,* vol. 43, no. 5, p. 2180–2191, 2012.

[8] W. Contributor, "Windpower Engineering & Development - "How composite materials influence blade sizes and functions"," 6 Gennaio 2020. [Online]. Available: https://www.windpowerengineering.com/how-composite-materials-influence-blade-sizes-and-functions/. [Accessed 1 Settembre 2020].

[9] K. Wood, "Composites World - "Wind turbine blades: Glass vs. Carbon"," 31 Marzo 2020. [Online]. Available: https://www.compositesworld.com/articles/wind-turbine-blades-glass-vs-carbon-fiber. [Accessed 29 Agosto 2020].

[10] B. A. Strong, Fundamentals of Composites Manufacturing, Society of Manufacturing Engineers, 2008.

[11] S. V. Hoa, Principles of the Manufacturing of Composite Materials, Lancaster, Pennsylvania, U.S.A.: DEStech Publications, Inc., 2009.

[12] M. Nikforooz, J. Montesano, M. Golzar and M. M. Shokrieh, "Fatigue Behavior of Laminated Glass Fiber Reinforced Polyamide.," *Procedia engineering,* vol. 213, p. 816–823, 2013.

[13] Arkema , "Elium® resin: a disruptive innovation in the world of composites?," 3 Luglio 2019. [Online]. Available: arkema.com/en/webzine/story/Elium-resin-a-disruptive-innovation-in-the-world-of-composites/. [Accessed 5 Settembre 2020].

[14] A. Baumann, S. Backe and J. Hausmann, "Investigation of the Fatigue Behavior of Thermoplastic Composites by Load Increase Tests.," *Journal of composite materials ,* 2020.

[15] H. Hamada, J. Coppola, D. Hull, Z. Maekawa and H. Sato, "Comparison of Energy Absorption of Carbon/epoxy and carbon/PEEK Composite Tubes.," *Composites,* vol. 23, no. 4, p. 245–252, 1992.

[16] *Directive 2005/64/EC of the European Parliament and of the Council,* 2005.

[17] Borrum Energy Solutions, "Borrum Energy Solutions - About Us," [Online]. Available: https://borrumenergysolutions.ca/pages/about-us. [Accessed 10 Ottobre 2020].

[18] Arkema, "Elium® resins for composites," [Online]. Available: https://www.arkema.com/en/products/product-finder/range-viewer/Elium-resins-for-composites/. [Accessed 10 Ottobre 2020].

[19] B. McCleave, Cracking Behaviour of Glass Fibre-Reinforced Polymers Under Combined Compression-Shear Cyclic Loading, University of Waterloo, 2018.

[20] S. G. Advani and E. M. Sozer, Process Modeling in Composites Manufacturing, Boca Raton, Florida: CRC Press, 2010.

[21] I. M. Daniel and O. Ishai, Experimental Methods for Characterization and Testing of Composite Materials, Oxford UP, 2006.

[22] S. V. Lomov, Non-Crimp Fabric Composites: Manufacturing, Properties and Applications., Cambridge: Elsevier Science & Technology, 2011.

[23] N. Naik, M. Sirisha and A. Inani, "Permeability characterization of polymer matrix composites by RTM/VARTM," *Progress in Aerospace Sciences,* vol. 65, pp. 22-40, 2014.

[24] C. Polowick, "Optimizing Vacuum Assisted Resin Transfer Moulding (VARTM) Processing Parameters to Improve Part Quality," Carleton University, Ottawa, Ontario, Canada, 2013.

[25] W. Seemann, "Plastic Transfer Molding Techniques for the Production of Fiber". USA Patent US4902215A, 1989.

[26] R. F. Gibson, Principles of Composite Material Mechanics., Mechanical Engineering, 2016.

[27] R. Talreja and C. Singh, Damage and Failure of Composite Materials, Cambridge: Cambridge University Press, 2012.

[28] R. Talreja and J. Varna, Modelling damage, fatigue and Failure of Composite materials., Woodhead Publishing, 2015.

[29] J. Montesano and C. V. Singh, "A Synergistic Damage Mechanics Based Multiscale Model for Composite Laminates Subjected to Multiaxial Strains.," *Mechanics of materials,* vol. 83, pp. 72-89, 2015.

[30] V. G. K. Menta, "Advanced composites using non-autoclave processes: manufacturing and characterization," Missouri University of Science and Technology, Rolla, Missouri, 2011.

[31] S. Torkamani, S. Roy, M. E. Barkey, E. Sazonov, S. Burkett and S. Kotru, "A novel damage index for damage identification using guided waves with application in laminated composites.," *Smart Materials and Structures,* vol. 23, no. 9, 2014.

[32] A. Nagabhushana, M. Spiegel, S. Adu, N. Hayes, D. Paul, K. Trivedi, B. Fairbee, H. Zheng, A. Gerrity, S. Kotru, S. Roy, M. Barkey and S. Burkett, "Numerical analysis for stuctural health monitoring of a damages composite panel using PZT actuatoors and sensors.," *Smart Sensor Phenomena, Technology, Networks, and Systems Integration,* vol. 8346, 2012.

[33] T. Yokozeki, W. Yamazaki and Y. Kobayashi, "Investigation into property control of VaRTM composites by resin infusion process," *Advanced Composite Materials,* vol. 24, pp. 1-13, 2014.

[34] G. Ben, A. Hirabayashi, K. Sakata, K. Nakamura and N. Hirayama, "Evaluation of new GFRTP and CFRTP using epsilon caprolactam as matrix fabricated with VaRTM," *Science and Engineering of Composite Materials,* vol. 22, no. 6, p. 10, 2015.

[35] E. Louisy, F. Samyn, S. Bourbigot, G. Fontaine and F. Bonnet, "Preparation of Glass Fabric/Poly(l-lactide) Composites by Thermoplastic Resin Transfer Molding," *Polymers,* vol. 11, no. 339, p. 8, 2019.

[36] Arkema, "Elium® resin brochure," 2017. [Online]. Available: https://www.arkema.com/export/shared/.content/media/downloads/products-documentations/incubator/brochure-elium-2017.pdf.

[37] M. E. Kazemi, L. Shanmugam, D. Lu, X. Wang, B. Wang and J. Yang, "Mechanical properties and failure modes of hybrid fiber reinforced polymer composites with a novel liquid thermoplastic resin, Elium®," *Composites Part A: Applied Science and Manufacturing,* vol. 125, p. 12, 2019.

[38] M. Kazemi, L. Shanmugam, Z. Li, R. Ma, L. Yang and J. Yang, "Low-velocity impact behaviors of a fully thermoplastic composite laminate fabricated with an innovative acrylic resin," *Composite Structures,* vol. 250, p. 11, 2020.

[39] L. C. M. Barbosa, D. B. Bortoluzzi and A. C. Ancelotti, "Analysis of fracture toughness in mode II and fractographic study of composites based on Elium® 150 thermoplastic matrix," *Composites Part B: Engineering,* vol. 175, p. 10, 2019.

[40] W. Obande, D. Mamalis, D. Ray, L. Yang and C. M. Ó Brádaigh, "Mechanical and thermomechanical characterisation of vacuum-infused thermoplastic- and thermoset-based composites," *Materials & Design,* vol. 175, p. 13, 2019.

[41] P. Khalili, B. Blinzler, R. Kádár, R. Bisschop, M. Försth and P. Blomqvist, "Flammability, Smoke, Mechanical Behaviours and Morphology of Flame Retarded Natural Fibre/Elium® Composite," *Materials (Basel),* no. 2648, p. 12, 2019.

[42] M. Kazemi, L. Shanmugam, S. Chen, L. Yang and Y. J. , "Novel thermoplastic fiber metal laminates manufactured with an innovative acrylic resin at room temperature," *Composites: Part A,* p. 43, 2020.

[43] D. Mamalis, W. Obande, V. Koutsos, J. Blackford, C. O'Bradaigh and D. Ray, "Novel thermoplastic fibre-metal laminates manufactured by vacuum resin infusion: The effect of surface treatments on interfacial bonding," *Materials & Design,* vol. 162, pp. 331-344, 2018.

[44] M. Quaresimin and P. Carraro, "Damage Initiation and Evolution in Glass/epoxy Tubes Subjected to Combined Tension–torsion Fatigue Loading," *International journal of fatigue,* vol. 63, pp. 25-35, 2014.

[45] M. Quaresimin, P. Carraro and L. Maragoni, "Influence of Load Ratio on the Biaxial Fatigue Behaviour and Damage Evolution in Glass/epoxy Tubes Under Tension–torsion Loading.," *Composites. Part A, Applied science and manufacturing,* vol. 78, p. 294–302, 2015.

[46] F. Schmidt, M. Rheinfurth, P. Horst and G. Busse, "Effects of Local Fibre Waviness on Damage Mechanisms and Fatigue Behaviour of Biaxially Loaded Tube Specimens.," *Composites science and technology,* vol. 72, no. 10, p. 1075–1082, 2012.

[47] F. Schmidt, M. Rheinfurth, P. Horst and G. Busse, "Multiaxial Fatigue Behaviour of GFRP with Evenly Distributed or Accumulated Voids Monitored by Various NDT Methodologies.," *International journal of fatigue,* vol. 43, p. 207–216, 2012.

[48] C. Capela, J. Ferreira, T. Febra and J. Costa, "Fatigue Strength of Tubular Carbon Fibre Composites Under Bending/torsion Loading.," *International journal of fatigue,* vol. 70, p. 216–222, 2015.

[49] E. Rybicki and M. Kanninen, "A Finite Element Calculation of Stress Intensity Factors by a Modified Crack Closure Integral," *A Finite Element Calculation of Stress Intensity Factors by a Modified Crack Closure Integral,* vol. 9, no. 4, p. 931–938, 1977.

[50] K. N. Shivakumar, P. W. Tan and J. C. J. Newman, "A Virtual Crack-Closure Technique for Calculating Stress Intensity Factors for Cracked Three Dimensional Bodies," *International journal of fracture,* vol. 36, pp. 43-50, 1988.

[51] D. Xie and S. B. Biggers, "Progressive Crack Growth Analysis Using Interface Element Based on the Virtual Crack Closure Technique," *Finite elements in analysis and design,* vol. 42, no. 11, pp. 977-984, 2006.

[52] D. Xie and S. B. Biggers, "Strain Energy Release Rate Calculation for a Moving Delamination Front of Arbitrary Shape Based on the Virtual Crack Closure Technique. Part I: Formulation and Validation," *Engineering fracture mechanics,* vol. 73, no. 6, pp. 771-785, 2006.

[53] D. Swan (Arkema Inc.), *personal communication,* 24 September 2020.

[54] K. van Rijswijk and H. Bersee, "Reactive Processing of Textile Fiber-Reinforced Thermoplastic Composites – An Overview," *Composites Part A: Applied Science and Manufacturing,* vol. 38, no. 3, p. 666–681, 2007.

[55] A. D3171-15, Standard Test Methods for Constituent Content of Composite Materials, West Conshohocken, PA: ASTM International, 2015.

[56] Dynamic Mechanical Analysis (DMA). A Beginner's Guide., PerkinElmer, Inc., 2008-2013.

[57] N. Kuentzer, P. Simacek, S. G. Advani and S. Walsh, "Correlation of Void Distribution to VARTM Manufacturing Techniques.," *Composites. Part A, Applied science and manufacturing,* vol. 38, no. 3, p. 802–813, 2007.

[58] V. R. Kedari, B. I. Farah and K.-T. Hsiao, "Effects of vacuum pressure, inlet pressure, and mold temperature on the void content, volume fraction of polyester/e-glass fiber composites manufactured with VARTM process.," *Journal of Composite Materials,* vol. 45, no. 26, pp. 2727-2742, 2011.

[59] J. S. Rajadurai and G. Thanigaiyarasu, "Failure Envelope Generation Using Modified Failure Criteria for Wind Turbine Blade and Validation for FRP Laminates.," *Mechanics of advanced materials and structures,* vol. 16, no. 4, p. 275–292, 2009.

[60] A. T. Zehnder, Fracture Mechanics, Springer Netherlands, 2012.

[61] M. Janssen, J. Zuidema and R. Wanhill, Fracture Mechanics, Second Edition, DUP Blue Print, 2004.

[62] 3. D. Systémes, "Abaqus/CAE User's Guide - Understanding Interactions," 3ds Dassault Systémes, [Online]. Available: https://abaqus-docs.mit.edu/2017/English/SIMACAECAERefMap/simacae-c-itnconcepts.htm. [Accessed 28 Agosto 2020].

[63] G. Mehoub, "Adhesive wear and frictional behaviour of glass fibre reinforced thermoset composites.," 2013.

[64] B. Suresha, G. Chandramohan, S. Rao, S. P. R., S. S. P. and V. Venkateswarlu, "Friction and slide wear characteristics of glass-epoxy and glass-epoxy filled with SiCp composites.," *Indian Journal of Engineering and Materials Sciences ,* vol. 13, no. 6, 2006.

[65] N. El-Tayeb and R. Gadelrab, "Friction and Wear Properties of E-Glass Fiber Reinforced Epoxy Composites Under Different Sliding Contact Conditions.," *Wear,* vol. 192, p. 112–117, 1996.